CORA Cork Open Research Archive
Cartlann Taighde Oscailte Chorcaí

Title	Evolution of the magnetic field structure in the jet outflows from active galaxies
Authors	Knuettel, Sebastian
Publication date	2020-05
Original Citation	Knuettel, S. 2020. Evolution of the magnetic field structure in the jet outflows from active galaxies. PhD Thesis, University College Cork.
Type of publication	Doctoral thesis
Rights	© 2020, Sebastian Knuettel. - https://creativecommons.org/licenses/by-nc-nd/4.0/
Download date	2024-04-18 20:44:58
Item downloaded from	https://hdl.handle.net/10468/10052

UCC
University College Cork, Ireland
Coláiste na hOllscoile Corcaigh

Evolution of the Magnetic Field Structure in the Jet Outflows from Active Galaxies

Sebastian Knuettel
BSc
111312086

NATIONAL UNIVERSITY OF IRELAND, CORK

SCHOOL OF SCIENCE

DEPARTMENT OF PHYSICS

Thesis submitted for the degree of Doctor of Philosophy

May 2020

Head of Department: Prof. John G. McInerney

Supervisor: Prof. Denise C. Gabuzda

Research supported by The Irish Research Council

Contents

List of Figures . . . iii
List of Tables . . . vi
Acknowledgements . . . ix
. . . x
Abstract . . . xii

1 Introduction **1**
1.1 Active Galactic Nuclei . . . 1
1.1.1 A Brief History of Extragalactic Astronomy . . . 1
1.1.2 AGN Classification . . . 3
1.1.2.1 Radio Quiet AGN . . . 3
1.1.2.2 Radio Loud AGN . . . 4
1.1.2.3 A Unifying Model for AGN . . . 7
1.1.3 Physical Processes in AGN Jets . . . 9
1.1.3.1 Jet Launching and Collimation . . . 11
1.1.4 The Cosmic Battery . . . 13
1.1.5 Synchrotron Radiation . . . 17
1.1.6 Faraday Rotation . . . 23

2 Radio Interferometry Methods and Techniques **28**
2.1 Radio Interferometry basics . . . 29
2.1.1 The Radio Interferometer . . . 29
2.1.2 The Need for Calibration . . . 32
2.1.3 Imaging and Self-calibration . . . 34
2.2 Polarization in Radio Interferometry . . . 37
2.2.1 Stokes parameters and Polarized feeds in Radio Interferometers . . . 38
2.2.2 Polarization Calibration . . . 44
2.3 Analysis of Polarization Observations using Faraday Effects . . . 48
2.3.1 Calculating Faraday depth by fitting χ against λ^2 . . . 48
2.3.2 Rotation Measure Synthesis and QU Fitting . . . 51

3 Faraday RM gradients in Kiloparsec Scale Radio Jets **59**
3.1 Statistically Significant Results . . . 62
3.1.1 NGC 6251 . . . 62
3.1.2 3C 465 . . . 68
3.1.3 A2142a . . . 74
3.1.4 5C 4.114 . . . 78
3.1.5 Coma A . . . 81
3.1.6 IC 4296 . . . 86
3.1.6.1 RM synthesis of IC 4296 . . . 87
3.2 Tentative and Negative Results . . . 91
3.2.1 3C 303 . . . 91
3.2.2 5C 4.152 . . . 94
3.2.3 3C 219 . . . 97

3.3 Summary of Results 99

4 Estimating the magnetic field strength in the Faraday screen surrounding Coma A 103
4.1 Introduction 103
4.1.1 Coma A 104
4.1.2 Polarization and Faraday rotation 105
4.2 Observations and data reduction 106
4.2.1 Wide band VLA observations 106
4.2.2 Archival VLA observations 109
4.2.3 Hα observations 110
4.3 QU model fitting procedure 110
4.4 Results 111
4.4.1 Radio structure of Coma A 111
4.4.2 QU model fitting 113
4.4.2.1 Northern lobe 113
4.4.2.2 Southern lobe 116
4.4.3 Estimation of magnetic field strengths 121
4.4.3.1 Magnetic field strength in Faraday screen of Northern lobe 123
4.4.3.2 Magnetic field strength in Faraday screen of Southern lobe 125
4.5 Summary 128

5 Faraday Rotation Measure study of the magnetic field environments of 3C 433 and 3C 382 130
5.1 Rotation Measure mapping and Polarization Model Fitting Procedure 131
5.2 3C 433 132
5.2.1 Observations and data reduction 135
5.2.2 Results 136
5.2.2.1 Rotation measure mapping 137
5.2.2.2 *QU* model fitting 141
5.3 3C 382 151
5.3.1 Observations and data reduction 155
5.3.2 Rotation measure Mapping 156
5.3.3 *QU* Model fitting 160
5.4 Summary 165

6 Conclusions 167
6.1 Magnetic fields in AGN jets on large scales: The Cosmic Battery 168
6.2 The interplay between external gas and the lobes of the radio galaxy Coma A 170
6.3 Rotation measure analysis of 3C 433 and 3C 382 using wideband observations 171

List of Figures

1.1 Example of a typical FR I radio jet, with labelled features. . . . 5
1.2 Example of a Typical FR II radio jet, with labelled features. . . . 6
1.3 Diagram explaining unified model for AGN. 9
1.4 Montage of the FR-I radio galaxy M87, on scales from the outer lobes to near the black hole. 10
1.5 Schematic of the system of magnetic fields expected by the cosmic battery. 14
1.6 A figure showing the range of angles for which the synchrotron radiation would be Doppler boosted. 19
1.7 Figure showing how LCP and RCP combine to give linear polarization angle. 26

2.1 A diagram of a simple 2 element interferometer. 30
2.2 Diagram of a phase referencing observation with a radio interferometer. 33
2.3 Diagram of polarization ellipse with principal axes at angle. . . 39
2.4 How the axes and components of the electric field vector are set up to define the Stokes parameters. 41
2.5 Schematic showing how polarized correlated flux changes with parralctic angle. 47
2.6 Example of χ versus λ^2 fit to determine RM. 49
2.7 Example of RMTF function for VLA observation. 54
2.8 Example of a cleaned Faraday spectrum for a VLA observation. . 55
2.9 Schematic of internal depolarization in λ^2 and Faraday space. . 57
2.10 Schematic of external depolarization in λ^2 and Faraday space. . 57

3.1 Schematic of toroidal magnetic field as gradient in RM. 61
3.2 RM and χ_0 map of NGC 6251 made using 1.3–4.8 GHz archival data. 64
3.3 Inner region of RM map of NGC 6251 and RM gradient significance as function of distance along jet. 65
3.4 RM map of NGC 6251 made using 4.5–6.5 GHz data and plot of RM gradient significance as function distance along jet. 67
3.5 RM map of 3C 465 made using 4–9 GHz data. 70
3.6 χ_0 map of 3C 465. 71
3.7 Plot of gradient significance as function of distance along the jet for 3C 465. 72
3.8 Spectral index map of 3C 465 made using 1–2 GHz data. 73
3.9 RM map of 3C 465 made using RM synthesis with 1–2 GHz data. 75
3.10 RM map of A2142A made using 4.5–8.5 GHz data. 76
3.11 Plot of gradient significance as function of distance along the jet for A2142A. 77
3.12 Map of χ_0 for A2142A. 77

3.13 RM map of 5C 4.114 made using 1.4–4.9 GHz data with RM gradients plotted. 79
3.14 Map of χ_0 for 5C 4.114. 80
3.15 Plots of RM gradient significance as function of distance along the jet for 5C 4.114. 80
3.16 RM map of Coma A made using 1.4–15 GHz data. 82
3.17 Slice of transverse RM values associated with RM gradient for Coma A 83
3.18 Plot of RM gradient significance as function of distance along the jet for Coma A. 83
3.19 Map of χ_0 for Coma A. 84
3.20 RM map of Coma A made using 1–2 GHz data. 84
3.21 Transverse slice of RM values associated with gradient in 1–2 GHz RM map. 85
3.22 RM map of IC 4296 made using 1–2 GHz data with plots of RM gradient significance as function of distance along the jets. . . . 88
3.23 Map of χ_0 for IC 4296 89
3.24 Zoomed in region of Southern jet feature in RM map of IC 4296 89
3.25 RMTF for 1–2 GHz data of IC 4296 with example of RMCLEANed Faraday depth spectrum. 90
3.26 RM map of IC 4296 made using $\phi_{\rm peak}$ from RM synthesis. 91
3.27 RM maps of 3C 303 made using 1.3–15 GHz data. 92
3.28 Map of χ_0 for 3C 303. 93
3.29 Plot of gradient significance as function of distance along the jet for 3C 303. 94
3.30 Maps of RM and χ_0 for 5C 4.152 made using 4.5–8.3 GHz data. 95
3.31 Plots of RM gradient significance as function of distance along the jet for 5C 4.152. 96
3.32 RM map of 3C 219 made using 1.3–4.8 GHz data with accompanying slice of RM values associated with a transverse gradient. . 97
3.33 Map of χ_0 for 3C 219. 98
3.34 Plot of transverse RM gradient significance as function of distance along the jet for 3C 219 98

4.1 Spectral index and contour map of Coma A made using 2–4 GHz data with features labelled. 107
4.2 Model fit for the 1–2 GHz data. 112
4.3 Model fit data for the 2–4 GHz data. 113
4.4 Maps of the RM and $\sigma_{\rm RM}$ values from the model fitting to 1–2 GHz data. 114
4.5 Maps of RM, $\sigma_{\rm RM}$, p_0, and χ_0 values from the model fitting to the 2–4 GHz data. 115
4.6 X-ray and Hubble images showing jet deflection point in detail for Coma A. 116
4.7 Histograms of the RM distribution in the lobes of Coma A. . . . 117

4.8 Images showing fractional polarization at 4.9 GHz and Hα intensity in Coma A. 119
4.9 Images showing fractional polarization at 15 GHz and Hα intensity in Coma A. 120

5.1 Spectral index and contour map of 3C 433 made using 2–4 GHz data. 135
5.2 RM map and contour map of 3C 433 for 2–4 GHz data. 138
5.3 χ_0 and fractional polarization maps for 3C 433 at 3 GHz. 139
5.4 The RMTF for the 3C 433 data in the 1–4 GHz range. 140
5.5 $F(\phi)$ for a high polarized intensity region in the Southern lobe of 3C 433. 141
5.6 RM map of 3C 433 made using the $\phi_{\rm peak}$ value from RM syhthesis from 1–4 GHz. 142
5.7 Plots of RMCLEANed Faraday spectra for various regions in 3C 433. 143
5.8 High resolution maps of 3C 433 at 8.4 GHz. 144
5.9 Model fit for the Southern hotspot of 3C 433. 145
5.10 Stokes I contours and polarization vectors at 8.4 GHz for 3C 433. 146
5.11 Model fit for the upper region in the Southern lobe of 3C 433. . 148
5.12 Model fit for a region with high fractional polarization in the Eastern wing off the Southern jet of 3C 433. 149
5.13 Model fit for the knot in the North-Eastern wing of emission in 3C 433 150
5.14 Spectral index and contour map of 3C 382 made using 2–4 GHz data. 152
5.15 Spectral index and contour map of 3C 382 made using 1–2 GHz data. 153
5.16 Stokes I VLBA contour map of 3C 382 at 15 GHz 154
5.17 RM map of 3C 382 made using the 2–4 GHz data. 157
5.18 Maps of χ_0 and fractional polarization at 3 GHz for 3C382. . . . 158
5.19 RM map of 3C 382 made using the $\phi_{\rm peak}$ value from RM synthesis from 1–4 GHz. 159
5.20 Selection of cleaned Faraday spectra for 3C 382. 160
5.21 Model fit for the knot in the Northern hotspot of 3C 382. 161
5.22 Model fit for the core of 3C 382 163
5.23 Model fit for the Southern hotspot of 3C 382. 164

List of Tables

3.1 Table outlining VLA observations and data used 63
3.2 Table summarizing the RM gradients and their associated electrical currents for large scales, combining the results from Christodoulou et al. (2016) and this thesis. 102

4.1 Table outlining the VLA observations of Coma A. 107
4.2 Table outlining the archival VLA observations of Coma A. . . . 109

5.1 Table outlining the VLA observations of 3C 433 and 3C 382. All observations were done in the VLA B configuration and were part of the same project, 17B-016. 131
5.2 Table outlining the *QU* fitting parameters for a 2 component fit with common Burn depolarization term to the 3C 433 Southern hotspot region and for 2 component fit with individual depolarization terms. 144

I, Sebastian Knuettel, certify that this thesis is my own work and I have not obtained a degree in this university or elsewhere on the basis of the work submitted in this thesis.

Sebastian Knuettel

To my family

Acknowledgements

Firstly, I would like to thank my supervisor, Prof. Denise Gabuzda, for guiding and encouraging me through the years of my PhD. Thank you for inspiring me to study radio astronomy from my early experiences as an undergraduate intern. Thank you for being an amazing supervisor and mentor throughout this journey.

I would like to thank the Irish Research Council, for providing me with the means to pursue my PhD research through the Government of Ireland Postgraduate Scholarship. Thank you to my thesis examiners, Prof. Paul Callanan of UCC and Prof. Martin Hardcastle of the University of Hertfordshire, your suggestions and comments have made this a better thesis.

Thanks also to Dr. Shane O'Sullivan and the research staff at Universidad Nacional Autónoma de México (UNAM) and the University of Hamburg for hosting me during summer research visits, providing me with new insights and refreshing environments for research in radio astronomy.

I would like to thank my colleague in the lab, Fred, for all the discussions and great times shared, making the lab a welcoming and warm environment. I especially thank Dr. Juliana Motter, who visited from Brazil and helped me through my first year as a PhD student, you were welcome company at the beginning of my postgraduate adventure.

Thanks to my housemates and friends Simon and Davis, who made Aldergrove a home that was worth coming in the door to every evening.

My friends, Shane, Amy, Kevin, Tom, Daire and many more made during my undergraduate and postgraduate time at UCC. I thank you for the fun we shared, providing a welcome distraction. Thanks also to David Rae for vital and insightful coffee breaks when needed most.

Finally, I would like to thank my parents Mona and Stefan, who have always supported me in good times and bad. Without you I would not be the person I am today.

"That may be the most important thing to understand about Humans. It is the unknown that defines our existence. We are constantly searching, not just for answers to our questions but for new questions. We are explorers. We explore our lives day by day, and we explore the galaxy, trying to explore the boundaries of our knowledge, and that is why I am here – not to conquer you with weapons or with ideas, but to coexist and learn."

– Capt. Benjamin Sisko,
Star Trek: Deep Space Nine

Abstract

This thesis concerns studies into the magnetic fields in the jets from active galactic nuclei (AGN). Helical and toroidal magnetic fields are expected to exist in AGN jets close to the jet base and to assist in the launching and collimation of these structures, however if they can persist to the large kiloparsec scales and whether they still affect the jet on those scales is unknown. The magnetic fields of AGN jets are studied using Faraday rotation measure, which is proportional to the line of sight magnetic field strength, a transverse gradient in this value being an indicator of a toroidal magnetic field. It has been predicted by the "Cosmic Battery" model that the direction of any observed kiloparsec scale toroidal field component is such that an associated outward electrical current is present in the jet. Multiwavelength observations of 9 AGN are studied in this thesis. Of these 9 sources, 6 display significant transverse RM gradients on kiloparsec scales, of which 5 indicate toroidal fields with outward associated electrical currents, as predicted by the Cosmic Battery. Furthermore, the magnetic field environments of the jets are analysed as to how much the jets interact with their external medium. These effects can be studied using spectropolarimetry, where the behaviour of fractional polarization and polarization angle over a wide and continuous range of wavelengths can show evidence of strong depolarization and other complex magnetic field effects, some of which can be attributed to interactions with external media. An in-depth analysis of Coma A using wide band observations is presented here with accompanying Hα observations, showing regions of significant depolarization spatially correlated with observed Hα. The Hα can be used to estimate electron density, and in combination with the rotation measure values, the magnetic field can be calculated directly. It is shown that in a particular region, the depolarizing screen features a magnetic field strength upward of 36 μG, indicating the Hα gas was mixing with the radio lobe. In a similar vein, investigations into the radio galaxies 3C 382 and 3C 433 are also presented albeit without accompanying Hα data. However useful new rotation measure maps are provided for these sources, of which none have been published earlier, made using traditional χ versus λ^2 fitting and rotation measure synthesis. Some of the interesting features in these sources are fitted for depolarization models to infer more complex underlying structure and were compared with previous published data at higher resolutions.

Chapter 1

Introduction

1.1 Active Galactic Nuclei

This section features an introduction to Active Galactic Nuclei and their jets. The textbooks Böttcher et al. (2012) and Beckmann & Shrader (2012) were used as a basis for the following introduction.

1.1.1 A Brief History of Extragalactic Astronomy

Active Galactic Nuclei are some of the most luminous objects in the known universe and are the subjects of intense research at all wavelengths due to their high luminosity at all parts of the spectrum from radio waves all the way to gamma rays. Historically the knowledge that there are such vast objects external to our Galaxy is only relatively recent.

The concept of extragalactic astronomy was first discussed by English astronomer Thomas Wright in 1750 and by the German philosopher Emannuel Kant in 1755, who proposed that the many new nebulae that were being discovered at the time were actually collections of stars external to our own Galaxy, romantically dubbed *Welteninseln*–"Island Universes" by Kant. These claims only slowly gathered support with the development of new telescopes and the release of the Herschel catalogue with information gathered in the late 17^{th} and early 18^{th} centuries by William Herschel. Almost a century after Wright and Kant's hypotheses, the new 72 inch diameter Leviathan telescope commissioned by Lord Rosse in Ireland in 1845 allowed astronomers to

distinguish individual stars in these "nebulae" for the first time, which lent further credence to Kant's and Wrights' ideas.

In the early 20^{th} century, the mystery was close to being solved when Vesto Slipher collected spectroscopic observations of a variety of objects and the redshifts calculated for many of these objects predicted a relative velocity to Earth that far exceeded the known value for the escape velocity of the Galaxy, suggesting an extragalactic origin.

It was only in the 1920's that the issue was finally resolved when Edwin Hubble used observations of Cepheid stars in these distant nebulae with the 100" Mt. Wilson telescope to estimate their distances. Using measurements of Cepheids in M31 and M33, Hubble could classify these as being truly extragalactic objects due to their calculated distance of 285 kpc (Hubble underestimated the distance by a factor of $\sim$3). This opened the door for extragalactic astronomy, allowing many more galaxies to be classified.

It was only in the 1940's that research into active galaxies began, when Karl Seyfert classified galaxies with especially luminous centres, whose spectra also showed strong emission lines on top of stellar spectra. The Balmer lines observed in some of these were broader than expected and highly redshifted with observed widths of $> 1000\,\mathrm{km\,s^{-1}}$, much wider than observed in any other known objects at the time. The origin of these luminous regions with unusual emission profiles remained a mystery, and at the time, they were assumed to be due to a very densely populated region of stars or a hyper massive star. Further observations showed that the luminosity came from a compact region of $\sim 100\,\mathrm{pc}$ that must contain a mass of at least $10^8 M_\odot$ for many of these objects.

Later, in 1964, the theory that the centre of an AGN contained a black hole that was actively accreting was put forward (Salpeter 1964). The existence of black holes was not taken to be fact, and it was believed that such singularities were merely hypothetical solutions to Einstein's theories. The black hole model for AGN was a powerful choice, as it explained the large energy output from such a compact region. It is now widely believed that the centre of every galaxy contains such a supermassive black hole, some of which are classified as active while others are not. Our Galaxy, the Milky Way, also holds such a black hole at its centre named Sagittarius A*, as was inferred by the orbits of stars around a massive compact region no larger than 45 AU in the Galactic centre (Ghez et al. 2008), the mass of which is estimated to be approximately

$4 \times 10^6 M_\odot$. The existence of a black hole through direct observations was only demonstrated in 2019, using VLBI to observe the centre of M 87, a bright, radio loud AGN located approximately 16.5 Mpc away. (Event Horizon Telescope Collaboration 2019)

1.1.2 AGN Classification

Due to the large abundance and large variety in the appearance of observed AGN, it is only natural that these be put into categories so they can be better studied, with these categories ultimately being unified under one common model explaining all the various AGN phenomena. Firstly, AGN can be classified according to their radio luminosity under 'radio-loud' and 'radio-quiet' AGN. These terms can be misleading as radio-quiet does not necessarily mean radio silent, just that the ratio of optical to radio flux is quite low. The radio-loudness is defined as (Kellermann et al. 1989):

$$R^* = \left(\frac{f_{5\,\mathrm{GHz}}}{f_{2500\,\text{Å}}} \right), \tag{1.1}$$

where $f_{5\,\mathrm{GHz}}$ is the radio flux at 5 GHz and $f_{2500\,\text{Å}}$ is the optical flux at 2500 Å. One has to be careful with this parameter, however, as measurements can depend on the resolution of the instrument and whether just the core region is considered or the entire galaxy. In the case of radio observations, considerations must be taken of whether lobes are also included in the measurements.

1.1.2.1 Radio Quiet AGN

Seyfert galaxies make up a large number of observed radio quiet AGN. These are AGN that are identified by their optical line properties, and are generally divided into two groups, Seyfert 1 and Seyfert 2 (Khachikian & Weedman 1974). Generally, Seyfert galaxies appear as spiral galaxies with very luminous inner regions. The optical spectra of the cores of Seyfert 1 galaxies show broad Balmer lines such as Hα, Hβ, Hγ and Hδ, and narrow 'forbidden' lines such as the [O II] or [O III] lines, or [N II], [Ne III] and Ne IV, lines. A 'forbidden' line is named such because the atomic transition probability to make such a spectral line is quite low and was therefore not expected to be observed; however these

lines are observed due to the unique conditions present in astronomical objects and environments, such as planetary nebula and AGN, in particular very low densities. Seyfert 2 galaxies, on the other hand, show narrow Balmer and forbidden lines, and usually also feature a less dominant AGN compared to the host galaxy.

Other classifications include Narrow Line Seyfert 1 (NLS1) galaxies (Osterbrock & Pogge 1985), which feature narrow Hβ but broad Hα lines and low luminosity AGN such as low-ionisation nuclear emission line regions (LINER) (Heckman 1980), which have very faint core luminosities compared to host galaxies, making them similar to Seyfet 2s although they have lower luminosities and feature stronger forbidden lines. These low luminosity AGN are believed to be the link between galactic nuclei such as the Milky Way's own Sgr A* and Seyfert Galaxies.

1.1.2.2 Radio Loud AGN

Radio Loud AGN can be very luminous at radio wavelengths. In most cases radio loud AGN reside in elliptical galaxies while the radio quiet variety tend to reside in spiral galaxies. Radio loud AGN often show impressive jet structures which can extend far beyond their host galaxy. The jet structure and luminosity, in particular, can be used to categorise these galaxies further as either Fanaroff-Riley I or II type galaxies (Fanaroff & Riley 1974).

FR I radio galaxies typically have radio luminosities no higher than $L_R = 10^{32}\,\mathrm{erg\,s^{-1}\,Hz^{-1}\,sr^{-1}}$ at 175 MHz. These galaxies usually have jets which have a more plume-like appearance, with the brightest features usually very close to or indeed at the core of the host galaxy itself. It is believed that the lower power of these jets results in a slower jet which moves through the intergalactic medium creating these plumes over scales of many kiloparsecs (De Young 1993). See an example of a typical FR I galaxy in Figure 1.1.

FR II radio galaxies usually have higher radio luminosities and feature a more energetic jet that terminates with bright hotspots, where the jet is believed to impact the intergalactic medium with a resulting shock. These hotspots are associated with lobes of trailing diffuse emission, which can form a cocoon around the inner jet. The hotspots are usually the brightest features in the jets and are located at large distances from the central core. An example is given in Figure 1.2, which shows the typical lobes and hotspot features of an FR II

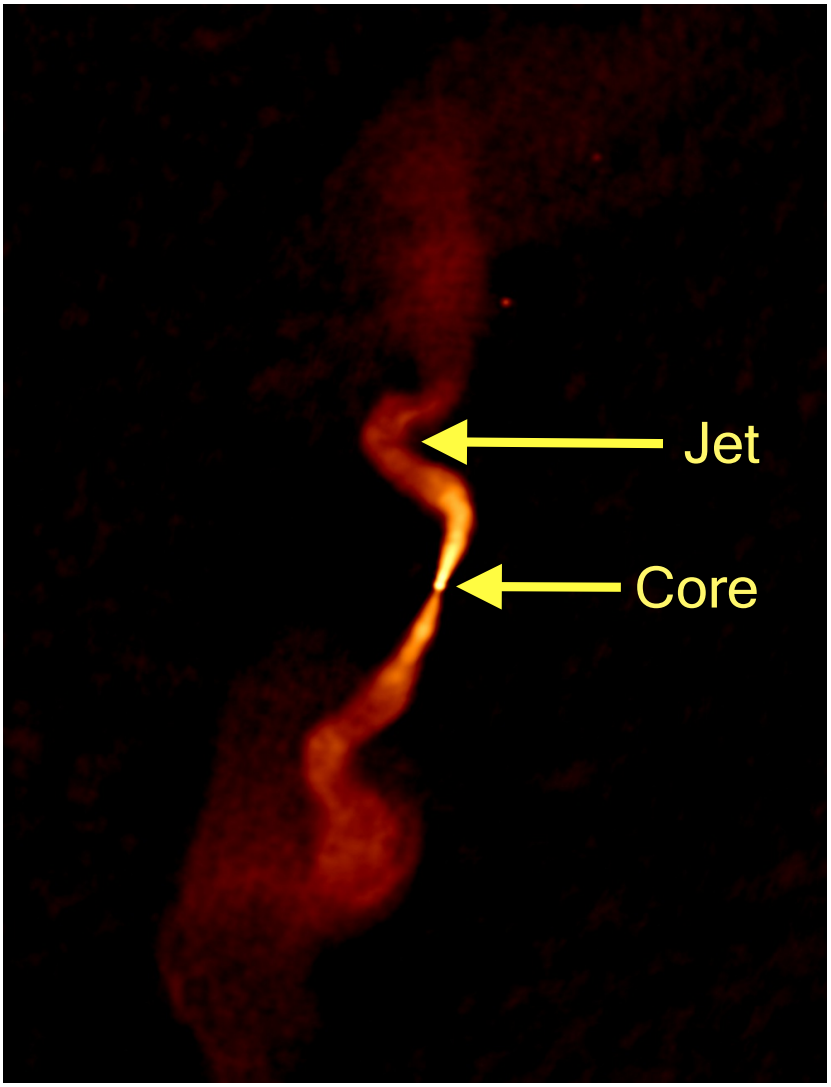

Figure 1.1: Original image of the radio jet of the FR I radio galaxy 3C 31 at 5 GHz, with typical features labelled. Note the distinctive fluffy plume-like jets. Image made using data calibrated in the making of this thesis.

radio galaxy.

The cores of such galaxies, where the central AGN is located, can often feature optical emission line phenomena similar to those of Seyfert galaxies, allowing for further classification according to the spectral line structure in the compact nucleus. Narrow-line radio galaxies (NLRG) share the narrow emission line properties associated with Seyfert 2 galaxies, similarly broad-line radio galaxies (BLRG) feature the broad Balmer lines associated with Seyfert 1 galaxies, the only difference for the NLRG's and BLRG's being the strong radio emission indicating the presence of a jet.

Blazars are another special subclass of radio loud quasars. These are very

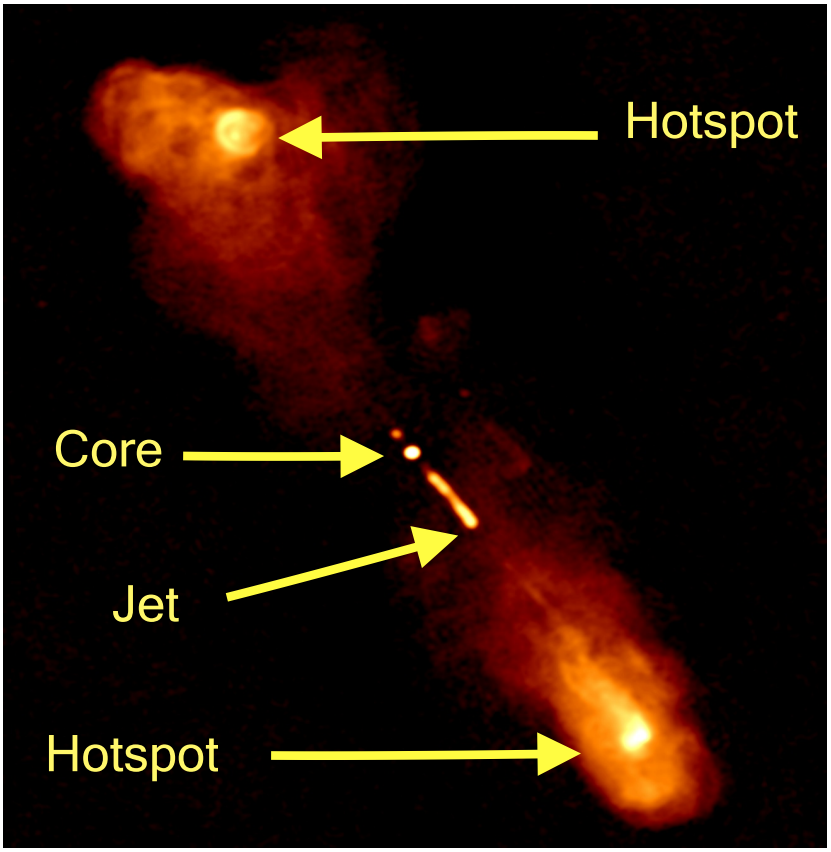

Figure 1.2: Original image of the radio jet of the FR II radio galaxy 3C 219 at 5 GHz, with typical features labelled. Note the narrow jet and hotspots with accompanying lobes.

bright in the radio and are often unresolved on kiloparsec scales. Blazars emit radiation at a wide range of wavelengths, from radio (Lister et al. 2018) all the way to high energy gamma rays and TeV energies as observed with VERITAS (Very Energetic Radiation Imaging Telescope Array System)(Benbow & VERITAS Collaboration 2012), Fermi (Ghisellini et al. 2017), and other new high energy telescopes. The radiation is also quite variable, with variations over days or weeks observed, making extensive monitoring of such sources very important in understanding their physics (Jorstad & Marscher 2016). When observed using Very Long Baseline Interferometry (VLBI) on the milliarcsecond/parsec scales, the individual components in the jet can be resolved and are observed to move downstream along the jet over multiple observations. The measured speeds of these components in the jets have been calculated to be superluminal in many cases (Lister et al. 2018). This can be easily explained as being due to the axis of a relativistic jet inclined at an angle close to the line of sight, which would also explain the high luminosity at all wavelengths, due to Doppler boosting in a jet pointing roughly at the observer.

Blazars can again be divided into BL Lac objects and flat spectrum radio quasars, FSRQ's. FSRQ's are distinguished by the presence of strong, broad Balmer lines, while BL Lac objects typically have featureless spectra; however this dividing line is not always clear cut and there are exceptions. Another difference between FSRQs and BL Lac objects is the Eddington ratio of the detected Balmer lines (Sbarrato et al. 2012), $\lambda_{\rm Edd,Bal}$, where

$$\lambda_{\rm Edd,Bal} = \frac{L_{\rm Balmer}}{L_{\rm Edd}}, \tag{1.2}$$

with usually $L_{\rm Balmer}$ being the luminosity of the broad Balmer lines and $L_{\rm Edd}$ being the Eddington luminosity of the objects. As a result the emission line intensities are given in Eddington units allowing the spectra of objects of different black hole masses to be compared. Values of $\lambda_{\rm Edd,Bal} < 5 \times 10^{-4}$ are expected for BL Lac objects as they often show little to no Balmer emission and $\lambda_{\rm Edd,Bal} > 5 \times 10^{-4}$ for FSRQs.(Sbarrato et al. 2012)

Another class to consider are radiatively inefficient, radio-loud AGN, also known as low-excitation radio galaxies, weak-line radio galaxies or 'jet-mode' objects. These are objects with active jets providing the radio emission however have little evidence of a luminous accretion disk, torus, or emission lines associated with the accretion onto a black hole. The dichotomy between the conventional 'Radiatively efficient' AGN and these 'Radiatively inefficient' AGN is associated with the Eddington scaled accretion rate $L_{\rm Edd} = \frac{4\pi G M_{\rm BH} c m_p}{\sigma_{\rm T}}$, where objects with a total luminosity of only a few per cent or less of this Eddington rate are considered radiatively inefficient. Objects with higher luminosities above a certain value can support a standard radiatively efficient accretion disk; this critical value will depend on the details of the accretion disk model. This is the model put forward by Ghisellini & Celotti (2001) and Merloni & Heinz (2008). It has been put forward by Hardcastle et al. (2007) that this dichotomy may be due to the environment around these galaxies, with the radiatively efficient AGN mainly residing in a relatively cool gaseous medium and accreting it, while radiatively ineficient AGN tend to reside in hotter IGM environments, accreting this hotter material more inefficiently.

1.1.2.3 A Unifying Model for AGN

An important topic in AGN research is whether the different phenomena in AGN can be attributed to a common underlying set of processes with some

small varying factors, or whether the different classes are intrinsically different. There have been many attempts over the decades to unify various groups of AGN. An early attempt by Rowan-Robinson (1977) attempted to unify the known Seyfert and radio galaxies. This attempt correctly assumed that absorption by dust played an important role in the observed optical and infra-red emission, however did not take into affect the beaming effects for the radio loud AGN. A further step was taken by Blandford & Rees (1978), who suggested that that an observed AGN is a blazar if the jet is closely aligned with the line of sight, initiating the theory that orientation plays an important role in observed radio jets.

A first complete picture, which is still widely accepted today is that of Antonucci (1993) and discussed also in the review by Urry & Padovani (1995). This scheme proposes the existence of two types of AGN, radio loud and radio quiet, both sharing an common underlying structure– namely an actively accreting supermassive black hole at the centre of the AGN, which may or may not be launching an astrophysical jet, causing the radio loud/ quiet dichotomy, as the jets are known to be powerful synchrotron radio emitters. The remaining Seyfert 1/2, BLRG/NLRG or type 1/2 quasar dichotomy was ascribed by Antonucci (1993) simply to orientation effects through the angle of inclination of the black hole accretion disc to the observer, with the existence of a dusty obscuring torus of material surrounding the accretion disc. The region inside the dusty absorber, the broad line region, gives rise to the observed broad Balmer lines, while an outer narrow line region contributes the narrow Balmer lines. In type 1 AGN, like Seyfert 1 and BLRGs, both the narrow and broad line regions contribute to the spectra, producing the observed broad Balmer lines; in type 2 AGN, such as Seyfert 2s, the broad line region is obscured by the dusty torus, meaning only the outer narrow line region contributes, creating the observed narrow Balmer lines in the observed spectra. This is outlined in the diagram in Figure 1.3, which presents a schematic of the expected inclination angles for various AGN types. The upper half of this figure shows how inclination angle and total radio power affects radio loud AGN, indicated by the presence of a jet in the upper half; the lower half does not feature a radio jet and is therefore a representation of radio quiet AGN.

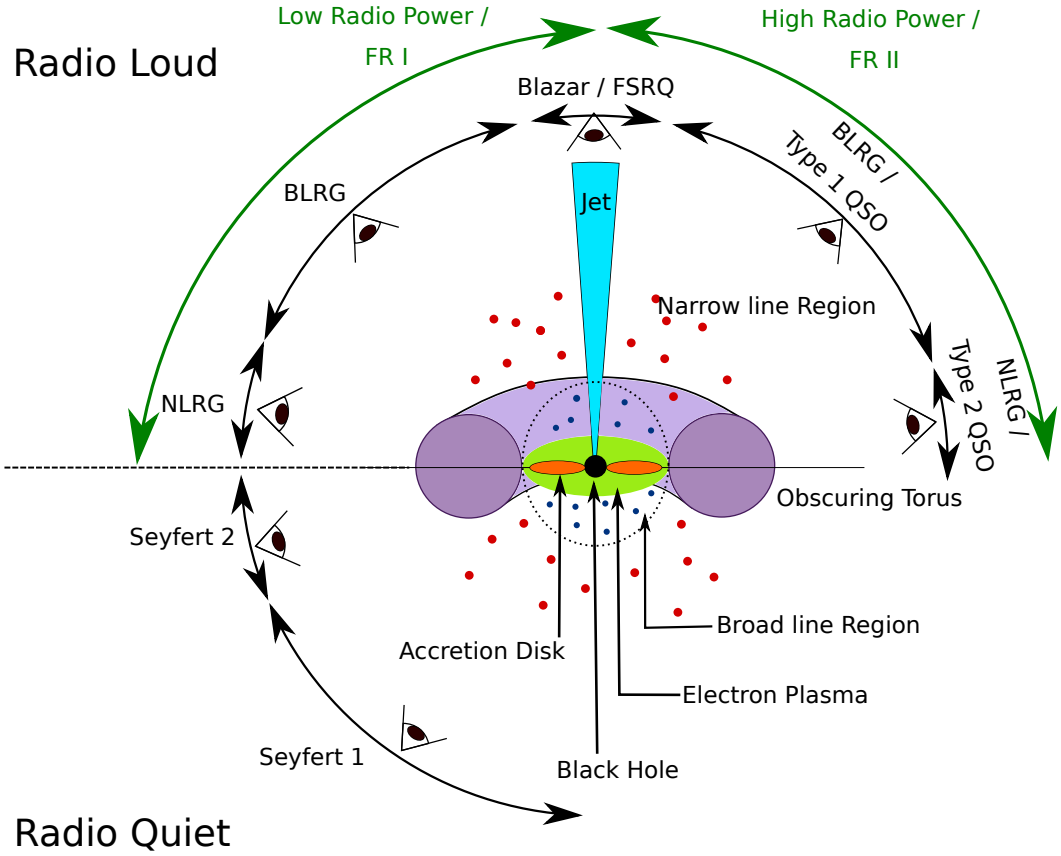

Figure 1.3: Diagram explaining unified model for AGN. The upper two quadrants are for radio loud and the bottom for radio quiet AGN. Features in the AGN have been labelled. Figure adapted from Figure 4.16 in Beckmann & Shrader (2012).

1.1.3 Physical Processes in AGN Jets

Extragalactic astrophysical jets can be defined as highly energetic, well-collimated outflows from the compact central engines of AGN. The first recorded observation of a jet was in 1918 from the elliptical galaxy M 87 by H. D. Curtis, who described the observed feature as a "A curious straight ray [that] lies in a gap in the nebulosity in p.a. 20°, apparently connected with the nucleus by a thin line of matter" (Curtis 1918) what he detected was the optical synchrotron emission from the jet in M 87. This discovery was not properly understood and dismissed as a curiosity. It was not until later in the 20th century, with the advent of high resolution radio imaging and advances in angular resolution and sensitivity in both the optical and radio, that these features were more commonly observed and deemed worthy of further study.

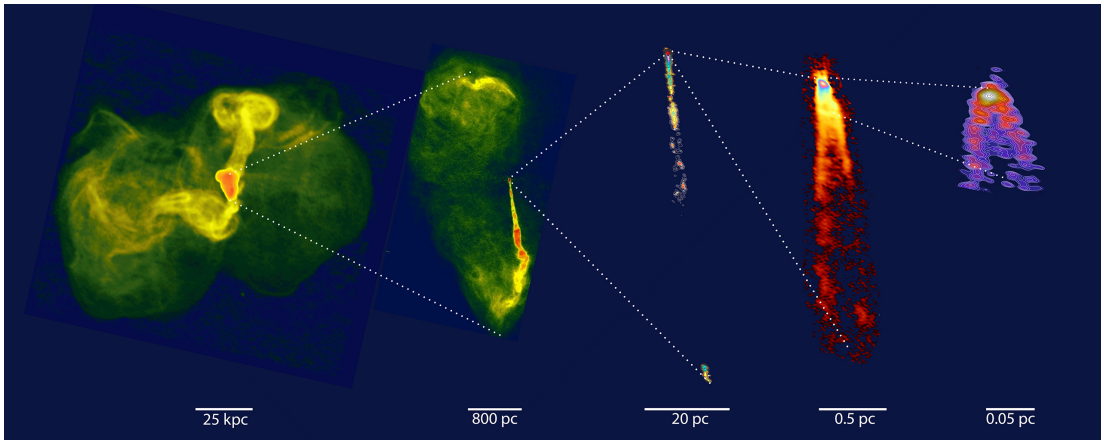

Figure 1.4: Montage of the FR-I radio galaxy M87, on scales from the outer lobes to near the black hole. From left: (a) Scales of tens of kpc, showing the present ejection direction and a more ancient one almost perpendicular to the former; (b) kpc scale jet and inner lobes observed with the VLA; (c) The jet contained within the host galaxy on VLBI images are shown; (d) innermost jet observed with millimeter VLBI; (e) jet launching region near the SMBH. The last four images show the striking effects of relativistic beaming, even with the jet pointing at a modest 17° to our line-of-sight (Walker et al. 2018). Credit: (a) NRAO, 90 cm VLA; (b) NRAO, 20 cm VLA; (c) NRAO: 20 cm VLBA (Cheung et al. 2007); (d) NRAO, 7 mm VLBA (Walker et al. 2018), (e) 3 mm global VLBI network (Kim et al. 2018). Image credit Blandford et al. (2019)

This led to the class of radio loud AGN and the various properties and appearances their jets can have over a wide range of scales from sub parsec to megaparsec. Jets can be studied over a range of scales covering a factor of almost 10^{10} between the smallest and largest, as can be seen in Figure 1.4.

Yet even after many years of research and intense debate on these objects some very essential questions about them remain open, including:

1. How are the jets launched?
2. How are these immense structures collimated over such large distances?
3. What are the jets made of?

It may seem that with such fundamental questions still open, very little is known about AGN jets, however a lot of research and many competing models and theories exist addressing each of these questions.

1.1.3.1 Jet Launching and Collimation

It is commonly agreed that the jets are launched from the vicinity of the central engine of the AGN, fuelled by accretion onto the supermassive black hole. The launching of the jet itself can be modelled according to two popular mechanisms; either the jet is launched from a magnetized accretion disk (Lynden-Bell 1969, Lovelace 1976, Blandford & Payne 1982) or from an actively accreting and rotating black hole (Blandford & Znajek 1977). The former, commonly known as the Blandford-Payne mechanism, assumes some type of dynamo process within the accretion disk, which creates the necessary poloidal magnetic field to accelerate the jet outwards, combined with the rotation of the accretion disk to create a toroidal or helical field to collimate it.

The latter process, described by Blandford & Znajek (1977), postulates that an ambient magnetic field, frozen into the rotating plasma of the accretion disc becomes stronger as the magnetic flux density increases as matter gets closer to the event horizon. The large amount of magnetic flux threading the event horizon coupled with the rotating black hole forms helical magnetic field carried outward by the jet (consisting of charged particles) at high velocity. The source of the ambient magnetic field could be simply the ambient magnetic field of the ISM in the host galaxy being pulled into the black hole and amplified to the high fluxes needed for jet the launching and collimation. Alternatively, there could exist some dynamo producing poloidal magnetic field in the accretion disk, which is amplified to the required levels as it is transported inward, with the rotating black hole providing the source of the toroidal component. Another possible source of the initial "seed field" is the action of a "Cosmic Battery", as in the simulations of Contopoulos et al. (2018), which successfully provides poloidal magnetic fields that are amplified close to the event horizon to launch and collimate an astrophysical jet. This model is of particular interest as it provides a complete picture of the predicted system of magnetic fields and associated currents in such a jet.

As these theorized processes occur on extremely small scales, currently unresolvable by modern radio telescopes, it is necessary to employ highly complex computer simulations of the jet close to the event horizon, which create larger scale structures, which can then be compared to observation. Three dimensional General Relativistic Magneto-Hydrodynamical (3D GRMHD) simulations have successfully replicated the structures of jets using magnetically launched and collimated jets by the Blandford-Znajek (McKinney

2006) and Blandford-Payne (Tchekhovskoy & Bromberg 2016, Nakamura et al. 2018) scenarios. More recently, simulations such as those of Chatterjee et al. (2019) have replicated the structure of the M87 jet over 5 orders of magnitude in scale, successfully creating the paraboloidal and conical structure of the jet observed using millimetre VLBI, with the spine and sheath structure of a fast inner region and slower moving outer region observed in Kim et al. (2018), which the authors ascribe to mass loading and entrainment in the jet. The jet was simulated with a rotating black hole entraining a poloidal magnetic field from the accretion disk. These simulations also investigate how the jet interacts with the ambient media and how this affects the jet morphology, with various launching models and effects such as "toroidal kink instability" and ambient media decelerating the jet, possibly creating the observed FR I/II dichotomy (Tchekhovskoy & Bromberg 2016). In terms of jet collimation, magnetic fields are believed to play a vital role, however Globus & Levinson (2016) and Levinson & Globus (2017) argue for a more hydrodynamical approach with a strong wind from the accretion disk providing collimation on the small scales using a semi-analytical model applied and compared to observations of M87. On large scales, gas pressure is expected to provide collimation, also shown in the simulations of Tchekhovskoy & Bromberg (2016) with the backflow in the large scale lobes of FR II galaxies collimating the typically narrow jets observed in these sources.

In terms of the observed magnetic field of the jet, the expected toroidal magnetic fields theorized and simulated (McKinney & Blandford 2009, Broderick & McKinney 2010) should persist to observable scales and be detected through observations of the Faraday rotation measure of the jet radio emission (see Sections 1.1.6). These magnetic fields are believed to be important in the jet launching process, and helical fields are used in simulations to support the jet, however their effect on jet collimation is widely debated. Observational evidence of helical fields has been reported however, in the form of significant transverse rotation measure gradients across jets, which indicate toroidal behaviour through the change in the line of sight magnetic field across the jet(Laing 1981, Asada et al. 2002), and have been observed and catalogued (Gabuzda, Nagle & Roche 2018, Christodoulou et al. 2016). Evidence of toroidal and helical fields in the form of an RM gradient was found in one of the highest resolution observations of a jet to date – the *RadioAstron* observation of BL Lac by Gómez et al. (2016). This is consistent with simulations, suggesting jets may be magnetically confined on small

scales. However, hydrodynamical effects may also play a role on the scales further from the central engine; as suggested for example, by the presence of re-collimation shocks in the form of knots downstream in the jet of BL Lac (Marscher et al. 2008, Gómez et al. 2016).

In terms of kiloparsec scale jets, simulations of "magnetic tower" jets by Gan et al. (2017) have shown how magnetically dominated jets featuring large scale toroidal fields and associated currents can be affected by violent intra-cluster weather. The cluster member 3C 465 and its wide angle tail morphology are correctly reproduced in these simulations, supporting the view that jets are electromagnetic structures and should be treated as such.

1.1.4 The Cosmic Battery

The "Cosmic Battery" or "Poynting-Robertson Battery" (Contopoulos & Kazanas 1998, Contopoulos et al. 2009) is an interesting model which may be potentially able to unify the magnetic field structure in astrophysical jets on all scales and provides a plausible source of a magnetic "seed" field in the region near the jet base.

The process creating this starts with the Poynting-Robertson drag experienced by the electrons and protons in the accretion disc. In the rest frame of the accretion disc, the radiation from the vicinity of the nucleus appears slightly anisotropic due to aberration. This gives rise to the aforementioned Poynting-Robertson drag force, which for an electron is given by (Contopoulos & Kazanas 1998):

$$F_{\mathrm{PR}} = -\frac{L\sigma_{\mathrm{T}} - \mathrm{T}}{4\pi r^2 c}\frac{v_\phi}{c}, \tag{1.3}$$

where L is the luminosity of the source of the radiation, r is the distance from the source of the radiation, σ_{T} is the Thompson cross-section for an electron and v_ϕ is the rotational velocity of the accretion disc. The protons will have a vastly different value for their Thompson cross-section differing by a factor of $(m_p/m_e)^{-2}$, making the force felt by the protons almost 10^{-6} times that felt by the electrons, so that it can safely be taken to be negligible. The electrons will therefore effectively have slower rotational velocities relative to those of the protons, which creates an azimuthal electrical current in the accretion disc. Following Ampère's law, a poloidal magnetic field is produced, which will be wound up by the rotation of the accretion disc, creating a helical magnetic

field whose direction is by definition linked to the rotational direction of the accretion disc.

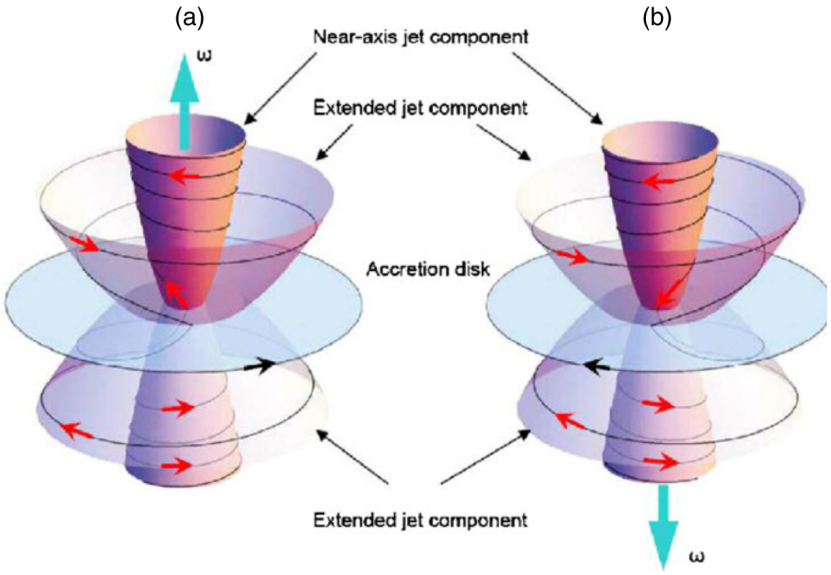

Figure 1.5: Schematic of the system of magnetic fields expected by the cosmic battery model, note the direction of the fields components transverse to the jet remains the same in both (a) and (b). Image credit: Contopoulos et al. (2009)

A consideration for magnetic fields in astrophysical jets is the need for the magnetic field lines to close –the lines cannot simply extend outwards to infinity. In the "Cosmic Battery" model this is considered. The poloidal field created in the disc by the process previously outlined will have a return field forming loops that are anchored in the disc. Now adding the rotation of the disc, the field loop will be wound up creating nested helices, an inner helix and an outer one, with this field structure present in both the jet and counter-jet from the AGN.

The direction in which the field lines are wound up into a helix is also an interesting prediction of this model. Typically the direction in which the helix is wound up should have a random probability of being one way or the other for all observed sources. In the "Cosmic Battery" scenario however, as the field is wound up, the net direction of the field lines in the plane of the sky will be the same, irrespective of the direction of rotation of the accretion disc or black hole. In Figure 1.5 this is shown visually, for example if the direction of rotation of the accretion disc were to change (Figure 1.5(a) to (b)) then the direction of the poloidal field would also change and thereby the direction in which the field is wound up would remain the same.

This can also be thought of in terms of the electrical currents associated with the helical fields. In the "Cosmic battery" model it is expected that the inner helix will always feature a toroidal field with an associated electrical current in the jet showing an *inward* (toward jet base) direction, and the outer helix associated with the return field will have an associated *outward* electrical current. This configuration of currents and fields is not too different from a common coaxial cable, where a core wire carries a current in one direction separated by an insulating sheath and then another layer of current carrying metal in the opposite direction. Each of these layers would have its own associated toroidal magnetic fields associated with the right hand grip rule.

Considering the location of the synchrotron emitting plasma in this regime relative to the Faraday rotating medium, the Faraday rotation that is observed is not necessarily internal. It is supposed that the Faraday rotating plasma is close to the jet base and is located in a sheath layer further out in the jet between the inward and outward current regions, making the observed Faraday rotation external. Some internal Faraday rotation is not ruled out, however this would give rise to significant depolarization and deviations from the linear λ^2 behaviour for the Faraday rotation which are not typically substantial, although they are observed in some regions. Using a Blandford-Znajek type jet as an example here, the helical magnetic field from the cosmic battery process accreted onto the event horizon through the accretion disk would be involved in launching and collimating the relativistic jet plasma, which here is external to the jet, causing external Faraday rotation. For the larger scale magnetic fields on kiloparsec scales, the observed Faraday rotation is due to the return magnetic field from this process. This is located in the outer layers around the jet and external to the synchrotron radiating plasma in the jet. The idea that this magnetic field is in the outer layers of the jet and more external is supported by the fact that often this field is difficult to detect when intercluster effects are seen, making it difficult to discern Faraday rotation gradients, and making gradients appear patchy and non monotonic over large distances, as can be seen in some of the RM images presented in Chapter 3.

The direction of these fields can be inferred with detections of transverse Faraday rotation measure (RM) gradients (see Section 1.1.6 and Chapter 3). As the rotation measure is directly proportional to the line of sight magnetic field component, the direction in which the values of RM increase will indicate the direction of the toroidal magnetic field component. A vast amount of work

has been done on the detection of significant transverse RM gradients gradients on parsec scales, in the region closer to the jet base, using VLBI measurements (e.g. Asada et al. 2002, Gabuzda et al. 2017, Motter & Gabuzda 2017, Gabuzda, Nagle & Roche 2018). In Gabuzda, Nagle & Roche (2018), in particular, a summary of all known significant transverse Faraday rotation measure gradients is shown; at the time of publication 33 of 47 implied an inward current on parsec scales, and applying a binomial probability distribution analysis indicates that there is only an approximately 0.4% likelihood that this asymmetry came about by chance, and that more likely a physical effect is causing this bias towards inward currents.

On the larger scales therefore, it should be expected that the significant RM gradients measured should preferentially imply toroidal/helical fields corresponding to outward associated electrical currents. Results from such an analysis for large scale RM gradients are presented in Chapter 3.

Another consideration in this mechanism is existence of low-luminosity radio loud AGN, also known as radiatively inefficient AGN. These are AGN which appear not to have a bright accretion disk, yet have the bright radio emission indicating a jet is present. The complete lack of an active accretion disk would have a detrimental effect on the production of the currents and magnetic fields theorized by the Cosmic Battery. However as accretion is also presumed to be occurring in these radiatively inefficient AGN, albeit with warmer material and at much lower accretion rates with respect to the black hole mass (Merloni & Heinz 2008, Hardcastle et al. 2007), it must be investigated whether such an accretion process would result in such a system of currents and fields or whether this model would only be applicable to radiatively efficient AGN with high accretion rates.

A final consideration is the spin of the black hole in a Blandford-Znajek type jet and how winding up of the magnetic field from the accretion disk is affected by the spin of the black hole. The rotational direction of the accretion disk and black hole spin are not coupled in any way. Recent simulations in Contopoulos et al. (2018) have shown how the Cosmic battery effect can make all accretion disks change from SANE (Standard And Normal Evolution) to MAD (Magnetically Arrested Disk) for a non-rotating and a rotating black hole, affecting the radiation field around the black hole only. The rotation of the black hole is not expected to affect the structure of the larger parsec to kiloparsec scale jet magnetic field (Christodoulou et al. 2016). The rotation of

the black hole winding up a random magnetic field and creating a helical field in the jet is another option, however the reported observed directional bias in Faraday rotation gradients observed matches with the prediction of the Cosmic Battery. A helical field due to the black hole rotation combined with a Blandford-Znajek type jet would produce a random orientation of transverse RM gradients, due to the random isotropic distribution of black hole spins, inferring either inward or outward currents in the jets, which does not match the observed preference for a particular orientation of the observed transverse RM gradients favouring the Cosmic Battery model.

1.1.5 Synchrotron Radiation

The radio emission observed from AGN is in most cases synchrotron radiation. This is radiation created by the relativistic electrons gyrating in a magnetic field in the hot plasma in the jet. The following derivation is based on Rybicki & Lightman (1979, Chapter 6). Consider a relativistic particle of mass m and charge q moving in a magnetic field and the force acting upon it,

$$\frac{\mathrm{d}}{\mathrm{d}t}\left(\gamma m\vec{v}\right) = q\vec{v}\times\vec{B}, \tag{1.4}$$

where $\vec{v}$ is the particle's velocity, $\vec{B}$ is the magnetic field strength and γ is the Lorentz factor. No overall work is done by magnetic forces meaning $|v|$ and γ are constant. Now,

$$m\gamma\frac{\mathrm{d}\vec{v}}{\mathrm{d}t} = q\vec{v}\times\vec{B}. \tag{1.5}$$

Letting $\frac{\mathrm{d}\vec{v}}{\mathrm{d}t} = \vec{a}$ be the acceleration, isolating this and then reducing to scalar terms,

$$a = \frac{qvB\sin\alpha}{\gamma m}, \tag{1.6}$$

where α is the angle between $\vec{v}$ and $\vec{B}$. Now the power P' emitted by the accelerating, relativistic charged particle in its own frame of reference is given by Larmor's formula:

$$P' = \frac{q^2a'^2}{6\pi\epsilon_0c^3}, \tag{1.7}$$

where ϵ_0 is the permittivity of free space and c is the speed of light in a vacuum. Now to relate this back to the power emitted in the observers frame, some transformations have to be investigated first. If the energy $\mathrm{d}E'$ is emitted

in some time $\mathrm{d}t'$ in the rest frame, then in the observer's frame,

$$\mathrm{d}E = \gamma \mathrm{d}E' \tag{1.8a}$$

$$\mathrm{d}t = \gamma \mathrm{d}t' \tag{1.8b}$$

Hence it follows,

$$\frac{\mathrm{d}E'}{\mathrm{d}t'} = \frac{\mathrm{d}E}{\mathrm{d}t} \quad \Rightarrow P' = P. \tag{1.9}$$

This only leaves the acceleration term to transform into the observers frame. Looking at the relationship in special relativity between a and a',

$$a'_{\parallel} = \gamma^3 a_{\parallel} \quad \text{parallel to direction of motion} \tag{1.10a}$$

$$a'_{\perp} = \gamma^2 a_{\perp} \quad \text{perpendicular to direction of motion} \tag{1.10b}$$

As the particle is gyrating in circular motion around the magnetic field $a'_{\parallel} = 0$ and therefore we are left with simply, $a' = \gamma^2 a$. Now writing Larmor's formula in terms of the observer's frame,

$$P = \frac{q^4 \gamma^4 a^2}{6\pi\epsilon_0 c^3} \tag{1.11}$$

and now subbing in the acceleration from Equation 1.6,

$$P = \frac{q^4 \gamma^2 v^2 B^2 \sin^2 \alpha}{6\pi\epsilon_0 m^2 c^3}. \tag{1.12}$$

This is the power radiated by one charge with a "pitch angle" α as it gyrates in a magnetic field. For a collection of charges with an isotropic distribution of velocities leaving a collection of all possible angles α we can consider the average angle,

$$\langle \sin^2 \alpha \rangle = \frac{\int \sin^2 \alpha \mathrm{d}\Omega}{4\pi} = \frac{2}{3}, \tag{1.13}$$

where $\mathrm{d}\Omega$ is the unit solid angle. Now the average power $\langle P \rangle$ can be written as:

$$\langle P \rangle = \frac{q^4 \gamma^2 v^2 B^2}{9\pi\epsilon_0 m^2 c^3}. \tag{1.14}$$

Note how the power depends on $\frac{1}{m^2}$, meaning the synchrotron emission is most likely dominated by electrons compared to the 1000 times more massive protons. Now to investigate the spectrum and further properties of synchrotron radiation we consider the relativistic motion of the charge. Emission radiated from such a relativistic particle will be highly Doppler

boosted in its forward direction towards the observer. The equation of motion

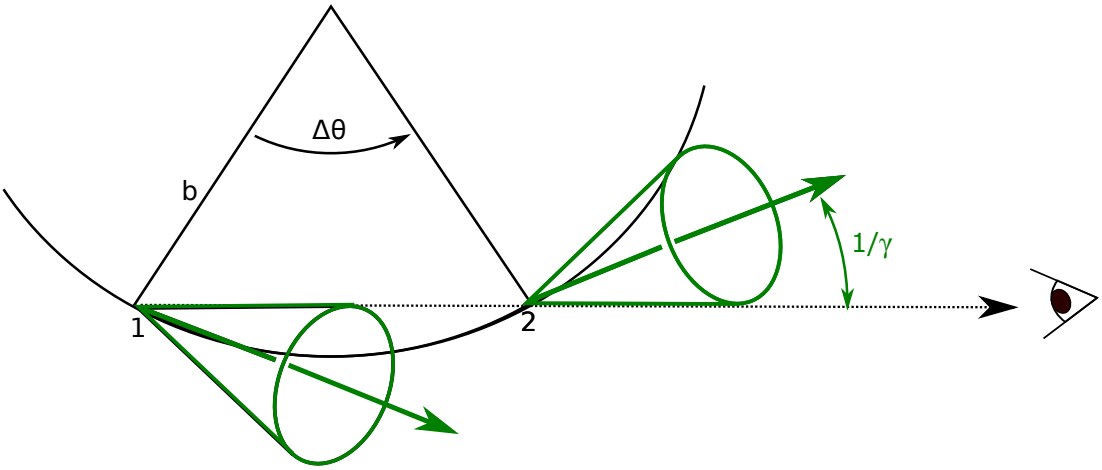

Figure 1.6: A figure showing the range of angles for which the synchrotron radiation, emitted as cones of solid angle $\frac{1}{\gamma}$ would be Doppler boosted toward an observer. Figure adapted from Figure 6.2 in Rybicki & Lightman (1979).

(Equation 1.4) for the particle, gyrating with radius b can be rewritten as,

$$m\frac{\mathrm{d}v}{\mathrm{d}t} = \frac{qvB\sin\alpha}{\gamma} = \frac{mv^2}{b}. \tag{1.15}$$

The radius b can be written,

$$b = \frac{v}{\omega_B \sin\alpha}, \tag{1.16}$$

where $\omega_B = \frac{qB}{\gamma m}$ is the angular frequency of gyration for the particle in the field. Recall now that the gyrating particle will be highly relativistic, therefore radiation will be Doppler boosted toward the observer, making the radiation appear as pulses much shorter than the overall period of gyration $\frac{\omega_B}{2\pi}$. Qualitatively this means the observed spectrum will be much broader than the gyration period. Radiation will be observed as shown schematically in Figure 1.6 with radiation from cones of solid angle $\frac{1}{\gamma}$ boosted toward the observer from the angle $\Delta\theta$ between points 1 and 2. Over the path length ΔS and using the geometry shown we have,

$$\Delta S = b\Delta\theta = \frac{v}{\omega_B \sin\alpha}\frac{2}{\gamma}, \tag{1.17}$$

and in terms of the times t_1 and t_2 when the particle passes points 1 and 2 indicating the beginning and end of the pulse, setting $\Delta S = v(t_2 - t_1)$,

$$t_2 - t_1 \approx \frac{2}{\gamma \omega_B \sin\alpha} \equiv \Delta t \tag{1.18}$$

However, the observed pulse must be considered, which corresponds to the arrival time of the photons emitted at 1 and 2, which will be called $t_2^A - t_1^A \equiv \Delta t^A$. This will differ by $\frac{\Delta S}{c}$, the time taken for a photon to move through ΔS. The arrival time width of the pulse will be,

$$\Delta t^A = \frac{2}{\gamma \omega_B \sin\alpha}\left(1 - \frac{v}{c}\right) \tag{1.19}$$

and since for the highly relativistic charges $\gamma \gg 1$,

$$1 - \frac{v}{c} \approx \frac{1}{2\gamma^2} \tag{1.20}$$

the pulse width becomes,

$$\Delta t^A \approx \frac{1}{\gamma^3 \omega_B \sin\alpha} \tag{1.21}$$

This differs from the gyration period by a factor of γ^3, meaning that the expected spectrum will be broad, a feature of synchrotron radiation. Further detailed analysis shows that most radiation from an electron is emitted at the critical frequency ω_c,

$$\omega_c \equiv \frac{3}{2}\gamma^3 \omega_B \sin\alpha \tag{1.22}$$

Furthermore it can be shown that the power can be written using as:

$$P = \int_0^\infty P(\omega)\mathrm{d}\omega = C_1 \int_0^\infty F\left(\frac{\omega}{\omega_c}\right)\mathrm{d}\omega, \tag{1.23}$$

where $F(\omega/\omega_c)$ is an unknown function. Setting $x \equiv \frac{\omega}{\omega_c}$ the integral can be rewritten as:

$$P = \omega_c C_1 \int_0^\infty F(x)\mathrm{d}x. \tag{1.24}$$

The integral $\int F(x)\mathrm{d}x$ is unknown for now but as it has a non-dimensional value a normalization can be set. The constant C_1 can be evaluated as P and ω_c are known from Equations 1.12 and 1.22. The power as a function of frequency can be written:

$$P(\omega) = C_n \frac{q^2 B \sin\alpha}{9\pi\epsilon_0 m c^2} F\left(\frac{\omega}{\omega_c}\right), \tag{1.25}$$

for the case when $\beta \approx 1$ for the highly relativistic case, C_n is a normalisation constant.

It is often observed that a synchrotron spectrum can be very well approximated using a power law such that:

$$P(\omega) \propto \omega^{-s}, \tag{1.26}$$

where s is the spectral index. This can come about if the particles energy distribution (or Lorentz factors) also obey a power law such that:

$$N(E)\mathrm{d}E = CE^{-p}\mathrm{d}E, \qquad E_1 < E < E_2 \tag{1.27a}$$

or in terms of Lorentz factors:

$$N(\gamma)\mathrm{d}\gamma = C\gamma^{-p}\mathrm{d}\gamma, \qquad \gamma_1 < \gamma < \gamma_2 \tag{1.27b}$$

where $N(E)dE$ represents a number density of particles with energies between E and $E + dE$ and p is the particle distribution index. The value of C can depend on may factors such as the pitch angle α. The total power radiated per unit volume and frequency can be written as the integral of $N(\gamma)\mathrm{d}\gamma$ multiplied by the power for a single radiating particle using Equation 1.25 and then considering only the proportionalities,

$$P_{\mathrm{tot}}(\omega) = C\int_{\gamma_1}^{\gamma_2} P(\omega)\gamma^{-p}\mathrm{d}\gamma \propto \int_{\gamma_1}^{\gamma_2} F\left(\frac{\omega}{\omega_c}\right)\gamma^{-p}\mathrm{d}\gamma. \tag{1.28}$$

Using the substitution $x \equiv \omega/\omega_c$, and recalling that $\omega_c \propto \gamma^2$;

$$P_{\mathrm{tot}}(\omega) \propto \omega^{-(p-1)/2}\int_{x_1}^{x_2} F(x)x^{(p-3)/2}\,\mathrm{d}x \tag{1.29}$$

The limits of integration, x_1 and x_2 correspond to the Lorentz factors, γ_1 and γ_2 and depend on ω. If the energy distribution of the particles is sufficiently wide it can safely be approximated that $x_1 \approx 0$ and $x_2 \approx \infty$ making the integral constant, yielding:

$$P_{\mathrm{tot}}(\omega) \propto \omega^{-(p-1)/2}, \tag{1.30}$$

showing the synchrotron spectrum does indeed obey a power law, where the spectral index s is now related to the particle distribution index p,

$$s = \frac{p-1}{2} \tag{1.31}$$

The lifetime of synchrotron emission processes can be calculated by dividing the energy of the electrons by the rate at which the energy is emitted, namely the power P,

$$\tau_{\text{synch}} = \frac{E}{P} \tag{1.32a}$$

$$\tau_{\text{synch}} = \gamma mc^2 \left(\frac{q^4 \gamma^2 v^2 B^2}{9\pi\epsilon_0 m^2 c^3} \right)^{-1} \tag{1.32b}$$

$$\tau_{\text{synch}} = \frac{9\pi\epsilon_0 m^3 c^5}{q^4 \gamma v^2 B^2}. \tag{1.32c}$$

From this it can be seen that the more energetic, high γ, particles will have shorter lifetimes and, in an isolated region of relativistic particles, the spectrum of the emission will steepen with time, as the higher energy particles with higher frequency emission will lose their energy faster compared to lower energy particles.

Therefore, a region with more energetic electrons will have a flatter spectrum. Such a region in a a radio jet would occur near the jet base or at a knot or hotspot in the jet where there is a continual supply of highly relativistic electrons. A more diffuse region where there is no fresh supply of energised material, such as the outer radio lobe in an FR II or in the more distant regions in an FR I, the spectrum will be steeper at higher frequencies and flatter at lower frequencies, as only less energetic electrons will be contributing to the spectrum making the spectrum more curved as the population of energetic electrons reduces. This makes the synchrotron spectrum a useful tool in the relative ageing of a radio emitting plasma, identifying regions of recently emitted or re-accelerated material or outer diffuse regions that have been there for some time.

Synchrotron radiation can also be highly linearly polarized. For example, a single gyrating charge will produce elliptically polarized synchrotron radiation. However in a distribution of particles with a smooth variation of pitch angles, the elliptical component will be cancelled out as emission cones will contribute from sides of the line of sight; thus the radiation will be linearly polarized to some degree. The degree of linear polarization is given by:

$$\Pi(\omega) = \frac{P_\perp(\omega) - P_\parallel(\omega)}{P_\perp(\omega) + P_\parallel(\omega)}, \tag{1.33}$$

where $P_\perp(\omega)$ and $P_\parallel(\omega)$ are the radiated powers per unit frequency in

directions parallel and perpendicular to the projected magnetic field on the plane of the sky. This has a theoretical upper limit of approximately 75%.

1.1.6 Faraday Rotation

Faraday rotation measure is a physical effect on the polarization angle of an electromagnetic wave. This effect was discovered by Michael Faraday in 1845, while investigating the effect magnetic forces have on light as it passes through various substances, as he believed light to be an electromagnetic phenomenon. When experimenting with polarized light as it passed through glass containing lead traces and applying a magnetic field to the glass, an observed polarization angle change was noted.

In terms of astrophysical plasmas, the following derivation of the Faraday rotation measure is adapted from that in Chapter 8 of Rybicki & Lightman (1979). We consider an electromagnetic wave propagating through a plasma which has a uniform magnetic field. Assume a local magnetic field $\vec{B_0}$, which is much stronger than the field strength in the electromagnetic wave that is passing through. The equation of motion of an electron in the plasma is given by:

$$m\frac{\mathrm{d}\vec{v}}{\mathrm{d}t} = -e\vec{E} - \frac{e}{c}\vec{v} \times \vec{B_0}, \tag{1.34}$$

where m is the electron mass, e is the electron charge, $\vec{v}$ is the electron velocity and $\vec{E}$ is the electric field of the incident electromagnetic wave. Let us also assume that the electromagnetic wave is circularly polarized and sinusoidal such that,

$$\vec{E}(t) = Ee^{-i\omega t}\left(\vec{\epsilon_1} \mp i\vec{\epsilon_2}\right), \tag{1.35}$$

where $\vec{\epsilon_1}$ and $vec\epsilon_2$ describe the orthogonal polarized components of the electric field, the '$-$' corresponds to right circular polarization and the '$+$' corresponds to left circular polarization and ω is the angular frequency of the radiation. Now suppose, for simplicity, that the wave is propagating along the direction of the local magnetic field.

$$\vec{B_0} = B_0\vec{\epsilon_3} \tag{1.36}$$

Combining Equations 1.34, 1.35 and 1.36, the velocity $\vec{v}(t)$ can be shown to be:

$$\vec{v}(t) = \frac{-ie}{m\left(\omega \pm \omega_B\right)}\vec{E}(t), \tag{1.37}$$

where $\omega_B = \frac{eB_0}{mc}$ is the cyclotron frequency, the frequency at which the electrons gyrate about the magnetic field lines. The remaining $\pm$ indicates that populations of electrons will experience different velocities in response to the right and left circularly polarized components of the electric field of the propagating wave.

We can use this to find the conductivity for each component,

$$\vec{j} = \sigma\vec{E} = -ne\vec{v} \tag{1.38a}$$

$$\sigma\vec{E} = \frac{ine^2}{m\left(\omega \pm \omega_B\right)}\vec{E} \tag{1.38b}$$

$$\sigma = \frac{i\epsilon_0\omega_p^2}{\omega \pm \omega_B} \tag{1.38c}$$

where $\vec{j}$ is the current density, σ is the conductivity, n is the charged particle density and $\omega_p = \sqrt{\frac{e^2 n_e}{m_e \epsilon_0}}$ is defined to be the plasma frequency. The different conductivities imply different speeds of propagation through the plasma. Connecting σ to ϵ,

$$\epsilon_{\mathrm{R,L}} = 1 - \frac{\sigma}{i\epsilon_0\omega} = 1 - \frac{\omega_p^2}{\omega(\omega \pm \omega_B)} \tag{1.39}$$

where the R and L correspond to the'$+$' and '$-$' cases in the denominator, respectively. Therefore, considering a linearly polarized wave, comprised of a right and left circularly polarized wave, the plane of polarization will not remain constant as the wave propagates through the plasma and will *rotate*, as the differently circularly polarized components will have different velocities. This is Faraday rotation. For consistency it can be noted that for the case where $\vec{B_0} = 0$ and thereby $\omega_B = 0$, $\epsilon = 1 - \frac{\omega_p^2}{\omega^2}$, which is the case for electromagnetic radiation in an unmagnetised plasma.

The phase angle ϕ through which the plane of polarization rotates while traversing a distance d through the magnetised plasma is simply $\vec{k} \cdot \vec{d}$ where k is the wave number ($k = \frac{\omega}{v}$). If the wave number is not constant along the

path, the phase angle rotated is

$$\phi_{\mathrm{R,L}} = \int_0^d k_{\mathrm{R,L}} \mathrm{d}s, \tag{1.40a}$$

where

$$k_{\mathrm{R,L}} = \frac{\omega}{c}\sqrt{\epsilon_{\mathrm{R,L}}} \tag{1.40b}$$

In terms of the phase difference between the RCP and LCP components $\Delta\theta$ we can write

$$\Delta\theta = \int_0^d (k_{\mathrm{R}} - k_{\mathrm{L}})\, \mathrm{d}s. \tag{1.41}$$

Now using Equation 1.40b and substituting in for $\epsilon_{\mathrm{R,L}}$

$$k_{\mathrm{R,L}} = \frac{\omega}{c}\left[1 - \frac{\omega_p^2}{\omega(\omega \pm \omega_B)}\right]^{\frac{1}{2}} \tag{1.42}$$

This can be simplified using the assumptions that $\omega \gg \omega_p$ and $\omega \gg \omega_B$ to

$$k_{\mathrm{R,L}} \approx \frac{\omega}{c}\left[1 - \frac{\omega_p^2}{\omega^2}\left(1 \mp \frac{\omega_B}{\omega}\right)\right] \tag{1.43}$$

Now to solve for $k_{\mathrm{R}} - k_{\mathrm{L}}$ the separate cases from Equation 1.43 are simply subtracted from each other to give:

$$k_{\mathrm{R}} - k_{\mathrm{L}} = \frac{n\, e^3 B_0}{\omega^2 c m^2 \epsilon_0} \tag{1.44}$$

and solving for $\Delta\theta$:

$$\Delta\theta = \frac{e^3}{m^2 \epsilon_0 c \omega^2} \int_0^d n\vec{B} \cdot \mathrm{d}\vec{s} \tag{1.45}$$

where the magnetic field has been generalised such that a component along the line of sight unit vector $\mathrm{d}\vec{s}$ is used for any uniform B-field in the plasma. The particle density n has been kept in the integral as this can vary along the line of sight. To relate this phase angle change $\Delta\theta$ to the change in polarization angle $\Delta\chi$ look at the example given in Figure 1.7, here it becomes clear that the change in polarization angle is simply half the phase difference, $\Delta\chi = \frac{\Delta\theta}{2}$. Now substituting this into Equation 1.45 and writing ω in terms of wavelength λ,

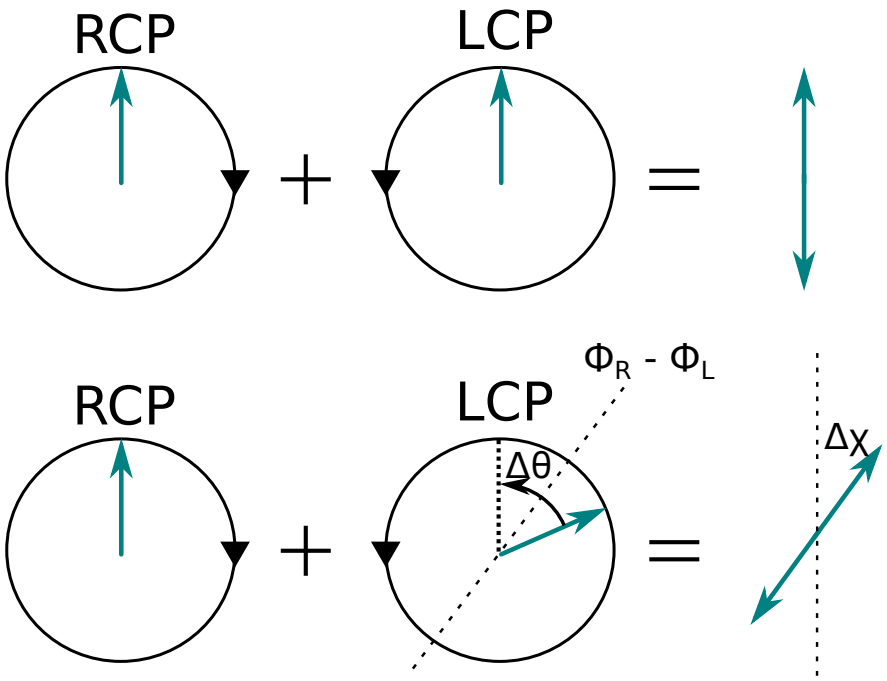

Figure 1.7: Figure showing how LCP and RCP combine to give linear polarization angle. On top a linear polarization with no Faraday rotation is given, the bottom figure has a delay in LCP due to Faraday rotation causing polarization angle to change by $\Delta\chi$. Figure adapted from Figures 8.1(a) and (b) in Rybicki & Lightman (1979)

$$\Delta\chi = \frac{e^3}{8\pi^2\epsilon_0 m_e^2 c^3}\int_0^d n_e\vec{B}\cdot\mathrm{d}\vec{s}\,\lambda^2 \tag{1.46}$$

This shows the total effect a region of magneto ionic material will have on the linear polarization of an electromagnetic wave as it passes through.

The change in the polarization angle will be proportional to the wavelength squared λ^2 and can be written (Burn 1966),

$$\chi = \chi_0 + \mathrm{RM}\lambda^2, \tag{1.47}$$

where χ denotes the observed polarization angle at a wavelength λ, χ_0 is the polarization angle of the radiation as it was emitted and RM is simply the constants and integral related to the Faraday rotation from Equation 1.46 grouped together. Using Faraday rotation to investigate the magnetic field and ionised environment along the line of sight is particularly advantageous in the case of synchrotron radio emission from AGN jets. Not only can synchrotron radiation be highly linearly polarized, it is also emitted over a wide range of wavelengths, from metres to sub-millimetres, allowing multiwavelength

observations to effectively fit polarization angle against wavelengths squared to calculate RM. Further methods exploiting the Faraday rotation phenomenon and how it is calculated using data from radio interferometers are discussed later in Section 2.3.

Chapter 2

Radio Interferometry Methods and Techniques

This Chapter deals with the practical aspects of radio astronomy and explains the basic principles of how radio interferometers work and how observed data are calibrated and imaged. Particular attention is also paid to the Stokes parameters and how these are used to detect and measure polarization from radio emission. This Chapter also explains methods for analysing polarization information and extracting useful information on magnetic field effects along the line of sight from the synchrotron radio sources using Faraday effects; methods such as χ versus λ^2 fitting, rotation measure synthesis and QU fitting are explained.

The radio interferometry methods use Thompson (1999) and Thompson et al. (2017) as a reference.

The polarization theory and calibration use Rybicki & Lightman (1979) and Conway & Kronberg (1969) as a basis for their derivation.

2.1 Radio Interferometry basics

2.1.1 The Radio Interferometer

The maximum angular resolution of a telescope, or any device with an imaging aperture can be calculated using the Rayleigh criterion;

$$\theta \simeq 1.22\frac{\lambda}{D}, \tag{2.1}$$

where λ is the observing wavelength and D is the diameter of the telescope. In the case of optical telescopes with a typical diameter of ~ 1 m and observing wavelengths of ~ 540 nm (V Band), this gives a maximum theoretical resolution of ~ 0.14", ignoring any atmospheric effects, which greatly lower the resolution. The long wavelengths used in radio telescopes drastically lower the maximum theoretical resolution. Consider observations at a wavelength of 6 cm ($\simeq 5$ GHz) with a radio telescope with a dish of 100 m diameter. Equation 2.1 gives a resolution of ~ 150", and to enhance this would require unfathomably large single dish telescopes with diameters of many kilometres to achieve the same resolution as a typical optical telescope. This is where the technique of interferometry is useful as a method to achieve much higher resolutions by networking a number of radio antennas together so that the effective diameter of the telescope is the maximum distance between two antenna. To show how this principle works, consider a two element interferometer such as the one in Figure 2.1.

Each telescope will read a voltage that is directly proportional to the incident electric field, E, from the incoming radiation, we will call these voltages v_1 and v_2. The displacement vector, $\vec{B_0}$, between the telescopes is called the baseline –the distance between the two telescopes. The voltages read can be defined as:

$$v_1 \propto E\cos\omega t \tag{2.2a}$$

$$v_2 \propto E\cos\left(\omega\left(t-\tau\right)\right) \tag{2.2b}$$

where ω is the angular frequency of the incoming radiation and τ is the time difference in the signals received by each telescope due to the different positions of the telescopes creating a phase difference between the signals. We

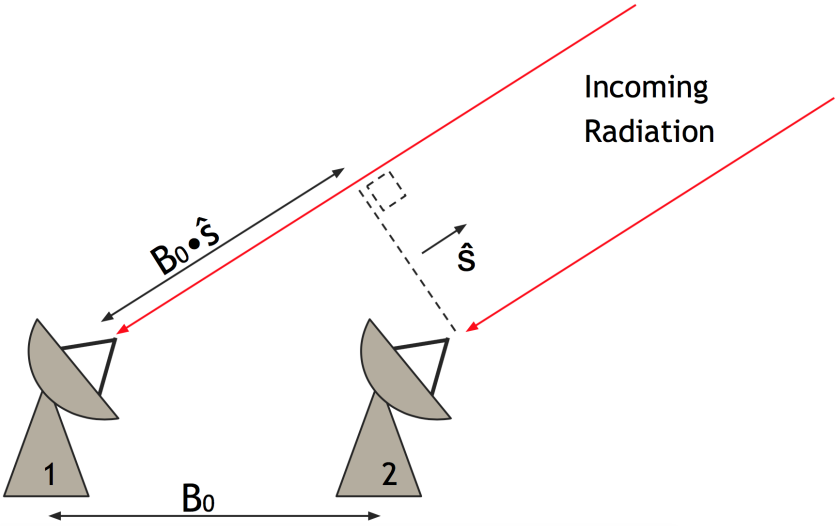

Figure 2.1: A diagram of a simple 2 element interferometer featuring two telescopes labelled 1 and 2. Both are observing the same object but will receive the signal at a slight time delay due to the difference in position of the antenna.

can write

$$\tau = \frac{\vec{B_0} \cdot \hat{s}}{c}, \tag{2.3}$$

Where $\hat{s}$ is the unit vector in the direction of the incoming radiation and c is the speed of light. Now the correlation between the two signals is a measure of the similarities between the two signals as a function of the phase difference between them. This is multiplying one signal by the complex conjugate of the other and averaging over time, where the complex conjugate is denoted by x^* ($x \in \mathbb{Z}$ The complex numbers) and the time average of a function is denoted by $\langle f(t) \rangle$. Now writing the correlation of v_1 and v_2:

$$\begin{aligned}
\langle v_1 v_2^* \rangle &\propto \left\langle E^2 \cos\omega t \cos\left(\omega\left(t-\tau\right)\right)\right\rangle \\
\langle v_1 v_2^* \rangle &\propto E^2 \left\langle \cos\omega t \cos\left(\omega\left(t-\tau\right)\right)\right\rangle \\
\langle v_1 v_2^* \rangle &\propto E^2 \left\langle \cos^2\omega t \cos\omega t + \cos\omega t \sin\omega\tau \sin\omega t\right\rangle \\
\langle v_1 v_2^* \rangle &\propto E^2 \left(\cos\omega\tau \left\langle \cos^2\omega t\right\rangle + \sin\omega\tau \left\langle \cos\omega t \sin\omega t\right\rangle\right) \\
\langle v_1 v_2^* \rangle &\propto E^2 \left(\cos\omega\tau \times \frac{1}{2} + \sin\omega\tau \times 0\right) \\
\langle v_1 v_2^* \rangle &\propto E^2 \cos\omega\tau
\end{aligned}$$

Furthermore E^2 is proportional to I, the intensity, we can also write τ in terms

of the baseline as in Equation 2.3 and write ω in terms of the wavelength λ.

$$\langle v_1 v_2^* \rangle \propto I \cos\left(\frac{2\pi c}{\lambda}\frac{\vec{B_0}\cdot\hat{s}}{c}\right) \tag{2.4}$$

$$\langle v_1 v_2^* \rangle \propto I \cos\left(2\pi\vec{B}\cdot\hat{s}\right) \tag{2.5}$$

Here $\vec{B}$ is the baseline vector converted to units of wavelengths. This interference pattern that is produced will be quasi-sinusoidal with an amplitude proportional to the intensity, with a frequency that will depend on how the projected baseline length, $\vec{B}\cdot\hat{s}$, changes with time. This would be the response to an unresolved point source in the sky. To describe more extended emission this can be considered as a sum of point sources with varying positions and intensities. Consider a point source located at a position vector $\vec{a}$ on the plane of the sky from the phase centre of the telescope, which corresponds to the direction of the $\hat{s}$, writing the general response to a point source now as:

$$\langle v_1 v_2^* \rangle \propto I(\vec{a}) \cos\left(2\pi\vec{B}\cdot(\vec{a}+\hat{s})\right), \tag{2.6}$$

then for an extended source considered as a sum of such point sources, the correlation can be now written as an integral over $\vec{a}$:

$$\langle v_1 v_2^* \rangle \propto \int_{-\infty}^{+\infty} I(\vec{a}) \cos\left(2\pi\vec{B}\cdot(\vec{a}+\hat{s})\right) \mathrm{d}\vec{a}. \tag{2.7}$$

Now for clarity Equation 2.7 can be re-written in complex exponential notation when we consider the real part:

$$\langle v_1 v_2^* \rangle \propto \int_{-\infty}^{+\infty} I(\vec{a}) e^{2i\pi\vec{B}\cdot(\vec{a}+\hat{s})} \mathrm{d}\vec{a} \tag{2.8}$$

$$\langle v_1 v_2^* \rangle \propto e^{2i\pi\vec{B}\cdot\hat{s}} \int_{-\infty}^{+\infty} I(\vec{a}) e^{2i\pi\vec{B}\cdot\vec{a}} \mathrm{d}\vec{a} \equiv e^{2i\pi\vec{B}\cdot\hat{s}} V(\vec{B}), \tag{2.9}$$

where $V(\vec{B})$ is the visibility function. Now it can be easily recognised that $I(\vec{a})$ and $V(\vec{B})$ form a Fourier pair, where the inverse Fourier transform of the visibility function, as read by the correlated voltages from the interferometer, yields the source intensity on the plane of the sky.

$$V(\vec{B}) = \int I(\vec{a}) e^{2i\pi\vec{B}\cdot\vec{a}} \,\mathrm{d}\vec{a} \tag{2.10a}$$

$$I(\vec{a}) = \int V(\vec{B}) e^{-2i\pi\vec{B}\cdot\vec{a}} \,\mathrm{d}\vec{B} \tag{2.10b}$$

Considering that the field of view of a radio interferometer is very small

compared to the whole celestial sphere we can assume that $\vec{a}$ is perpendicular to $\vec{s}$ and that $\vec{B} \cdot \vec{a} \approx \vec{b} \cdot \vec{a}$, where $\vec{b}$ is the baseline vector $\vec{B}$ projected onto the plane of the sky. The vectors $\vec{a}$ and $\vec{b}$ can be converted into coordinates in two dimensions, which are chosen to be in the North and East directions, so $\vec{b} \rightarrow (u, v)$, and $\vec{a} \rightarrow (x, y)$; rewriting Equations 2.10 (a) and (b) therefore yields:

$$V(u,v) = \int I(\vec{a}) e^{2i\pi(ux+vy)} \, \mathrm{d}x\mathrm{d}y \tag{2.11a}$$

$$I(x,y) = \int V(\vec{B}) e^{-2i\pi(ux+vy)} \, \mathrm{d}u\mathrm{d}v, \tag{2.11b}$$

where (u, v) represent the baseline distances in terms of North and East displacement and (x, y) describes the coordinates on the sky, which are chosen to be right ascension and declination. To build up visibility data, a network of antennas with more than just two antennas is used so a large number of baselines of varying length covering a variety of (u, v) coordinates is observed. Furthermore, as most radio sources observed are assumed to be constant over the course of a few hours or days a long observation in time can be used to build up the coverage in (u, v) space, as the rotation of the Earth over the course of a long observation will change the projected baseline length, $\vec{b}$.

2.1.2 The Need for Calibration

The correlated data obtained from such an observation will need some calibration to be of any use for imaging and extracting useful polarization information, which will be covered later. In the case of the Very Large Array (VLA), which was the primary instrument used for observation in this thesis, the following basic steps are required.

The flux density calibration needs to be applied to the data, as the fluxes initially obtained from the correlator are only relative and therefore a standard set of calibrator sources is required. These are bright, relatively compact radio sources with known fluxes across all bands that are regularly monitored (Perley & Butler 2017). Typically a scheduled VLA observation will have at least one scan of one or perhaps two of these sources. Commonly used sources include 3C 286, 3C 48 and 3C 138, which are also doubly useful as they also serve as polarization angle calibrators. The amplitudes of the visibilities can be set and converted to Janskys using these sources and transferred onto the

phase calibrator, which will be used to calibrate the primary source being observed.

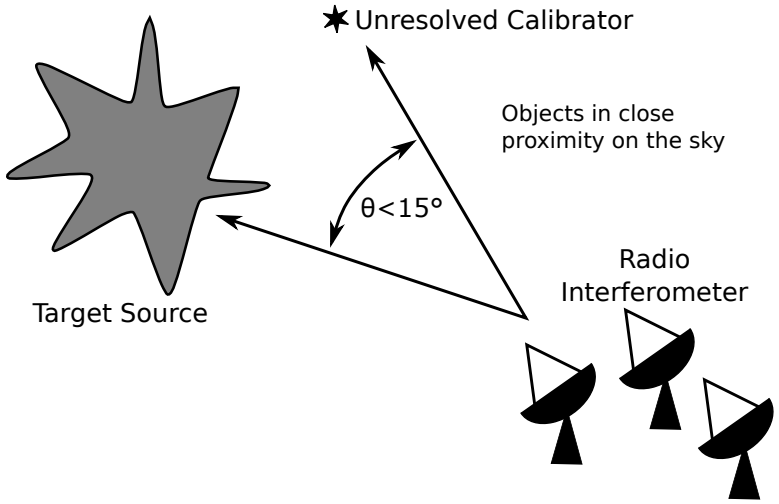

Figure 2.2: A schematic diagram of a phase referencing observation with a radio interferometer.

The amplitude and phase calibration is done most often using a phase referencing technique with the VLA. The amplitudes and phases of the measured visibilities will most likely be corrupted by a multitude of effects, such as atmospheric and instrumental effects that cannot be removed from the data. To improve the quality of the data, the observations of the desired target object are interrupted by regular scans of a nearby, bright, compact or point-like source which is called the phase calibrator. Ideally this source is at least a few hundred milli-Janskys in intensity and within 10–15° of the target source on the sky, with the smaller separations needed at higher observing frequencies; a brief schematic is given in Figure 2.2. The visibility of a point source is well known in (u, v), with a constant phase and amplitude across all baselines, allowing for the observer to correct the corrupted visibilities of the known point source to appear more point-like and applying the same corrections to the nearby target source. The duration and frequency of such scans on the phase calibrator depend on the observing frequency, as at higher frequencies (>20 GHz) the phases are more sensitive to change and therefore require more regular scans approximately every 3 minutes. At lower observing frequencies such as from 1–6 GHz, which are most commonly used in this thesis, a scan time of 10–15 minutes on the target between calibrator scans suffices. Furthermore, the correct amplitudes, in Janskys, determined earlier using the flux density calibrator, can be transferred to the constant amplitudes in the scans of the phase calibrator, which are well sampled in time; now the

correct phases and amplitudes can be transferred to the target source by interpolating between the calibrator scans onto the target scans.

The outlined calibration steps should suffice for archival, narrow-bandwidth observations using the VLA. However in observations with the upgraded Jansky VLA, some further steps are necessary to fully exploit the wideband capabilities of the VLA.

A bandpass calibration is necessary. This is simply accounting for the fact that, in a wideband receiver, some channels will be less sensitive than others, especially near the edges of the observing band. To correct this, a single scan of a bright calibrator source, such as the flux density calibrator, can be used to correct for the lower gain near the edges and result in a smooth spectrum which truly represents the data. This technique is historically more known for use with spectral line data, however with the dawn of wideband radio receivers and wideband spectro-polarimetric techniques such as rotation measure synthesis and QU fitting, this step is vital to ensure as many wavelengths as possible can be correctly sampled and imaged. A delay calibration will also be necessary as this corrects for any instrumental delays across a wide band, seen as slopes in the phase versus frequency. These are again removed with scans of a bright unresolved calibrator used as a reference.

2.1.3 Imaging and Self-calibration

When the calibration steps described briefly above have been correctly applied, the data can then be imaged. However when performing the inverse Fourier transform to produce an image many sidelobes and symmetric artefacts can be seen in the image. This is because an observation using an interferometer can never truly completely sample the sky in the (u, v) plane. The observed visibility function can be described as the product of the true visibility multiplied by a gridding function such that:

$$V_{\rm obs} = V_{\rm true}\,(u, v)\,G(u, v) \tag{2.12}$$

where $V_{\rm obs}$ and $V_{\rm true}$ are the observed and true visibility functions, while the gridding function, G, is valued 1 where data were obtained and 0 where no (u, v) data were obtained making this function highly dependent on the observation set up. The resulting inverse Fourier transform of this product can

be described using Equation 2.11 as:

$$I_{\rm obs}(x,y) = \int V_{\rm true}\,(u,v)\,G(u,v)e^{-2i\pi(ux+vy)}\,{\rm d}u{\rm d}v = I_{\rm true} * \hat{G}(x,y) \qquad (2.13)$$

where the convolution theorem of Fourier transforms has been applied. Thus, the observed source structure, $I_{\rm obs}(x,y)$ is the convolution of the true source structure and the Fourier transform of the gridding function, called the dirty beam, which is entirely dependent on the values of (u,v) at which observations are made. This results in an observed source structure that exhibits a high level of noise and symmetric patterns, known as side-lobes, around the source, due to the incomplete sampling of the (u,v) plane. It is therefore typically required that *deconvolution* is performed of the observed image to extract the best possible estimate of the true source structure. The most basic method of deconvolution of radio interferometer data is the CLEAN algorithm (Högbom 1974), which operates in an iterative method on the data.

1. The visibility data are inverse Fourier transformed to display the image, which is called the "dirty image". An image of the point spread function is made by inverse Fourier transforming the visibilities with zero phase and unit amplitude, yielding the "dirty beam".
2. The peak in the dirty image is located, which is assumed to be real emission and not associated with sidelobes.
3. The dirty beam is multiplied by some gain factor (usually 0.1) and subtracted from the image at the peak position located in step 2. This removes the effects due to that peak of emission and some corresponding sidelobes also.
4. The location and amplitude of the amount subtracted, commonly referred to as a "CLEAN component", are added to a model image, or table of CLEAN components.
5. Steps 2–4 are repeated until no more discernible peaks can be found in the image. It is common that the process is terminated when no discernible peak is higher than 2 or 3 times the background RMS of the image. The remaining image is called the "residual" image.
6. A Gaussian is fitted to the central peak of the dirty image and then convolved with the model image corresponding to the CLEAN components, with the residual image added, which may feature

structures not well sampled by CLEAN or too faint to be CLEANed, creating an image without any sidelobes.

This iterative process is quite successful at reconstructing the true source structure and removing the sidelobes and, as the cleaning occurs, it is often noted that fainter extended emission obscured by the sidelobes can be made out. There are some limitations to CLEAN however, considering more extended emission structure, where attempts have been made which have successfully mitigated these limitations.

The CLEAN process assumes that the observed source structure is sampled well by a collection of point sources. This works very well for compact radio sources with little structure, however when source structure becomes more extended the process cannot work as efficiently. A multi-scale CLEAN (Cornwell 2008) was devised, which cleans by using CLEAN components that are extended in structure. This involves not only searching in the image for a peak but also fitting this peak for some appropriately sized CLEAN component. Often this is not as computationally expensive as it seems, as there is a finite list of CLEAN component sizes (0 , 1, 3–5 beamwidths for example), and a multi-scale CLEAN can often save time, as it can CLEAN a structure in fewer iterations than a traditional Högbom CLEAN, especially when the source is quite extended. This method also helps in reducing the effect of negative "bowls" of emission which often feature in high resolution observations without shorter baselines to better sample the large scale flux, leaving negative regions of emission around extended structures. The multiscale CLEAN can help estimate and fill in these regions by using the more extended CLEAN components.

A further advancement is the application of a multi-term multi-frequency synthesis deconvolution technique, which makes use of wide bandwidths in the cleaning process (Rau & Cornwell 2011). This process makes use of all the frequencies in a band in an effort to increase the (u, v) coverage and sensitivity of the resulting image. It involves fitting a Taylor polynomial to the spectra of amplitudes at each baseline during the CLEANing process, which works quite well for the synchrotron radio emission, which follows a power law with frequency. For example, if imaging in the wide band between 2 and 4 GHz with this technique, an image at the central frequency, 3 GHz, will make use of all the visibilities from 2 to 4 GHz. This creates a synergy, allowing the resulting image to show the extended structures of the lower frequencies at the higher resolutions of 4 GHz, provided the spectrum is well fitted by the

Taylor polynomial. Multi-term multi-frequency synthesis also produces a spectral index image in parallel to the imaging, which can be useful in scientific analysis of the data, while the model image created can be used to self calibrate across the whole available bandwidth using the polynomial fit. When used in conjunction with a multi-scale CLEAN, this method can create images from VLA data with unparalleled dynamic ranges.

Self-calibration is a method by which the amplitudes and phases of the visibility data of the target object can be corrected further. This involves an iterative process using deconvolution as an aid. The model image created in step 4 of the CLEAN algorithm is used as an estimate of the true source structure. First the phases are corrected in rough time intervals in the data using this model, which slightly corrects the data, reducing the noise. This allows a deeper CLEAN to be made in the next step allowing for an improved model that can correct the phases on an even shorter time interval, iteratively improving the dynamic range of the image. This procedure is repeated until the phases are well corrected, at which point the amplitudes and phases can be corrected in parallel, which reduces the noise further. The self-calibration is particularly useful for polarization observations, as the process corrects the visibility phases and amplitudes based on the Stokes I information, but solves the polarized correlations also, which typically have a much lower signal to noise ratio.

2.2 Polarization in Radio Interferometry

Observations using radio interferometers can be used to detect polarized emission from astronomical objects and measure polarized intensity and polarization angle if the observations are set up properly. The radio telescopes are set up to measure different components of the incoming electric fields. For example in circular feed telescopes the left and right circularly polarized component of the incoming radio waves may be recorded separately, yielding four possible correlations, with the right–right (RR) and left–left (LL) correlations relating to the total intensity while the other correlations, LR and RL can be used to calculate the Stokes parameters corresponding to the linear polarization of the radiation (see Section 2.2.1).

The Stokes parameters can be used to measure the polarization properties of

the radio emission such as polarized intensity, degree of polarization, and polarization angle.

2.2.1 Stokes parameters and Polarized feeds in Radio Interferometers

The oscillations of the electric field vector in a monochromatic electromagnetic wave can be written in the plane perpendicular to the propagation as:

$$E_x = \mathcal{E}_1 \sin(\omega t - \phi_1), \qquad E_y = \mathcal{E}_2 \sin(\omega t - \phi_2), \tag{2.14}$$

where E_x and E_y are the amplitudes of the oscillations in the two mutually perpendicular directions, ω is the angular frequency of the monochromatic radiation and ϕ_1 and ϕ_2 indicate the phases of these oscillating components. This corresponds to an elliptically polarized wave, with the tip of the electric field vector tracing out the shape of an ellipse on the (x, y) plane. Considering an ellipse with its own principal axes x' and y', which are at an angle χ to the x- and y-axes (see Figure 2.3),

$$\frac{E_{x'}^2}{a^2} + \frac{E_{y'}^2}{b^2} = 1 \tag{2.15}$$

we can set

$$\frac{E_{x'}^2}{a^2} = \cos^2 \omega t \rightarrow E_{x'} = \pm a \cos \omega t \tag{2.16a}$$

$$\frac{E_{y'}^2}{b^2} = \sin^2 \omega t \rightarrow E_{y'} = \pm b \sin \omega t \tag{2.16b}$$

where now the electric vectors are described in terms of the principal axes of the ellipse. Now re-parametrise a and b in terms of the amplitude $\mathcal{E}$ and phase β,

$$a = \mathcal{E}_0 |\cos \beta|, \qquad b = \mathcal{E}_0 |\sin \beta|, \tag{2.17}$$

where $-\pi/2 \leq \beta \leq \pi/2$. Now we can rewrite $E_{x'}$ and $E_{y'}$ using Equations 2.16 and 2.17 for a general elliptically polarized wave:

$$E_{x'} = \mathcal{E}_0 \cos \beta \cos \omega t, \qquad E_{y'} = -\mathcal{E}_0 \sin \beta \sin \omega t \tag{2.18}$$

where the signs are chosen to conform with the standard that for $0 < \beta < \pi/2$ the ellipse will be traced out in a clockwise manner as t increases and in a

counter-clockwise manner for $-\pi/2 < \beta < 0$ when viewed by an observer towards whom the wave is propagating. This is called *right* and *left-handed* elliptically polarized radiation, respectively. For the cases when $\beta = \pm\pi/2$ or $\beta = 0$ the a or b term in Equation 2.17 will vanish, meaning the ellipse narrows down to a simple line which represents a completely linearly polarized wave. When $\beta = \pm\pi/4$, we get $a = b$ and the wave becomes completely left or right circularly polarized.

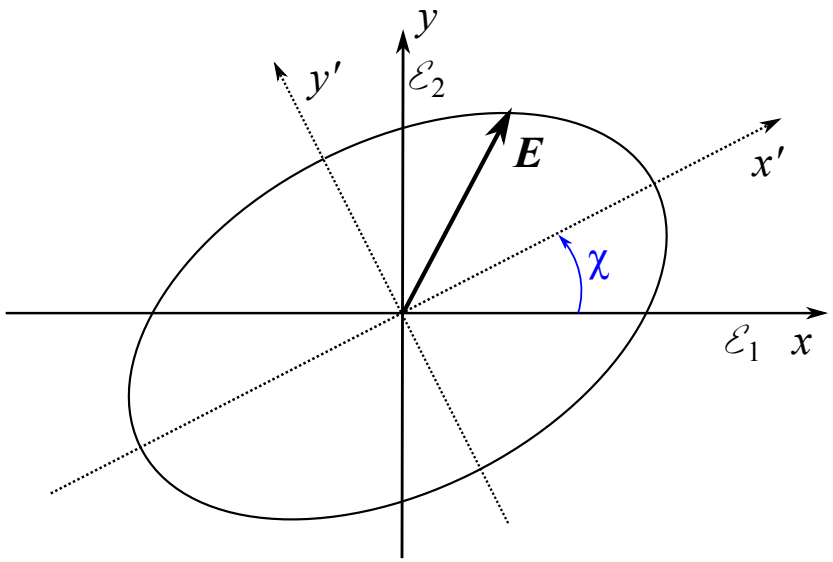

Figure 2.3: Diagram of the x and y electric field axes rotated through the angle χ to coincide with principal axes of the polarization ellipse

To connect this to the monochromatic wave in the x, y plane given in Equation 2.14, all that is required is to rotate the electric field components in Equation 2.18 by the angle χ to make the axes coincide; this transforms the equations as:

$$E_x = E_{x'} \cos\chi - E_{y'} \sin\chi, \tag{2.19a}$$

$$E_y = E_{x'} \sin\chi + E_{y'} \cos\chi, \tag{2.19b}$$

which, when substituting in for $E_{x'}$ and $E_{y'}$ from Equation 2.18 yields,

$$E_x = \mathcal{E}_0(\cos\beta\cos\chi\ cos\omega t + \sin\beta\sin\chi\sin\omega t) \tag{2.20a}$$

$$E_y = \mathcal{E}_0(\cos\beta\sin\chi\cos\omega t - \sin\beta\cos\chi\sin\omega t) \tag{2.20b}$$

Grouping the $\cos\omega t$ and $\sin\omega t$ terms between Equations 2.14 and 2.20 and

equating yields:

$$\mathcal{E}_1 \cos\phi_1 = \mathcal{E}_0 \cos\beta \cos\chi \tag{2.21a}$$
$$\mathcal{E}_1 \sin\phi_1 = \mathcal{E}_0 \sin\beta \sin\chi \tag{2.21b}$$
$$\mathcal{E}_2 \cos\phi_2 = \mathcal{E}_0 \cos\beta \sin\chi \tag{2.21c}$$
$$\mathcal{E}_2 \sin\phi_2 = -\mathcal{E}_0 \sin\beta \cos\chi \tag{2.21d}$$

Knowing the parameters $\mathcal{E}_1$, $\mathcal{E}_2$, ϕ_1, ϕ_2 means that $\mathcal{E}_0$, β and χ can be solved for. In radio astronomy, this is usually done using the Stokes parameters for monochromatic waves which are defined as:

$$I \equiv \mathcal{E}_1^2 + \mathcal{E}_2^2 = \mathcal{E}_0^2 \tag{2.22a}$$
$$Q \equiv \mathcal{E}_1^2 - \mathcal{E}_2^2 = \mathcal{E}_0^2 \cos 2\beta \cos 2\chi \tag{2.22b}$$
$$U \equiv 2\mathcal{E}_1\mathcal{E}_2 \cos(\phi_1 - \phi_2) = \mathcal{E}_0^2 \cos 2\beta \sin 2\chi \tag{2.22c}$$
$$V \equiv 2\mathcal{E}_1\mathcal{E}_2 \sin(\phi_1 - \phi_2) = \mathcal{E}_0^2 \sin 2\beta, \tag{2.22d}$$

where the final values are calculated by manipulating Equations 2.21 and using simple trigonometric identities. Equations 2.22 can be reduced further to:

$$\mathcal{E}_0 = \sqrt{I} \tag{2.23a}$$
$$\sin 2\beta = \frac{V}{I} \tag{2.23b}$$
$$\tan 2\chi = \frac{U}{Q} \tag{2.23c}$$

This shows that the only parameters required to describe elliptically polarized radiation are $\mathcal{E}_0$, β and χ. It also follows that for a purely elliptically polarized wave that,

$$I^2 = Q^2 + U^2 + V^2 \tag{2.24}$$

meaning that the Stokes I can be interpreted as being the total energy flux or intensity. The Stokes V quantity relates to the circular polarization, with a positive or negative value indicating right- or left circularly polarized waves respectively; when $V = 0$, implying that $\beta = 0$ (Equation 2.23b), the result is purely linearly polarized light. The Stokes Q and U parameters deal with linear polarization and determine the angle χ the ellipse makes with the x-axis. To define the Stokes parameters as given by Conway & Kronberg (1969) we specify the axes as in Figure 2.4, where the A and B axes are

aligned along North and East respectively, the C and D axes are at 45° to the A, B axes, and finally the right-circularly polarized component is increasing in the counter-clockwise direction, measured from North through East. Now

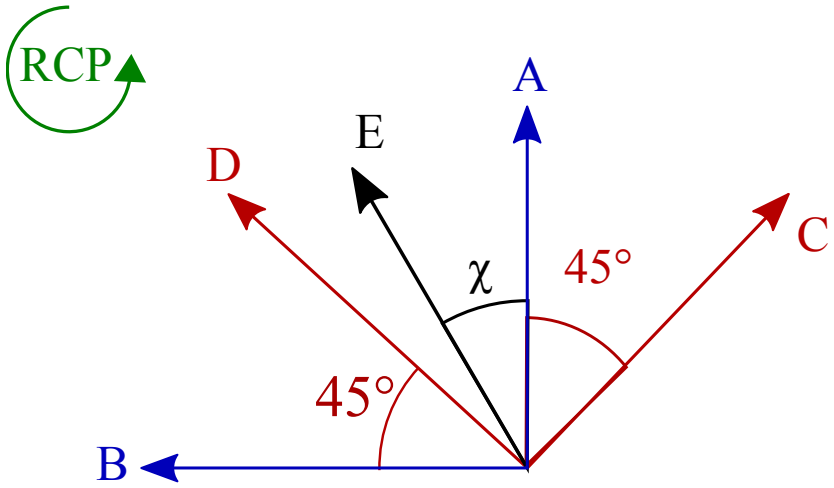

Figure 2.4: How the axes and components of the electric field vector are set up to define the Stokes parameters

rewriting the Stokes parameters as given in Conway & Kronberg (1969) but defining the direction of rotation and the axes to coincide with the IAU standard,

$$I = \langle E_A^2 \rangle + \langle E_B^2 \rangle = \langle E_C^2 \rangle + \langle E_D^2 \rangle = \langle E_R^2 \rangle + \langle E_L^2 \rangle \tag{2.25a}$$

$$Q = \langle E_A^2 \rangle - \langle E_B^2 \rangle \tag{2.25b}$$

$$U = \langle E_C^2 \rangle - \langle E_D^2 \rangle \tag{2.25c}$$

$$V = \langle E_R^2 \rangle - \langle E_L^2 \rangle. \tag{2.25d}$$

Now, consider a sources with a polarized component $E_{\rm pol}$ and an unpolarized component $E_{\rm unpol}$ to the radiation, with $I \geq \sqrt{Q^2 + U^2 + V^2}$:

$$E_A = \frac{E_{\rm unpol}}{\sqrt{2}} + E_{\rm pol} \cos\chi \tag{2.26a}$$

$$E_B = \frac{E_{\rm unpol}}{\sqrt{2}} + E_{\rm pol} \sin\chi \tag{2.26b}$$

$$E_C = \frac{E_{\rm unpol}}{\sqrt{2}} + E_{\rm pol} \sin(45 - \chi) \tag{2.26c}$$

$$E_D = \frac{E_{\rm unpol}}{\sqrt{2}} + E_{\rm pol} \cos(45 - \chi) \tag{2.26d}$$

This means that a feed designed to receive any of these components will detect

the same amount of flux from the unpolarized component, which should be proportional to $\frac{E^2_{\rm unpol}}{2}$. Calculating the Stokes Q and U parameters given in Equation 2.25 using the expressions given in Equation 2.26 we get:

$$\begin{aligned} Q &= (\langle E^2_{\rm unpol}\rangle + \langle E^2_{\rm pol}\rangle \cos^2\chi) - (\langle E^2_{\rm unpol}\rangle + \langle E^2_{\rm pol}\rangle \sin^2\chi) \\ Q &= \langle E^2_{\rm pol}\rangle \cos 2\chi \end{aligned} \tag{2.27}$$

$$\begin{aligned} U &= (\langle E^2_{\rm unpol}\rangle + \langle E^2_{\rm pol}\rangle \cos^2(45-\chi)) - (\langle E^2_{\rm unpol}\rangle + \langle E^2_{\rm pol}\rangle \sin^2(45-\chi)) \\ U &= \langle E^2_{\rm pol}\rangle \sin 2\chi \end{aligned} \tag{2.28}$$

Here the $\langle E_{\rm unpol}E_{\rm pol}\rangle$ terms have disappeared as the polarized and unpolarized components are uncorrelated and therefore the time average of their product should be zero. It can be seen again that the polarization angle, χ, is given by $\tan 2\chi = U/Q$, and the linearly polarized flux is $\langle E^2_{\rm pol}\rangle = \sqrt{Q^2+U^2}$. These values for χ and the amplitude $\langle E^2_{\rm pol}\rangle$ allow for the construction of a complex number value to define the linear polarization,

$$\mathbf{P} \equiv Q + iU = mIe^{2i\chi}, \tag{2.29}$$

where m is the degree of linear polarization and I is the total intensity. When $\mathbf{P}$ is plotted in a complex polar coordinate plane, it will simply be a vector with amplitude mI and phase angle 2χ. We now wish to connect the Stokes parameters and the correlator output in order to relate the polarized quantities to measured values. In a circular feed array– as is the case with the VLA and the Very Long Baseline Array (VLBA) – the left- and right-circularly polarized components are recorded by separate feeds which can form four possible correlations,

$$\langle LL^*(u,v)\rangle \tag{2.30a}$$

$$\langle RR^*(u,v)\rangle \tag{2.30b}$$

$$\langle LR^*(u,v)\rangle \tag{2.30c}$$

$$\langle RL^*(u,v)\rangle, \tag{2.30d}$$

where the R and L represent the telescope responses to the right- and left-circularly polarized components of the incoming radio emission and $\langle LL^*(u,v)\rangle$, for example, denotes correlation of the left circularly polarized response of one antenna with the left-circularly polarized response of the

second in a baseline pair. On inspection it is relatively easy to recognise that the $\langle LL^*(u,v)\rangle$ and $\langle RR^*(u,v)\rangle$ correlations respectively correspond to the $2\langle E_L^2\rangle$ and $2\langle E_R^2\rangle$ components in the definition of the Stokes parameters in Equation 2.25; solving for $\langle LL^*(u,v)\rangle$ and $\langle RR^*(u,v)\rangle$ using Equations 2.25a and 2.25d yields:

$$\langle LL^*(u,v)\rangle = I - V \tag{2.31}$$

$$\langle RR^*(u,v)\rangle = I + V. \tag{2.32}$$

This indicates that the $\langle LL^*(u,v)\rangle$ and $\langle RR^*(u,v)\rangle$ correlations carry information relating to the total intensity and the circular polarization, the $\langle LR^*(u,v)\rangle$ and $\langle RL^*(u,v)\rangle$ must therefore be used to form the Stokes Q and U which relate to the linear polarization. To do this the linearly polarized electric field components E_A and E_B can be written in terms of the circular components E_R and E_L:

$$E_A = E_R \cos\omega t + E_L \cos\omega t \tag{2.33a}$$

$$E_B = E_R \sin\omega t - E_L \sin\omega t. \tag{2.33b}$$

Recall from Figure 2.4 that angles are measured from North through East and the right-circularly component rotates in this positive direction. For simplicity $\chi = 0$ means the different circularly polarized components are in phase with each other and both point North at $t = 0$ ($\phi_l = \phi_r = 0$). Now writing this in complex form:

$$E_A = (E_R + E_L)e^{i\omega t} \tag{2.34a}$$

$$E_B = -i(E_R - E_L)e^{i\omega t}, \tag{2.34b}$$

where the real parts will return Equation 2.33. Now writing E_L and E_R in terms of E_A and E_B:

$$E_R = \frac{1}{2}\left(E_A + iE_B\right)e^{-i\omega t} \tag{2.35a}$$

$$E_L = \frac{1}{2}\left(E_A - iE_B\right)e^{-i\omega t} \tag{2.35b}$$

This allows us to write the correlation between R and L in terms of the

linearly polarized components,

$$\langle RL^*(u,v)\rangle = 2\langle E_R E_L^*\rangle \tag{2.36a}$$
$$= \frac{1}{2}\left(E_A + iE_B\right)\left(E_A + iE_B\right) \tag{2.36b}$$
$$= Q + iE_A E_B, \tag{2.36c}$$

because $\frac{1}{2}\left(E_A^2 - E_B^2\right) = \langle E_A^2\rangle - \langle E_B^2\rangle = Q$. Now recall Equation 2.22 which is of a similar form with the $\mathcal{E}_1$ and $\mathcal{E}_2$ terms equivalent to the E_A and E_B terms here. In Equation 2.22d, for the case where $\chi = 0$, the cosine term will go to unity, leaving $U = 2\mathcal{E}_1\mathcal{E}_2$ which in terms of E_A and E_B means:

$$U = 2\langle E_A E_B\rangle = E_A E_B. \tag{2.37}$$

Subbing into Equation 2.36 yields:

$$\langle RL^*(u,v)\rangle = Q + iU \tag{2.38}$$

In a similar fashion it can be shown that $\langle LR^*(u,v)\rangle = Q - iU$. Writing all four possible correlations in terms of the Stokes parameters:

$$\langle RR^*(u,v)\rangle = I + V \tag{2.39a}$$
$$\langle LL^*(u,v)\rangle = I - V \tag{2.39b}$$
$$\langle RL^*(u,v)\rangle = Q + iU \tag{2.39c}$$
$$\langle LR^*(u,v)\rangle = Q - iU. \tag{2.39d}$$

The various Stokes parameters and polarization information can be calculated from the observed correlations from the radio interferometer . The cross correlations $\langle RL^*(u,v)\rangle$ and $\langle LR^*(u,v)\rangle$ are equal to the complex number $\mathbf{P}$ for the linear polarization defined in Equation 2.29 and its complex conjugate.

These correlations as initially recorded will not represent the true source polarization, however, as instrumental effects must be considered and calibrated for, as will be covered in the following section.

2.2.2 Polarization Calibration

To properly measure the polarization of an observed astrophysical object using a radio interferometer, instrumental polarization effects often called “leakage”

or "D–terms" must be identified. These arise when observing as the individual feeds each receiving a different polarization are not perfect. In the case of circular feeds the L and R receivers may in fact measure some of each others radiation, i.e some of the L polarization may be measured by the R and vice-versa. A method to identify these "leakages" and subtract them from the data will be outlined as follows and closely follows the method first presented by Conway & Kronberg (1969). In the ideal case, the complex voltages measured by the telescope in each individual feed are:

$$V_L = g_L E_L e^{i\phi} \tag{2.40a}$$

$$V_R = g_R E_R e^{i\phi}, \tag{2.40b}$$

where the g's are complex gains that are determined through the amplitude, phase and self calibration of the data, the E_L and E_R are the induced electric fields in complex notation, and ϕ is the parallactic angle, that is, the angle between the paths on the sky connecting the observed source to the zenith and to the North celestial pole. This angle will change with time as the source moves across the sky due to the Earth's rotation, making this variable time dependent. The parallactic angles play a very important role in calculating the instrumental polarizations. To include the leakage terms, we introduce the D terms as follows,

$$V_L = g_L \left[E_L e^{i\phi} + D_L E_R e^{-i\phi} \right] \equiv L \tag{2.41a}$$

$$V_R = g_R \left[E_R e^{-i\phi} + D_R E_L e^{i\phi} \right] \equiv R \tag{2.41b}$$

these complex voltages are equivalent to the L and R in the correlations that are produced.

Considering a simple two element interferometer with antennas 1 and 2 forming a single baseline, the four possible correlations of Equations 2.41 (a)

and (b) may be written as follows:

$$L_1 L_2^* = g_{L1} g_{L2}^* E_{L1} E_{L2}^* e^{i(\phi_1 - \phi_2)} \tag{2.42a}$$

$$R_1 R_2^* = g_{R1} g_{R2}^* E_{R1} E_{R2}^* e^{-i(\phi_1 - \phi_2)} \tag{2.42b}$$

$$R_1 L_2^* = g_{R1} g_{L2}^* \left[E_{R1} E_{L2}^* e^{-i(\phi_1 + \phi_2)} + D_{L2}^* E_{R1} E_{R2}^* e^{-i(\phi_1 - \phi_2)} + D_{R1} E_{L1} E_{L2}^* e^{i(\phi_1 - \phi_2)} \right] \tag{2.42c}$$

$$L_1 R_2^* = g_{L1} g_{R2}^* \left[E_{L1} E_{R2}^* e^{i(\phi_1 + \phi_2)} + D_{R2}^* E_{L1} E_{L2}^* e^{i(\phi_1 - \phi_2)} + D_{L1} E_{R1} E_{R2}^* e^{-i(\phi_1 - \phi_2)} \right], \tag{2.42d}$$

where $R_1 L_2$, for example, stands for the correlation between the left-circularly polarized signal from antenna 1 with the right-circularly polarized signal from antenna 2. From observations it is noted that the instrumental polarizations typically fall in the range ∼1–10%, making it safe to ignore terms of order D^2. The observed source polarizations of astronomical objects are also expected to lie in a similar range, making it safe to ignore any $DE_L E_R$ and $DE_R E_L$ terms also. For the next step we take the approximation that Stokes $V \approx 0$ which is true for synchrotron radiation. This simplifies Equations 2.39a and 2.39b to $\langle LL^*(u,v) \rangle \approx \langle RR^*(u,v) \rangle \approx I$. Writing Equations 2.42 in terms of the Stokes I and the complex polarized vector $\mathbf{P}$:

$$L_1 L_2^* = g_{L1} g_{L2}^* I e^{i(\phi_1 - \phi_2)} \tag{2.43a}$$

$$R_1 R_2^* = g_{R1} g_{R2}^* I e^{-i(\phi_1 - \phi_2)} \tag{2.43b}$$

$$R_1 L_2^* = g_{R1} g_{L2}^* \left[P e^{-i(\phi_1 + \phi_2)} + I \left(D_{L2}^* I e^{-i(\phi_1 - \phi_2)} + D_{R1} e^{i(\phi_1 - \phi_2)} \right) \right] \tag{2.43c}$$

$$L_1 R_2^* = g_{L1} g_{R2}^* \left[P^* e^{i(\phi_1 + \phi_2)} + I \left(D_{R2}^* e^{i(\phi_1 - \phi_2)} + D_{L1} e^{-i(\phi_1 - \phi_2)} \right) \right], \tag{2.43d}$$

It is possible to simplify this further by specifying $\phi_1 = \phi_2 = \chi$, which holds true for a connected element array, such as the VLA, where all the antennas are close together and have almost identical parallactic angles:

$$L_1 L_2^* = g_{L1} g_{L2}^* I \tag{2.44a}$$

$$R_1 R_2^* = g_{R1} g_{R2}^* I \tag{2.44b}$$

$$R_1 L_2^* = g_{R1} g_{L2}^* \left[P e^{-2i\chi} + I \left(D_{L2}^* I + D_{R1} \right) \right] \tag{2.44c}$$

$$L_1 R_2^* = g_{L1} g_{R2}^* \left[P^* e^{2i\chi} + I \left(D_{R2}^* + D_{L1} \right) \right], \tag{2.44d}$$

Now it can be seen that the source polarization changes with time as the antenna rotates, while the D terms do not change with time, as they are fixed within the antenna. This makes it possible to solve for the D terms by observing an unresolved source of known or unknown polarization for a variety of parallactic angles over the course of the observing session, in order to disentangle the terms and calculate both the source polarization and the antenna leakage. For a graphical interpretation see Figure 2.5, where as an example the RL correlation is plotted in the complex plane. In the right panel the 'X's' correspond to multiple observations at different values for $\chi(t)$ showing that the RL vector is tracing a circle in the complex plane; the best fit for this circle will yield the D terms which correspond to the location of the centre of the circle. Repeating this for multiple interferometer baselines allows then to solve for the D_L and D_R terms for each antenna. Conceptually this makes sense, as when the parallactic angle of the telescope changes, the polarization angle of the source observed will be expected to rotate accordingly, but the instrumental polarization will remain fixed inside the rotating frame of the antenna allowing the two components of source and instrumental polarization to be disentangled given good parallactic angle coverage. Similarly this step can also be completed using at least one scan of a

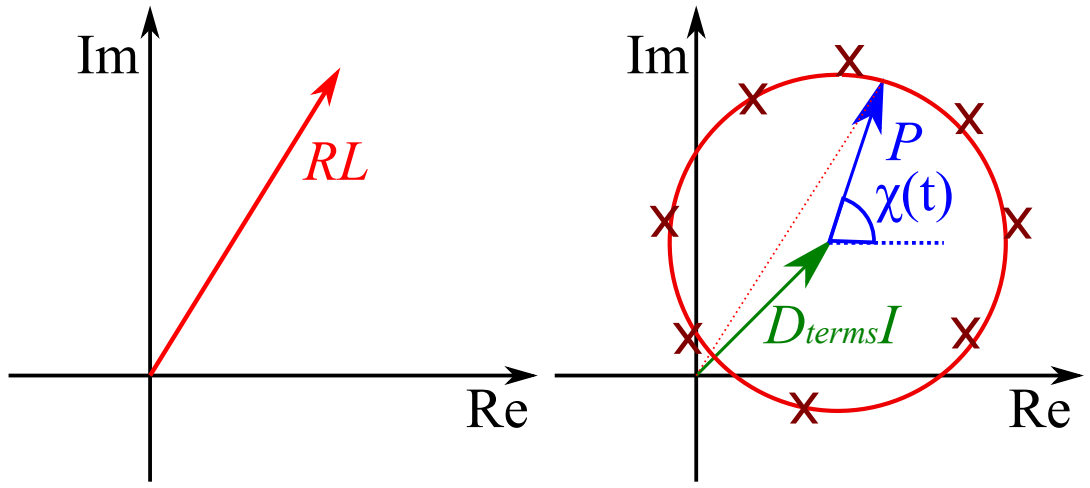

Figure 2.5: Figure showing an exaggerated schematic of how the RL or LR vector P behaves as the parallactic angle of the antenna changes, causing the target polarization angle to rotate. The crosses indicate individual measurements of the RL vector and the circle is the best fit to this data, used to estimate the instrumental polarization $D_{\mathrm{term}}I$ which remains fixed.

bright calibrator source known to be completely unpolarized. In terms of Figure 2.5 this would simply be a single scan with $|P| = 0$; any measured

polarization can only be associated with the D-terms and can be subtracted from the data.

The final step in the polarization is the calibration of the electric vector position angle (EVPA). For a VLA observation that is adequately scheduled and has good solutions for its calibrators, this is quite straightforward; a scan of a point source of known polarization angle is required. One or more scans of polarization angle calibrators are required, typically either 3C 286 or 3C 138, which are often also used as flux density calibrators. These sources have known polarization angles for each frequency and are point-like at most VLA configurations and observing frequencies. Otherwise a uv-range can be selected to ignore baselines with large or small scale structure. Recall from Equation 2.39c how the RL correlated visibilities correspond to $Q + iU$, so their phases should be 2χ, where χ is the polarization angle. Take for example 3C 286, whose polarization angle is known to be close to 33° across most of the VLA observing bands. To calibrate the polarization angles, the phases of all the phase and D-term corrected RL phases must be rotated to have an average value of 66° across all baselines; similarly the LR phases are corrected to be equal to -66°. These phase corrections can be then applied to all the data in an observation and should then display the correct polarization angle when imaged.

2.3 Analysis of Polarization Observations using Faraday Effects

2.3.1 Calculating Faraday depth by fitting χ against λ^2

The Faraday rotation caused by a magneto-ionic material is outlined earlier in Section 1.1.6 and Equations 1.47 and 1.46, where the polarization angle changes linearly with wavelength squared. This allows for the calculation of the RM by fitting the observed polarization angle χ against the wavelength squared λ^2 with the best straight line fit to the data, yielding the RM as the slope and the intrinsic synchrotron polarization angle χ_0 as the intercept on the y-axis. An example of such a fit is given in Figure 2.6, showing a fit to a region in IC 4296. This method has proven to be extremely reliable, as in the majority of cases the RM is dominated by a single component, meaning the

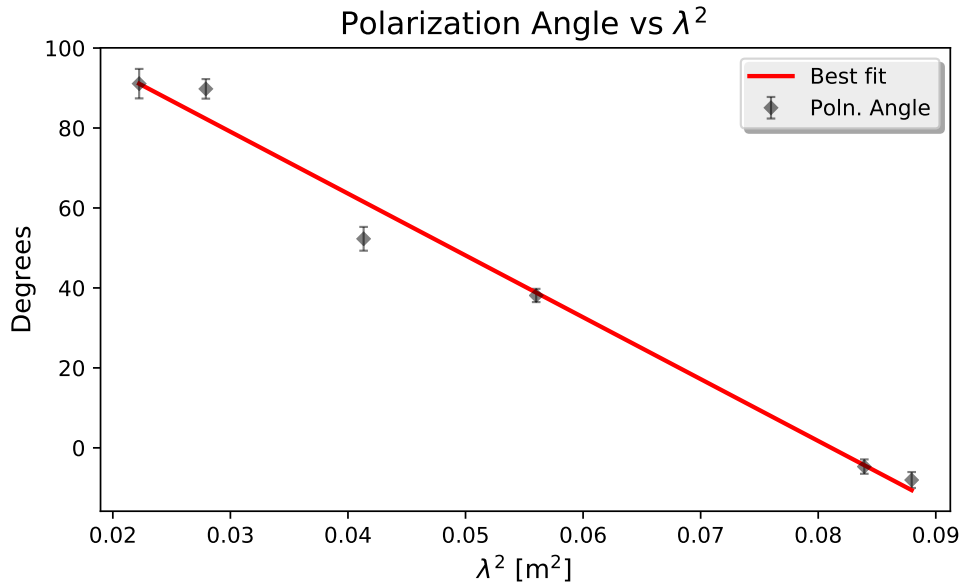

Figure 2.6: Figure showing an example of a χ versus λ^2 fit for a region in IC 4296. The fitted RM is -27 rad m^{-2} and $\chi_0 = 125°$.

polarization angle behaves linearly with wavelength squared. This method works best when a weighted least squares fit is applied to χ and λ^2 data, with the data weighted according to the associated error in the measured polarization angle.

In order to correctly characterise the errors in the rotation measures calculated in this method, which is particularly important for the following analysis in Chapter 3, we look at how the polarization angle and RM are calculated in more detail. The polarization angle is calculated using the observed Stokes Q and U parameters and recalling Section 2.2.1 the polarization angle is given by:

$$\chi = \frac{1}{2}\text{atan}\left(\frac{U}{Q}\right). \tag{2.45}$$

From this representation it can be seen that the error in polarization angle will depend on the errors in the observed Stokes Q and U, namely σ_Q and σ_U. Following the treatment of Hovatta et al. (2012), the error in χ is given by:

$$\sigma_\chi^2 = \left(\frac{\partial\chi}{\partial Q}\right)\sigma_Q^2 + \left(\frac{\partial\chi}{\partial U}\right)\sigma_U^2 \tag{2.46}$$

The partial derivatives are:

$$\frac{\partial \chi}{\partial Q} = \frac{1}{4}\frac{U}{(Q^2+U^2)} \tag{2.47a}$$

$$\frac{\partial \chi}{\partial Q} = \frac{1}{4}\frac{Q}{(Q^2+U^2)} \tag{2.47b}$$

Now substituting this into Equation 2.46, this results in:

$$\sigma_\chi^2 = \frac{U^2\sigma_Q^2 + Q^2\sigma_U^2}{4(Q^2+U^2)^2} \tag{2.48}$$

This gives a good estimate of the errors in the polarization angle, which depend not only on the noise in Q and U but also in the amount of polarized flux ($P = \sqrt{Q^2+U^2}$), with regions with low levels of polarized flux having higher associated errors. The noise in Q and U is typically estimated using the background RMS in images of Stokes Q and U, however the on-source errors are typically higher than the background noise. To accommodate this, the background $\sigma_{Q\mathrm{RMS}}$ and $\sigma_{U\mathrm{RMS}}$ can be multiplied by a factor of 1.8, which was estimated using Monte Carlo simulations of VLBI observations with snapshot u, v coverage in Hovatta et al. (2012). In particular, this factor corresponds to the case when the contribution to the Q and U uncertainties due to uncertainties in the polarization D-terms is negligible, which will be the case for all but unusually bright source regions. This is an appropriate approximation for all the images considered here. This was confirmed again in Monte Carlo simulations in Coughlan (2014), who investigated the on-source errors in images introduced by deconvolution. This study shows that on-source errors in extended regions can be almost twice as high as the background noise. The resulting values of χ, σ_χ and λ^2 can then be used in a weighted least squares fit. The unnormalised weight for each polarization angle measurement is $\frac{1}{\sigma_\chi^2}$. The data can then have a linear fit applied to solve for Equation 1.47.

In a weighted linear least squares fit, a line of the form $f(x) = ax + b$ is fitted to a set of n data points $\{x_1, x_2, \ldots x_n\}$ and $\{y_1, y_2, \ldots y_n\}$ with errors in y, $\{\sigma_1, \sigma_2, \ldots \sigma_n\}$, where the x data represents λ^2 and y and σ are the measured polarization angle, χ with associated 1σ errors. The fitted slope a will be the RM and the y-axis intercept b will be the intrinsic polarization angle χ_0. These parameters are determined by minimizing the following equation:

$$\chi^2 = \sum_{i=1}^{n} w_i(y_i - ax_i + b), \tag{2.49}$$

where χ^2 is used in a statistical sense and does not represent polarization angle, w_i is the unnormalised weight for each data point $\left(\frac{1}{\sigma_i^2}\right)$. The solutions for the fit parameters which can be calculated numerically from the data are:

$$a = \frac{\sum x_i w_i \sum y_i w_i - \sum x_i y_i w_i \sum w_i}{\left(\sum x_i w_i\right)^2 - \sum x_i^2 w_i \sum w_i} = \mathrm{RM} \tag{2.50a}$$

$$b = \frac{\sum x_i y_i w_i - a \sum x_i^2 w_i}{\sum x_i w_i} = \chi_0 \tag{2.50b}$$

The uncertainties in these fit parameters are given by:

$$\sigma_a = \sqrt{\frac{\sum w_i}{\left(\sum x_i w_i\right)^2 - \sum x_i^2 w_i \sum w_i}} = \Delta\mathrm{RM} \tag{2.51a}$$

$$\sigma_b = \sqrt{\frac{\sum x_i^2 w_i}{\sum x_i^2 \sum w_i - \left(\sum x_i w_i\right)^2}} = \Delta\chi_0 \tag{2.51b}$$

The derivations for the terms a and b and their associated error can be found in standard statistical textbooks such as Barlow (1993). The error in the fitted RM can be taken in this case to be the error in the fit, which can often lead to very accurate determinations of the RM if a wide range of λ^2 is used. One caveat that must be considered is the appearance of $n\pi$ ambiguities in the polarization angle, as often for high RM sources a polarization angle being fitted may need to be rotated by $n\pi$ to fit the data better. Such rotations can sometimes be done in error, especially when the number of data points being fitted in λ^2 is low, resulting in artificially high or low RM's. In order to ensure the most reliable fit for the rotation measures, various small numbers of $n\pi$ rotations for the polarization angle measurements can be considered, searching for the fit producing the lowest χ^2 (again in a statistical sense). The smoothness and plausibility of the resulting RM map must also be considered when determining the appropriate number of $n\pi$ rotations to allow for the various frequencies used to obtain the RM fits. In practice, it is rare for adjustments of more than $\pm\pi$ or $\pm 2\pi$ to be required.

2.3.2 Rotation Measure Synthesis and QU Fitting

The situation can however be a little more complex, as multiple RM's and polarized waves can be combined in a beam observed in an interferometer,

which can lead to a multitude of effects on the spectrum of the polarized intensity, causing depolarization (Burn 1966), which is a decrease in fractional polarization as the wavelength increases. It is this insight in Burn (1966) that led to the coupling of polarized flux as a function of wavelength and polarized flux as a function of Faraday depth (rotation measure) as a Fourier pair using the "Faraday dispersion function",

$$P(\lambda^2) = \int_{-\infty}^{\infty} F(\phi) e^{2i\phi\lambda^2} \mathrm{d}\phi, \tag{2.52}$$

where $F(\phi)$ describes the distribution of polarized flux as a function of Faraday depth (ϕ) along the line of sight and possesses units of Jy m^2 rad^{-3}, which in theory will identify many values of RM along the line of sight and also regions extended in RM arising due to the mixing of the synchrotron plasma and Faraday rotating medium, for example. Given the limitations of radio telescopes at the time and the sparse sampling of λ^2, the expected linear behaviour of χ versus λ^2 was accepted, and this incredible insight was not fully utilised until the development of wide-band receivers in radio astronomy, enabling observations over a wide range of λ. Brentjens & de Bruyn (2005) outline a method to apply this approach and perform these calculations for observations of the Perseus cluster using the Westerbork Synthesis Radio Telescope (WSRT).

The following explanation of the rotation measure synthesis method is a summary of their findings. The goal is to be able to use a Fourier transform to solve for $F(\phi)$, however some considerations and assumptions must be made. Given physical measurements of $P(\lambda)$, it is obvious that $\lambda^2 < 0$ cannot be measured, and not all values of λ^2 can be measured. Given the setup of the radio receiver or interference due to RFI, a weight function is introduced to represent this, $W(\lambda^2)$, where $W(\lambda^2) = 1$ for measured values and 0 elsewhere. The omission of values for $\lambda^2 < 0$ can be made when we consider the function of $P(\lambda^2)$ to be Hermitian, i.e $P(-\lambda^2) = P^*(\lambda^2)$, and as a result $F(\phi)$ must be a real-valued function. Now re-writing the previous equation to include the weighting, we get:

$$P_{\mathrm{obs}}(\lambda^2) = W(\lambda^2) \int_{-\infty}^{\infty} F(\phi) e^{2i\phi\lambda^2} \mathrm{d}\phi, \tag{2.53}$$

Making the substitution $\lambda^2 = u\pi$, Brentjens & de Bruyn (2005) define the

rotation measure transfer function (RMTF) to be:

$$R(\phi) = \frac{\int_{-\infty}^{+\infty} W(u\pi) e^{2i\phi\lambda^2} \mathrm{d}u}{\int_{-\infty}^{+\infty} W(u\pi) \mathrm{d}u}, \tag{2.54a}$$

such that:

$$W(u\pi) = \left(\int_{-\infty}^{+\infty} W(u\pi) \mathrm{d}u \right) \int_{-\infty}^{+\infty} R(\phi) e^{2i\pi} \mathrm{d}\phi. \tag{2.54b}$$

Substituting into Equation 2.53 yields:

$$P_{\mathrm{obs}}(u\pi) = \left(\int_{-\infty}^{+\infty} W(u\pi) \mathrm{d}u \right) \int_{-\infty}^{+\infty} R(\phi) e^{2i\pi\phi u} \mathrm{d}\phi \times \int_{-\infty}^{+\infty} F(\phi) e^{2i\pi\phi u} \mathrm{d}\phi \tag{2.55}$$

Taking the Fourier transform of this yields:

$$F(\phi) * R(\phi) = \frac{\int_{-\infty}^{+\infty} P_{\mathrm{obs}}(u\pi) e^{2i\pi\phi u} \mathrm{d}u}{\int_{-\infty}^{+\infty} W(u\pi) \mathrm{d}u}. \tag{2.56a}$$

Subsituting back for $u = \lambda^2/\pi$

$$F(\phi) * R(\phi) = K \int_{-\infty}^{+\infty} P_{\mathrm{obs}}(\lambda^2) e^{2i\phi\lambda^2} \mathrm{d}\lambda^2. \tag{2.56b}$$

This shows how the Fourier transform of the polarized flux as a function of wavelength results in the polarized flux as a function of Faraday depth convolved with the RMTF, which depends on how well or poorly sampled the λ^2 plane is. Retrieving the flux as a function of Faraday depth is a useful tool, as it can reveal multiple rotation measures or regions that are extended in Faraday depth, indicating where multiple values of RM are combined within the beam of the telescope, or where synchrotron emitting regions are mixed with the Faraday rotating medium resulting in a continuous range of rotation measures combined. One difficulty in this method is the fact that the produced Faraday depth spectrum ($F(\phi)$) is convolved with the RMTF ($R(\phi)$), which introduces sidelobes and noise, as can be seen by a sample RMTF in Figure 2.7. This essentially puts limits on the sensitivity and resolution at which RM's can be determined. The largest possible Faraday depth that can be detected ϕ_{max}, the highest resolution that can be achieved $\delta\phi$ and the largest possible scale in Faraday depth ϕ_{maxscale} that can be detected using this method

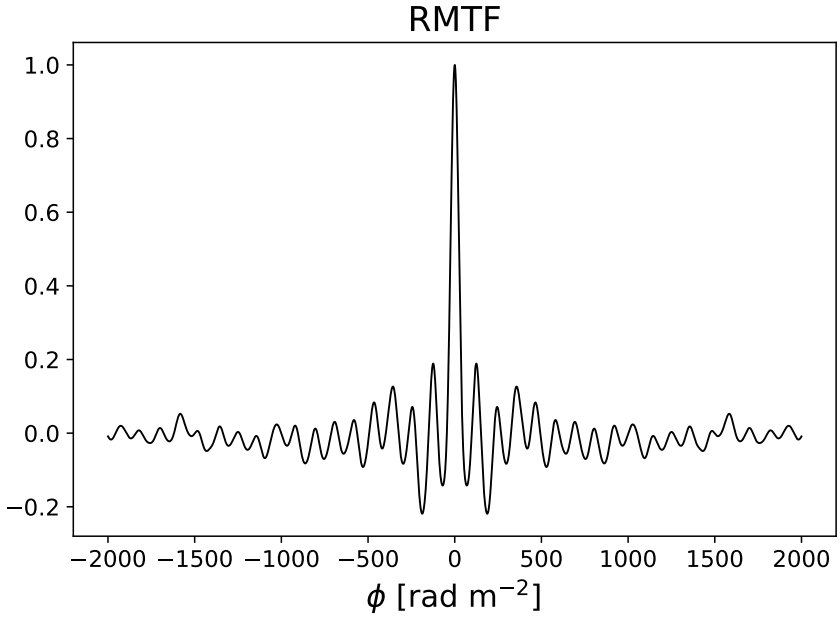

Figure 2.7: Example of an RMTF function for a VLA observation of 3C 433 (see Chapter 5) from 1–4 GHz with a 2 MHz minimum channel width.

are calculated in Brentjens & de Bruyn (2005) to be:

$$\phi_{\rm max} \approx \frac{\sqrt{3}}{\delta\lambda^2}, \tag{2.57a}$$

$$\delta\phi \approx \frac{2\sqrt{3}}{\Delta\lambda^2}, \tag{2.57b}$$

$$\phi_{\rm maxscale} \approx \frac{\pi}{\lambda^2_{\rm min}}, \tag{2.57c}$$

where $\delta\lambda^2$ is the smallest interval in λ^2, which in observing terms is the smallest channel width in λ^2, $\Delta\lambda^2$ is the overall range in λ^2 values, and $\lambda^2_{\rm min}$ is the smallest value of λ^2 in the dataset. This method of using the Fourier pair of polarized flux as a function of λ^2 and as a function of Faraday depth bears a striking resemblance to using radio interferometry and aperture synthesis to make an image using the Fourier pair between observed flux as a function of baseline coverage and as a function of sky coordinates, right ascension and declination. Here the sparse λ^2 coverage is an analogue to baseline coverage where the largest possible Faraday depth observable is given by the shortest spacing between λ^2, and the accuracy and resolution is the width of the main peak in the RMTF, calculated from the longest separation between λ^2 values, which corresponds to the longest baselines in interferometry. It is therefore intuitive to assume that traditional deconvolution can be applied, indeed the

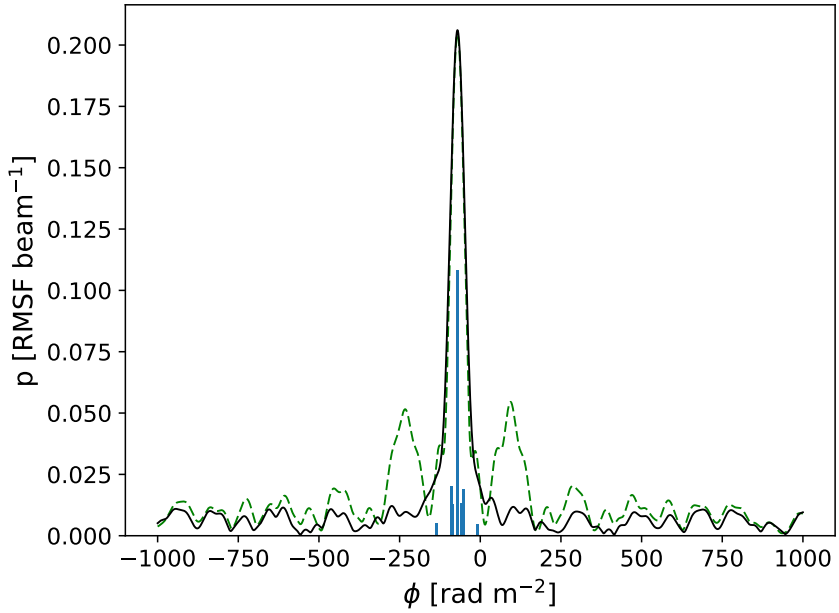

Figure 2.8: Example of a cleaned Faraday spectrum for a VLA observation of 3C 433 from 1–4 GHz, where the cleaned spectrum is given by the solid black line, the dirty spectrum convolved with the RMTF is given in the green dashed line and the locations and intensities of the "clean components" is given by the blue bars.

CLEAN algorithm has been used on Faraday spectra to remove the effects of sidelobes from the RMTF and make the peaks in the Faraday depth spectrum more clear. This process, known as RMCLEAN (Heald et al. 2009) uses the CLEAN algorithm on the one-dimensional Faraday depth spectra. An example of the application of this method is given in Figure 2.8 where such an RMCLEAN is performed, showing how the sidelobes in green from the dirty RM synthesis have effectively been removed leaving only the clean, deconvolved spectrum in black, with the location of the clean components as blue bars.

Another consideration is the uncertainty in the $\phi_{\rm peak}$ value. Brentjens & de Bruyn (2005) specify this to be related to the width and signal to noise ratio of the peak in the Faraday spectrum by

$$\sigma_\phi = \frac{\mathrm{FWHM_{RMTF}}}{2 \times \mathrm{SNR}}, \tag{2.58}$$

where $\mathrm{FWHM_{RMTF}}$ is the full width half maximum of the fit to the central peak in the rotation measure transfer function; commonly this is the fitted Gaussian used in the RMCLEAN, a process which will also increase the signal to noise ratio of the spectrum.

The structure of this Faraday spectrum and various features it can possess and what physical phenomena these correspond to are described in detail in Sokoloff et al. (1998), which describes various depolarization effects which are summarized below.

1. **Internal Faraday dispersion** occurs when the Faraday rotating medium is mixed with the synchrotron emitting region. Here the depolarization is caused because a variety of RM's are produced. Depending on where in this region synchrotron radiation is emitted, it will experience a different Faraday rotation, as the radiation will have a different amount of magneto-ionic material to pass through; these rays with varying RM's then combine in an observing beam and interfere destructively to depolarize the signal, an effect which increases with wavelength, but may display some complex behaviour such as reverse depolarization in parts. The rotation measures combining into the observing beam will have a top-hat like distribution if a uniform Faraday rotating medium with a uniform B-field is considered. Furthermore, knowing of the Fourier relationship between polarized flux as a function of wavelength squared (λ^2) and polarized flux as a function of Faraday depth (ϕ), the top-hat like RM distribution should resemble a sinc function in the observable polarized flux. Note, however that such a pattern in the RM could also come about due to an ordered magnetic field external to the synchrotron plasma. An unresolved gradient in the rotation measure across the beam would cause a similar top-hat like function in ϕ space and a sinc function pattern in the polarized flux spectrum:

$$P(\lambda) \sim \frac{\sin(\Delta\mathrm{RM}\lambda^2)}{\Delta\mathrm{RM}\lambda^2}, \tag{2.59}$$

   where $\Delta\mathrm{RM}$ is the gradient of RM values ($|\mathrm{RM}_{\mathrm{max}} - \mathrm{RM}_{\mathrm{min}}|$). A figure showing a visualisation of such a structure as a spectrum in λ^2 and in Faraday depth is given in Figure 2.9.

2. **External Faraday dispersion and rotation** occur when the Faraday rotating medium of magneto-ionic plasma is external to the synchrotron plasma and along the line of sight to the observer. The dispersion can occur due to the presence of a random magnetic field and/or clumpy region of free electrons unresolved by the observing beam. This causes slight variations in the RM, creating a Gaussian distribution of RM about

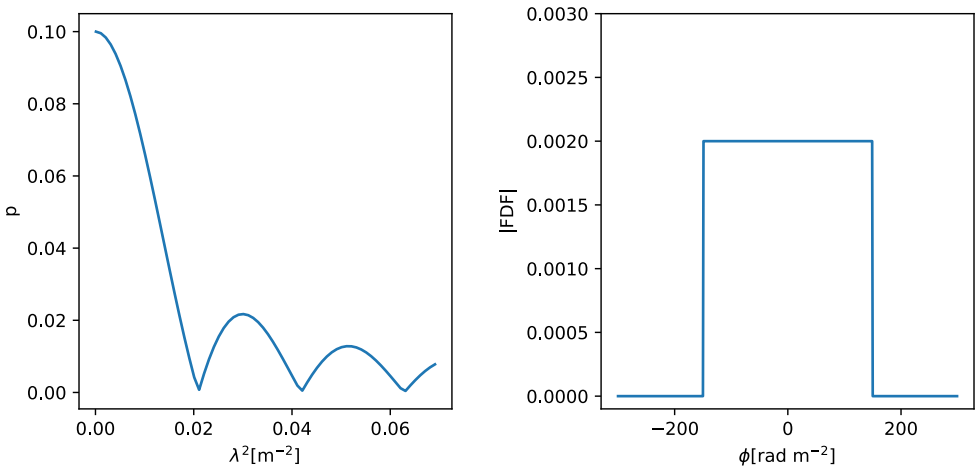

Figure 2.9: **Left panel:**Schematic of a polarized spectrum for a region with initial polarization $p_0 = 10\%$ affected by a $\Delta\mathrm{RM}$ of 150 rad m^{-2}, by an either internal process or external, ordered, unresolved and twisted magnetic field. **Right panel:** The corresponding spectrum on the Faraday depth axis showing the gradient of RM values from -150 to 150.

some mean value, which is the RM associated with the magneto-ionic material with some net electron density and line of sight magnetic field component causing a linear χ versus λ^2 behaviour:

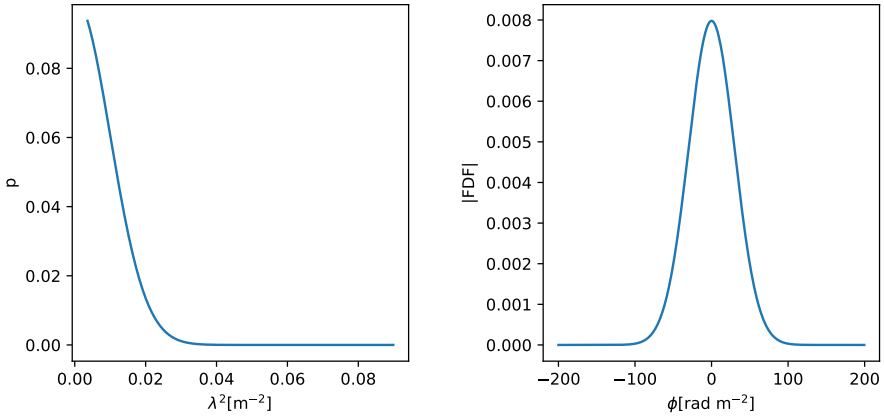

Figure 2.10: **Left panel:**Schematic of a polarized spectrum for a region with initial polarization $p_0 = 10\%$ affected by a σ_{RM} of 30 rad m^{-2} and $\mathrm{RM} = 0$, by an external process. **Right panel:** The corresponding spectrum on the Faraday depth axis showing the corresponding Gaussian distribution of RM values.

$$P(\lambda) \sim e^{2i(\chi_0+\mathrm{RM}\lambda^2)} e^{-2\sigma^2_{\mathrm{RM}}\lambda^4}, \tag{2.60}$$

where the first exponential term describes the basic single RM component and polarized vector by combining Equations 2.29 and 1.47,

and the second term describes depolarization due to the Gaussian distribution of Faraday depth about RM with a width of σ_{RM}. A schematic of this for $p_0 = 10\%$, $\mathrm{RM} = 0\,\mathrm{rad\,m^{-2}}$, and $\sigma_{\mathrm{RM}} = 30\,\mathrm{rad\,m^{-2}}$ is shown in Figure 2.10, with the polarized spectrum plotted on the left and the Faraday depth spectrum on the right with a corresponding Gaussian of width σ_{RM}. An RM value will simply change the position of the Gaussian.

If multiple unresolved RM components with or without dispersion terms exist, these can simply be summed up. Any terms for internal dispersion, or due to ordered magnetic fields, can be included as outlined in Equation 2.59.

Using the terms in both the above regimes, a generalized model for fitting to polarized spectra can be defined,

$$P(\lambda) = \sum_{j=1}^{n} p_{0j} e^{2i(\chi_{0j} + \mathrm{RM}_j \lambda^2)} \times e^{-2\sigma^2_{\mathrm{RM}_j} \lambda^4} \times \frac{\sin(\Delta \mathrm{RM}_j \lambda^2)}{\Delta \mathrm{RM}_j \lambda^2}. \tag{2.61}$$

Here, multiple polarized components can be summed over, while also the terms for the external screen depolarization and the ordered magnetic field or internal depolarization can be set to unity to be ignored for a fit, or grouped to be common to a set of single polarized components. Such fitting has been performed in O'Sullivan et al. (2012) and Anderson et al. (2019) for example, where the fitting is done to fractional Stokes Q and U named q and u, in order to remove spectral index effects. Equation 2.61 is split into the separate q and u components for fitting, where the complex exponential term will be separated into sine and cosine terms with the external and/or internal depolarizing terms being in common for each. Typically no more than 3 components are fitted and the number of depolarizing screens and internal/ordered magnetic field depolarization terms are kept to a minimum in an effort to not over-interpret the data being fitted.

Chapter 3

Faraday RM gradients in Kiloparsec Scale Radio Jets

To investigate the effects of the cosmic battery (Contopoulos & Kazanas 1998, Contopoulos et al. 2009) and whether it truly is the mechanism giving rise to the magnetic field structure in astrophysical jets, we need to study the effects such a field would have on jets at all possible scales. To briefly recap the effects of the cosmic battery from Section 1.1.4, this model predicts that, in the large scale jets a toroidal field component with an associated outward electrical current should dominate; this is the outer helical magnetic field forming the "return field" for the loops of magnetic field rooted in the accretion disc and wound up by its rotation. On small scales observable with VLBI, a helical field with an associated inward electrical current is expected to dominate, as has been shown in detailed studies(Gabuzda, Knuettel & Reardon 2015, Gabuzda, Nagle & Roche 2018). For the large scale jets no such detailed study has been done, making the following study considered here vital in investigating the effects of the possible cosmic battery mechanism. The detection of the toroidal field components is done using observations of the Faraday rotation measure (RM), which is proportional to the line of sight magnetic field component and the electron density. Faraday rotation changes the polarization angle as the polarized radiation passes through such a region. The rotation measure is given by

$$\mathrm{RM} = \frac{e^3}{8\pi^2\epsilon_0 m_e^2 c^3} \int_0^l n_e \vec{B} \cdot \mathrm{d}\vec{l}, \tag{3.1}$$

where n_e is the electron density, $\vec{B}$ is the magnetic field and $\mathrm{d}\vec{l}$ is a the unit vector along the line of sight. The electron charge and mass, e and m_e, permittivity of free space, ϵ_0, and speed of light c, are constants. The effect on the observed polarization angle for a homogeneous source and uniform region of Faraday rotation,

$$\chi_{\mathrm{obs}} = \chi_0 + \mathrm{RM}\lambda^2 \tag{3.2}$$

shows a linear change in polarization angle with the wavelength squared, where χ_{obs} is the observed polarization at wavelength λ and χ_0 is the intrinsic polarization angle as emitted before being affected by RM. This intrinsic angle is also useful in determining the magnetic field direction on the plane of the sky, as this is perpendicular to the magnetic field in predominantly optically thin regions.

Using multiwavelength polarization observations and fitting for χ versus λ^2 will yield values for the RM, which traces the line of sight magnetic field and electron density. A transverse gradient in the RM across the jet is an indicator of such a toroidal magnetic field component, as it reflects a similar change in the line of sight magnetic field across the jet as shown in Figure 3.1; in particular, a change in sign of the rotation measure from one end of the gradient to the other can only be explained by a change in the line of sight magnetic field component, not a change in electron density. Note, however, that a gradient due to a helical field need not change in sign across the jet, as the gradient may be dominated by values of one particular sign, depending on the viewing angle.

The significance of a transverse RM gradient also plays a very important role, as the gradient structure needs to be well defined given the errors in the calculated RM values. A good way to characterize the significance is by using the RM values and their associated 1σ errors at the end points of the gradients,

$$\mathrm{significance}(\sigma) = \frac{|\mathrm{RM}_1 - \mathrm{RM}_2|}{\sqrt{\Delta\mathrm{RM}_1^2 + \Delta\mathrm{RM}_2^2}}, \tag{3.3}$$

where the RM values indicate the endpoint rotation measures of a purported gradient and the $\Delta\mathrm{RM}$ values are the associated errors. The significance will simply be the total change in RM values across the gradient divided by the errors at the end points added in quadrature.

Typically, for observations of jets the end points have the highest calculated

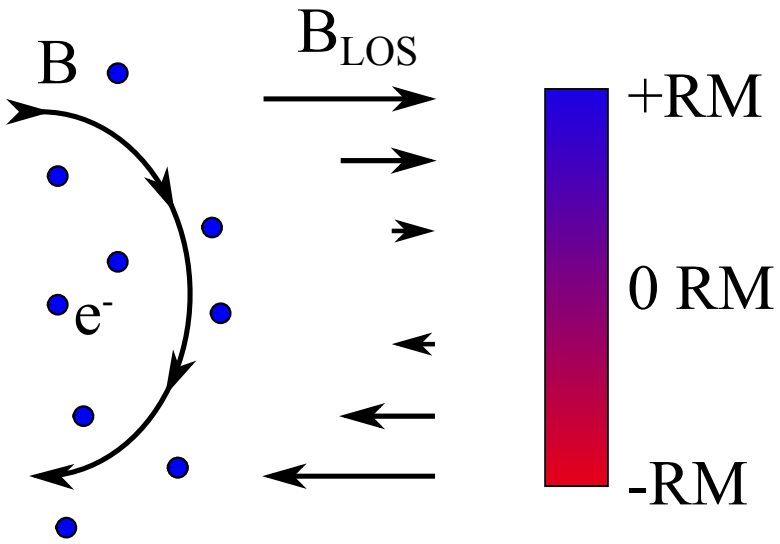

Figure 3.1: Schematic of how a toroidal magnetic field component is detected as a gradient in the observed RM.

error in the rotation measure making this a conservative estimate of significance. The errors in the RM in the studies here are calculated from the error in the fitted value for RM in the χ versus λ^2 fits, from a weighted least squares fit which is discussed in Section 2.3. The errors being higher at the end points corresponds to edges of the jet where the signal-to-noise ratio of the polarized flux typically decreases and thus the error in the calculated polarization angle increases as $\Delta\chi \propto P^{-4}$

The analysis of significant gradients can be made more robust when long portions of the jet show transverse gradient structure. Here the significances of multiple gradients can be plotted as a function of distance along the jet. This is particularly helpful in identifying extended regions of high significance, while also removing selection bias displayed results. This can be done quite efficiently using PYTHON routines on rotation measure maps made from Stokes Q and U images rotated that the jet direction is horizontal so that RM gradients can be calculated along columns of cells with their significances found using Equation 3.3. Such an analysis is presented for NGC 6251, 3C 465, A2142a, 5C 4.114, IC 4296 and 3C 303 in the following sections. It must be noted that these figures show the significance of gradients as a function of distance along the jet and are sampled according to the cell (pixel) size, which is much smaller then the beam size. Although the presence of formally statistically significant RM gradients in a small number of cells spanning much less than a beam width cannot be considered reliable evidence for a real transverse RM gradient, an extended region with multiple adjacent

cells showing $> 3\sigma$ detections spanning of the order of a beam-width or more shows that the $> 3\sigma$ gradients are not isolated spurious results but actual gradients present in the image.

A table outlining all the VLA data analysed in this study is laid out in Table 3.1 with project codes, observing dates and frequencies listed. The data were calibrated and analysed using the software packages AIPS and CASA. The calibrated visibility data for 5C 4.114, 5C 4.152 and A2142a, were kindly provided by A. Bonafede and F. Govoni (Bonafede et al. 2010, Govoni et al. 2010).

3.1 Statistically Significant Results

The following section discusses statistically significant transverse Faraday rotation measure gradients in kiloparsec scale AGN jets, and their implied toroidal magnetic fields. These are sources for which transverse rotation measure gradients have significances higher than 3σ, according to Equation 3.3. Featured in this section are NGC 5251, 3C 465. A2142a, 5C 4.114, Coma A and IC 4296.

3.1.1 NGC 6251

Results for this source have been published by Knuettel & Gabuzda (2019).

This is a bright FRI radio galaxy that is relatively nearby ($z = 0.02471$, Wegner et al. (2003)). The radio structure, and in particular, the rotation measure distribution in this source were discussed in detail by Perley et al. (1984). In particular, they noted a transverse RM gradient in the inner portion of the jet, and suggested the possibility of a toroidal or helical magnetic field component associated with the jet. It has been argued that the confinement of the jet may be due to the surrounding X-ray environment. However Mack et al. (1997) argue that the intergalactic medium is not dense enough to confine the hot X-ray plasma in the vicinity of the jet, and that a magnetic process with forces parallel to the jet may need to be present, making further analysis of the RM gradients and their statistical significance a worthwhile endeavour.

Table 3.1: Table outlining the VLA observations and data personally downloaded and calibrated from the VLA archive. ν is the observing frequency. The bandwidth is $\Delta\nu$ and t is the total integration time on the source in hours.

Object	Project	ν [MHz]	$\Delta\nu$ [MHz]	VLA Config.	Observing Date	t [hrs]
Coma A	VANB[a]	1413	25	A	1981 Mar 18	4.7
	VANB[a]	4885	50	B	1981 Jun 01	4.1
	AB348	14940	100[b]	C	1985 Aug 26	6.2
	13B-083	994–2006	1×1024	B	2013 Dec 29	1.8
3C 465	AE61	4535/4665	50/50	BC	1989 Oct 01	4.6/4.6
	AE61	4845/4965	50/50	BC	1989 Oct 01	4.6/4.6
	AE61	8085/8335	50/50	BC	1989 Sep 20	4.3/4.3
	AE61	8535/8785	50/50	BC	1989 Sep 20	4.3/4.3
	12A-215	1000–2032	1×1024	B	2012 Aug 20	2.7
NGC 6251	PERL[c]	1479.9	12.5	Mixed[d]	1979 Nov 05	12
	PERL[c]	4885	50	Mixed[d]	1980 Mar 31	10.5
	PERL[c]	1370 / 1662	25	A	1980 Dec 05	6/6
	13A-153	4488–6512	2×1024	B	2013 Dec 01	5.5
IC 4296	15A-305[e]	1008–2032	1×1024	A	2015 Jul 11	0.7
3C 303	KRON [f]	4866.35	12.5	A	1981 Apr 20	1.2
	AZ29	14939.9	100[b]	C	1986 Dec 08	1.1
3C 219	AC149[g]	1385	25	B	1986 Sep 06	7
	AC149[g]	1665	25	B	1986 Sep 06	7
5C 4.114	AB1299[h]	1365/1515	25	A	2008 Dec 11	4.6
	AB1311 [h]	4535/4935	50	B	2009 Apr 26	5.1
5C 4.152	AF418[h]	4535/4935	50	B	2006 Aug 04	1.5
	AF418[h]	8085/8465	50	B	2006 Aug 04	1.2
A2142A	AD485[i]	4535/4885	50	B	2003 Dec 23	3.3
	AD485[i]	8085/8465	50	C	2004 Apr 13	3.1

[a] Data previously published in van Breugel et al. (1985).
[b] Data consist of two channels 50 MHz apart each with 50 MHz bandwidth. Central frequency is given.
[c] Data previously published in Perley et al. (1984).
[d] Mixed configuration was a limited number of VLA antenna during the commissioning phase of the instrument. The longest baseline corresponds to an A configuration observation, however short baselines sensitive to large scale structures are present also.
[e] Data previously published in Grossová et al. (2019).
[f] Data previously published in Kronberg et al. (2011).
[g] Data previously published in Clarke et al. (1992).
[h] Data previously published in Bonafede et al. (2010).
[i] Data previously published in Govoni et al. (2010).

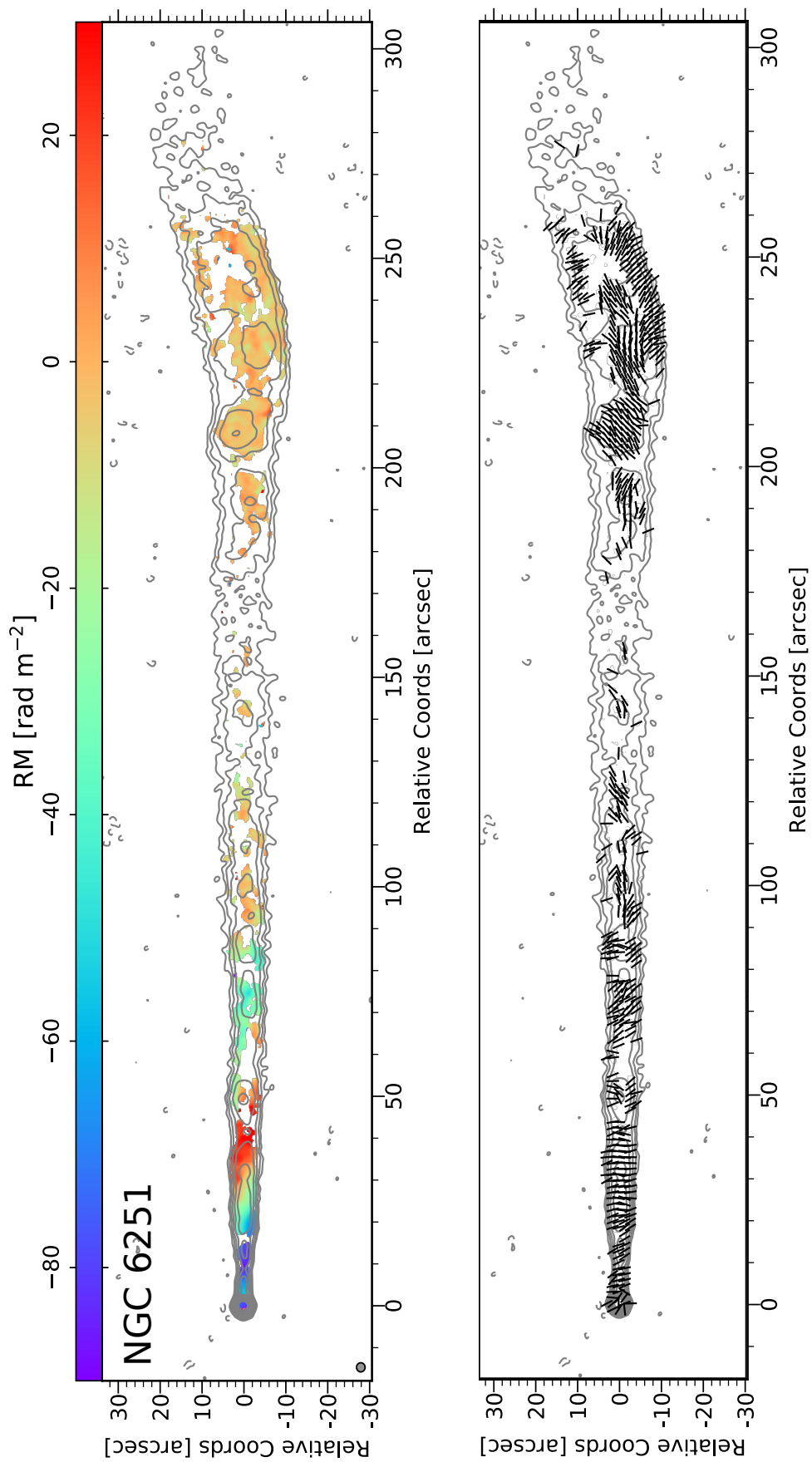

Figure 3.2: **Top Panel:** Rotation measure map of NGC 6251 in colour scale with overlaid contours of Stokes *I* at 1.37 GHz, the contour levels are at 0.35, 0.7, 1.4, 2.8, 5.6, 11.2, 22.4, 44.8, 89.6, 179.2 mJy beam^{-1} with a dashed negative contour at -0.35 mJy beam^{-1} the image has been rotated by 26° in the clockwise direction to save space, and therefore only relative coordinates in arcseconds are given. A common circular restoring beam of 2" was used and is shown in the bottom left corner of the figure. **Bottom Panel:** Map of the intrinsic polarization angle χ_0, corrected for Faraday rotation plotted as vectors. The contours and convolving beam are identical to the top panel.

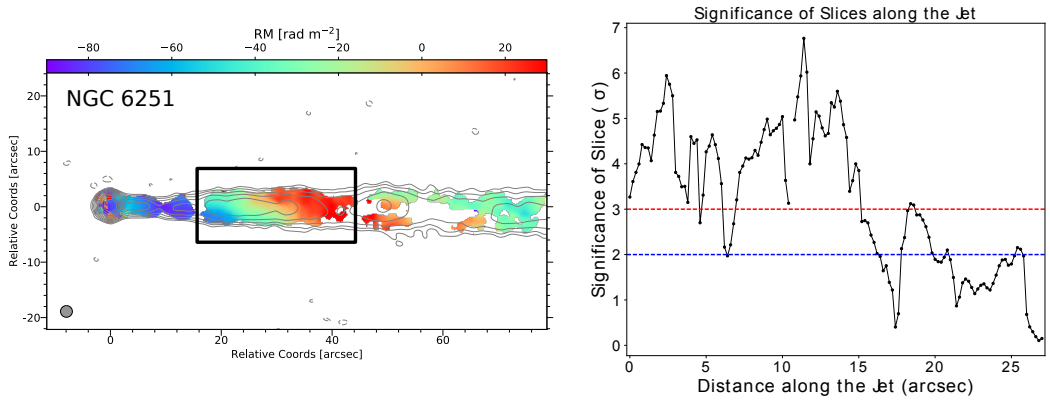

Figure 3.3: **Left panel:** A zoomed in image of the inner jet of NGC 6251 with the same contour levels as in Figure 3.2 showing the region with the transverse RM gradients in the black rectangle. **Right panel:** A plot of the calculated significance of the transverse RM gradients as a function of distance along the jet for the region indicated by the black rectangle in the left panel.

For this analysis the original data published by Perley et al. (1984) were downloaded from the VLA archive and calibrated using standard procedures in AIPS with 3C 286 used as the flux and polarization angle calibrator for each dataset, and J1800+7828 (S5 1803+784) used as the phase calibrator and the polarization leakage calibrator, due to its good parallactic angle coverage. Since NGC 6251 is dominated by a strong unresolved core at the jet base, using a carefully selected range of the longer baselines, the source will appear point like over the course of a single scan. This allows the scans of NGC 6251 to be used in conjunction with the phase calibrator scans to correct the phases and amplitudes of all the baselines and scans for NGC 6251. Baselines longer than 20,000 wavelengths were selected from the NGC 6251 data for this self phase-referencing. This process loses the absolute position information for the source, however due to the age of the data (some of the observations were taken during commissioning of the VLA), the determined position of NGC 6251 differs for each observation, making image alignment difficult. This process aligns the bright radio core to the centre of the image making it easy to fit for χ versus λ^2 later in the RM analysis.

Images of Stokes Q and U images were made using a common convolving beam of 2”, and were then used to construct a rotation measure map using procedures in PYTHON with a weighted least squares fitting algorithm for χ versus λ^2. The RM map is given in Figure 3.2, with the jet rotated by 26° in the clockwise direction so that the inner part of the jet is horizontal. An

accompanying χ_0 map of the Faraday rotation measure corrected EVPAs is also given. This map shows polarization angles perpendicular to the inner jet with no unusual deviations, suggesting the RM and χ_0 was calculated correctly. The region with gradients is given with a box around it in Figure 3.3. Using automated PYTHON scripts the significances of a series of gradients at different distances along the jet were calculated and plotted as a function of distance along the jet. The right hand panel of Figure 3.3 shows this plot with the 2 and 3 sigma levels given as horizontal lines, where the significances were calculated using the end-point RM values as given in Equation 3.3. There are many regions in the jet showing significances above 3 sigma, making the gradients less likely to be due to a random process such as turbulence and more likely to be due to large–scale ordered structures in the line–of–sight magnetic field or electron density. An integrated RM value for the Galactic contribution to the RM was also subtracted from the map using the value of –49 rad m^{-2} used in Perley et al. (1984), which is the mean RM in the outer region of the jet where the RM is constant across the decelerated jet, making this a likely value for the RM due to any foreground magneto-ionic material between NGC 6251 and the observer. A similar value of $\simeq -50$ rad m^{-2} was calculated for this outer region around the knot using LOFAR HBA (110–190 MHz) observations and RM synthesis in Cantwell (2018); the stripes and gradients observed using the VLA cannot be seen using LOFAR, as the lower frequencies and resolutions have depolarized these structures within the observing beam.

While there appear to be significant gradients with directions implying outward electrical currents in that region, further out in the jet there appear to be gradients in the opposite direction (see right hand panel in Figure 3.2). The RM structure in the jet appears like a positive "stripe" of RM at an angle of $\sim$30° to the jet direction, which causes gradients in the RM 20–40" from the core and apparently again at 50–75" from the core in an opposite direction, this can be seen most clearly in the left panel of Figure 3.3.

To supplement the analysis, another previously unpublished observation at 4.5–6.5 GHz was also downloaded from the VLA archive and calibrated using standard procedures in CASA. Images of Stokes Q and U were made using 128 MHz bandwidth bins. As with the older data, the Q and U images were used to make RM maps via χ versus λ^2 fitting in PYTHON. The resulting RM map is given below in Figure 3.4. As expected, due to the smaller range of λ^2 values used, the errors in the fitted RM's are higher, meaning that a smaller

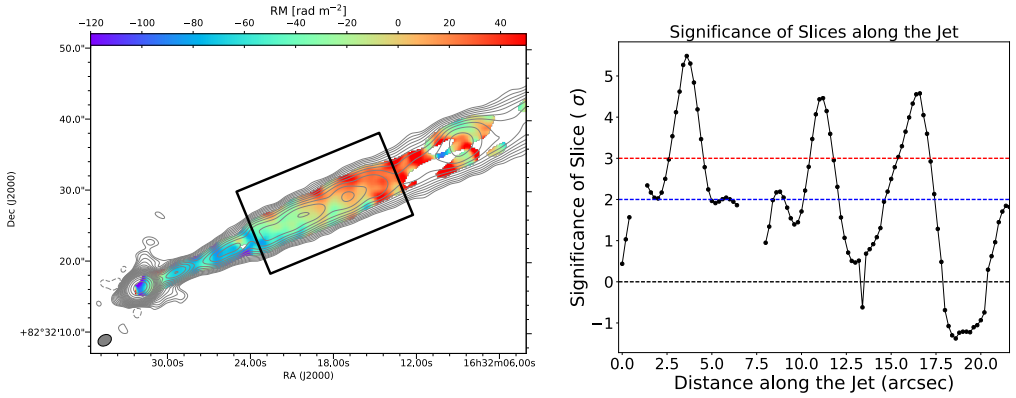

Figure 3.4: **Left panel:** Rotation map of the inner region of the jet in NGC 6251 using the 4.5–6.5 GHz data, the rotation measure is given in the colour scale with contours at 5.5 GHz overlaid with levels at 0.075, 0.106, 0.15, 0.21, 0.3, 0.43, 0.6 0.85, 1.2, 1.7, 2.4, 3.4, 4.8, 6.8, 9.6, 13.6, 19.2, 27.15, 38.4, 76.8, 153, 307.2 mJy beam^{-1}, with a dashed negative contour at -0.075 mJy beam^{-1}. **Right panel:** Plot of the significances of transverse rotation measure gradients against distance along the jet in the region indicated by the black rectangle in the left panel. Horizontal lines at a significance of 2σ and 3σ are given in blue and red, respectively.

area of the jet has accurate RM values. The values for the RM are very similar to the values seen in Figures 3.2 and 3.3 and share similar features, including the transverse gradient in the RM confirming the presence of this feature. The region with transverse RM gradients in the opposite direction further does not feature, however this is most likely due to the decreased sensitivity to Faraday rotation measure in these observations. The significances of the gradients in this dataset were tested in a similar manner to the previous observation. Only some regions have gradients reaching above 3 sigma significances, as can be seen in Figure 3.4, where the significance of the transverse gradients is plotted as a function of distance along the jet for the region inside the black box. The overall decrease in significance compared to the older observations was to be expected considering the higher errors in the fitted RMs. The persistence of the gradient pattern with similar ranges in RM in the same region of the jet shows that this transverse gradient is real and likely associated with a toroidal or helical magnetic field component. The dominant direction of this gradient indicates that the helical magnetic field will have an associated outward electrical current, consistent with previous results.

It has been suggested that the RM gradient may be due to “Magnetic Draping” (Dursi & Pfrommer 2008) from extragalactic magnetic fields. This is often

seen in large scale lobes and jets (Guidetti et al. 2011) or in galaxy clusters, in the form of stripes of RM across the jet, and is due to the expansion or movement of a "bubble", such as a radio lobe, through a large scale magnetic field, causing the field to drape around the "bubble". While there does appear to be a stripe in RM at an angle roughly 30° to the jet direction in NGC 6251 it is difficult to ascribe this to some external magnetic field effect. While there is a diffuse X-ray environment around the source, this is spherically distributed around the host galaxy, which would imply any induced RM variations should have the form of stripes directly across the jet rather than at an oblique angle. There is also some X-ray emission along the jet, but this only features in the first ~ 30" from the core (Figure 8. Evans et al. 2005) and again at the knot $\sim 220''$ from the core. Furthermore, the lack of any RM variation in the region of RM further out in the jet, outside of the influence of the diffuse thermal X-ray emission from the host galaxy, makes an intergalactic or intracluster effect less likely, as magnetic draping is usually seen in denser environments and more towards jet termination points or the edges of large scale lobes. Furthermore, the sign of the RM changes on either side of the stripe, meaning the line of sight magnetic field is changing direction, which cannot be attributed to a particle density effect from the thermal X-ray environment alone. A magnetic field with a changing direction with respect to the line-of-sight must be present around the jet to some extent. The origin of this field is not entirely clear, however the high significance of the inner gradients observed at multiple epochs lends credence to a local toroidal field around the jet.

3.1.2 3C 465

The results presented here were published in the conference proceedings proceedings by Knuettel et al. (2017). The wide-band VLA observations and analysis into their RM structure are a further addition.

This is an AGN at redshift $z = 0.0302$ (Wegner et al. 1999) with an impressive jet structure. The radio source is classified as an FR I radio galaxy with large plumes seen in each of the jets, with the structure characteristic of a "wide-angle-tail radio source" (Owen & Rudnick 1976). 3C 465 is the brightest member of the A2634 cluster and is located close to the center of the group; an interaction with the cluster environment may be the reason for the unusual

bending in the jet. In Eilek et al. (1984) the unusual morphology is discussed. They conclude that a purely hydrodynamical reason for the shape is unlikely and that an electromagnetic interaction between the jet and environment may be occurring, in particular an electrical current carried in the jet and its associated magnetic field may be interacting with the large scale magnetic field in the cluster. More recently using a simulated "magnetic tower" jet, which also features a nested helical magnetic field and associated electrical current, Gan et al. (2017) replicated the morphology of 3C 465 by simulating such a jet affected by violent intra-cluster weather. While the magnetic tower model is somewhat different from the "Cosmic battery" we are considering here, it does present evidence for a magnetically dominated jet with a helical or toroidal field in this case.

Observations of 3C 465 in the 4.5–5 and 8–9 GHz ranges were downloaded from the VLA archive. These data were originally published by Eilek & Owen (2002), whose rotation measure map shows a possible transverse RM gradient across the Southern jet (see Figure 6. in Eilek & Owen 2002). The data were observed in 1989, with the 4.5–5 GHz data observed on October 1st and the 8–9 GHz data taken on September 20th, both in a mixed BC VLA configuration. The data were calibrated using standard procedures in AIPS with 3C 286 used as the flux density and polarization angle calibrator and J2340+266 (B2 2337+26) as the phase calibrator. With its good parallactic angle coverage J2340+266 served as the polarization leakage calibrator. The *uv* data were tapered in the imaging process to have a common convolving circular beam of 7" in the resulting Stokes Q and U images used to create the rotation measure map, which was made by fitting χ versus λ^2 using a weighted least-squares fitting algorithm in PYTHON. An integrated rotation measure for this source, calculated in Taylor et al. (2009) to be -47.5 rad m^{-2}, was subtracted from the image shown in Figure 3.5. A map of the intrinsic polarization angle χ_0 is calculated using the RM map is shown in Figure 3.6.

Looking at the RM map of 3C 465 there is a preference for negative or less positive RM values on the left hand side of the uppermost and lower part of the eastern jet. The significance plot in Figure 3.7, shows that there are many regions along this jet where the transverse RM gradients have significances of over 3σ, particularly across the upper knot in the eastern jet and in the middle of the lower plume of the jet. The change in sign of the RM from one side of the jet to the other at these locations can only be explained by systematic variations in the line of sight magnetic field. The direction of these gradients

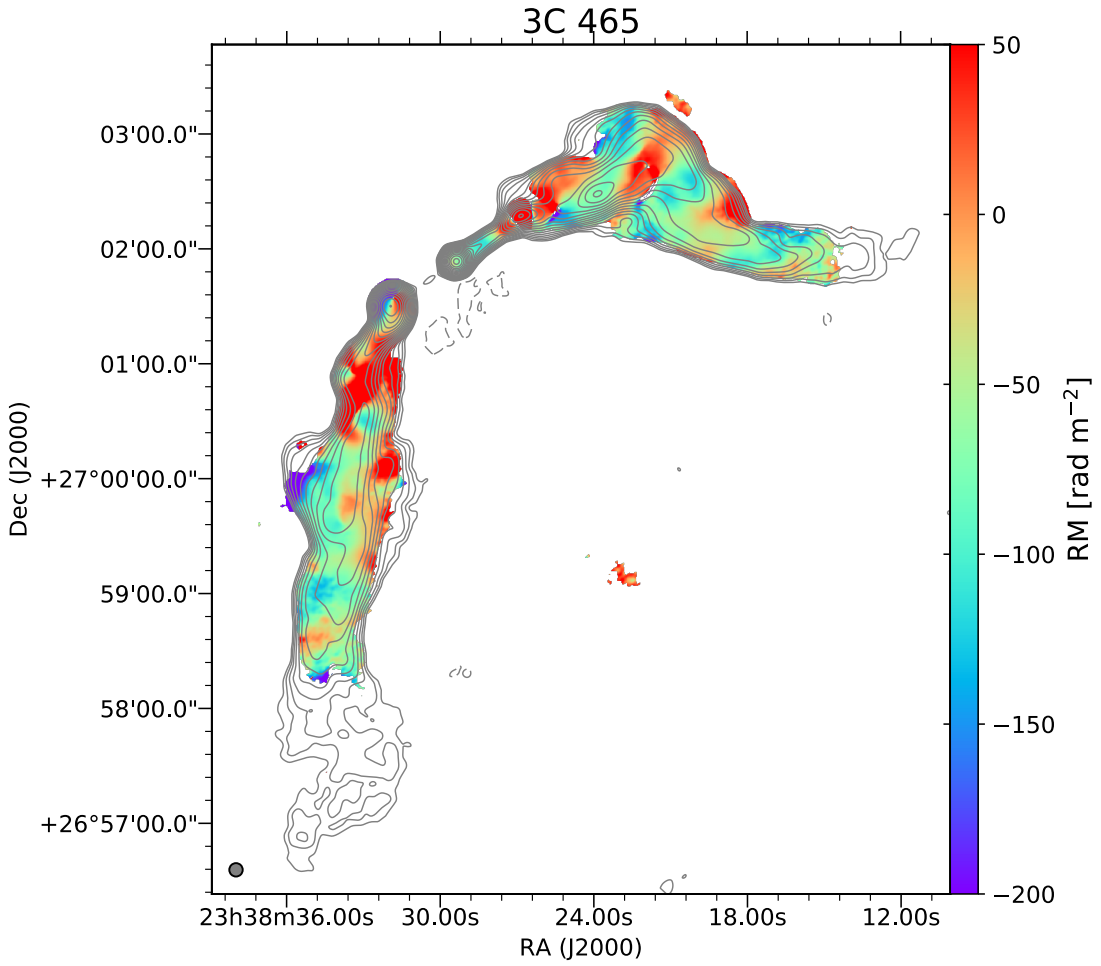

Figure 3.5: RM map of 3C 465 made using matched resolution archival VLA data at 4–5 and 8–9 GHz, the Stokes I contours given are from the 4.5 GHz data and are at 0.4, 0.5656, 0.8, 1.132, 1.6, 2.264, 3.2, 4.524, 6.4, 9.052, 12.8, 18.1, 25.6, 36.204, 51.2, 72.404, 102.4, 144.8, 204.8 mJy beam^{-1} with a dashed negative contour at -0.4 mJy beam^{-1}. The Faraday rotation measure is given in the colour scale and the common 7" convolving beam is given in the bottom left hand corner.

implies the existence of a toroidal magnetic field with an associated outward electrical current, as predicted by the cosmic battery. There is a region at $+27^\circ\,00'\,40''$ with transverse RM gradients that increase in the opposite direction, as indicated by negative significances in Figure 3.7, however this RM pattern is more likely due to the sudden bending in the jet in this region.

The strange "stripes" of RM in the North-Western jet are more puzzling. These stripes are almost perpendicular to the direction into which the jet is deflected, creating an undulating pattern of RM which changes from -125 – 50 rad m^{-2}. This is reminiscent of the patterns in the lobes of AGN jets presented in

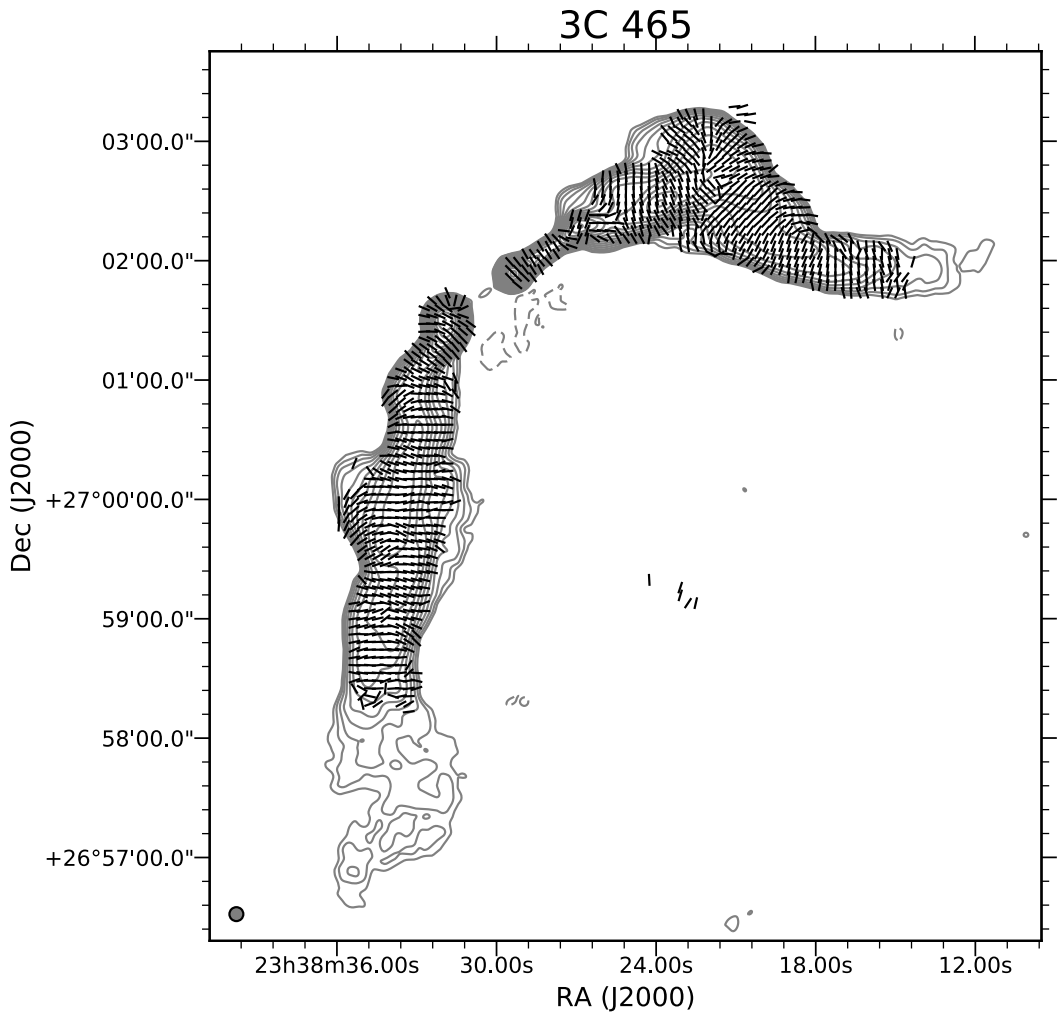

Figure 3.6: Map of the intrinsic polarization EVPA χ_0 calculated using the RM map in Figure 3.5, the total intensity contours and beamsize used are identical to the ones given in Figure 3.5.

Guidetti et al. (2011), however, as in the case of NGC 6251 discussed above, they are not perpendicular to the jet direction. As the stripes are somewhat perpendicular to the direction into which the jet is deflected, perhaps the observed RM in this portion of the jet is due to an interaction between the jet and an intra-cluster magnetic field or a change in jet morphology due to such an interaction. Such oblique stripes are not observed in the lower region of the Southern jet, where the gradients are reported. Only the high RM region at a declination of $+27^\circ\,00'\,40''$ where the jet is deflected shows an unusual RM pattern. This however may be due more to a sudden change in jet direction than draping effects.

Overall the intrinsic polarization angles are very smooth across the jets, with

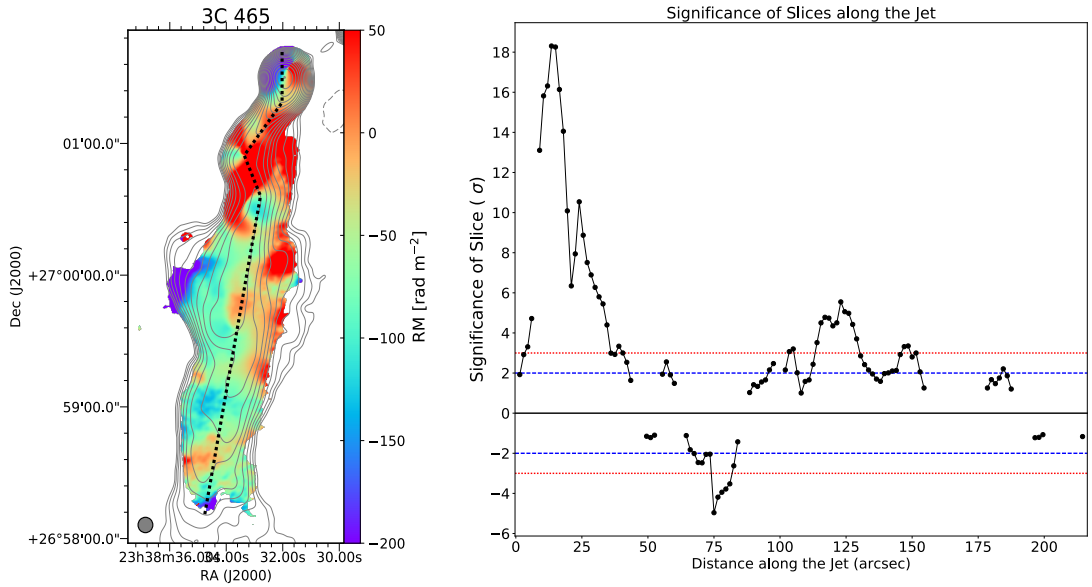

Figure 3.7: **Left Panel:** Rotation measure map of the Eastern jet of 3C 465 with identical contours and resolutions as in Figure 3.5. The dashed line indicates the assumed path taken by the jet with RM gradient significances calculated perpendicular to this line. **Right Panel:** Plot of the significances of RM gradients along the jet for the path traversed by the dashed black line. Horizontal lines representing the ± 2 and ± 3 σ levels are given in blue and red, respectively. A negative significance implies an increasing direction of the RM gradient opposite to the positive one.

the angles generally aligned perpendicular to the jet direction, meaning the magnetic field in the jet in the plane of the sky is aligned with the jet direction. This smooth structure, indicates that there is no overall violent processes affecting the jet shape, especially in the regions with significant transverse RM gradients. This suggests that most of the RM pattern in the Eastern jet is due to a toroidal magnetic field in the outer layer of the jet.

Further study of this source was clearly warranted. A wide band 1–2 GHz observation in VLA B configuration was downloaded from the VLA archive and calibrated using standard techniques in CASA. The frequencies and VLA configuration used ensured a similar resolution as the previous results. For these observations 3C 138 served as the primary flux calibrator and polarization angle calibrator, the nearby unresolved source J2254+2445 was used as the phase calibrator and polarization leakage calibrator, and the bandpass was calculated using the bright source 3C 48. The capabilities of the upgraded VLA allowed for extremely high dynamic range imaging and detailed images of the twin jets could be made, using a multi-term multi-frequency

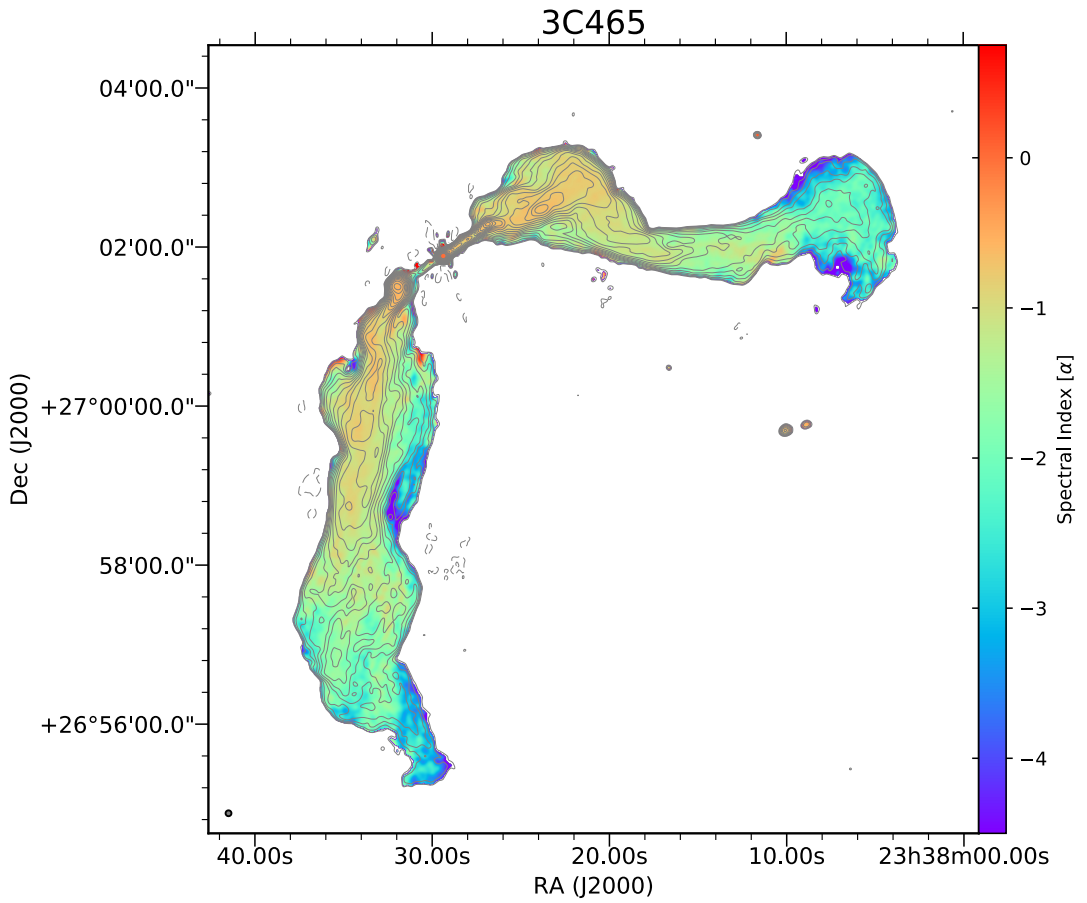

Figure 3.8: Image made using the multi-term multi-frequency synthesis imaging technique from 1–2 GHz, a restoring beam of 4.42 × 4.41” at a position angle of -76°. The spectral index map used in the imaging process is given in the colour scale.

synthesis imaging technique using a 3rd order Taylor polynomial (`nterms=3`), to take into account the spectral change of the intensity across the 1–2 GHz band. This method was also applied to provide an accurate model for self-calibration of the data across the entire spectral range using two iterations of phase-only self calibration and one iteration of amplitude and phase self-calibration.

The Stokes I contours and spectral index map presented in Figure 3.8 show the source structure in great detail, better than any maps available in the existing literature.

The self calibrated data were then imaged in Stokes Q and U in separate channels 1 MHz in width for the central 54 channels of each 64 MHz spectral window. The uv data were tapered and the final images smoothed also to

ensure all the images had an identical 7" resolution and convolving beam, corresponding to the approximate resolution of the images closer to 1 GHz. The images were then cropped and re-gridded to have a cell-size of 1", to speed up the RM synthesis process later. The Stokes Q and U images were then exported as *FITS* files and passed to the *pyrmsynth* code where RM synthesis followed by an RMCLEAN (Heald et al. 2009) of the data were applied, in an effort to better resolve the peak Faraday depth.

The RM map of the peak Faraday depth $\phi_{\rm peak}$ is rather patchy. The $\phi_{\rm peak}$ maps for the lower jet and upper jet were synthesized separately for computing efficiency and are reproduced in Figure 3.9. Some of the features, such as the stripes in the rotation measure can be made out in the upper jet although they do not transition as smoothly as in the previous analysis. The region at a declination of $+27°00'00''$, where gradients were previously found, does show a prevalence for positive RM on the right hand side of the jet, while lower and negative values are seen on the left, indicating some change in the line-of-sight magnetic field across the jet here, however not recorded as smoothly. This patchiness may be as a result of the similarly patchy distribution of polarized flux at these lower frequencies, scattered among regions of little to no significant measured polarization.

To summarize this source, there is strong indication of the existence of a helical magnetic field with an associated outward electrical current as seen in the 4–9 GHz data analysed, with large swathes of the lower jet featuring significant transverse RM gradients. A follow up analysis using wide band observations at 1–2 GHz at a similar resolution does not show the characteristic RM features visible in the 4–9 GHz RM map as clearly, but does provide some broad confirmation of these features.

3.1.3 A2142a

Results for this source have been published by Christodoulou et al. (2016), on which the author of this thesis is a co-author. A brief study into the Faraday rotation measure structure was done on the radio galaxy and cluster member A2142a at redshift $z = 0.091$ (Struble & Rood 1999). The rotation measure map for this source was first published in Govoni et al. (2010), where a rotation measure gradient can be made out across the jet. Govoni et al. (2010) kindly provided the calibrated visibility data for this source for further

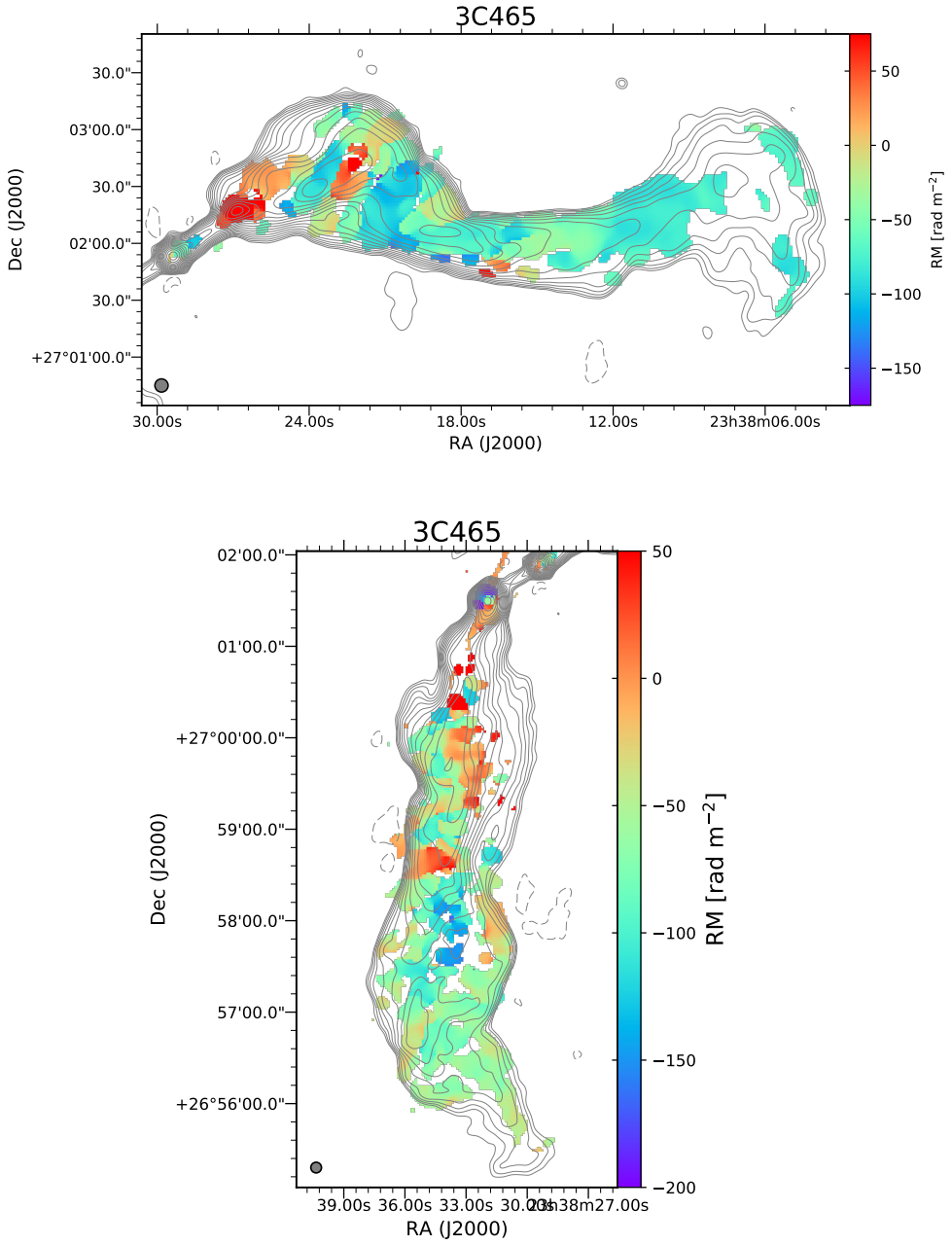

Figure 3.9: $\phi_{\rm peak}$ maps of the upper (top panel) and lower (bottom panel) jets in 3C465 made using RM synthesis given in the color scale. The given Stokes I contours are for 1.5 GHz and start at 0.5 mJy beam^{-1} and increase in factors of $\sqrt{2}$ to a highest level of 256 mJy beam^{-1}, a dashed negative contour at -0.5 mJy beam^{-1}. The common convolving circular beam of 7" for all the images from the RM synthesis process and the contour map is given in the bottom left.

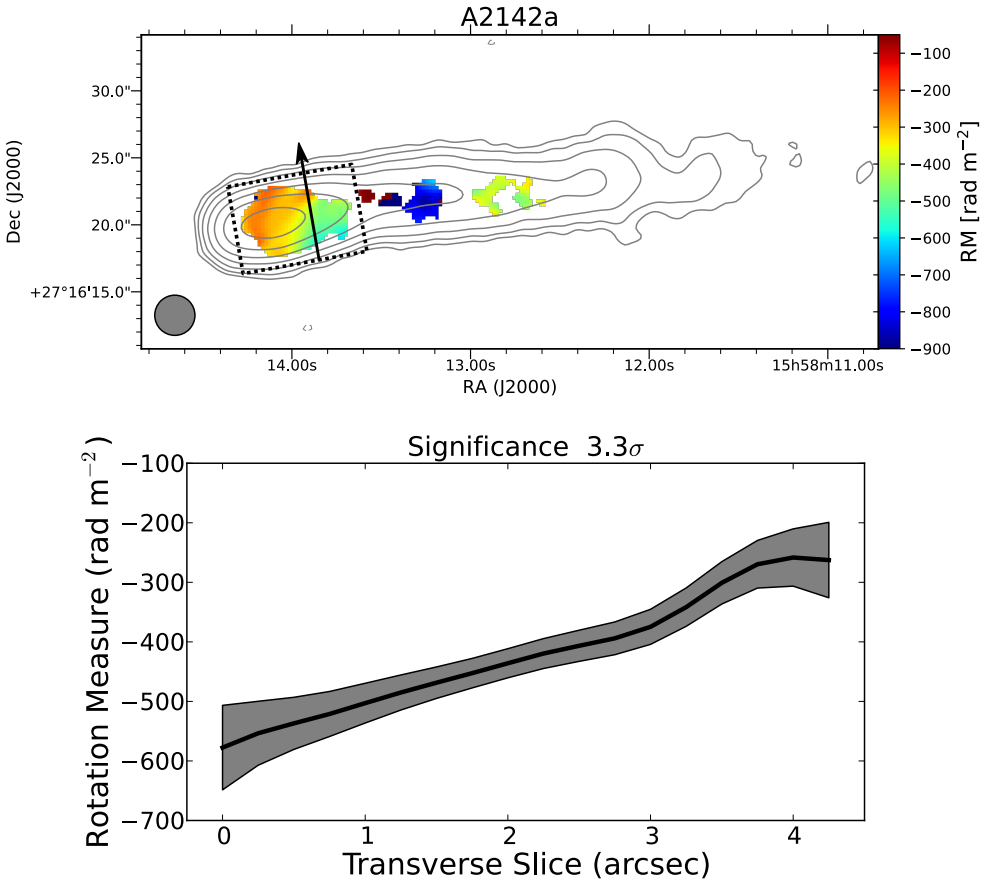

Figure 3.10: **Top panel:** Rotation measure map of A2142A given in the colour scale, Stokes I contours at 4.535 GHz are overlaid with levels starting at 0.1 mJy beam^{-1} increasing in factors of 2 with the highest contour at 51.2 mJy beam-1 a dashed negative contour at -0.1 mJy beam^{-1} is given too. A common convolving circular beam of 3" is used and is shown in the bottom left corner. The black dashed rectangle indicates where transverse slices were taken and tested for their significance. **Bottom panel:** A sample slice of the significant transverse RM gradient taken along the path followed by the black arrow.

investigation into the rotation measure gradient and whether it is statistically significant. The data were observed using the VLA at 4.535 and 4.885 GHz in B configuration on 23 December 2003, and at 8.085 and 8.465 GHz on 13 April 2004 in C configuration, ensuring the observations had a matched resolution and *uv* coverage. Images of the Stokes I, Q and U were made using a standard CLEAN in AIPS, with a common circular convolving circular beam of 3". The images were exported as *FITS* files, and a weighted least-squares fit of χ versus λ^2 was performed using the Q and U images. The RM map was also used to make a map of the intrinsic polarization angle.

The rotation measure map was reproduced correctly and can be seen in

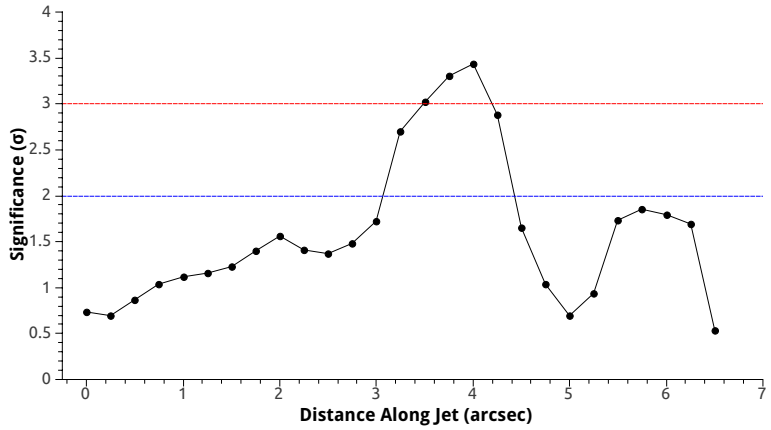

Figure 3.11: Plot of the significance (σ) of transverse RM gradients as a function of distance along the jet, inside the black dashed rectangle in Figure 3.10, with the x-axis starting where the first valid RM values are given in that figure. The blue and red dashed lines indicate the 2 and 3 sigma levels respectively.

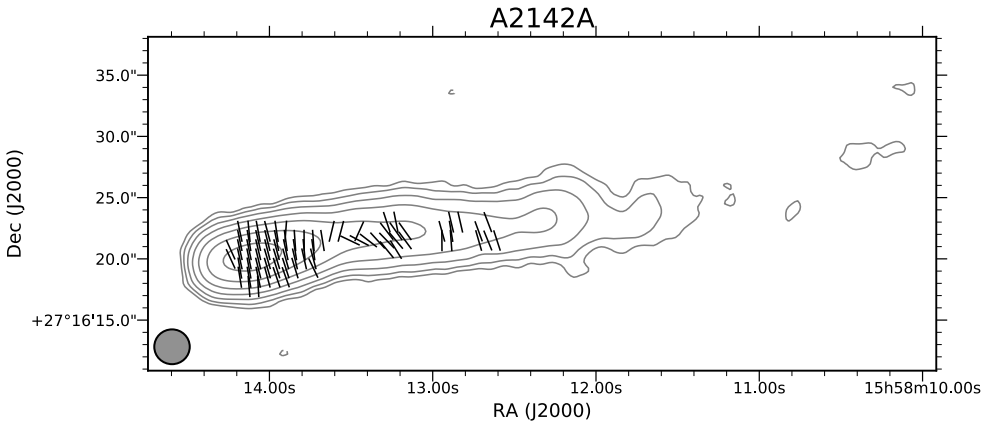

Figure 3.12: Map of the intrinsic EVPA plotted as vectors for regions where the RM was accurately calculated. The contours and convolving beam are identical to those presented in the RM map in Figure 3.10.

Figure 3.10, a significant transverse rotation measure gradient corresponding to the path taken by the black arrow is shown below the RM map. The black dashed rectangle around the portion of the rotation measure map with visible gradients corresponds to the region where the significance of the transverse gradients is plotted as a function of the distance along the jet in Figure 3.11. The χ_0 map reproduced in Figure 3.12 shows that in general the intrinsic electric field vectors are perpendicular to the jet, indicating that the intrinsic magnetic field vectors in the plane of the sky follow the jet direction.

As can be seen by the plot of the RM significance in Figure 3.11, the occurrence of a $> 3\sigma$ gradient is not a one off occurrence, with a region of significance spanning several cells and a further large portion of the jet displaying RM-gradient significances above 2σ, as well as a region further out in the jet almost approaching 2σ. The direction of these RM gradients imply a toroidal field with an associated outward electrical current. As this source is at redshift $z = 0.091$, the gradients are at a distance of > 10 kpc from the base of the jet.

3.1.4 5C 4.114

The results presented here were published by Gabuzda, Knuettel & Bonafede (2015), on which the author of this thesis was a co–author.

This twin jet FR I radio galaxy is located in or behind the Coma cluster of galaxies. No optical identifier has been located in the Coma cluster for this galaxy making it most likely a background source further away with a redshift $z > 0.023$ (Struble & Rood 1999), the redshift of the Coma cluster. The source has an end-to-end angular size of $\sim 15''$. The data published here have been previously calibrated and published in Bonafede et al. (2010), which featured a multi-wavelength observation of 5C 4.114 at 1.365, 1.516, 4.535 and 4.935 GHz using the VLA. The 1.365, 1.516 GHz data were observed in December 2008 in the VLA A configuration and the 4.535 and 4.935 GHz data were observed in April 2009 in the VLA B configuration, ensuring relatively well matched uv coverage for the data. The purpose of the original observation was to use integrated rotation measures of individual sources in or behind the Coma cluster to probe the rotation measure and magnetic field structure of the Coma cluster as a whole. On closer analysis of the rotation measures of 5C 4.114, clear gradients can be made out by eye in both the Northern and Southern jets.

Images of the Stokes I, Q and U were made with a common convolving beam of 1.3". An RM map was made using these images and a χ versus λ^2 fitting procedure in PYTHON. The map is reproduced here in Figure 3.13. This map clearly shoes the gradients in each jet. The Northern jet in particular shows a striking transverse RM gradient. A map of the intrinsic polarization angle χ_0 is shown in Figure 3.14. This shows how the intrinsic angles are aligned with the jet directions near the jet base and the Southern jet as a whole, while being perpendicular to the jet direction at the Northern hotspot where the highly

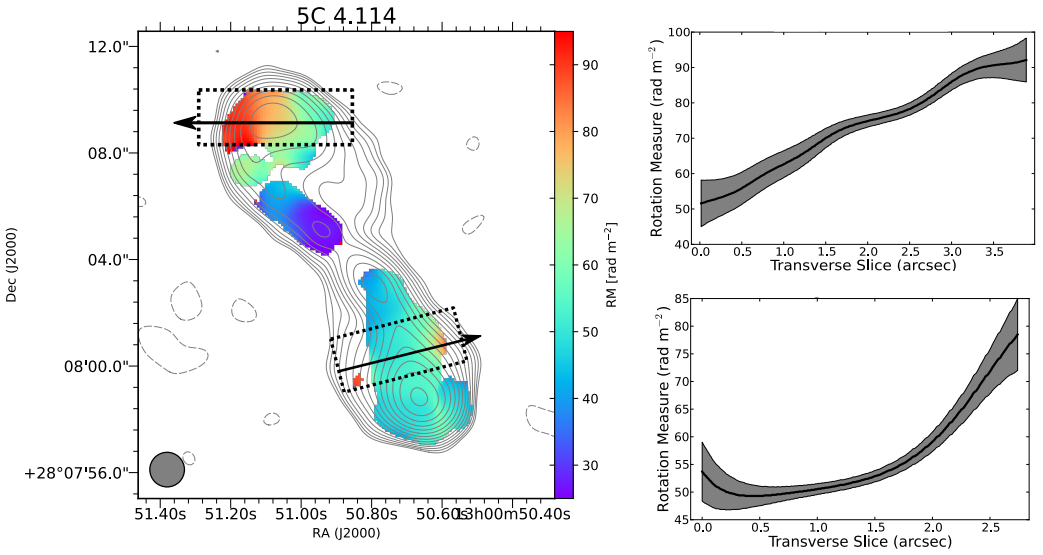

Figure 3.13: **Left panel:** RM map of 5C 4.114 showing gradients in both the Northern lobe and Southern jet, the RM is given in the colour scale with Stokes I contours at 1.365 GHz with levels at -0.1, 0.1, 0.141, 0.2, 0.283, 0.4, 0.566, 0.8, 1.131, 1.6, 2.263, 3.2, 4.525, 6.4, 9.051 mJy beam^{-1}, with the negative contour dashed. The arrows indicate the path taken by the slices plotted on the right. The common 1.3" convolving beam is given in the bottom left hand corner of the figure. The dashed boxes indicate region in the jet along which the significance of transverse gradients. was plotted for each transverse section of cells. **Right panels:** The slices of RM values corresponding to the arrows on the RM map are given. The RM values are plotted against distance in black with the grey region specifying the 1σ errors in the RM.

significant gradients are reported.

Figure 3.15 shows plots of the significance of transverse RM gradients as a function of distance along the jet for the regions enclosed by the dashed boxes in Figure 3.13 in the Northern and Southern jets. These plots show that the 3 sigma gradients in the jets shown in Figure 3.13 are not isolated incidents and there are multiple occurrences in sections along the jet. In the left panel of Figure 3.15, the Northern jet section shows gradients over 3σ, with a maximum of 4.2σ, for a portion over an arcsecond in length along the jet, and the significances never decrease to below $2\,\sigma$. In the Southern jet section, a small portion of the region does feature $> 3\sigma$ gradients with a maximum of 3.6σ and a large portion of $> 2\sigma$ gradients.

The significant transverse gradients observed across both of the jets in 5C 4.114 show evidence for toroidal or helical magnetic fields with associated outward electrical currents.

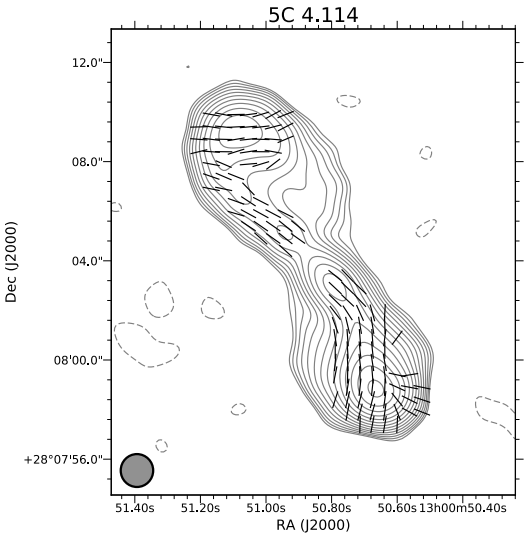

Figure 3.14: Map of the intrinsic polarization angle EVPA χ_0 plotted as vectors over the 1.4 GHz contours, which are at the same levels as in Figure 3.13. The χ_0 values were calculated using the RM map shown.

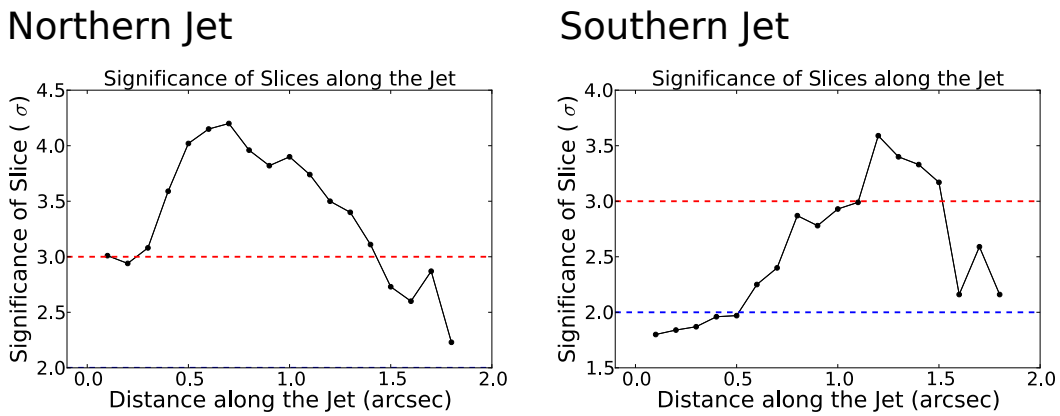

Figure 3.15: Plots of transverse gradient significance versus distance along the jet for the regions in the dashed boxes in Figure 3.13 in the Northern and Southern jets of 5C 4.114. The 2 and 3σ significance levels of the gradients have been plotted as blue and red dashed horizontal lines respectively in the plots.

Note that the RM gradients reported for this source do not encompass a change in the sign of the RM. The presence of the Coma cluster and its intra-cluster medium along the line of sight may be interacting with the observed RM on larger scales, which was the focus of the initial analysis of the data in Bonafede et al. (2010), where the mean RM for each source and fluctuations of the RM were used to infer the intra-cluster magnetic field. The conclusions of that study however need not contradict the results from the analysis of the RM gradients in 5C 4.114 presented here. The observed RM could be a combination of the effect of an ordered external magnetic field

close to the jet and a disordered magnetic field in the intra-cluster medium of the Coma cluster. While quite often the latter dominates the RM structure observed in kiloparsec scale AGN jets, making it difficult to discern transverse gradients due to helical fields, in this case the former seems to dominate especially in the Northern lobe.

3.1.5 Coma A

The results presented here were published by Knuettel et al. (2017).

Coma A, also known as 3C 277.3, is a hybrid FR I/II radio galaxy at $z = 0.0857$ (Bridle et al. 1981), with a twin lobe structure. This classification is used due to the unusual deflected jet in the Southern lobe giving it the appearance of an FR I, while the Northern lobe and hotspot are typical for an FR II. The morphology and kinematics are discussed in detail in van Breugel et al. (1985) and again in a detailed study of the Faraday screen surrounding this source in Chapter 4 of this thesis. The polarization structure is also quite interesting, as the lobes appear to be surrounded by a Faraday screen, seen in H α, causing significant depolarization in parts of the Southern lobe. Upstream from this depolarizing region the fractional polarization is quite high at the edges of the jet ($\sim$30% at 15 GHz), a feature which can be indicative of a toroidal magnetic field component. For the analysis of the rotation measure, older archival VLA and modern wide-band 1–2 GHz VLA observations were calibrated and analysed. The details of the observations used are outlined in Table 4.2. The older archival observations used were made at 1.4, 4.9 and 15 GHz in the A, B and C VLA configurations, respectively, which ensured matched resolutions of 1.5–2". The initial calibration of the data was performed in AIPS using standard procedures with 3C 286 serving as the flux and polarization angle calibrator and the unresolved source 3C 287 used as the phase and polarization leakage calibrator. The calibrated *uv* data were exported to CASA for imaging with a multiscale CLEAN to better image the large scale lobes of Coma A. Images of Stokes I, Q and U were made and convolved with a common 2" circular beam. The Stokes Q and U images were used to make a rotation measure map by fitting χ versus λ^2 using a weighted least squares fitting algorithm in PYTHON. In conjunction with this method, a map of the intrinsic polarization angle χ_0 was made to compare with previous measurements and to ensure calculate rotation measures resulted in consistent

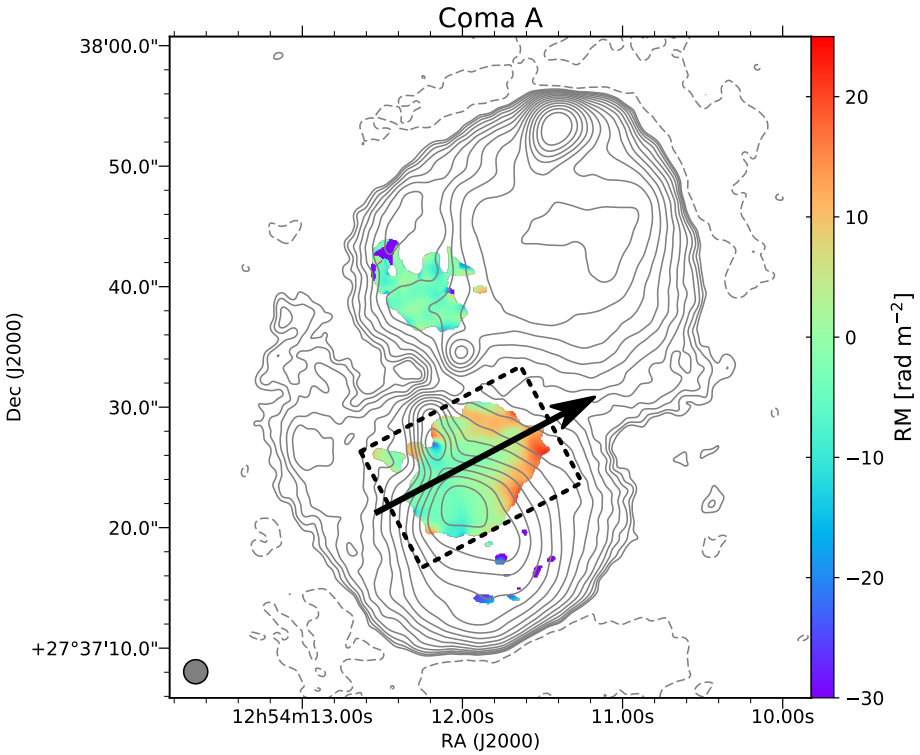

Figure 3.16: RM map of Coma A made using matched resolution archival VLA data at 1.4, 4.9 and 15 GHz. The Stokes I contours given are from the 1.4 GHz data and start at 0.5 mJy beam^{-1} and increase in factors of $\sqrt{2}$ up to a level of 90.5 mJy beam^{-1} with a dashed negative contour at -0.5 mJy beam^{-1}. The Faraday rotation measure is given in the colour scale. The common 2" convolving beam is given in the bottom left hand corner.

and reasonable χ_0 values.

Looking at the RM map in Figure 3.16, made using matched resolution observations at 1.4, 4.9 and 15 GHz, an RM gradient can be seen across the upper part of the Southern jet. A slice of RM values corresponding to the black line in Figure 3.16 is given in Figure 3.17. the transverse gradient is close to monotonic, especially considering the long distance covered by the gradient and the likelihood of some any turbulences associated with any random magnetic field components introduced by the jet and/or the Faraday screen surrounding the lobes, as is discussed in detail in Chapter 4. The significance of the transverse gradients was plotted as a function of distance along the jet, for the region enclosed in the dashed black rectangle shown in Figure 3.18. The upstream region has no significances plotted, as the RM in this region is patchy and no clear gradient structure is visible. The region around the path traced by the arrow shows an extended region of highly significant transverse RM gradients with significances of $> 3\sigma$ spanning a region just under 5" in

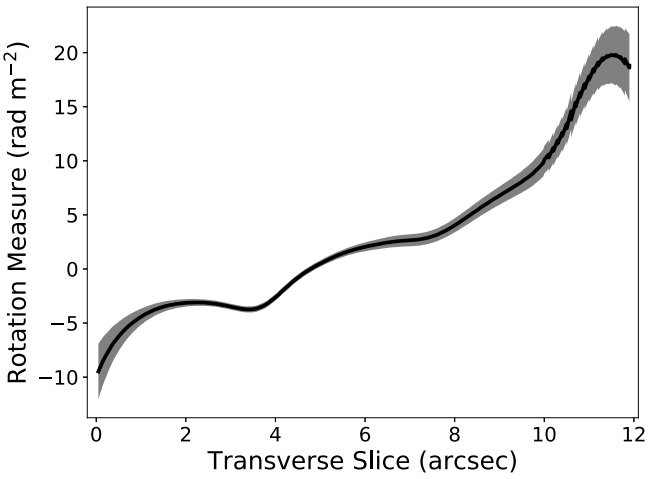

Figure 3.17: A slice of RM values and associated 1σ errors in grey taken along the same path traced by the arrow in Figure 3.16

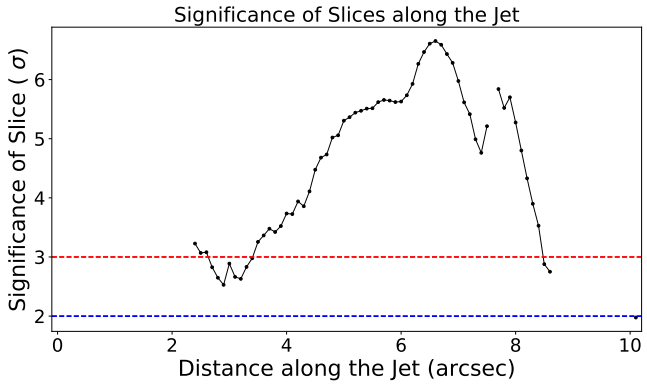

Figure 3.18: Plots of transverse gradient significance versus distance along the jet for the regions in the dashed box in Figure 3.16. The 2 and 3σ significance levels of the gradients have been plotted as blue and red dashed horizontal lines respectively in the plots.

length along the jet.

The calculated χ_0 values, shown in Figure 3.19, are smooth and are consistent with those produced by model fitting at a slightly lower resolution for 2–4 GHz data in Chapter 4, Figure 4.5. This is reassuring, given that only three frequencies were used to produce the RM map, which could potentially be subject to $n\pi$ ambiguities in the fitting.

The wide band observations from 1–2 GHz give continuous wavelength coverage and 30% more coverage of λ^2 compared to the older archival data, allowing for a more accurate determination of the RM. The data will be shown again in detail in Chapter 4 and were calibrated using standard procedures in CASA with 3C 286 used as the flux, phase, bandpass and leakage calibrator due

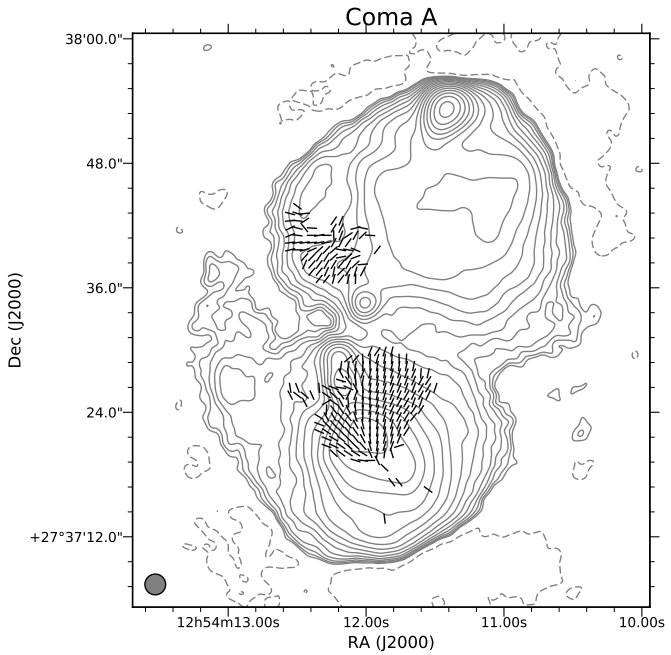

Figure 3.19: Map of the intrinsic electric field vectors corrected for Faraday rotation using the RM map in Figure 3.16. The overlaid Stokes I contours at 1.4 GHz are identical to those in Figure 3.16.

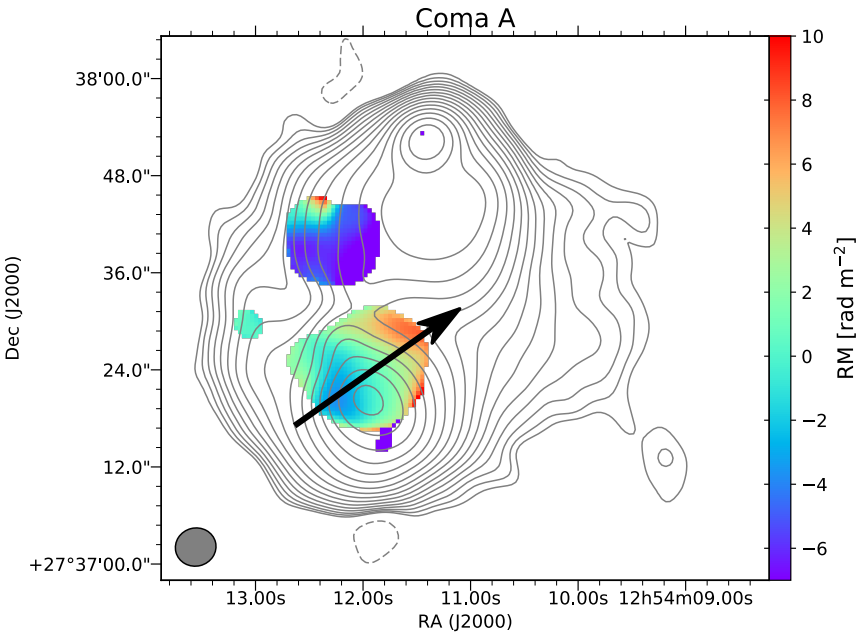

Figure 3.20: RM map of Coma A made with Stokes I contours at 1.5 GHz at contours 1, 1.414, 2, 2.83, 4, 5.66, 8, 11.31, 16, 22.63, 32, 45.25, 64, 90.51, 128, 181.01 mJy beam^{-1} with a dashed negative contour at -1 mJy beam^{-1}. The Faraday rotation measure is given in the colour scale. The common convolving beam of 5" is displayed in the bottom left corner. The black arrow indicates the path traced by the slice of RM values in Figure 3.21 .

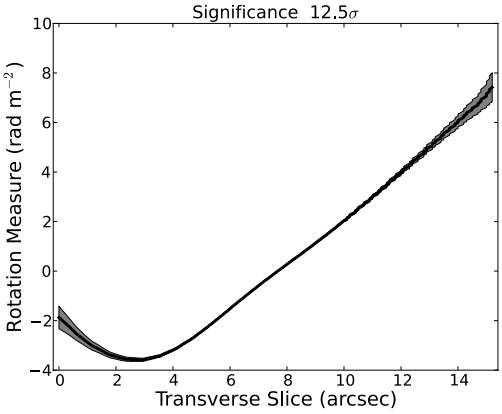

Figure 3.21: A slice of RM values and associated 1σ errors in grey taken along the same path traced by the arrow in Figure 3.20 .

to its proximity to Coma A. The RM map is displayed in Figure 3.20 and was made by fitting 16 evenly spaced frequencies between 1 and 2 GHz with the *uv* data tapered and images smoothed to ensure a common resolution and convolving beam of 5". The RM map was calculated using the *rmfit* task in CASA. Not only is the gradient seen in both the broadband and the archival data RM maps, made by fitting χ vs λ^2, it is also visible in the RM maps made using the QU model fitting procedure in Chapter 4. In each case ,the RM gradient is statistically significant and also changes sign from positive to negative, indicating a change in direction of the line of sight magnetic field. This sign change could not be explained by a change in the electron density alone. Coma A is not part of a cluster environment nor does our Galaxy affect it much due to Coma A's location very close to the Galactic pole (Galactic latitude $\approx 89.21°$); thus the value for Galactic RM is calculated to be quite low at $4.3 \pm 2.3\,\mathrm{rad}\,m^{-2}$ (Taylor et al. 2009).

This clear evidence for a toroidal magnetic field in the Southern jet of Coma A implies an associated outward electrical current . This gradient could potentially arise from the Faraday screen surrounding Coma A, however the effects from this screen appear to be quite minimal in the region being considered here, and only start to strongly depolarize and interact with the lobe further downstream from the RM gradient region, as will be discussed in Chapter 4.

3.1.6 IC 4296

IC 4296 (PKS 1333-33) is a bright FR I radio galaxy at redshift $z = 0.01247$ (Smith et al. 2000). The radio morphology is discussed in detail in Killeen et al. (1986), who present a rotation measure map made using data at 20 and 6 cm; while made using only two frequencies, the contour RM map presented does show signs of gradients in the RM, manifest as contour lines parallel to the jet direction. To verify this a more recent wide-band 1–2 GHz observation, made using the VLA, was downloaded from the archive and calibrated using standard procedures in CASA. The wide range of λ^2 values and high resolution made this dataset very suitable for RM mapping. These observations were first published in Grossová et al. (2019), however without any analysis of the polarization, and on inspection of the data from the VLA archive, the observation was not set up for accurate polarization leakage calibration, which is needed to correctly determine the polarization of the observed radio emission. Fortunately, on the same day as the observation of IC 4296, a scan of 3C 147 was taken for a different experiment with the same receiver setup; since this source is effectively depolarized at L-band, the polarization leakage terms could be calculated for all but one of the antennas. This method of transferring the polarization leakage terms is possible, as these have been observed to be quite stable over time (Perley & Sault 2014), with the changes in antenna polarization being negligible over time scales of a few days. The data for IC 4296 were calibrated using 3C 286 as the flux, bandpass and polarization angle calibrator and J1316-3338 (PKS 1313-333) as the phase calibrator, with the scan of 3C 147 appended to the data and used for the polarization leakage calibration. The data were split and self calibrated, and an RM map was made by imaging each of the 64 MHz spectral windows in Stokes Q and U, some of which were lost due to RFI. Using images at 7 frequencies between 1 and 2 GHz, a very accurate RM map could be constructed, presented in Figure 3.22. This map shows RM values consistent with those published in Killeen et al. (1986). The corrected intrinsic polarization angle, χ_0, map matches too, with electric vectors aligned parallel to the jet, as can be seen in Figure 3.23. Looking at the RM maps in detail, RM gradient like structures exist in both of the kiloparsec scale jets and these gradients have significances over 3 sigma in some places. RM gradient significance plots were also created in the same way as for the previous sources using automated python routines. The boxes on the map indicate

where this analysis was done with the increasing x-axis direction on the plot being the outward jet direction. There is a surprising region featuring negative significances close to the end of the plot in in Figure 3.22 for the left jet (a), indicating that the gradients are significant and monotonic in the opposite direction; looking at the Stokes I contours and rotation measure structure for this region, it can be seen that the total intensity decreases and increases in this region along the jet, which is shown in a zoomed in image of the region in Figure 3.24. This suggests the rotation measure pattern here is due to the jet morphology and the environment with which it is interacting with.

3.1.6.1 RM synthesis of IC 4296

The finely imaged data were also investigated using Faraday rotation measure synthesis (Brentjens & de Bruyn 2005) using the *pyrmsyth* code in PYTHON; this gives an insight into the behaviour of the Faraday rotation measure along the line of sight, and whether the behaviour of the Faraday depth is more complex than just being a single RM component (Faraday thin). Figure 3.26 presents a rotation measure map made using the peak Faraday depth ($\phi_{\rm peak}$) in the Faraday spectra for each cell in the image and then blanking according to the produced polarized flux image, with only values having $>0.75\,\mathrm{mJy\,beam^{-1}}$ being shown. The overall structure of the RM is preserved, with the aforementioned transverse RM gradients still intact and visible by eye. Looking at the individual spectra of the Faraday depth, for example in Figure 3.25, one component in RM space clearly dominates, with some extension to the left or right indicating perhaps some finer structure, which however remains unclear given the comparatively sparse and incomplete sampling of λ^2, leading to sidelobes in the rotation measure transfer function (RMTF) and resulting Faraday spectra. The resolution is also limited by the total bandwidth of the observation of 1–2 GHz; this, combined with the channels lost to RFI corresponds to a maximum resolution of $\delta\phi \approx 63\,\mathrm{rad\,m^{-2}}$ according to Equation 2.57b. The RMTF is plotted in the left panel of Figure 3.25 showing the sidelobes in the response of the RM-synthesis method to a point source given the λ^2 coverage available. An RMCLEAN (Heald et al. 2009) was also performed on the data to remove the effect of these sidelobes, with some success, as can be seen in the right panel of Figure 3.25.

Similar to the sample spectrum given in the right panel of Figure 3.25, the spectra are all dominated by a single RM component indicated by the $\phi_{\rm peak}$ in

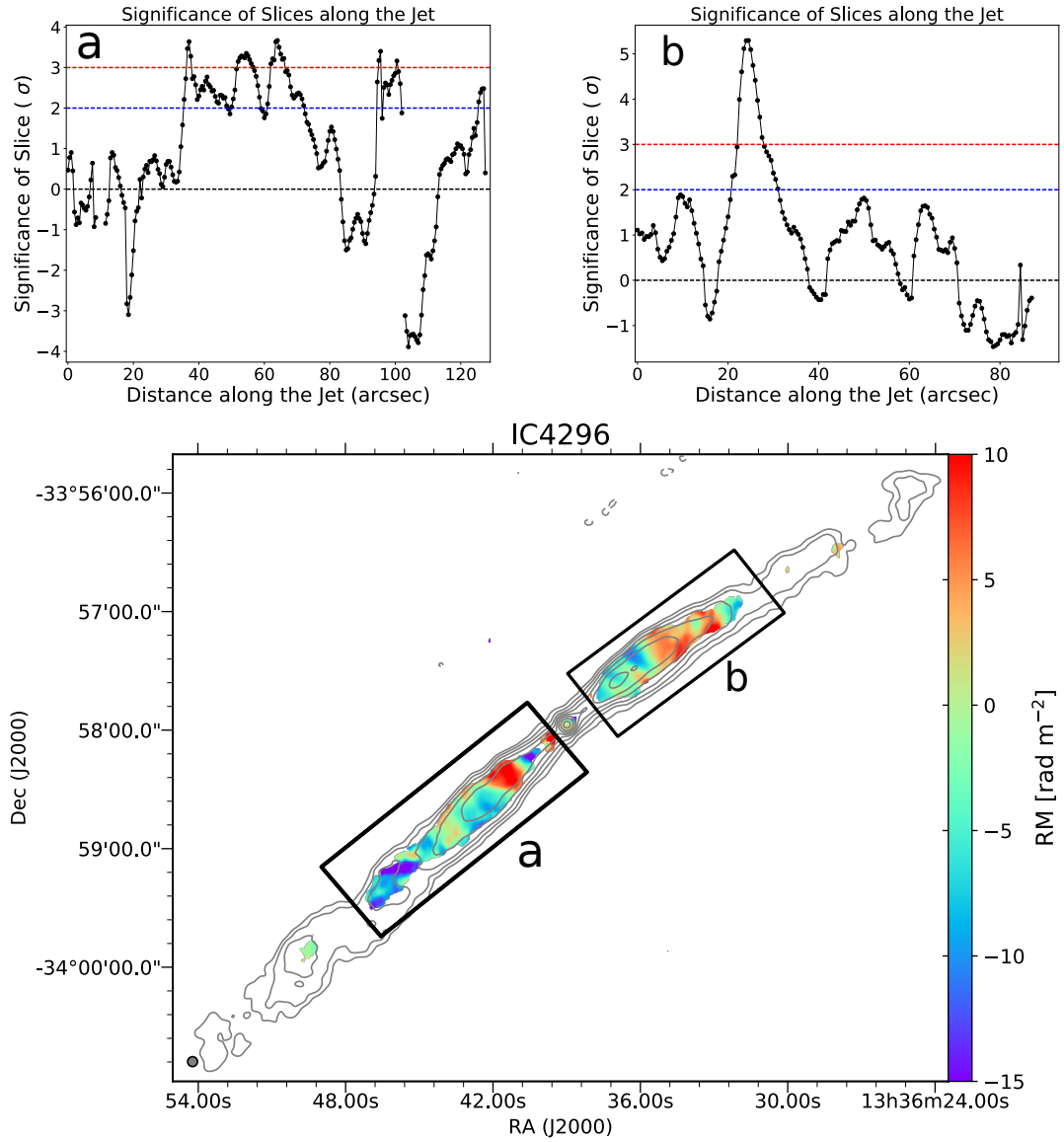

Figure 3.22: RM map of IC 4296 made using 7 frequencies between 1 and 2 GHz, the rotation measure is given in the colour scale and the Stokes I contours at 1.488 GHz, a central frequency. The levels are at 1.1, 2.2, 4.4, 8.8, 17.6, 35.2, 70.4, 140.8, mJy beam^{-1}, a galactic contribution to the RM of -21.1rad m^{-2} has been subtracted. The common convolving circular beam of 5" is given in the bottom left hand corner. In the upper left corner of the figure is a plot of the significance of transverse gradients versus distance along the jet for the left hand side of the jet enclosed in the black rectangle. Similarly in the bottom right corner a plot of the significances versus distance along the jet for the region of the jet enclosed in the rectangle on the right hand side.

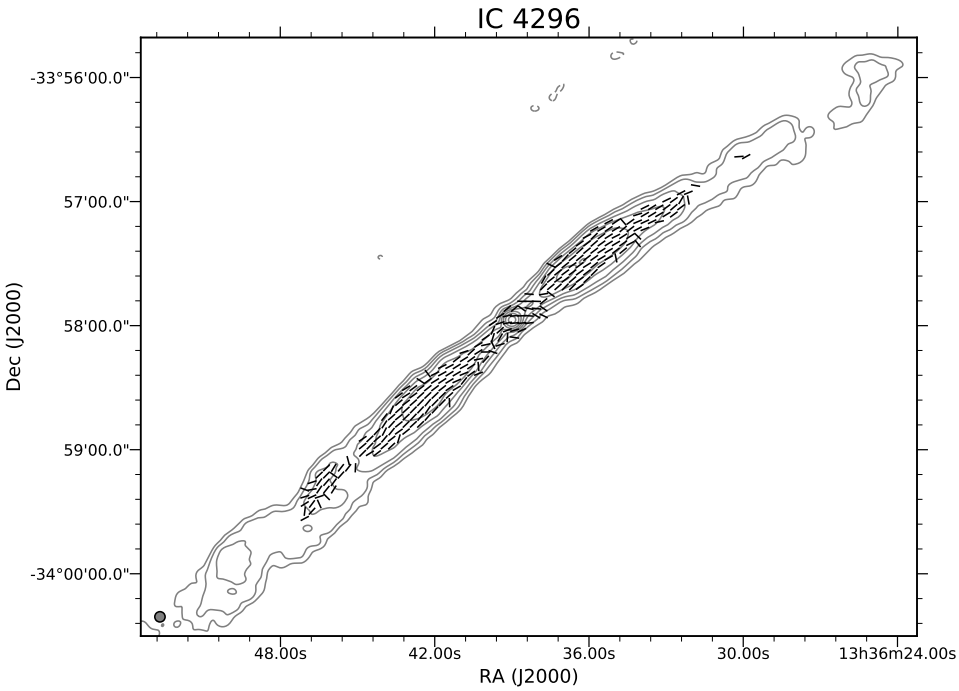

Figure 3.23: Map of the intrinsic polarization vectors corrected using the RM map made in Figure 3.22. The Stokes I contours shown are at the same frequency and have the same levels as Figure 3.22. The common 5" convolving beam is given in grey in the bottom left hand corner.

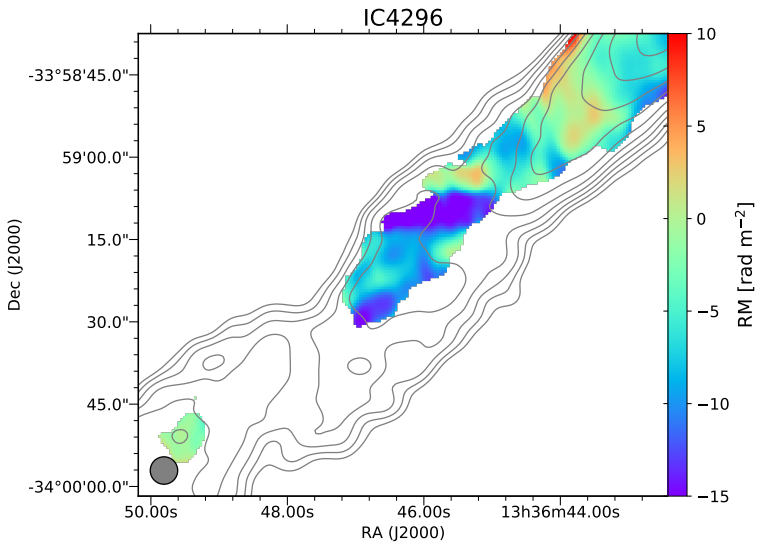

Figure 3.24: Zoomed in region of Southern jet intensity feature with contours at close levels starting at 1.1 mJy beam^{-1} and increasing in factors of $\sqrt{2}$. The denser contours increase the clarity of the total intensity features.

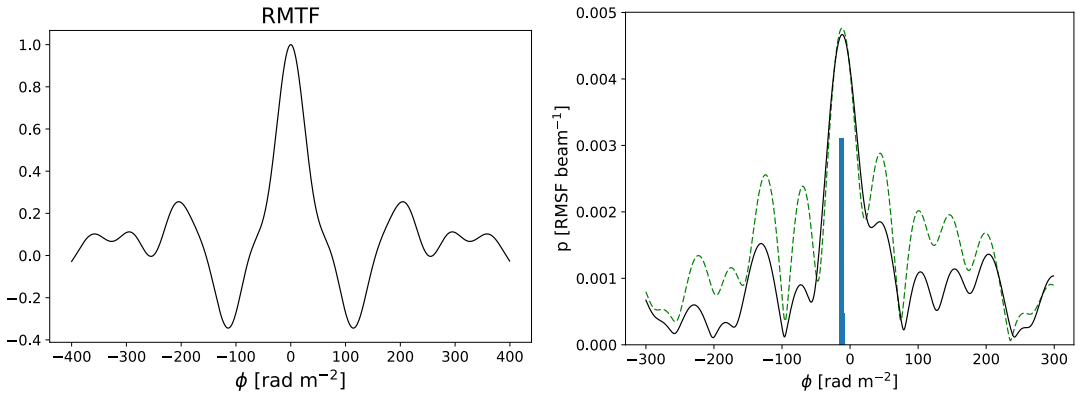

Figure 3.25: **Left panel:** The RMTF for the IC 4296 data in the 1–2 GHz range. The FWHM of the central peak is 53 rad m^{-2}, **Right panel:** Faraday depth spectrum for a region in the Southern jet in IC 4296, the basic 'dirty' synthesis is given in the dashed green line, the CLEANed spectrum is given in the black solid line while the RMCLEAN components are indicated by the blue vertical bars; the peak and corresponding clean components are located at $\phi_{\rm peak} = -10.5$ rad m^{-2}.

Figure 3.26. A slight extension to the positive side of the spectrum is indicated by the slightly asymmetrical shape of the final cleaned spectrum, however it cannot be clearly distinguished as another RM component or extended structure in $F(\phi)$ given the lower resolution of the RM synthesis and the remaining effect of the side lobes in the CLEANed Faraday depth spectrum.

The rotation measure map produced by this process bears a striking resemblance to the one produced previously using the χ versus λ^2 fits in Figure 3.22, with the gradient structures still clearly visible. With only one Faraday thin component most likely producing this RM it is safe to suppose this is due to some magnetic field in the immediate vicinity of the jet with some toroidal component.

Given its high rotation measures and a relatively low depolarization this source is an ideal candidate to be studied in detail in Faraday depth as was done for NGC 6251 by Cantwell (2018) using LOFAR. Given its low declination, the MWA or ASKAP may be good instruments for this. While such observations may not resolve individual features spatially, the large scale lobes seen in Killeen et al. (1986) would be more prominent, and the fine spectral imaging and wide range of data in λ^2 make RM synthesis and QU fitting a promising approach.

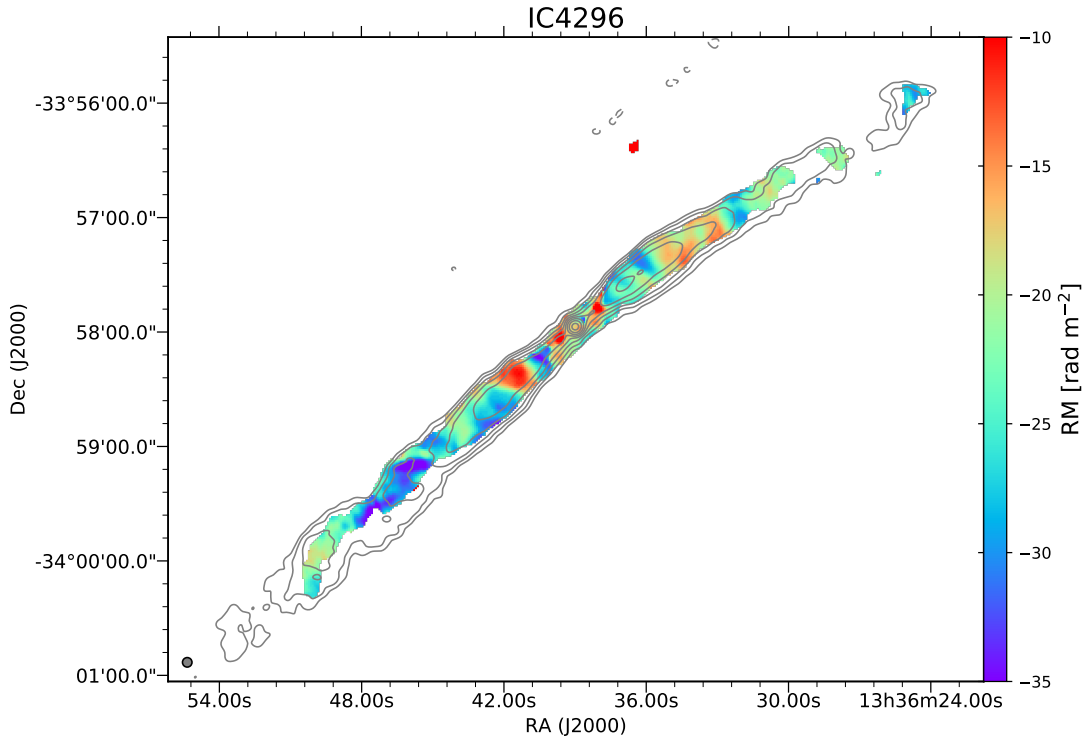

Figure 3.26: RM map of IC 4296 made using RM synthesis between 1 and 2 GHz using a spectral resolution of 8 MHz with all the remaining data uncorrupted by RFI, the rotation measure is given in the colour scale and the Stokes I contours at 1.488 GHz, a central frequency. The levels are at 1.1, 2.2, 4.4, 8.8, 17.6, 35.2, 70.4, 140.8, 281.6, 563.2 mJy beam^{-1}, unlike in Figure 3.22 the Galactic RM has **not** been subtracted.

3.2 Tentative and Negative Results

3.2.1 3C 303

Results for this source have been published by Knuettel & Gabuzda (2019).

3C 303 is classified as an FR II radio galaxy and is located at a redshift of $z = 0.141$(Eracleous & Halpern 2004). It features a prominent knotty jet travelling westwards with a prominent hotspot at the end. The Eastern jet is not as prominent and only displays more diffuse, unboosted lobe radiation; a feature which can be associated with a hotspot and lies on the radio jet axis can be made out at lower frequencies, as can be seen in the upper panel of Figure 3.27 in the 1.4 GHz contours. The environment surrounding 3C 303 is expected to be rarified, and the line of sight to this radio galaxy passes through little material from the Galactic plane since 3C 303 is located at a very high

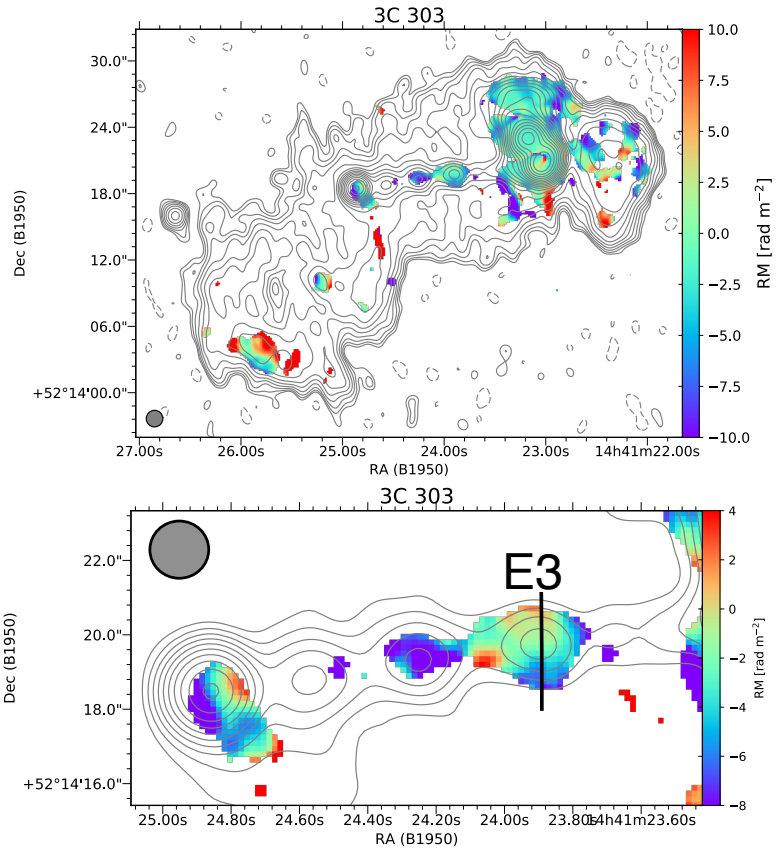

Figure 3.27: **Top panel:** Image of 3C 303 showing the RM in the colour scale and the Stokes I contours at 1.4 GHz with levels of ± 0.5 to 256 mJy / beam in steps of factors of $\sqrt{2}$ with the negative contour dashed. The convolving beam of 1.5" is displayed in the bottom left corner of the panel. **Bottom Panel:** A zoomed in image showing the core and knotty inner jet of 3C 303. The RM is given in the colour scale and the Stokes 1.4 GHz I contours run from 4 to 256 mJy beam^{-1} in steps of factors of $\sqrt{2}$. The location of the previously claimed gradient is marked by the black vertical line. The convolving beam of 1.5" is displayed in the top left corner of the panel.

Galactic latitude of $\sim 90°$. This makes it an ideal source for investigating magnetic field effects local to the jet itself.

A transverse RM gradient across the kiloparsec scale jet of 3C 303 was reported in Kronberg et al. (2011). They attempt to use this transverse RM gradient to calculate the associated electrical current from the inferred toroidal magnetic field to be of order $10^{18.5 \pm 0.5}$ A and travelling outward. Some uncertainty exists however, as no uncertainties in the RM were presented and the RM map was calculated using only two frequencies, 1.4 and 4.9 GHz. To confirm this result and get a better insight into the rotation measure and its associated errors, the original data for 1.4 and 4.9 GHz observed on the 20 April 1981 were downloaded from the VLA archive and calibrated using AIPS. 3C 286 served as

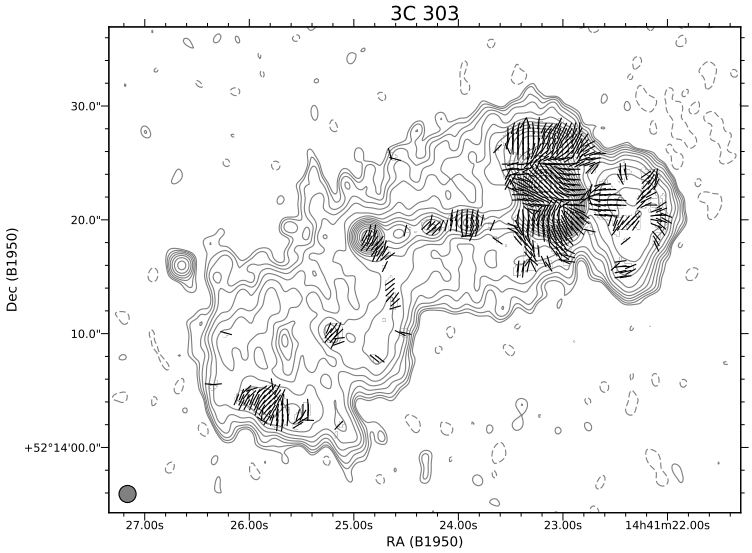

Figure 3.28: Map of the intrinsic polarization angle, χ_0 for 3C 303 plotted as vectors, made using using the RM map produced in the top panel of Figure 3.27, with the same convolving beam and overlaid Stokes I contours.

the flux density and polarization angle calibrator for the observation, while J1419+5423 (OQ 530) served as the phase calibrator and D-term calibrator.

To extend the range of wavelengths and provide adequate data for the χ versus λ^2 fits, an archival observation at 15 GHz observed on 8 December 1986, at a similar resolution, was also downloaded from the archive and calibrated. The calibrator sources were the same ones as those used in the lower frequency observations. As the rotation measure image produced in Kronberg et al. (2011) was made using only two frequencies (1.4 GHz and 4.9 GHz), adding the 15 GHz data gives a better insight into the errors in the χ vs λ^2 fits and therefore a better estimate of the error in the RM, while also providing a longer range of λ^2 values, which should provide a more accurate estimate of the RM. The RM image was also corrected for Galactic Faraday rotation by subtracting the integrated value of $18 \pm 2\,\mathrm{rad\,m^{-2}}$ (Simard-Normandin et al. 1981) from the calculated RM, as was done in Kronberg et al. (2011). The RM map is presented in Figure 3.27 together with a zoomed in region of the knot labelled 'E3' in Kronberg et al. (2011), where the purported transverse RM gradient was first reported. A gradient is visible by eye across this knot at the location of the black line through E3 in Figure 3.27. A map of the Faraday corrected intrinsic polarization angle χ_0 is presented in Figure 3.28. This shows smooth angles aligned perpendicular to the jet, which reassures us that the calculated RM values yield plausible results.

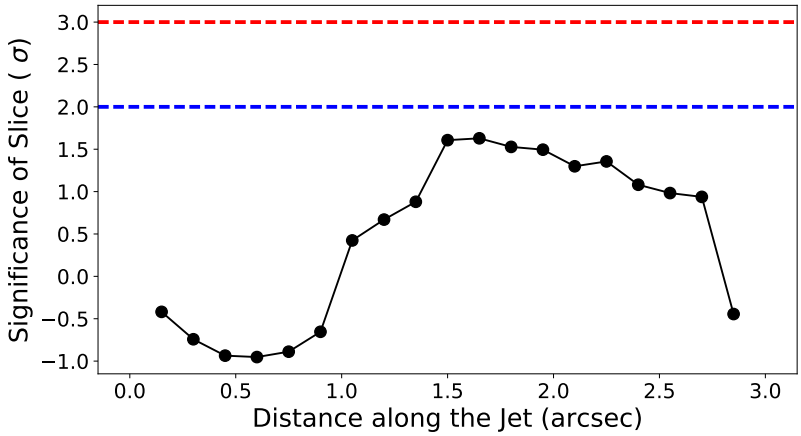

Figure 3.29: Plot of the significance of transverse RM gradients in the E3 knot of 3C 303 with significance on the y-axis and distance along the jet on the x-axis. The blue and red dashed lines represent the 2 and 3 sigma levels respectively.

The possible transverse RM gradients in the 'E3' knot region were analysed and tested for their significance. This analysis is plotted in Figure 3.29 which shows that the significances of transverse gradients in this region are no more then 1.5σ. It is therefore difficult to associate these results with a toroidal magnetic field component and associated outward electrical current, given the relativlely low significance. The transverse RM gradient previously reported in the vicinity of E3 cannot be accepted as statistically significant, and most likely came about by chance. The overall appearance of the RM is quite patchy, as can be seen in the upper panel of Figure 3.27, with random variations in the RM across the map, which are most likely also dominant in the vicinity of in E3.

3.2.2 5C 4.152

Results for this source have been published in Christodoulou et al. (2016), on which the author of this thesis is a co-author.

This is an FR II radio galaxy which was previously analysed by Bonafede et al. (2010). Transverse rotation measure gradients were visible by eye in both of the lobes, however their statistical significance was unknown. There is no known redshift for this source and, similarly to 5C 4.114, this AGN is most likely in the background of the Coma cluster and not a member. Bonafede et al. (2010) kindly made the calibrated visibility data available for an analysis into the RM structure of this source. These data included observations taken in

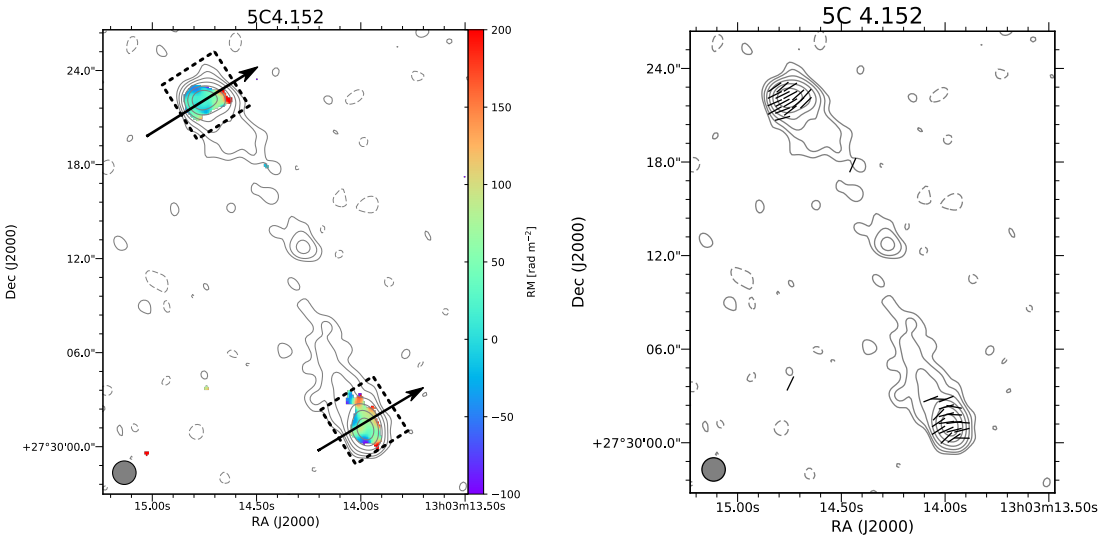

Figure 3.30: **Left Panel:** RM map of 5C 4.152 made using data from 4.535, 4.935 and 8.275 GHz. The Stokes I contours corresponding to 4.535 GHz start at 0.1 mJy beam^{-1} and increase in factors of 2 up to a level of 6.4 mJy beam^{-1}. A dashed negative contour is given at -0.1 mJy beam^{-1}. The common 1.5" convolving beam is given in the bottom left hand corner. The black arrows indicate the direction of possible transverse rotation measure gradients.The black dashed boxes indicate the segments along the jet where plots of gradient significance as a function of distance alone the jet are plotted. **Right Panel:** Map of the RM corrected, intrinsic polarization angle χ_0 plotted as vectors with identical contours to the left panel.

August 2006 at 4.535, 4.935, 8.085 and 8.465 GHz. However, due to technical issues during the observations the observing time was reduced, and in an effort to improve the signal to noise ratio of the 8 GHz data the 8.085 and 8.465 GHz observations were averaged together in Bonafede et al. (2010), creating a single channel at 8.275 GHz. This procedure was followed for the RM analysis presented here. Stokes I, Q and U with a common 1.5" convolving beam were produced and χ versus λ^2 fitting was performed using a weighted least squared fitting procedure in PYTHON.

The resulting rotation measure map is shown in Figure 3.30, with the location of possible gradients given by the solid black arrows. The typical end point RM error values for gradients in this source were ≈ 100 rad m^{-2}. This value is unfortunately quite high, due to the limited range of λ^2 and the high level of noise in the averaged 8,275 GHz images. The RM distribution is fairly patchy with the gradients not appearing completely monotonic. Plots of the significance of the RM gradients as a function of distance along the jet for each

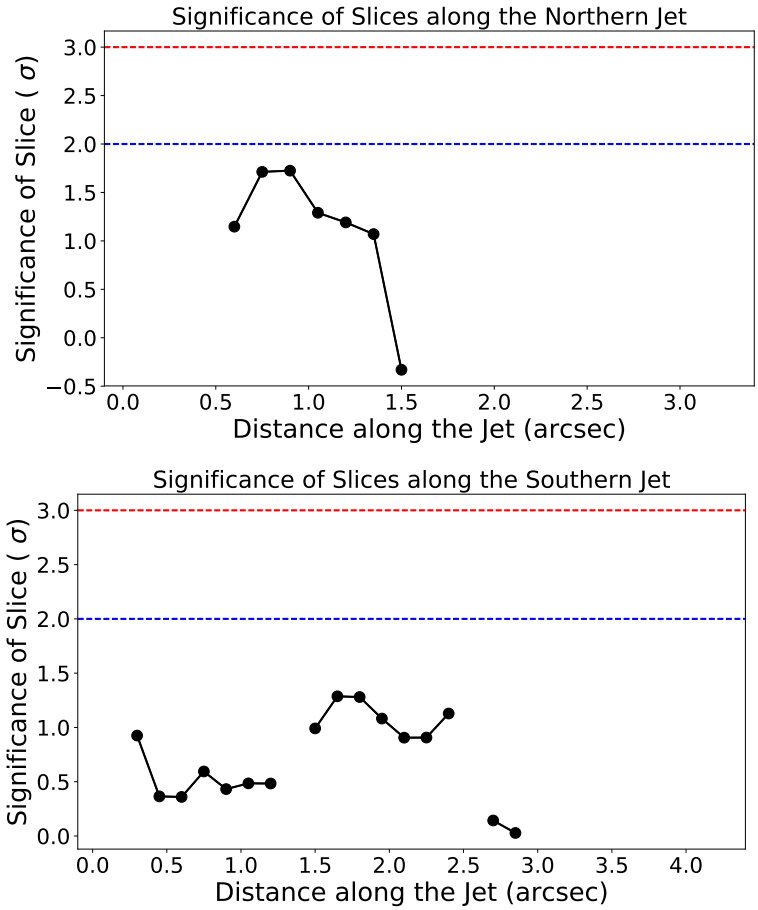

Figure 3.31: **Top panel:** Plot of transverse RM gradient significance as function of distance along the jet for the region enclosed by the dashed black rectangle in the Northern jet of 5C 4.152. The 2σ and 3σ levels are marked as blue and red dashed horizontal lines. **Bottom panel:** Plot of transverse RM gradient significance as function of distance along the jet for the region enclosed by the dashed black rectangle in the Southern jet of 5C 4.152, with 2σ and 3σ levels marked as in the top panel. Regions with no plotted points indicate that no monotonic gradients were detected in that region.

of the dashed boxes in Figure 3.30 are given in Figure 3.31. In both the Northern and Southern lobes the gradients are never above 2σ, with significant gaps in the plots where gradients were not monotonic. The direction of the reported gradient in the Northern jet corresponds to an associated inward electrical current, while the Southern jet shows a gradient implying an outward electrical current. It must be noted that due to the low significances and patchiness of the rotation measure distribution, these cannot be taken into serious consideration without further observations.

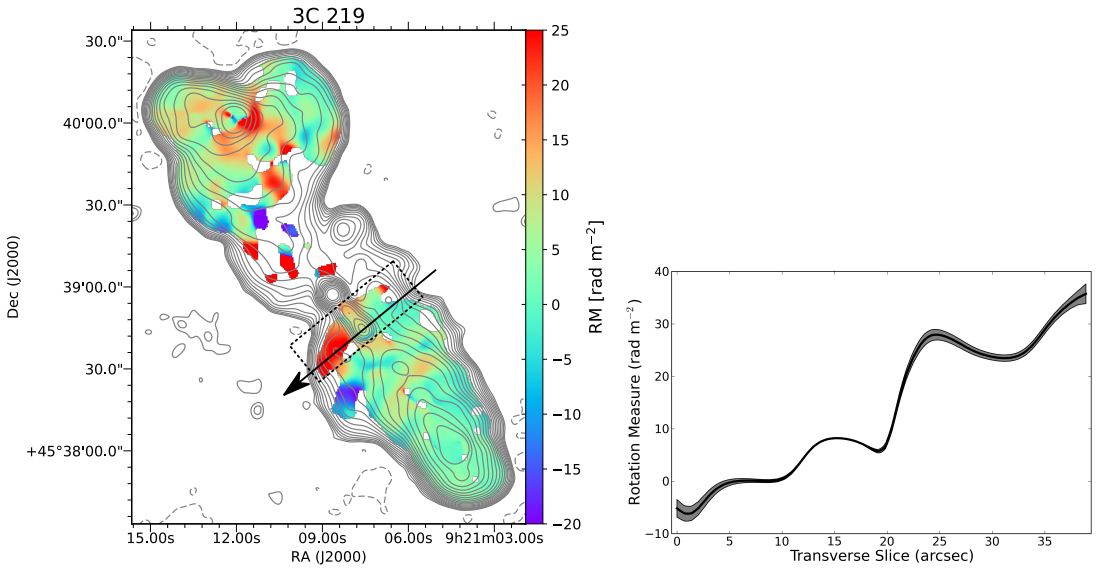

Figure 3.32: **Left panel:** Image of 3C 219 showing the RM in the colour scale and the Stokes I contours at 4.8 GHz with levels of ± 0.075 to 38.4 mJy beam^{-1} in steps of factors of $\sqrt{2}$ with the negative contour dashed. The arrow traces the direction of the RM gradient. **Right panel:** A plot of RM versus transverse jet distance plotted corresponding to the black arrow in the left panel.

3.2.3 3C 219

Results for this source have been published in the conference proceedings by Knuettel & Gabuzda (2019).

A prime example of a classical double, a morphologically regular FRII, 3C 219 is a twin lobed radio galaxy at redshift $z = 0.1745$ (Hewett & Wild 2010), for which an RM gradient was reported in Clarke et al. (1992). The possible presence of a helical or toroidal magnetic field threading the jet was noted by Clarke et al. (1992), however this was not the focus of that paper, and the possible transverse RM gradient was not fully analysed. The raw data at 1.3, 1.6 and 4.9 GHz observed on 6 September 1986 and used in Clarke et al. (1992) were downloaded from the VLA archive and calibrated using CASA. The RM map was made using a common convolving beam of 5" and is shown in Figure 3.32. A Galactic contribution to the RM of -12.6 rad m^{-2} (Taylor et al. 2009) was subtracted, in order to achieve a better insight into the RM local to the radio source. A slice of RM values in the region of transverse RM gradients reported in Clarke et al. (1992) taken at the position, indicated by the path of the black arrow in the left panel, is given in the right panel.

The slice is not completely monotonic, most likely due to the more turbulent

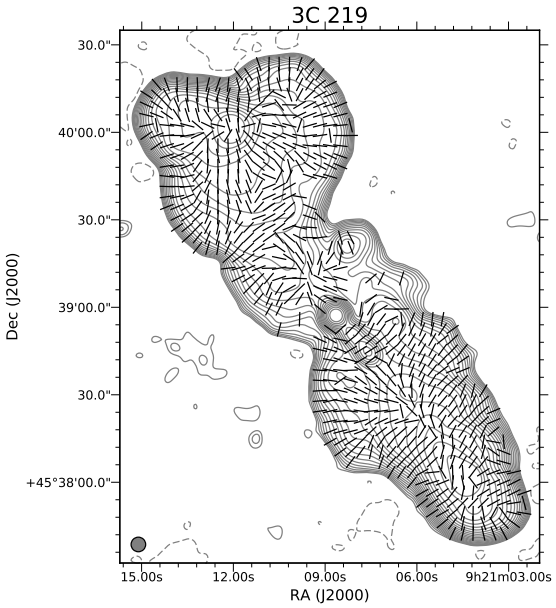

Figure 3.33: Map of the RM corrected Electric field vectors plotted. The contours and convolving beam are identical to Figure 3.32

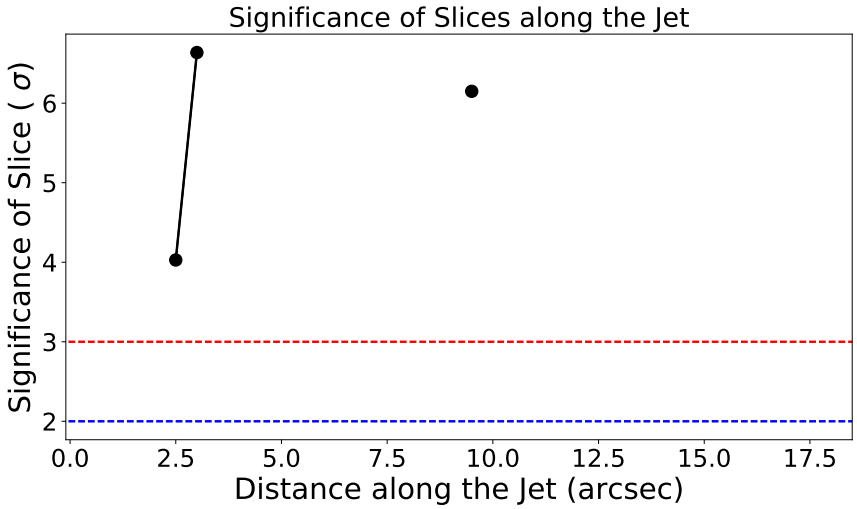

Figure 3.34: Plot of transverse RM gradient significance as function of distance along the jet for the region enclosed in the dashed rectangle in Figure 3.32. The 2 and 3σ significance levels are given as blue and red dashed horizontal lines. The connected points indicate contiguous gradients. The non detection of points indicates the gradients were not monotonic within tolerances.

nature of this more diffuse region of the radio lobe, but there is nevertheless a trend in the RM across the jet in this region. The difference in the end point RM values of the transverse gradient, when taking errors in the RM into account is however highly significant ($\sim 14\sigma$). In addition, the sign of the RM changes from one end of the slice to the other, indicating a change in the line of sight magnetic field component, and this cannot be explained by a change in the electron density alone. The significances of the gradients are analysed in detail by plotting the significance of the transverse gradients as a function of distance along the jet for the region enclosed by the dashed black rectangle in Figure 3.32 and is shown in Figure 3.34. The highly significant gradients are few and isolated and indicate most likely spurious detections given the vast majority of gradients are not completely monotonic as can be seen by the example in the right panel of Figure 3.32. Some random fluctuations in the RM structure due to local patchiness and turbulence are not unexpected, and it is possible that we are seeing the result of a transverse RM gradient due to a toroidal field component with a random RM distribution superposed. The RM structure in the rest of the radio lobes is rather patchy, with no indication of an organised large scale magnetic field structure. All considered, this is regarded only as a tentative transverse RM gradient, particularly given that it is localized in only a very small region of the jet with the remainder of he jet showing a turbulent and disorganised RM structure.

3.3 Summary of Results

This analysis into transverse RM gradients as evidence of toroidal magnetic field components in jets and their associated currents has yielded some support for the cosmic battery model proposed by Contopoulos et al. (2009). A total of 6 sources with statistically significant transverse RM gradients on kiloparsec scales were found, of which 5 imply outward associated electrical currents. While this sample size is quite small it does suggest a bias toward outward currents on larger scales. A simple binomial-distribution analysis indicates that the probability of observing 5 out of 6 RM gradients implying outward current by chance is about 9.4%. This probability is low enough to be suggestive, but not conclusive.

Christodoulou et al. (2016) have considered a number of additional sources displaying transverse RM gradients on large scales. In this publication a

summary of known statistically significant and tentative transverse RM gradients from a review of the literature is discussed. The analyses for A2142A and 5C 4.152 presented above were part of that paper, and results of VLBI observations at comparatively lower frequencies probing decaparsec scales were considered also. The effects of the larger scale magnetic field are expected to become more dominant at distances of around $10 - 20$pc from the jet base (Christodoulou et al. 2016), making lower frequency VLBI observations of sources with extended jets very suitable for such studies.

Large scale significant transverse RM gradients have been detected using VLBI, for example in the jets of 3C 380 and Mrk 501 in Gabuzda, Cantwell & Cawthorne (2014) and Croke et al. (2010), respectively. In fact, reversals in transverse RM gradient structures, where transverse RM gradients in opposite directions can exist in different parts of the jet at different distances from the jet base, have been observed in a number of sources. Mahmud et al. (2013), for example, detected reversals in transverse RM gradients in the BL Lac objects 0716+714 and 1749+701, with the inner transverse RM gradients implying inward currents and the outer transverse RM gradient implying outward currents. Another more recent example is the RM gradient reversal in the jet of 0954+408 reported by Gabuzda, Knuettel, Richardson, Kyprianou & Spillane (2018). This result is very significant, but preliminary, however has been added to the list of significant results for now. These gradient structures are indicators of regions in the jet where the dominance of the internal helical magnetic field, associated with an inward current, and external field associated with an outward current is changing. Christodoulou et al. (2016)consider 8 individual sources displaying significant RM gradients, two of which have been discussed in this thesis.

The work presented in this thesis has identified 3 new significant transverse RM gradients in jets on kiloparsec scales, in NGC 6251, Coma A and IC 4296, while also moving 3C 465 from a tentative to a statistically significant case. Table 3.3 presents an updated version of Table 1 of Christodoulou et al. (2016), including the new results in presented here. Fifteen jets now display significant transverse RM gradients on large scales (greater than 10–20 pc). Of these, only the two jets of IC 4296 show large scale transverse RM gradients implying inward currents in kiloparsec scales, while all the others imply outward currents.

To find the statistical significance of this dominance of outward electrical

currents, a binomial probability distribution can be applied, as was done in Gabuzda, Nagle & Roche (2018), where the dominance of inward currents on parsec scales was demonstrated. The binomial probability distribution can be used to determine how likely a certain outcome can come about by chance. In the case of the large scale RM gradients, the likelihood that the dominance transverse RM gradients supporting outward currents is given by (Gabuzda, Nagle & Roche 2018, Equation 3.)

$$P_{\rm chance} = \frac{1}{2^{(N_{\rm in}+N_{\rm out})}} \frac{(N_{\rm in}+N_{\rm out})!}{N_{\rm in}!N_{\rm out}!}, \tag{3.4}$$

where $N_{\rm in}$ is the number of sources with transverse RM gradients implying inward currents and $N_{\rm out}$ is the number of sources with transverse gradients implying outward currents. $P_{\rm chance}$ is the probability that $N_{\rm in}$ and $N_{\rm out}$ can came about be chance, if the probability of a gradient indicating an inward or outward current were 0.5, like a coin toss. Substituting $N_{\rm in} = 2$ and $N_{\rm out} = 13$ from Table 3.3, the resulting probability is $P_{\rm chance} \approx 0.0032 \equiv 0.32\%$ showing that this preference for outward currents is quite unlikely to have come about by chance. This is a highly significant result and builds on the work of Christodoulou et al. (2016) and of Gabuzda, Nagle & Roche (2018) on the parsec scales. This strongly supports a picture in which the dominant jet currents are inward on parsec scales and outward on scales exceeding 10-20 pc, consistent with the predictions of the cosmic battery model of (Contopoulos et al. 2009). In this picture, the jets of AGN are like giant co-axial cables, carrying inward current close to the jet axis and outward current in a more extended region surrounding the jet. This large statistical analysis on all scales and distances along AGN jets helps build up a large amount of evidence for the action of a cosmic battery in the hearts of all AGN.

Of the tentative results from the original list in Table 1 of Christodoulou et al. (2016) the significance of 3C 465 was confirmed, and the significance of 3C 303 result was brought into question, making it an unlikely candidate without higher resolution and higher sensitivity observations. 5C 4.152 must be kept in the tentative list without renewed observation with higher sensitivity. The gradient in 3C 219 was brought into the tentative list based on the report of a transverse RM gradient in a small portion of the Southern jet and lobe. All of these tentative results could benefit massively from the upcoming VLA Sky Survey results, which aim to release images of the Northern sky at 2–4 GHz with polarization information, making renewed

Table 3.2: Table summarizing the RM gradients and their associated electrical currents for large scales, combining the results from Christodoulou et al. (2016) and this thesis.

Object	redshift z	Associated Current	Projected distance of gradient from core (kpc)	Reference
NGC 6251	0.02471	Out	12.5	K19, T
3C 465	0.0302	Out	24	K17, T
A2142A	0.091	Out	10	C16, T
5C 4.114 (N)	>0.023[b]	Out[a]	>1.5	G15, T
5C 4.114 (S)	>0.023[b]	Out[a]	>1.5	G15, T
Coma A	0.0857	Out	62	K17, T
IC 4296 (N)	0.01247	In[a]	11	T
IC 4296 (S)	0.01247	In[a]	11	T
3C 380	0.692	Out	0.07–0.21	G14a
0716+714	0.127	Out*	0.003–0.035	M13
1749+701	0.77	Out*	0.07–0.21	M13
Mrk 501	0.034	Out	0.02	C10
0923+392	0.695	Out*	0.02	G14b
2037+511	1.687	Out*	0.04	G14b
0954+408	1.25	Out*	0.25	G18

[a] In these instances the significant gradients were detected in both jets of the large scale source.
[b] Exact redshift not known, source is background to Coma cluster so redshift must exceed $z = 0.023$
[c] Previously confirmed however significance brought into question in this analysis.
* RM gradients with associated inward currents were present closer to the jet base.
Reference key: T = This thesis, K19 = Knuettel & Gabuzda (2019), K17= Knuettel et al. (2017), C16 = Christodoulou et al. (2016), G14a =Gabuzda, Cantwell & Cawthorne (2014), M13 = Mahmud et al. (2013), C10 = Croke et al. (2010), G14b = Gabuzda, Reichstein & O'Neill (2014), G18 = Gabuzda, Knuettel, Richardson, Kyprianou & Spillane (2018)

analysis of the rotation measures of these sources worthwhile, when these survey data are released.

Chapter 4

Estimating the magnetic field strength in the Faraday screen surrounding Coma A

This chapter deals with the magnetic field in a Faraday screen detected around the radio galaxy Coma A, , this chapter is also published as an article in Monthly Notices of the Royal Astronomy Society (Knuettel et al. 2019).

4.1 Introduction

The radio-emitting structures in the vicinity of supermassive black holes in the centres of active galaxies display a large variety of morphological properties. It is a long standing debate to what extent the differences between different types of radio sources are due to intrinsic properties of the central engine ('nature') or the properties of the interstellar and intergalactic medium (ISM and IGM) surrounding the central engine and host galaxy ('nurture'). Investigating this 'nature vs. nurture' debate for nearby radio galaxies is vital for understanding the properties and evolution of radio galaxies throughout the Universe (e.g. Fabian 2012, Heckman & Best 2014, and references therein).

Here a case is presented, where there are clear interactions between the radio lobes and the surrounding gas in the nearby radio galaxy Coma A, which has been the focus of studies at multiple wavelengths (van Breugel et al. 1985,

Bridle et al. 1981, Tadhunter et al. 2000, Morganti et al. 2002, Worrall et al. 2016). In particular, a study of the combination of wide-band polarimetric radio observations and deep H α images is presented. This combination provides a powerful tool to investigate the interactions between the lobes and their surrounding environment: the wide-band radio observations allow us to investigate the polarization and magnetic field structure of the radio emitting lobes and how this changes with wavelength, and the H α measurements allow estimation of the electron density in the shocked gas surrounding the lobes, which in turn enables the calculation of the magnetic field strength in the gas containing the free electrons using the effect of Faraday rotation.

4.1.1 Coma A

Coma A is a radio galaxy at redshift $z = 0.0857$ (Bridle et al. 1981) corresponding to a comoving radial distance of 371.6 Mpc and angular scale of 1.659 kpc/" (Wright 2006) using the values of $H_0 = 67.74\,\mathrm{km\,s^{-1}Mpc^{-1}}$, $\Omega_M = 0.3089$, and $\Omega_\Lambda = 0.6911$ from the Planck 2015 results (Planck Collaboration 2016). The source has two distinct radio lobes and an angular size of 45" in the north-south direction. Coma A is classified as a Fanaroff-Riley II galaxy in Fanaroff & Riley (1974). The Northern lobe shows a bright hotspot, and the Southern lobe has a bright plume expanding into a lobe structure. This plume is at a deflected angle to the expected jet direction due to a collision with a gas cloud, decelerating the jet and giving it the features of an FR I structure (van Breugel et al. 1985). Due to this feature and the fact that the power of this radio galaxy is lower that most FRII galaxies, Coma A is on the border between FRI and II classification (Fanaroff & Riley 1974, Table 1). It was classified as an FRI for this reason in Chiaberge et al. (1999). It is an example of a hybrid morphology radio source (HyMoRS Gopal-Krishna & Wiita 2000*a*, Gawronski et al. 2006, de Gasperin 2017).

Large scale arcs and filaments of H α emission have been observed surrounding the radio lobes (Tadhunter et al. 2000), which closely match the shape of the radio lobes of Coma A. The origin of this ionised gas is discussed in depth in Tadhunter et al. (2000). The most likely cause for the ionisation is the shock from the expanding radio lobes moving into a region of neutral gas surrounding the host galaxy. The origin of the gas has been investigated with HI absorption observations of Coma A. These show the presence of HI local to

both lobes and suggest that a large scale gas disk surrounds the galaxy, into which the radio lobes are expanding (Morganti et al. 2002). The origin of the gas itself is most likely from a merger in the Coma A host galaxy as the estimated mass of hydrogen is at least $10^9 M_\odot$, suggesting at least one gas rich galaxy was involved. The existence of such gas around the lobes is also observed in the X-ray. In particular, (Worrall et al. 2016, Figure 7) shows how regions of diffuse X-rays in the local environment display an anti-correlation to the H α filaments. They argue that the original group atmosphere has been shock ionised and now surrounds the lobes, causing the extended X-rays and the H α filaments.

In this chapter, new wide-band dual-polarization observations of Coma A using the enhanced Karl J. Jansky VLA are presented as well as VLA observations. These are used to investigate how the H α-emitting gas and radio lobes interact, through an analysis of the Faraday rotation of the polarized radio emission, together with RM synthesis and QU fitting.

4.1.2 Polarization and Faraday rotation

Radio galaxy lobes emit synchrotron radiation from relativistic electrons accelerated by magnetic fields. The properties of synchrotron radiation are presented in Section 1.1.5, Faraday rotation is discussed in Section 1.1.6, the Stokes parameters are defined in Section 2.2.1.

It is commonly observed that the fractional polarization, p, tends to decrease towards longer wavelengths, an effect known as depolarization. One of the most common models associated with this phenomenon is external Faraday dispersion (Sokoloff et al. 1998), where an external screen with free electrons and a turbulent magnetic field depolarizes the signal within the observing beam, due to the different resulting Faraday rotations occurring along individual lines of sight within the beam. It is possible to fit models to observed data with good λ^2 coverage in order to estimate the parameters of the source polarization and turbulent screen, as is described in Section 2.3.2 (e.g. O'Sullivan et al. 2012). The model used in this analysis has a single RM component and an external depolarizing screen, motivated in part by the picture of a shell of ionized gas surrounding the lobes of Coma A:

$$p(\lambda) = p_0 \mathrm{e}^{2\mathrm{i}\left(\chi_0 + \mathrm{RM}\lambda^2\right)} \mathrm{e}^{-2\sigma_{\mathrm{RM}}^2 \lambda^4} \tag{4.1}$$

Here, $p(\lambda)$ is the fractional polarization as a function of wavelength. The first exponential term is the complex linear polarization (Equation 2.29) with the observed polarization angle defined as in Equation 1.47(Burn 1966). The second exponential term represents the depolarization by an external Faraday screen where σ_{RM} is the standard deviation of the RM within the telescope beam, due to the turbulent magnetic field in the ionized gas. Using Equations. 2.29 and 4.1, the fractional Stokes Q and U parameters, $q(\lambda)$ and $u(\lambda)$, are described as follows.

$$q(\lambda) = p_0 \cos\left(2\chi_0 + 2\mathrm{RM}\lambda^2\right) \mathrm{e}^{-2\sigma_{\mathrm{RM}}^2\lambda^4} \tag{4.2a}$$

$$u(\lambda) = p_0 \sin\left(2\chi_0 + 2\mathrm{RM}\lambda^2\right) \mathrm{e}^{-2\sigma_{\mathrm{RM}}^2\lambda^4} \tag{4.2b}$$

These equations can be fit to observed data by creating cubes of the q and u images from the wide band observations with matching resolutions. This fitting yields calculated values of χ_0, RM, σ_{RM}, and p_0 for each pixel.

4.2 Observations and data reduction

4.2.1 Wide band VLA observations

The Karl G. Jansky Very Large Array (VLA) observations in L (994 – 2006 MHz) and S (1988 – 4012 MHz) bands were taken on the 29 December 2013 and 27 September 2013 respectively, in the VLA B configuration. The flux, phase and bandpass calibrations were done with regular scans of 3C 286, which is close to Coma A, every 20 minutes. A summary can be seen in Table 4.1, where ν_1 is the starting frequency of the observing band and ν_2 is the final frequency. The width of each channel in the wideband setup is $\Delta\nu$. The date is the observing date while t is the total integration time on Coma A for that observation.

The wide band VLA data were flagged, calibrated, and imaged using the Common Astronomy Software Applications package CASA. The data were first Hanning smoothed, which is a running mean across the spectral axis with a triangle as a smoothing kernel. This isolates and narrows the RFI interference peaks and removes Gibbs ringing, which produces artefacts in the spectrum near sharp intensity transitions such as RFI peaks. The data were then flagged

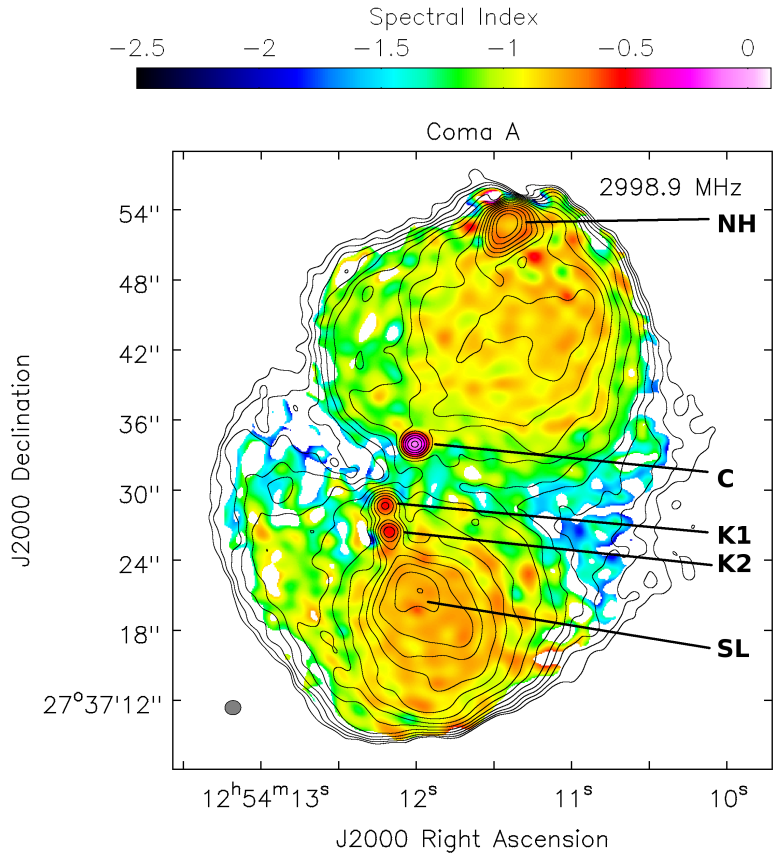

Figure 4.1: The 2–4 GHz data imaged using a multi-frequency synthesis method with a reference frequency at 3 GHz in order to observe the most structure with the best possible resolution. The contours are overlaid on the spectral index map used in the imaging process. The convolving beam is 1.37" × 1.23" at a position angle of -88.6°. The labelled features are: The Northern hotspot (**NH**), core (**C**), knots (**K1** and **K2**), and the Southern lobe (**SL**). The contours in Stokes I are 0.2 mJy beam^{-1} ×(1, 1.41, 2, 2.83, 4, 5.66, 8, 11.31, 16, 22.63, 32, 45.25, 64)

Table 4.1: Table outlining the VLA observations of Coma A.

Configuration	ν_1 MHz	ν_2 MHz	$\Delta\nu$ MHz	Date	t hrs
VLA B	1988	4012	2	2013 Sep 27	1.75[a]
VLA B	994	2006	1	2013 Dec 29	1.79

[a] Due to an unknown error in the instrumental polarization calibration, only the final two thirds of these scans had correct polarization calibration applied and were useable for polarization measurements. The Stokes I data are unaffected.

for RFI using the standard automated flagging procedures *TFCrop* and *RFlag* in CASA.

To calibrate the instrumental polarization and correct for the polarization angle, a polarized model for 3C 286 was used, as polarization angle and fractional polarization are known for this source. This was done (using *setjy* and *polcal* in CASA) because due to scheduling issues the parallactic angle coverage for these observations was not sufficient to solve for the calibrator polarization independently. Due to an unresolved issue with the polarization leakage calibration, only two thirds of the scans of Coma A for the 2–4 GHz data had stable amplitudes and phases for polarized correlations. This was indicated by noisy and irregular values in the corrected amplitudes and phases of the scans for 3C 286 adjacent to scans of Coma A. The 2–4 GHz data that did not display stable polarized amplitudes and phases were not used in the analysis.

The data were self calibrated over the full spectral range for each dataset using a multi-term multi-frequency synthesis method for imaging (Rau & Cornwell 2011). This was done to reduce the noise level in the image, and the wide-band image provided the most accurate model for self calibration.

For the model fitting, data cubes of Q and U images were made by imaging the data in discrete frequency bins of 8 MHz. A Clark (Clark 1980) clean was used for each separate Stokes parameter this deconvolution process is a streamlined version of the Högbom CLEAN which works faster with larger image sizes. The visibility data were tapered in the imaging process and the resulting images smoothed all to the same beam size of 7" , which corresponded to the 1 GHz image. This resulted in data cubes with 126 images along the spectral axis from 1 to 2 GHz.

For the 2–4 GHz data, the instrumental polarization calibration was not ideal; the quality of the per-channel instrumental polarization calibration was poor, due to the small range of parallactic angle coverage for the polarization leakage calibrator source. As a result significantly larger frequency bins were used in the imaging process. This was done in an attempt to reduce the effects of the Stokes Q and U values varying over each spectral window. The visibility data were tapered and images smoothed so that all resulting images had an identical 4.1" circular beam.

Cubes of Stokes Q and U images were made with frequency bins of 128 MHz

Table 4.2: Table outlining the archival VLA observations of Coma A.

Project	ν MHz	$\Delta\nu$ MHz	Configuration	Date	t hrs
VANB[a]	4885	50	VLA B	1981 Jun 01	4.1
AB348	14940	100[b]	VLA C	1985 Aug 26	6.2

[a] Data previously published in van Breugel et al. (1985)
[b] Data consist of two frequencies 50 MHz apart each with 50 MHz bandwidth. Central frequency is given.

from 2 to 4 GHz. The resulting cubes have 16 evenly spaced images along the frequency axis.

4.2.2 Archival VLA observations

To examine the behaviour at higher frequencies, and confirm the observed polarization structure at lower frequencies, archival observations at 4.9 and 15 GHz were used. The archival data are also at a higher resolution than the more recent wide-band observations. The raw data were downloaded from the VLA archive and calibrated again. These observations were useful in localising exact regions where depolarization occurs. A summary of the archival data analysed is given in Table 4.2, where ν is the observing frequency. The width of each channel in the setup is $\Delta\nu$. The date is the observing date while t is the total integration time on Coma A for that observation.

In addition to confirming the results of the VLA observations, the archival VLA data were used to investigate the polarization behaviour at higher frequencies and resolutions, where higher fractional polarization was expected. These were calibrated using the Astronomical Image Processing System (AIPS) software package, where the flux density calibrator used was 3C 286, which also served as the polarization angle calibrator and the phase calibrator was 3C 287; the parallactic angle coverage of this source was also used to successfully determine the D-terms in order to correctly determine the source polarization angles and fluxes.

The resulting visibility data were exported to CASA for imaging using a multiscale CLEAN, in an effort to better capture the large scale lobes in the deconvolution process and reduce the effects of "bowls" of negative emission where the large scale flux is missing due to the longer baselines being used in

these observations. Images of the polarized intensity were made with the standard polarization bias correction applied in CASA (e.g. VLA memo 161, (Leahy & Fernini 1989)). The fractional polarization images were made using only Stokes I as a blanking factor, in this case a blanking limit of 1 mJy beam^{-1} in Stokes I was used. This was especially important for mapping the heavily depolarized regions that are present even at high frequencies (4.9 and 15 GHz) to get an estimate of the upper limit of fractional polarization in these regions.

4.2.3 Hα observations

The deep Hα image used in this analysis is taken from Tadhunter et al. (2000), and was observed with the William Herschel Telescope in January 1998. The image is the result of a deep 2×900 second integration and has been continuum subtracted to show the pure H α emission. Further details about the observations and the calibration of this data can be found in Tadhunter et al. (2000).

4.3 QU model fitting procedure

To analyse the polarization and Faraday rotation properties of the lobes of Coma A, the data were fitted with an external Faraday dispersion model, as described in Section 4.1.2. However, to initially identify regions with significant polarization the cubes of Stokes Q and U images were first processed using RM synthesis (Brentjens & de Bruyn 2005). This was done using the python implementation of *pyrmsynth*[1].

The resulting total polarized flux image from the RM synthesis procedure was used to make a mask for the Q and U cubes. Only regions where the polarized flux in this image was greater than three times the noise level were included in the Q and U cubes. This was done as initial inspections of model fits showed that frequency-dependant instrumental polarization was contaminating the data in regions of low signal to noise especially in the 2–4 GHz range. It must also be noted that due to this instrumental polarization effect, the 1–2 GHz and 2–4 GHz datasets were analysed and modelled independently.

[1] `http://mrbell.github.com/pyrmsynth`

Before the model fitting, the Q and U cubes were converted to fractional Q and U cubes (referred to as q and u). This was done using model Stokes I images constructed from a spectral index map, which was made from the multi-frequency synthesis imaging, and an image at the central frequency for that band. This was done to avoid regions with negative Stokes I arising from dynamic range issues due to the brightness of Coma A and the narrow bands used in making the cubes. This also limited the propagation of noise fluctuations in the Stokes I images to the q and u data.

The cubes were fit according to the model in Equations 4.2a and 4.2b. A single component RM model was used with a depolarization term from an external screen, which is what was expected from the H$\,\alpha$ measurements and previous publications indicating a gas shell surrounding the lobes. The fitting was done for every unmasked pixel in the cubes using an "asexual genetic algorithm" (Cantó et al. 2009), which is very efficient in converging to the global best-fit. The best-fitting model values were quantified by minimizing the chi-squared function for each fit in each pixel. The results of this fitting were values of χ_0, RM, σ_{RM}, and p_0 for each unmasked pixel. The pixels from the resulting maps were also blanked according to the error in the model fit. For this the error in the σ_{RM} was a good discriminator between acceptable model fits and those contaminated by any remaining residual leakage errors in the low polarization regions.

4.4 Results

4.4.1 Radio structure of Coma A

In Figure 4.1 a Stokes I contour map of Coma A is presented overlaid on the spectral index map. This image was made from the 2–4 GHz data and imaged using the multi-term multi-frequency synthesis method centred on 3 GHz using three Taylor terms in the CASA task *tclean*. The spectral index map, made using only the 2–4 GHz data was cross checked with an inter–band spectral index map made using the central frequencies from both the 1–2 GHz and 2–4 GHz data (at a lower resolution of 4"), finding consistent values with the higher resolution 2–4 GHz spectral index map. Additionally the values for spectral index calculated for Coma A in van Breugel et al. (1985) using 1.4 and 4.9 GHz data agree with Figure 4.1 also. The Northern hotspot, the knots K1

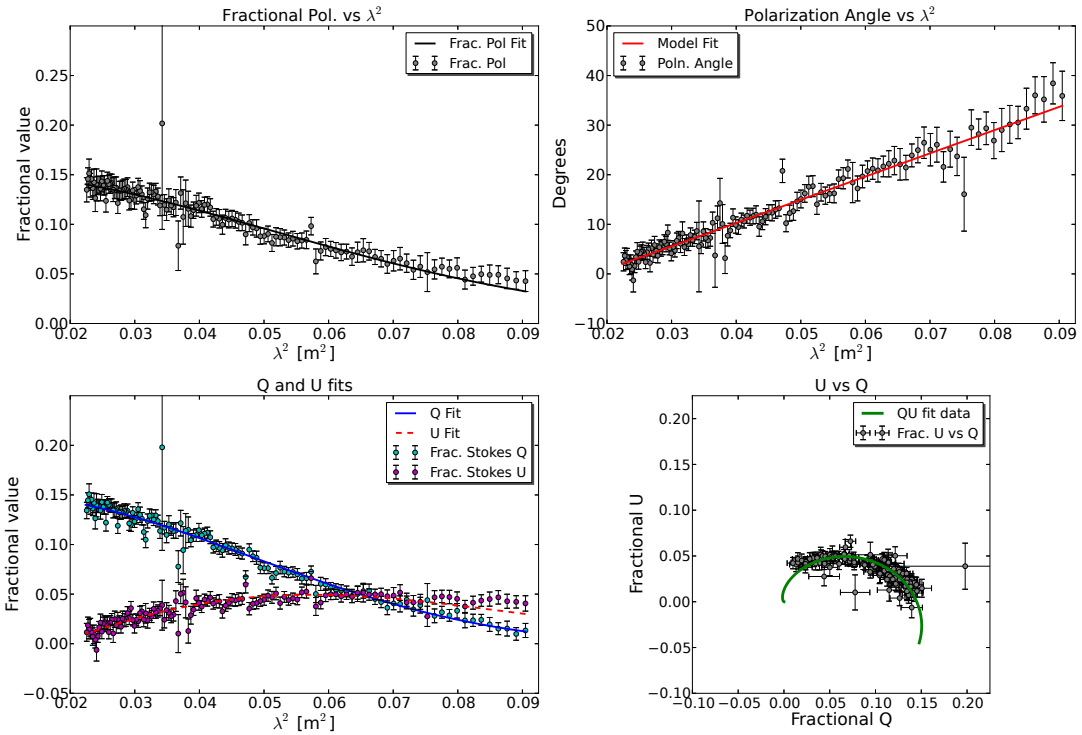

Figure 4.2: Model fit for the 1–2 GHz data. This is in the upper north western region of the Southern lobe, where the polarized flux is the highest. The bottom left panel shows the individual fractional Stokes Q and U fits. The upper left panel shows how the fractional polarization changes with wavelength squared (λ^2). This is made using $p = \sqrt{q^2 + u^2}$ from the fit data in the panel below it. Similarly for the top right panel the actual polarization angle data is plotted. The line passing through is calculated from the fit data as $\chi = 0.5 \arctan(u/q)$, not a linear fit. The bottom right panel simply plots the fractional Stokes Q and U against each other with model fitted data overlaid, the fitted line has been extended in λ^2 to show the fit spiralling toward the origin due to the depolarization. From this fitted region the fit values are: $p_0 = 0.15 \pm 0.001$, $\mathrm{RM} = 3.9 \pm 0.1\,\mathrm{rad\,m^{-2}}$, $\sigma_{\mathrm{RM}} = 9.8 \pm 0.1\,\mathrm{rad\,m^{-2}}$, $\chi_0 = -8.5 \pm 0.2°$.

and K2, which were first identified and named in Bridle et al. (1981), and the Southern lobe have been labelled. The hotspot to the north is typical for an FR II galaxy showing where the jet is impacting with the intergalactic medium. The knot K1 shows the location where the jet is colliding with a gas cloud, which can be identified in optical images(see right hand panel of Figure 8 in Worrall et al. (2016)) which is reproduced in Figure 4.6. The K2 knot and diffuse lobe are due to the deceleration of the jet after the deflection of $\sim 30°$ from the radio axis on the plane of the sky. The core has a relatively flat spectrum of $\alpha \simeq -0.1$, while outer features all have $\alpha \simeq -0.7$ or less, showing a steeper spectrum typical of optically thin synchrotron emission and older

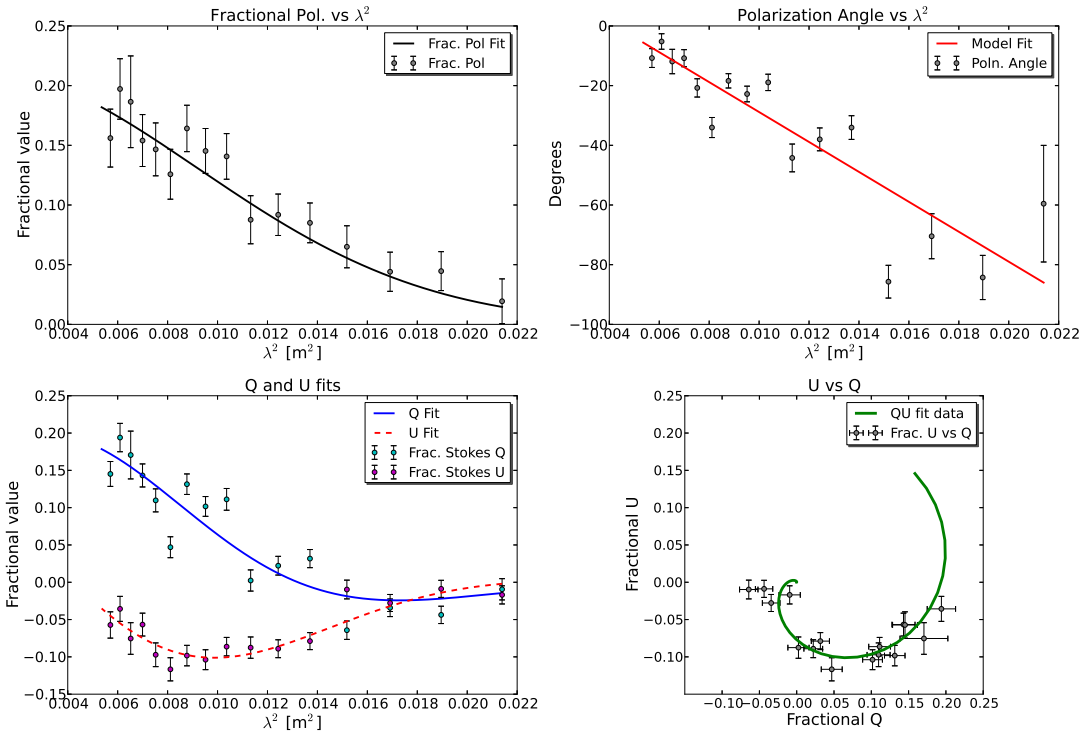

Figure 4.3: Model fit data for the 2–4 GHz data. This is for a region just to the south west of the H α filament in the Southern lobe. Note the strong depolarization. The graph panels are displayed in an identical manner as in Figure 4.2. From this fitted region the fit values are: $p_0 = 0.22 \pm 0.03$, RM $= -88 \pm 7\,\mathrm{rad\,m^{-2}}$, $\sigma_{\mathrm{RM}} = 54 \pm 7\,\mathrm{rad\,m^{-2}}$, $\chi_0 = -69 \pm 4°$.

regions of the jet emission.

4.4.2 QU model fitting

The model fitting showed that a single component RM and external depolarizing random screen provided an excellent fit to the data (Figures 4.2 and 4.3). The images of the calculated fitting parameters, RM, σ_{RM}, p_0, and χ_0 can be seen in Figures 4.4 and 4.5.

4.4.2.1 Northern lobe

The Northern hotspot did not have detectable polarization ($\leq 0.4\%$) in the 1–2 GHz range making the model fits poor. This is most likely due to depolarization from large RM variations in addition to intrinsic differences in polarization angle within the 7” beam across the complex hotspot structure.

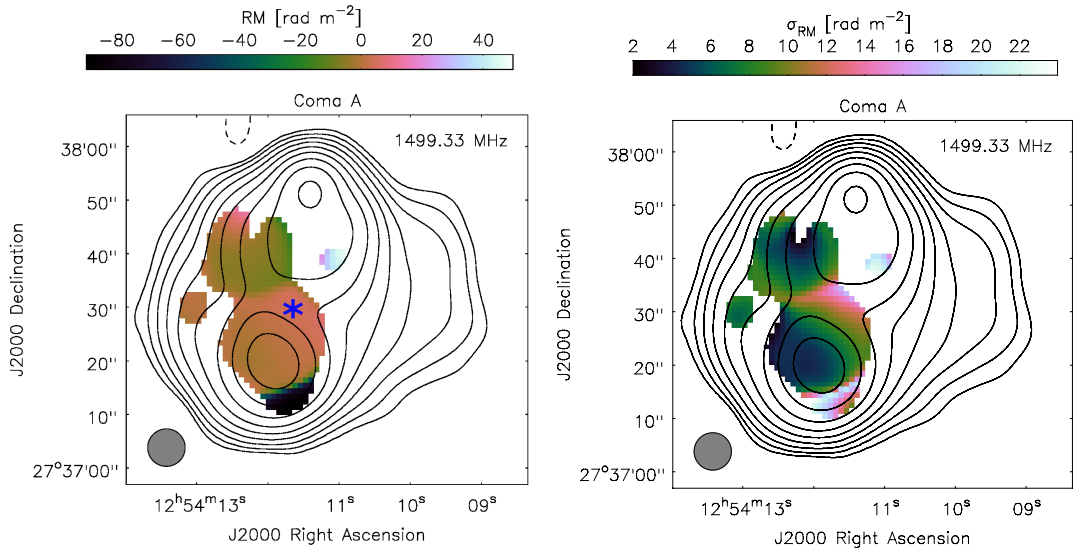

Figure 4.4: These are the RM (left) and $\sigma_{\rm RM}$ (right) images produced from the model fitting of the 1–2 GHz data. Due to the low resolution used, images of the fractional polarization at zero wavelength (p_0) and intrinsic polarization angle (χ_0) are not included. Note that the blue '$*$' is the location for which the data in Figure 4.2 are plotted. For the Stokes I contours, a 1–2 GHz image made using a multi-frequency synthesis technique is used. The uv data were tapered and the image smoothed to the same 7" resolution as the images used in the model fit. The central frequency is given in the top right corner of the images. The contours are given at the levels of 1 mJy beam^{-1} $\times$ (1, 2, 4, 8, 16, 32, 64, 128, 256)

The fractional polarization for the hotspot was also low in the 2–4 GHz observation where only some polarization is seen to the immediate east and west of the hotspot (ranging from $\sim 2\%$ to 4%). The centre of the hotspot has been blanked due to high error in the fits and low polarization. To confirm this, the archival dataset at 4.9 GHz (Figure 4.8(a)) was used as a reference. The polarized intensity at the exact hotpot is too faint to detect ($< 1\%$), only to the North and South of the hotspot is polarization reliably measured with values ranging between 2% and 9%, this confirms the results for the wideband 2–4 GHz observations. The 15 GHz observations at a similar resolution show some polarization (Figure 4.9(b)) for the hotspot at around 15%, however this frequency corresponds to a λ^2 value of $4 \times 10^{-4}\,\mathrm{m}^2$ which is close to zero wavelength. This indicates there is strong depolarization in the hotspot region. Note also that the lower 4" resolution used in the wide band 2–4 GHz observations may also lead to additional depolarization.

The Northern lobe as a whole shows a patchy polarization distribution,

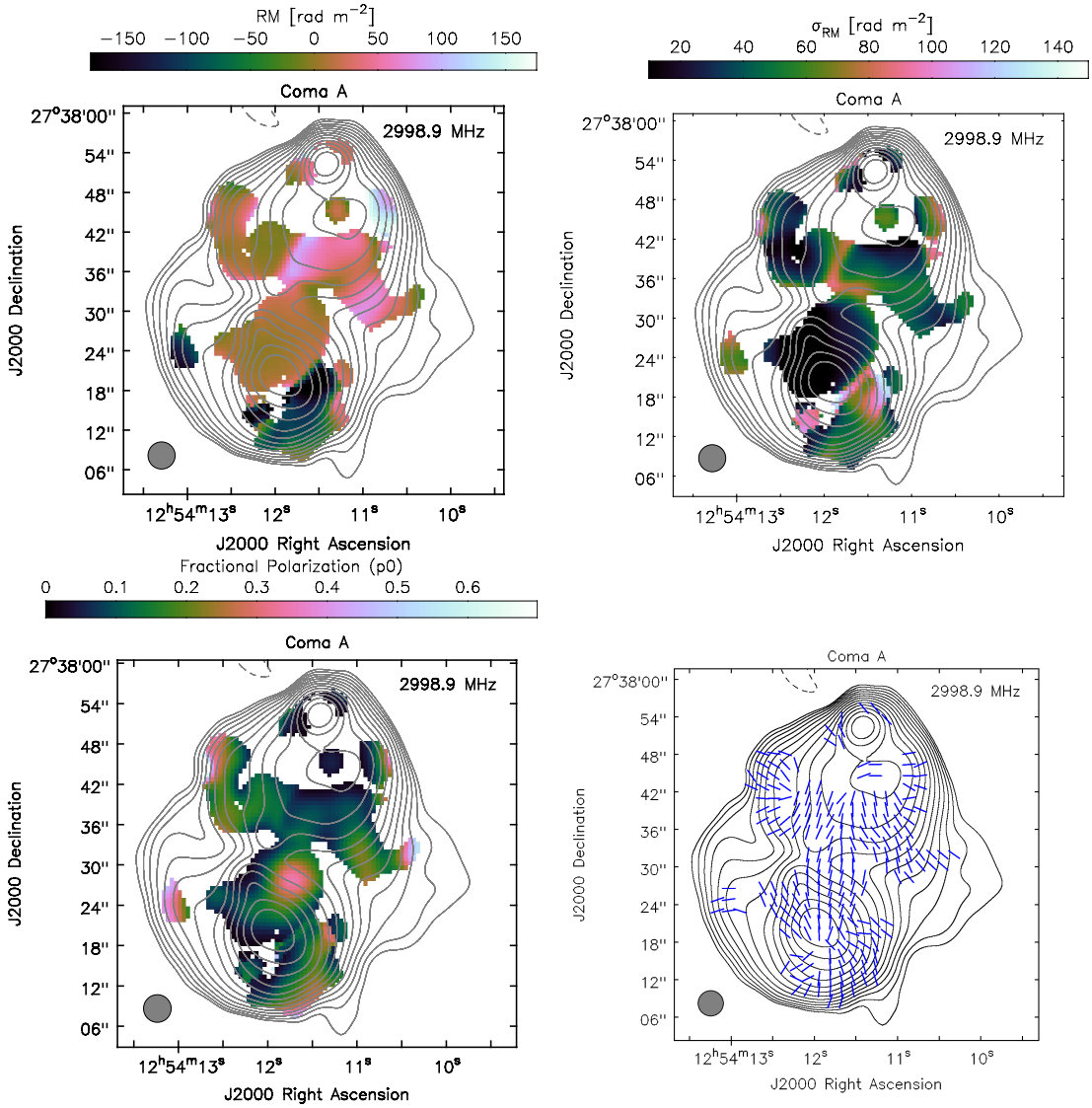

Figure 4.5: These are the RM (top left) and σ_{RM} (top right) images produced from the model fitting procedure for the 2–4 GHz data. The images of the fractional polarization at zero wavelength (p_0) and intrinsic polarization angle (χ_0) are given on the bottom left and bottom right respectively. The images were blanked according to the errors in σ_{RM} as this parameter had the highest errors and was a good indicator of the general quality of a fit for a depolarization model. The Stokes I contours are from a 2–4 GHz image made using a multi-frequency synthesis method using a central frequency of 3 GHz. The image was tapered and smoothed to the same 4.1" resolution as images used in model fit. The contours are given at the levels 1.4 mJy beam^{-1} × (-1, 1, 1.41, 2, 2.83, 4, 5.66, 8, 11.31, 16, 22.63, 32, 45.25, 64) with the negative contour dashed.

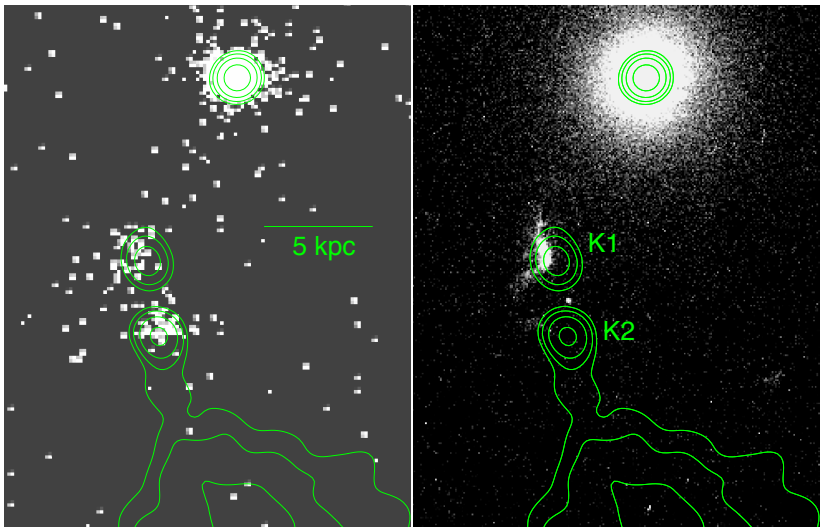

Figure 4.6: **Left panel:** X-ray data with radio contours overlaid showing where the jet is deflected at K1. **Right panel:** A high resolution Hubble telescope image showing the gas cloud which is being impacted by the radio jet and deflecting it. Image credit: Worrall et al. (2016)

presumably due to Faraday depolarization from the H α emitting gas, as the polarized emission is strongly anti-correlated with the H α emission (Figures 4.8(b) and 4.9(b)). The RM distribution is shown in the histogram in the top panel of Figure 4.7 with a mean (median) RM of 34.9 (24.9) rad m^{-2} and standard deviation (median absolute deviation) of 39 (22.6) rad m^{-2}. The high depolarization in the Northern hotspot and lobe as a whole can be interpreted as an example of the Laing–Garrington effect (Garrington et al. 1988, Laing 1988), which implies that the Northern jet is receding relative to the observer and the Southern, more strongly polarized jet is approaching. The fat projected shape of the lobes is also consistent with an orientation significantly inclined to the plane of the sky. One caveat to this is that the Southern jet, having been deflected by the collision in K1, has altered its orientation significantly relative to the inner radio axis.

4.4.2.2 Southern lobe

The polarization data for the Southern lobe agrees very well with the model in the 1–2 GHz range, as can be seen, for example, in Figure 4.2 (The data corresponds to the location indicated by the asterisk in Figure 4.4). At this pixel location, $p_0 = 0.15 \pm 0.001$, RM $= 3.9 \pm 0.1$ rad m^{-2}, $\sigma_{\rm RM} = 9.8 \pm 0.1$ rad m^{-2}, and $\chi_0 = -8.5 \pm 0.2°$. The model fit parameters from

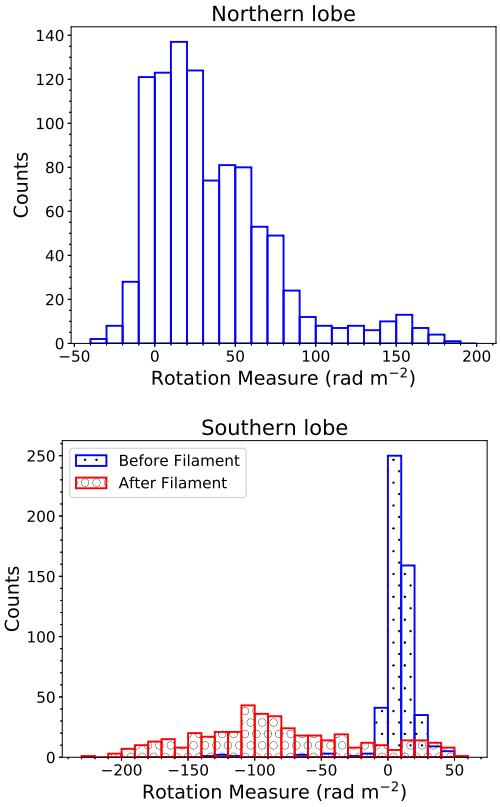

Figure 4.7: Histograms of the RM distribution in the lobes of Coma A taken from the RM image made for the S-Band model fit results. The top panel is the histogram of the RM distribution across the Northern lobe. The bottom panel shows the RM distribution in the Southern lobe, the blue histogram represents the part of the jet before the depolarizing H α filament; the red histogram represents the RM values after the filament and including the RM feature to the east.

the 2–4 GHz data, at the same location, are $p_0 = 0.33 \pm 0.03$, $\mathrm{RM} = 12 \pm 4\,\mathrm{rad\,m^{-2}}$, $\sigma_{\mathrm{RM}} = 25.6 \pm 6\,\mathrm{rad\,m^{-2}}$ and $\chi_0 = -14 \pm 3°$.

This shows the value of the higher resolution data at 2–4 GHz (4" beamsize) which more robustly probes the underlying Faraday rotation variations across the lobes. In particular, the higher value of p_0 indicates that most of the RM structure has been resolved in this region, as the fractional polarization at 15 GHz in this region is ∼0.35 (Figure 4.9(a)). Considering that the model of a Faraday depolarizing screen fits well to the data, the difference in the RM and σ_{RM}values between 1–2 GHz and 2–4 GHz can be ascribed to resolution dependent effects for an inhomogeneous Faraday screen produced by the patchy distribution of H α across the lobes.

Looking at the fractional polarization images for the higher resolution archival

observations at 4.9 GHz and 15 GHz, there are two regions of appreciably low fractional polarization. Firstly there is a region of low polarization along the centre of the jet in the region after the knot K2. The fractional polarization at 15 GHz varies from $\sim 14\%$ in the centre to over 30% on either side of this region. This may be due to entrainment of the external medium into the jet after deceleration following the collision with K1 (van Breugel et al. 1985) or wavelength-independent depolarization due to the jet magnetic field orientation being roughly orthogonal to the magnetic field orientation in the surrounding lobe. However, a toroidal or helical field in the jet giving high fractional polarization at the edges may be another explanation for this feature, which is discussed in Chapter 3, where the significant transverse RM gradient across the Southern lobe in both the archival and wide-band VLA data are presented.

The second feature is a 'trough' in polarized flux in a band transverse to the Southern lobe, visible in both the 4.9 GHz and 15 GHz fractional polarization images (Figure 4.8(a) and 4.9(a)). At 15 GHz, the fractional polarization in the 'trough' is estimated to be $\leq 3\%$. What is interesting about this feature is how the lack of polarized emission in this 'trough' correlates with a large filament of Hα emission. Figures 4.8(b) and 4.9(b) show images of the polarized flux and Hα emission for both frequencies. This indicates that a random magnetic field component coupled with a high electron density within a beamwidth in this 'trough' is causing very significant depolarization, even at 15 GHz. An estimate of the magnetic field and depolarization in this region is made in Section 4.4.3.

The maps of the various parameters from the model fitting in Figures 4.4 and 4.5 do not have a high enough resolution to show the 'trough', however, the parameters change drastically downstream in the jet after this feature. This can be seen in the histogram plots of the RMs for these regions (see bottom panel of Figure 4.7). Upstream from the filament the mean (median) RM is 8.4 (7.7) rad m^{-2} with standard deviation (median absolute deviation from the median) of 10 (4.9) rad m^{-2}, whereas after the filament, the RM has a mean (median) value of -83.3 (-90.3) rad m^{-2} and much higher standard deviation (median absolute deviation) of 75.4 (40.3) rad m^{-2}. The region after this filament also has a larger amount of Faraday depolarization, as can be seen from the data and model fit in Figure 4.3. The large depolarization of $\sigma_{\rm RM} = 54 \pm 7 {\rm rad\,m^{-2}}$, is typical for this region and can explain why only a small part of this region is detected in the 1–2 GHz data (Figure 4.4). The

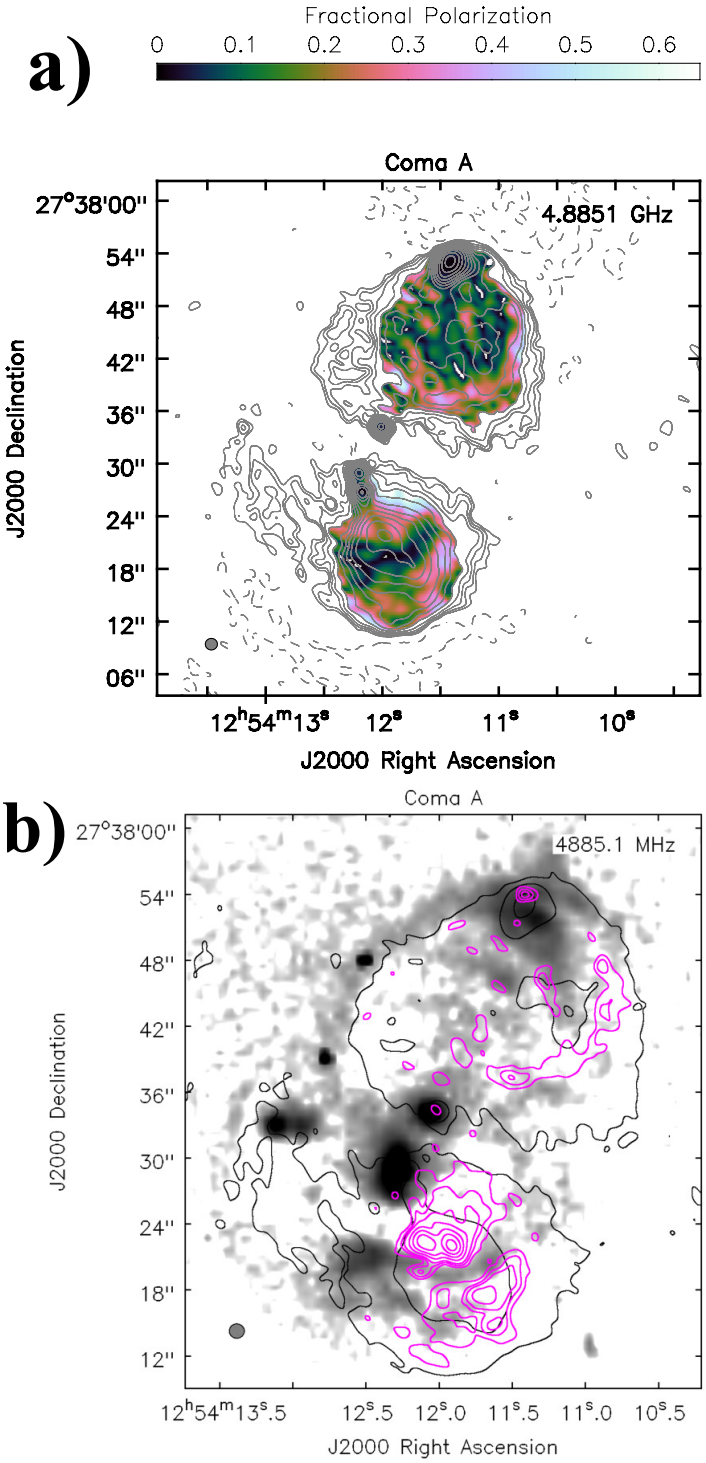

Figure 4.8: **(a)** 1.4" resolution 4.9 GHz image of Coma A from the VLA archival data. The colour image is the de-biased fractional polarization where the corresponding Stokes I intensity is greater than 1 mJy beam^{-1}at 4.9 GHz and the contours are the total Stokes I at that same frequency. The contours are given at the levels of 0.25 mJy beam^{-1} × (-1, 1, 1.41, 2, 2.83, 4, 5.66, 8, 11.31, 16, 22.63, 32, 45.25, 64, 90.51) with the negative contour dashed. **(b)** Image of Coma A showing polarized flux density in Jy beam^{-1} as purple contours with levels at 0.45 mJy beam^{-1} × (1, 1.5, 2, 3, 4, 5, 6). Stokes I contours are given in black at 27.5 mJy beam^{-1} × (0.008, 0.2, 0.6) which corresponds to 0.8, 20 and 60 percent of the peak value. The deep H α image is given in greyscale.

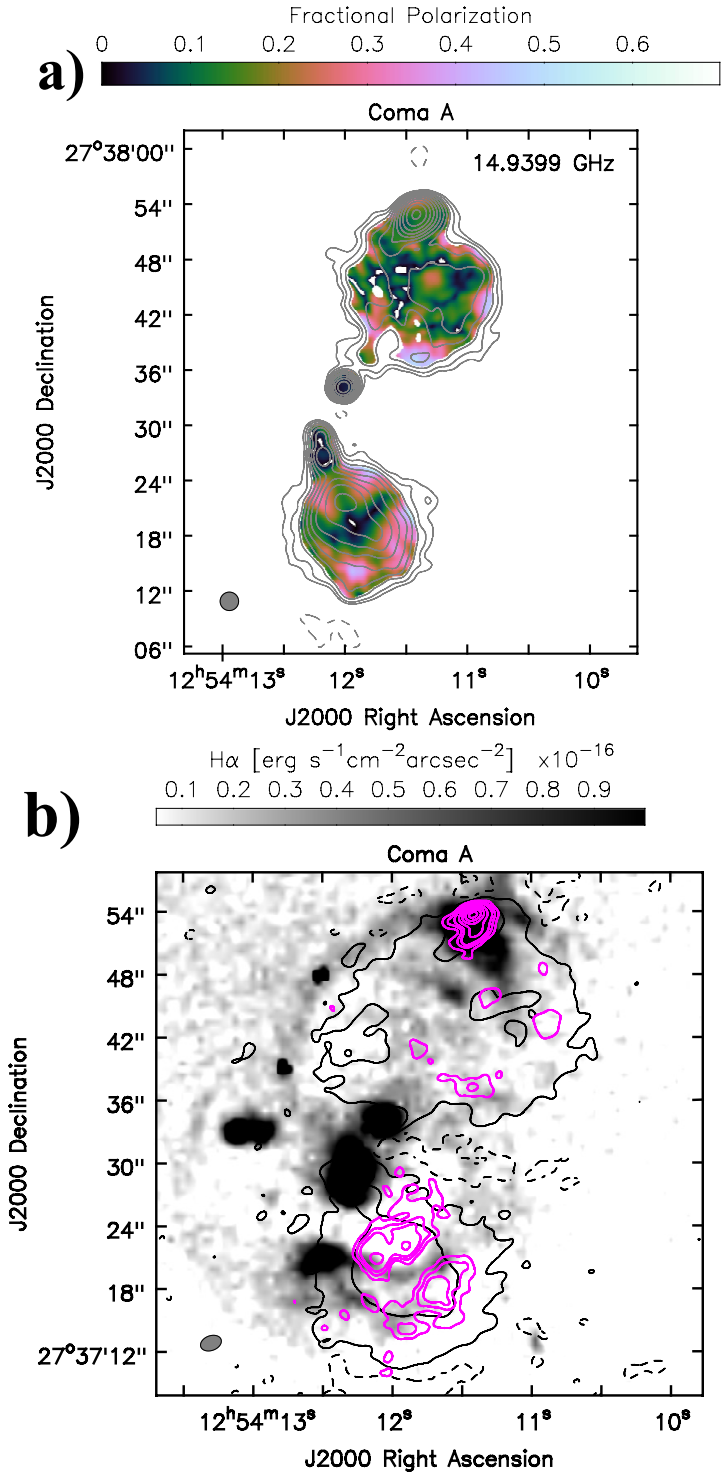

Figure 4.9: **(a)** 2" resolution 15 GHz image of Coma A from the VLA archival data. The colour image is the debiased fractional polarization at 15 GHz displaying only values where the corresponding Stokes I value is greater than 1 mJy beam^{-1}. The contours are the total Stokes I at that same frequency. The contours are given at the levels of 0.45 mJy beam^{-1} $\times$ (-1, 1, 1.41, 2, 2.83, 4, 5.66, 8, 11.31, 16, 22.63, 32) with the negative contour dashed. **(b)** Image of Coma A showing polarized flux density at 15 GHz in Jy beam^{-1} as purple contours with levels at 0.4 mJy beam^{-1} $\times$ (1, 1.5, 2, 3, 4, 5, 6, 7). Stokes I contours at the same frequency are given in black at 0.2 mJy beam^{-1} $\times$ (-1, 1 , 8, 32) with the negative contour dashed. The deep Hα image is given in greyscale.

systematically higher values of $\sigma_{\rm RM}$ after the filament can also be seen in the map of $\sigma_{\rm RM}$ values in Figure 4.5.

This drastic change in the RM downstream from the jet in the Southern lobe is an indicator that the jet/lobe has undergone a significant change in morphology or has interacted with external media. The presence of the Hα filament suggests the latter, especially as this behaviour is not mirrored in the Northern lobe. The evidence provided by Morganti et al. (2002) that the lobe is expanding into a disk of neutral gas and ionising it, creating the filaments observed, is a viable explanation for the depolarizing 'trough' feature. However, a potential complication to any models where there is a giant gas disk perpendicular to the radio jet axis (e.g. Gopal-Krishna & Wiita (2000*b*)), is the likely large inclination of the radio jet axis with respect to the line of sight (as evidenced by the fat-double shape of the lobes, and the Laing-Garrington effect). This would imply that any Hα filament related to this disk material is most likely behind the Southern lobe, unless the Southern jet has a large deflection back into some of this disk material. Further observations of the complex gas dynamics in this system are warranted.

4.4.3 Estimation of magnetic field strengths

The depolarization by the H α gas makes it challenging to detect the polarized emission. However, in some regions where there are reliable RM, $\sigma_{\rm RM}$, and H α values, an estimate of the magnetic field strength within the ionised gas shell can be made. The strong anti–correlation between the H α emission and the polarization (Figures 4.8(b) and 4.9(b)) is highly indicative that the Faraday rotation (and depolarization) is mainly occurring in the H α emitting shell around Coma A, as opposed to the extended hot X-ray emitting gas that is also likely present (Worrall et al. 2016). Therefore, this makes a combination of an estimate of the electron density from the H α data, and the Faraday rotation information from the radio data a powerful tool in directly calculating the magnetic field strengths in this region. Here the method outlined by McClure-Griffiths et al. (2010) is followed in an effort to calculate the magnetic field strengths using Hα measurements and Faraday rotation measure. The electron density is related to the H α emission through the emission measure, EM:

$$\mathrm{EM} = 2.75 \left(T/10^4\mathrm{K}\right)^{0.9} I_{\mathrm{H}\alpha} = n_0^2 f L \tag{4.3}$$

where T is the temperature of the gaseous region in Kelvin, $I_{\mathrm{H}\alpha}$ is the H α intensity in Rayleighs (1 Rayleigh = 5.7 $\times 10^{-18}\,\mathrm{erg\,cm^{-2}\,s^{-1}\,arcsec^{-2}}$ at H α), n_0 is the particle number density in cm^{-3}, f is a filling factor between 0 and 1, and L is the line of sight depth of the gaseous region in parsecs. Now using the Faraday rotation measure and solving for the average values:

$$\mathrm{RM} = 0.81 \int n_e\,(l)\, B_{\parallel} \mathrm{d}l \tag{4.4a}$$

$$\left\langle B_{\parallel} \right\rangle = 1.235 \frac{\langle \mathrm{RM} \rangle}{\int n_e\,(l)\,\mathrm{d}l} \tag{4.4b}$$

Now writing the column electron density in terms of the emission measure, EM, and assuming that the medium is fully ionised, so that $n_0 = n_e$,

$$\left\langle B_{\parallel} \right\rangle = 1.235 \frac{\langle \mathrm{RM} \rangle \sqrt{f}}{\sqrt{\mathrm{EM}\, L}} \tag{4.5}$$

The σ_{RM} parameter from Section 4.1.2 can be used to estimate the strength of the turbulent magnetic field component in the depolarizing shell of ionized gas. This can be calculated by considering the ionized gas as a collection of cells, each with their own Faraday depth and coherent magnetic field, which when combined along the line of sight gives a turbulent depolarizing screen. Using the definition of σ_{RM} given in Burn (1966), the diameter of such a cell, d, can be estimated as has been done in van Breugel et al. (1984):

$$\sigma_{\mathrm{RM}} = 0.81 n_e \langle B_{\mathrm{rand}} \rangle \sqrt{dL} \tag{4.6}$$

Similarly to Equation 4.5, this can be written in terms of the emission measure as:

$$\langle B_{\mathrm{rand}} \rangle = 1.235 \frac{\sigma_{\mathrm{RM}} \sqrt{f}}{\sqrt{\mathrm{EM}\, d}} \tag{4.7}$$

In Equation 4.6 all values except B_{rand} and d can be estimated directly from the data. A range of values for the turbulent cellsize can be estimated for each region using reasonable upper limits for B_{rand} and d. The lower limit for the cellsize occurs when the value for the magnetic field strength is at maximum within each cell; a reasonable estimate for the maximum magnetic field is the equipartition field strength of the radio lobe in that region. This assumes the H α gas is completely mixed with the outer region of the lobe and depolarizes the signal, as well as disordering the direction of any magnetic field in the lobe in that region, but maintaining the same field strength in each of the cells of

diameter d. The upper limit for d can be taken to be half of the observing beam for the highest resolution observation of Coma A that shows depolarization. van Breugel et al. (1985) have estimated the upper limit for d using this method to be 300 pc for all regions in Coma A, which yields the smallest possible $B_{\rm rand}$ for the given depolarization.

For all of the magnetic field calculations in Coma A it was assumed $T = 1 \times 10^4$ K, $L = 3.5$ kpc. The value used for f assumes full ionisation in the gas and is difficult to quantify. the value $f = 1$ would yield the highest possible magnetic field value, but this filling factor is not physically plausible. The temperature used here has been estimated in van Breugel et al. (1985) and a value of 10^4 K also ensures the gas is almost completely ionised, making the assumption that $n_0 = n_e$ a safe one. The thickness of the shell, L, was estimated by measuring the thickness of the projected shell in the H α image as seen in the filament of H α gas in the north east of the Northern lobe (Figure 4.8(b)). It must also be noted that the small Galactic contribution to the RM of $2.3 \pm 1.3\,\mathrm{rad\,m^{-2}}$ (Taylor et al. 2009) can be safely ignored due to the location of Coma A being very close to the Galactic pole, indicating little to no interference in the Faraday rotation from the local Galactic medium and making it safe to assume the vast majority of Faraday rotating medium is located in the immediate vicinity of Coma A.

4.4.3.1 Magnetic field strength in Faraday screen of Northern lobe

The Northern hotspot region shows bright H α emission and some of the 2–4 GHz polarization data for that region, particularly in the north western region of the hotspot, are reliable for fitting (see Figure 4.5). Values of $\mathrm{RM} \simeq 30\mathrm{rad\,m^{-2}}$, $\sigma_{\mathrm{RM}} \simeq 30\,\mathrm{rad\,m^{-2}}$, and $I_{\mathrm{H}\alpha} = 1.4 \times 10^{-16}$ erg cm^{-2} s^{-1}arcsec^{-2} $\equiv 24.6\,\mathrm{Rayleigh}$ were used to estimate the magnetic field in the gas. The emission measure can be calculated from the Hα intensity and temperature to be $67.65\,\mathrm{pc\,cm^{-6}}$. This led to a value of $\left\langle B_{\parallel} \right\rangle = 0.07\sqrt{f}\,\mu$G for the ordered magnetic field in the ionised shell. The random component can be estimated to be $B_{\rm rand} \geq 0.27\sqrt{f}\,\mu$G using the lower limit to the depolarizing cellsize of $d \leq 300$ pc. The smallest possible value for the cellsize d is estimated to be $d \simeq 0.008$ pc when the maximum possible magnetic field is assumed to be the equipartition estimate of 54 μG (Table 4. in van Breugel et al. 1985) for that region.

The archival data can also be useful for estimating RM and σ_{RM}, as the higher polarization fraction and range in λ^2 can give better estimates for the magnetic field strengths. Using the high frequency end of the 2–4 GHz data and the 4.9 GHz and 15 GHz archival datasets, a simple linear fit of the polarization angles was used to estimate the RM. To estimate σ_{RM}, the fractional polarization for the same hotspot region averaged over a 2" beamsize was fit with the exponential part of the depolarization model (Equation 4.1), namely:

$$p(\lambda) = p_0 \mathrm{e}^{-2\sigma_{\mathrm{RM}}^2 \lambda^4} \tag{4.8}$$

This method gave $\mathrm{RM} \simeq 180\,\mathrm{rad\,m^{-2}}$ and $\sigma_{\mathrm{RM}} \simeq 176\,\mathrm{rad\,m^{-2}}$, which are significantly higher but may better describe the hotspot environment due to the improved resolution.

Using the rotation measure values and the same value for $I_{\mathrm{H}\alpha}$, the magnetic field strengths were calculated to be: $\left\langle B_{\parallel} \right\rangle = 0.45\sqrt{f}\,\mu$G and $\langle B_{\mathrm{rand}} \rangle \geq 1.63\sqrt{f}\,\mu$G. These values are almost an order of magnitude different from the earlier attempt, however the higher frequency data shows more reliable polarization structure. These estimates may be broadly consistent with other studies (e.g. Laing et al. 2008, Guidetti et al. 2010, Bonafede et al. 2010) that commonly infer field strengths of 1 to 10 μG in the hot X-ray emitting gas phase that pervades the ambient intracluster/intragroup medium surrounding radio galaxies. In the case of Coma A, Worrall et al. (2016) argue that faint X-ray emission from thermal gas is also present, indicating a weak group atmosphere.

The random and uniform line-of-sight magnetic field strength estimates of O(1) μG suggest little or no mixing is occurring between the lobe and the surrounding gas near the Northern hotspot. However, as the exact size of the depolarizing cellsize is unknown, the random magnetic field strength cannot be precisely estimated. In Mao et al. (2008) and Gaensler (2005) a cell size of $\sim 90\,$pc is used for the Small and Large Magellanic Clouds. This value falls within the range of values estimated for d and if the conditions in the Coma A H α region are similar to the interstellar medium in the SMC and LMC the resulting turbulent magnetic field can be estimated as $0.5\,\mu$G for the 2–4 GHz results and $3\,\mu$G for the results including the archival data at higher frequencies and resolution.

4.4.3.2 Magnetic field strength in Faraday screen of Southern lobe

Another interesting region to probe is the depolarizing 'trough' feature transverse to the Southern lobe discussed in Section 4.4.1. It is difficult to estimate RM and $\sigma_{\rm RM}$ in this region as even at 15 GHz this region has no significant polarization. As the RM changes significantly in the jet downstream from this 'trough', this H α filament may be causing this. Using a typical RM value for the downstream region, $\mathrm{RM} \simeq -80\,\mathrm{rad\,m^{-2}}$. The H α intensity is measured to be $23.9\,\mathrm{Rayleigh}$; using Equation 4.3 this gives an emission measure of $65.7\,\mathrm{pc\,cm^{-6}}$. With a shell depth of 3.5 kpc, an estimate for the line-of-sight, coherent, magnetic field was calculated to be: $\left\langle B_{\parallel} \right\rangle = 0.31\,\sqrt{f}\,\mu$G.

Using the 15 GHz archival data, an estimate of $\sigma_{\rm RM}$ can be made from the turbulent depolarization model. Assuming that the fractional polarization in regions upstream and downstream from the 'trough' are very close to the intrinsic value at 15 GHz, this implies that $p_{15\,\mathrm{GHz}} \simeq p_0 \simeq 0.3$ for these regions. This is a safe assumption as the model fitting has shown that $\sigma_{\rm RM}$ is very low in the inner lobe compared to the 'trough' region. It is also assumed that the 'trough' region should have the same intrinsic polarization at zero wavelength as the regions on either side if not for strong depolarization by the H α gas. The fractional polarization in the 'trough' region at 15 GHz can be estimated to be less than 3% polarized ($p(\lambda) \lesssim 0.03$). This extremely high depolarization is indicative of internal depolarization, where the Faraday screen of H α gas is mixed with the synchrotron emitting plasma. The lower external depolarization in other parts of the jet, such as upstream in the Southern lobe being an example of external depolarization, is seen in the model fits in Figure 4.4. If the screen is spherically symmetric around the lobes than the depolarization should be uniform, if it is external. The nature of the intense depolarization in the Southern filament is therefore puzzling, but internal depolarization by mixing of the Hα gas and radio lobe is an elegant and simple way to explain this.

The following is an effort to calculate the magnetic field in this region using some constraints and an estimation of the filling factor f for this region. Assuming the H α emitting medium is mixed with the radio lobe, the filling factor f in this region that would correspond to the pressures in these two media being balanced can be estimated. This pressure balance can be calculated by equating the magnetic pressure in the lobe from equipartition

with the thermal pressure of the H α gas.

$$\frac{3}{2}n_0 kT = \frac{B_{\rm eq}^2}{8\pi}, \tag{4.9}$$

where n_0 is the particle density in cm^{-3}, k is Boltzman's constant, T is temperature in Kelvin and B is the magnetic field strength in Gauss. Using Equation 4.3 an expression for the filling factor can be derived such that:

$$f = \frac{144\pi^2 10^{24} \mathrm{EM} k^2 T^2}{4B^4 L}, \tag{4.10}$$

where EM is the emission measure from Equation 4.3 in $\mathrm{pc\,cm^{-6}}$, B is the field strength in μG and L is the length of the gaseous medium along the line of sight in parsecs. Using equipartition $B_{\rm eq} \approx 30\mu\mathrm{G}$ (van Breugel et al. 1985) and measured values for EM in the trough with temperature T and filament depth L chosen the same as before, this yields a value of $f = 1 \times 10^{-5}$ for the volume filling factor of the gas, if it is mixed with the lobe in this region as suggested by the intense depolarization. This estimated value of f is physically plausible, and can be used to calculate the lower limit for the random magnetic field strength in the depolarizing region in the southern lobe. The lower limit is achieved by taking the upper limit for the depolarizing cell size d in the region. Subbing into Equation 4.7 using the upper limit of $d = 300\mathrm{pc}$ gives a magnetic field strength of $75\,\mathrm{nG}$, however this can increase dramatically if a smaller depolarizing cell size is considered, which may be possible as a highly turbulent field could be expected in a shock ionised gas mixed with a deflected radio jet. A turbulent cell of diameter $0.1\,\mathrm{pc}$ or less would result in a magnetic field strength of O(1) $\mu\mathrm{G}$ or higher. Using the lower limit for such a depolarizing cellsize with $d \sim 10^{-4}\,\mathrm{pc}$ (van Breugel et al. 1985), the maximum possible magnetic field strength in this region is almost $130\,\mu\mathrm{G}$, over 4 times the equipartition field strength. This is however not completely implausible as such a high field strength could arise from the compression of a region of magnetic fields due to shocks. A mixing of this higher electron density medium will therefore only require a lower than equipartition magnetic field to depolarize the signal when mixed with the lobe, and allow the two to be in pressure equilibrium. However the possibility that the filament is external to the lobe is still a possibility and that a weaker $\sim 1\,\mu\mathrm{G}$ field coupled with the high electron density is causing this. One consideration though is the lack of this effect in the Northern hotspot, where the bow shock showing H α emission causes strong depolarization, however not as intensely as in the southern

region (the 15 GHz fractional polarization in the Southern region is roughly 3%, while the Northern hotspot has approximately 10–15% fractional polarization). The jet deflection and deceleration most likely has a more important part to play here, and adds another level of complexity in attempting to understand the physics of the Coma A jet and its interaction with the external medium.

In general, there are several potential reasons for the high depolarization. It may be due to a complex interaction between the lobe and the Hα filament, where mixing between the filament and the lobe has occurred or the shock-ionisation of the filament mixed with the lobe has compressed it to result in such a high magnetic field strength. Furthermore this filament is spatially correlated with a decrease in the total intensity which can be seen in the contours in Figures 4.1 and 4.9(a), and in van Breugel et al. (1985); Figure 5. It is difficult to explain what is causing this decrease as a dense obstacle should ordinarily compress and enhance the synchrotron emission. However, one possibility given by van Breugel et al. (1985) is that the interaction significantly increases the relative amount of the line-of-sight magnetic field component with respect to the perpendicular component at this location in the lobe. This would have the dual effect of decreasing the observed synchrotron emission and increasing internal Faraday rotation (and depolarization) at this location. This could be an effect from the mixing of the Hα gas with the lobe where the magnetic field in the lobe is randomised further, compared with the more ordered field upstream, creating the increase in ratio of line-of-sight magnetic field to perpendicular, particularly if the deflected jet axis lies on the plane of the sky. This appears plausible as the magnitude of the RM is at its highest downstream of the filament, indicating a stronger line of sight magnetic field component and the depolarization is very high in the filament region with $\sigma_{\mathrm{RM}} \geq 2700\,\mathrm{rad\,m^{-2}}$.

Another possibility is that there is mass entrainment in the jet, shown by the region of low polarization along the jet centre in the Southern lobe, and material has been 'dumped' in the transverse 'trough' region, which was proposed by van Breugel et al. (1985). This however is not an explanation for the high levels of Hα emission in the 'trough'/filament as no such emission is seen along the centre of the jet. The Hα filaments also extend along the entire eastern side of Coma A including the Northern lobe, where there is no evidence of mass entrainment. Therefore, the most plausible scenario is that the Hα gas shell is close to but external to the radio lobes, except in the

'trough' region of the Southern lobe, where the H α gas is mixing with the lobe plasma.

If the filling factor for the gas in and around the Northern hotspot is similar to the value estimated for the Southern filament, $f = 10^{-5}$, this would give magnetic field estimates of $\left\langle B_{\parallel} \right\rangle = 1.4\,\mathrm{nG}$ and $\langle B_{\mathrm{rand}} \rangle \geq 5.2\,\mathrm{nG}$. However, it is impossible to know if the filling factor for the gas in the Southern filament, which is presumed to be significantly interacting with the lobe medium, is similar to the filling factor for the gas in the North, which is assumed to be external to the lobe. If the filling factor of the gas is independent of whether the gas is mixed with the lobe of not, then this f value can be used for the magnetic field calculations in the Northern hotspot and lobe also.

4.5 Summary

An analysis was performed of the radio polarization structure of the twin lobed radio galaxy Coma A, using new wideband VLA observations from 1–4 GHz and also high resolution archival VLA observations at 1.4, 4.9 and 15 GHz. Large variations in the degree of polarization were seen across the lobes and in conjunction with deep Hα imaging, a strong anti-correlation between observed polarized flux and H α was seen. The large scale arcs and filaments of Hα were consistent with the picture that the radio lobes were expanding into a region of gas, such as a large scale gas disk, placed in the IGM by recent merger activity in the Coma A host galaxy.

It was found that the polarization structure of the lobes matched a scenario where a Faraday screen of ionised gas is hugging the lobes, causing significant depolarization in places with significant diffuse Hα. Employing *QU* model fitting on the wideband data allowed for fitting of the depolarization and showed the spectra agreed well for a situation with a Faraday screen around the source, and to calculate the rotation measure and depolarization accurately. In particularly a strong depolarizing transverse "trough" of depolarization is aligned very well with a strong Hα filament. Using estimates of the depolarization in this region and the fluxes of the Hα direct calculations of the magnetic field strengths in the Southern lobe could be made.

For the large scale Southern lobe using the results from the QU fitting, the magnetic field strengths in the Faraday screen of Hα gas around the lobe were

estimated to be $< 1\,\mu$G. The region of intense depolarization spatially correllated with a Hα filament is strong evidence that the Hα gas is mixing with the radio-plasma of the lobes, which in turn causes the significant depolarization. When this "mixing" between the radio plasma and Hα gas is presumed estimates of the filling factor and magnetic field can be made with a lower limit of roughly 0.075 μG but with an upper limit of the same order field strength as the lobe itself. This is interesting, as such interactions provide more evidence of the complex ways jets interact with the environment around them, providing some "feedback" on the local environment; this can both inhibit star formation in galaxies by removing cold gas from the environment and also modify the evolution of radio galaxies aiding in creating the diverse "Zoo" of radio galaxy morphologies.

Chapter 5

Faraday Rotation Measure study of the magnetic field environments of 3C 433 and 3C 382

In an effort to replicate the detailed multiwavelegth analysis of Coma A done previously, further wideband observations of Radio Loud AGN with interesting structures were obtained using the VLA in the 1–2 and 2–4 GHz ranges. Both 3C 433 and 3C 382 were observed. These are bright radio galaxies with impressive and unusual features in the radio Stokes I and polarization images available in the literature (e.g. van Breugel et al. 1983, Black et al. 1992). The original aims of these observations were to enable a detailed analysis into the polarization and Faraday depth structure of these galaxies, exploiting the wideband capabilities of the upgraded VLA, and in conjunction with information on the X-ray, Hα and HI environments from literature try to ascertain if the lobes of these galaxies are being affected by external media, or vice versa. The VLA observations are outlined in Table 5.1.

Deep Hα observations using the Gran Telescopio Canarias (GTC) were intended to be used in conjunction with the radio polarization observations, in an effort to match regions with depolarization to regions of Hα emission. In addition, HI spectral line observations were taken as part of the L–band observations, where a segment of the bandwidth was dedicated to narrow channel spectral line observations, in order to identify regions with neutral hydrogen. These observations have been taken, however due to time constraints on behalf of our optical and spectral line collaborator, they are not

Table 5.1: Table outlining the VLA observations of 3C 433 and 3C 382. All observations were done in the VLA B configuration and were part of the same project, 17B-016.

Source Name	ν_1 MHz	ν_2 MHz	$\Delta\nu$ MHz	Date	t hrs
3C 433	1008	1968	1	2017 Oct 24	1.3
	1988	4012	2	2017 Sep 19	1.3
3C 382	1008	1968	1	2017 Sep 20	1.3
	1988	4012	1	2013 Sep 17	1.3

calibrated and available for analysis as part of this thesis. Our intention is to include them in a final analysis for publication.

5.1 Rotation Measure mapping and Polarization Model Fitting Procedure

To better understand the rotation measures of these AGN at higher resolutions, rotation measure maps were made using the S-band data only, to investigate the RM, intrinsic polarization angle, and fractional polarization at a higher resolution. This is essentially the same procedure as was done to the wideband observations of NGC 6251, Coma A and IC 4296 in Chapter 3. Using a frequency bin width of 128 MHz, 16 images were made in Stokes I, Q and U between 2 and 4 GHz, with the visibility data tapered and images smoothed to a common resolution. The rotation measure maps were made by fitting the data for χ versus λ^2 using the CASA task *rmfit*. The maps were blanked when the error in the polarization angle was more than 3 degrees, and furthermore RM values were blanked if the associated error in the RM from the fitting exceeded a specified value. This also resulted in the calculation of the intrinsic polarization angles χ_0. For each source a de-biased fractional polarization map was also made, using images of the polarized intensity made with the standard polarisation bias correction applied in CASA (e.g. VLA memo 161, (Leahy & Fernini 1989)). This allows the fractional polarization map to be blanked using Stokes I, allowing regions which may feature significant depolarization within the lobes to be identified, as was done using the high resolution archival data for Coma A in Chapter 4.

Given the large range of λ^2 values and the high spectral resolution of the data,

results from the calibrated data using rotation measure synthesis (Brentjens & de Bruyn 2005) across the entire 1–4 GHz range can provide insight into the distribution of the Faraday depth along the line of sight. Images in I, Q and U were made using a fine spectral resolution of 2 MHz bandwidth per image for the 1–2 GHz data and 8 MHz for the 2–4 GHz data. The visibility data had an appropriate *uv* taper applied and the resulting images were all smoothed to a common convolving beam. The rotation measure synthesis was performed using the PYTHON routine *pyrmsynth* [1]. An RMCLEAN (Heald et al. 2009) was also performed on the data in order to deconvolve the true Faraday spectrum from the data, given the inherently incomplete sampling of λ^2.

Polarization model fits (O'Sullivan et al. 2012) were also performed for various features in the sources, using the image data created for the RM synthesis process. Features such as the hotspots, the various knots and also regions in the extended, more diffuse parts of the jets could have their polarization spectra modelled and analysed in detail. This was done by extracting spectra of Stokes I, Q and U using PYTHON routines, including background root-mean-squared values for each Stokes parameter from the image, to estimate the errors of the fluxes. The fractional $q = \frac{Q}{I}$ and $u = \frac{U}{I}$ were calculated and fitted as part of this procedure, in order to remove the effects of spectral index from the data. The data were fitted according to Equation 2.61 for various numbers of components and Faraday screens. The spectra were then fitted for various models using a PYTHON implementation of *multinest* using Bayesian methods for converging on the best fit using existing code[2]. This is a similar method to that used in Anderson et al. (2019), where fits were done on unresolved blazar spectra using Australia Telescope Compact Array (ATCA) data. The best fit was determined by the fit which had the lowest Bayesian information criterion (BIC) but also used relatively few free parameters for fitting, so as to not over-interpret any small fluctuations in the spectra.

5.2 3C 433

3C 433 is a radio galaxy at red shift, $z = 0.1016$ (Hewitt & Burbidge 1991). The structure and morphology are discussed in detail in van Breugel et al.

[1] `https://github.com/mrbell/pyrmsynth`
[2] `https://github.com/crpurcell/RM-tools`

(1983), with some interesting conclusions as to the origin of the unusual jet shape, suggesting a possible merger event having occurred with the host galaxy changing the orientation of the jet, or a precessing jet. Looking at the radio intensity contour map in Figure 5.1, the Southern jet has the typical appearance of an FR II radio jet, with a large bright lobe and hotspot toward the jet termination point. The Northern, fainter jet has a more complex appearance similar to a faint FR I like radio jet. However on both the Northern and Southern jets, large trails of diffuse emission are seen to the East and West of the Northern and Southern jets, respectively; this is particularly prominent in the Northern jet, with a "wing" of emission featuring a bright knot with a slightly higher spectral index. This peculiar morphology has labelled 3C 433 as a Hybrid Morphology Radio Source (HYMORS) (Miller & Brandt 2009), and 'X' or 'Z' shaped radio galaxy (XRG/ZRG)(Gopal-Krishna et al. 2012), whose unusual appearance has been attributed to the jet propagating into an off-axis super-disk of neutral gas (Gopal-Krishna & Wiita 2000*b*) around the host galaxy, most likely originating from a merger event between the host galaxy and another, a theory common to the origin of the circumgalactic gas in Coma A (Morganti et al. 2002). Further evidence of a recent merger is that there is a reported UV excess in the host galaxy (Wills et al. 2002), which is evidence of recent star formation, most likely due to the merger. The interacting galaxy has not been clearly identified, however two galaxies are located 10" to the North-East from the 3C 433 host galaxy, one of which, named 2MASX J21234458+2504272 has a very close redshift of $z = 0.102$ (Hernán-Caballero et al. 2016) and a similar angular size, making this a likely companion for 3C 433. The other galaxy to the North, as well as another galaxy $\sim$17 projected kpc to the South-West, have an unclear nature as to their relationship with 3C 433.

Another possible origin for the appearance of this source is that due to a merger event in the host, a reorientation of the jet axis has occurred, which creates the 'wings' of emission indicative of previous locations of the jet, as proposed in van Breugel et al. (1983). There are many possibilities and theories which could explain this morphology, however the environment around the radio galaxy is likely to play an important role.

Gopal-Krishna et al. (2012) use 3C 433 as an example of a possible jet-shell interaction, where a recent merger in the galaxy has expelled large scale shells of gas. The powerful FR II jet bores through the shell, however some jet material is deflected by the shell, whose rotation causes the trailing wings in

opposite directions. This is supported by multiwavelength studies, in particular the presence of cold denser gas surrounding the lobes in 3C 433, especially in the Southern lobe. This would provide an explanation for the unusual shape of the jet and lobe structure, indicating the jet has been contorted and slowed down by the cold, dense surrounding medium. The presence of atomic hydrogen around the source was first reported in Mirabel (1989); indeed, the Southern lobe and hotspot show evidence of HI absorption, as can be seen in more detail in Morganti et al. (2003), with an estimated $5\times10^8 M_\odot$ mass of neutral gas surrounding the Southern lobe and located over a projected distance of 60 kpc from the host galaxy. Furthermore, evidence of interaction between this neutral gas and the highly energetic lobe plasma can be seen in the images of diffuse X-ray emission around the Southern lobe, also seen in Figure 1.(a) of Miller & Brandt (2009).

Previously published radio images of this source include maps at 1.48 and 4.885, and 8.4 GHz in van Breugel et al. (1983) and Black et al. (1992) respectively, the latter providing some insight into the polarization structure as the integrated RM of $\sim -70\,\mathrm{rad\,m^{-2}}$ (Simard-Normandin et al. 1981, Taylor et al. 2009) will only affect the polarization angle slightly at 8.4 GHz corresponding to 0.00127 $\mathrm{m^2}$ in wavelength squared and about 5° of rotation.

The wideband VLA observations at L (1–2 GHz) and S (2–4 GHz) bands analysed here give an almost continuous coverage in wavelength from 30 to 7.5 cm. Such observations over a wide wavelength range and with a well sampled spectral axis allow for the employment of modern polarization analysis techniques such as RM synthesis (Brentjens & de Bruyn 2005) and *QU* model fitting (O'Sullivan et al. 2012). This enables not only accurate determination of the Faraday rotation measures, but also the distribution of the Faraday depth along the line of sight and whether synchrotron emitting components of different polarization angle, fraction and rotation measure are combining together within the observing beam. These tools are useful for investigating how the synchrotron emitting lobe plasma is interacting with the presumed external, dense gaseous medium on scales smaller then the interferometer can resolve at such wavelengths.

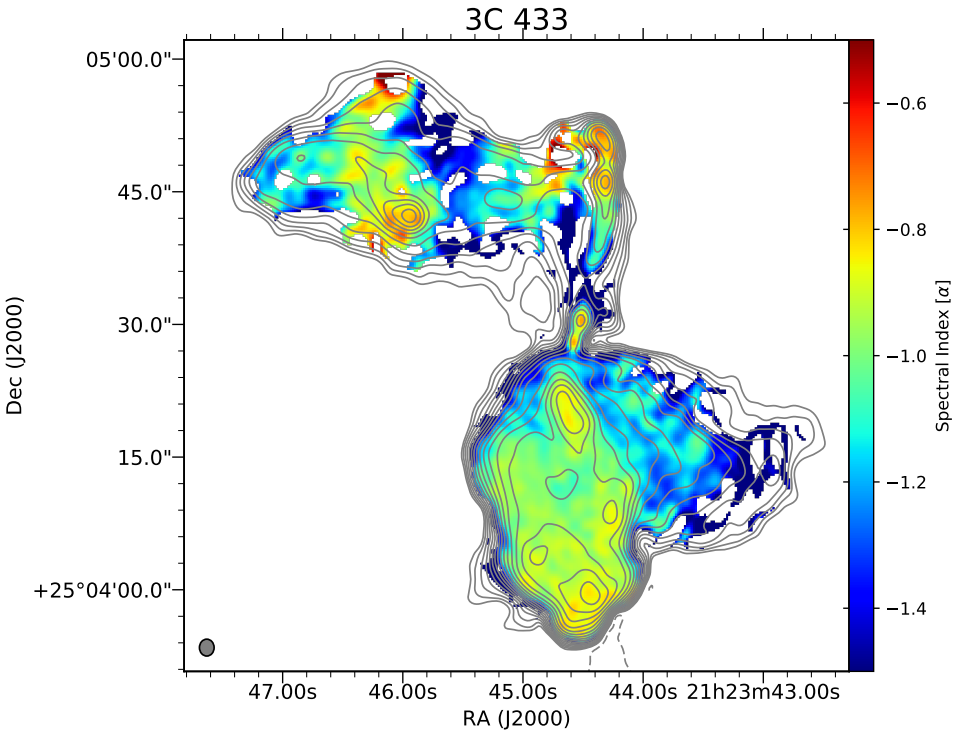

Figure 5.1: Spectral index and contour map of 3C 433 made using a multi-term multifrequency synthesis technique. The image has been made using super-uniform weighting to ensure the best possible resolution, the convolving beam is 1.91×1.65" at 0.4°. The spectral index map is given in the colour scale with the values blanked if the error in the calculated spectral index exceeds 0.15, Stokes I contours at 3 GHz are given, with levels starting at 0.6 mJy beam^{-1} and increasing by factors of $\sqrt{2}$, with a peak of 126.3 mJy beam^{-1} in the Southern hotspot feature.

5.2.1 Observations and data reduction

The observations of 3C 433 were taken in 2017, with the S-Band data observed on 19 September 2017, and the L-band data on 24 October 2017, with a total integration time of approximately 1.3 hours per observation. The flux density calibrator was 3C 286 which also acted as the bandpass and polarization angle calibrator. The phase calibrator was the nearby source J2115+2933 (B2 2113+29), which also acted as the polarization leakage calibrator due to its low polarization and the sufficient parallactic angle coverage during the observation. Both the datasets were calibrated using standard procedures in CASA with the RFI flagged using the *tfcrop* and *rflag* flagging modes in CASA. The 3C 433 data were binned into 8 MHz channels for S-Band and 2 MHz channels for L-Band and over 30 seconds in time, in an effort to speed up the imaging and self calibration. The data were self calibrated with three

iterations of phase only calibration and one iteration of phase and amplitude calibration. The self calibration was done across the whole band using a multi-term multi-frequency synthesis method. This method produces an image with high resolution and dynamic range, with an accompanying spectral index map, presented in Figure 5.1 for the 2–4 GHz S band data.

To analyse the rotation measure maps at a higher resolution, the S-band data were imaged in 128 MHz bins in Stokes I, Q and U, with the visibility data tapered and all images smoothed to a common convolving beam of 3.02×2.61" at 4°. These images were used to fit for χ versus λ^2, to produce RM and χ_0 maps of 3C 433, shown in Figure 5.2 and 5.3(left panel). The values were blanked again according to the error in the calculated RM, with values having RM errors higher than 15 rad m^{-2} being blanked. The fractional polarization map at 3 GHz is shown in Figure 5.3(right panel) which bridges the gap between known 20cm and 6cm images from van Breugel et al. (1983).

To analyse the polarization data using RM synthesis and *QU* fitting, cubes of the Stokes I, Q and U data were made. The L band data were imaged in 2 MHz channels and the S band data were imaged in 8 MHz channels, as polarization model fits and rotation measure synthesis are done in λ^2 space, making narrow imaging channels at higher frequencies less necessary. The data were imaged with a uv-taper on the visibility data to ensure a similar resolution showing emission at similar scales from 1–4 GHz, with the final images smoothed to a common restoring beam of 6.4×5.4" at an angle of 2.7°, ensuring the extracted spectra of I, Q, U were consistent.

5.2.2 Results

The results of the polarization analysis into 3C 433 show the polarization structure over a wide bandwidth for the source, especially in the 1–4 GHz ranges, of which little has been published. Rotation measure mapping using χ versus λ^2 shows the RM structure at a high resolution, while RM synthesis and *QU* fitting exploit the entire bandwidth available in an effort to look at more subtle effects in the Faraday depth.

5.2.2.1 Rotation measure mapping

Figure 5.2 shows a rotation measure map of 3C 433 made using the 2–4 GHz data only, to provide a rotation measure image with a higher resolution. The calculated rotation measure map and intrinsic polarization angle map are presented in Figures 5.2 and 5.3 respectively with a resolution of 3.02×2.61" at 4°, with the RM shown in colour scale in the first and the intrinsic polarization angles plotted as vectors in the second. A central frequency of 3 GHz was chosen for the overlaid Stokes I contours. Such rotation measure maps of this source have not been published previously in literature, making these and the following analyses useful tools in the continuing efforts to analyse the polarization structures of such hybrid sources.

The overall structure of the rotation measure is quite patchy. The Southern lobe features slightly higher values on the Eastern side and an unusual "ridge" where the values change quite suddenly from West to East in the centre just above the hotspot. This ridge has a lower overall polarization, as can be seen in Figure 5.3 with a long filament of low polarization ($< 5\%$) tracing the ridge. This low polarization may be leading to the ridge in the RM values, however the large spectral range and precise measurement of the RM make this less likely. Comparing with the high resolution Stokes I map in Figure 5.1, the ridge is aligned with the lower intensity region that bisects the Southern lobe parallel to the left edge of the lobe, in a position angle of $\simeq 30°$ from North. Similar features have been observed in broadband radio-polarimetric observations of Fornax A in Anderson et al. (2018), with their origins likely being an interaction between the radio lobe and the external medium; this is quite likely given the known presence of a diffuse X-ray environment in the Southern lobe of 3C 433 and the presence of dense neutral gas.

The Northern jet has a similar patchy structure with the RM having slightly different alternating values for each of the knots of the jet that are unresolved in the total intensity here. The extension to the East shows no particular structure in the RM, only the knot in this extension features a slightly higher RM than the rest of the Northern jet.

The intrinsic polarization angle distribution could also be calculated from the RM mapping process, this map is given in Figure 5.3. The direction of the vectors is consistent with those in the high frequency maps in Black et al. (1992) where the effects of Faraday rotation are expected to be minimal as

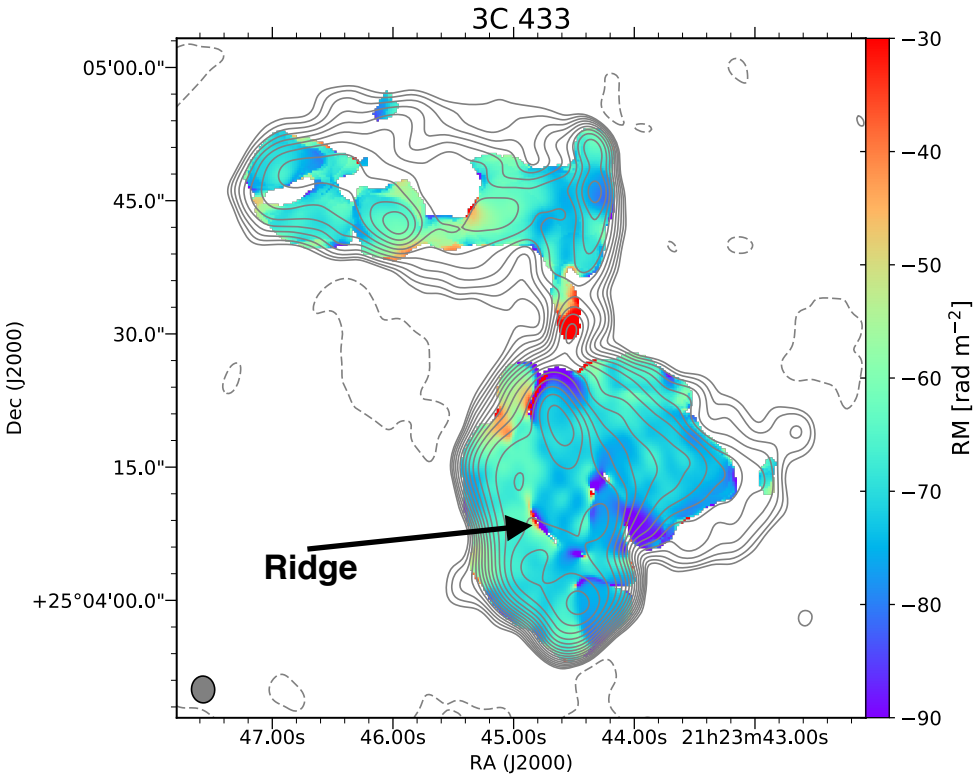

Figure 5.2: Rotation measure map and contour map of 3C 433 made by fitting polarization angle χ versus λ^2 for 16 frequencies between 2 and 4 GHz. The common convolving beam is 3.02×2.61" at 4°. The RM map is given in the colour scale with the values blanked if the error in the calculated rotation measure exceeds 3 rad m^{-2}, Stokes I contours at 3 GHz are given, with levels starting at 1.25 mJy beam^{-1} and increasing by factors of $\sqrt{2}$, with a negative contour given at -1.25 mJy beam^{-1}

with a wavelength squared of $3.6\,\mathrm{cm}^2 \equiv 0.001296\,\mathrm{m}^2$, an extreme value of $\sim -90\,\mathrm{rad\,m}^{-2}$ gives a change in polarization angle of only $\mathrm{RM}\lambda^2 \simeq -7°$.

The results from the rotation measure synthesis using the entire spectral range give supporting and encouraging results also. The synthesis was performed over a range of ϕ from -1000 to 1000 rad m^{-2} with a $\delta\phi$ of 0.2 rad m^{-2} to produce the figures and plots shown here. A plot of the rotation measure transfer function (RMTF) is given in Figure 5.4; this is equivalent to the "Dirty Beam" in synthesis imaging deconvolution.

The RMCLEAN reduced the effects of the sidelobes greatly. In Figure 5.5, $F(\phi)$ is plotted with the CLEANed spectrum in black, the dirty spectrum in dashed green, and the clean components from the deconvolution shown as blue vertical bars. The fitted Gaussian to the RMTF has a FWHM of 44 rad m^{-2}, which is close to the maximum theoretical resolution of 42 rad m^{-2}. The error

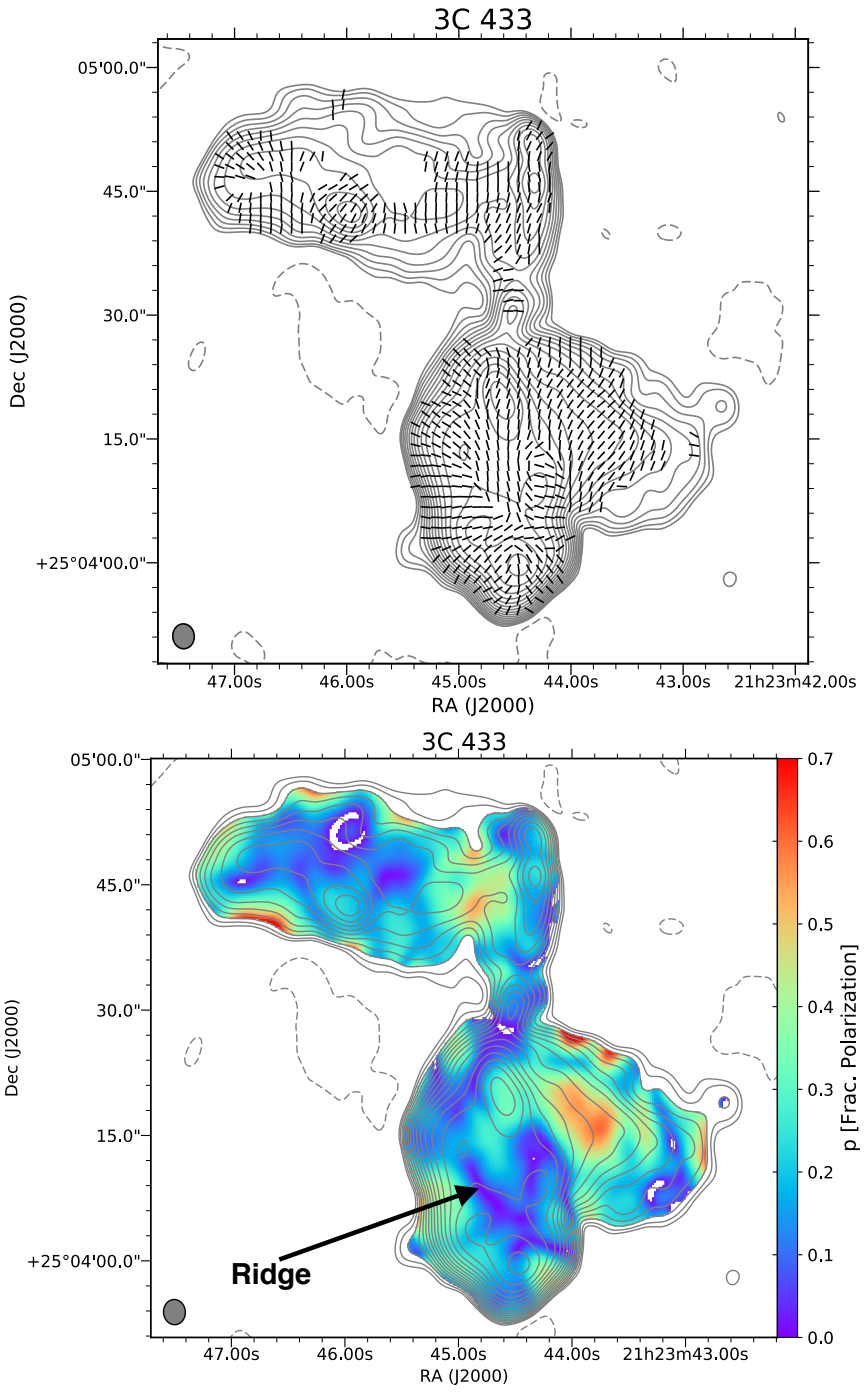

Figure 5.3: **Top:** The intrinsic polarization angle χ_0 is shown in the vectors, this map was made parallel to the RM map in in Figure 5.2. The convolving beam is 3.02×2.61" at 4°. The Stokes I contours at 3 GHz are also given, with levels starting at 1.25 mJy beam^{-1} and increasing be factors of $\sqrt{2}$, with a negative contour given at -1.25 mJy beam^{-1}. **Bottom:** Debiased fractional polarization map of 3C 433 at 3 GHz. Values are plotted for which the Stokes I > 2.5 mJy beam^{-1}. The contours and common convolving beam are identical to the top panel.

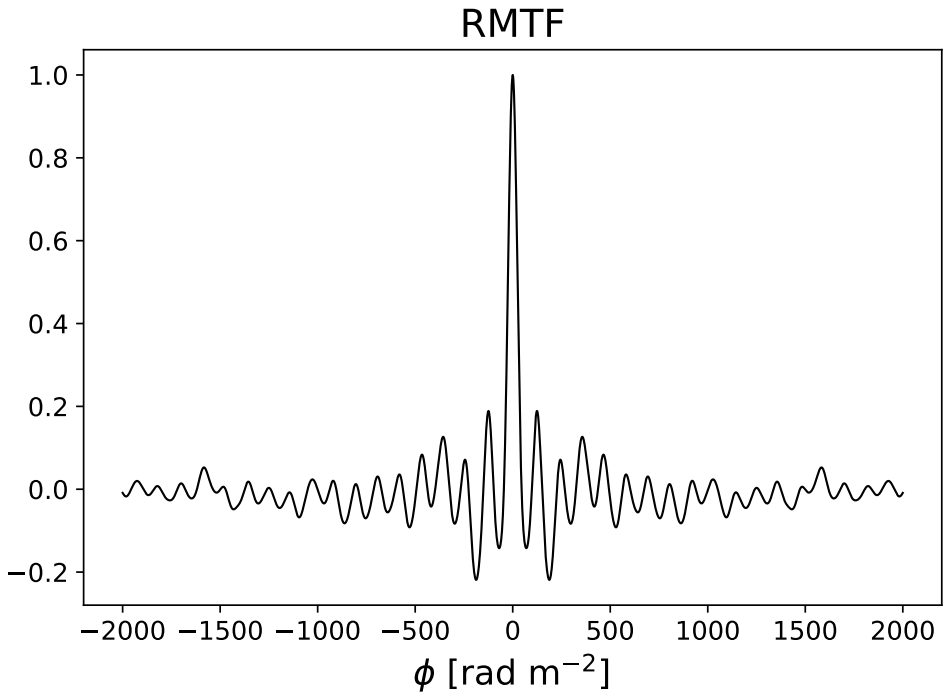

Figure 5.4: The RMTF for the 3C 433 data in the 1–4 GHz range. The FWHM of the central peak is 42 rad m^{-2}

in the $\phi_{\rm peak}$ was determined by Brentjens & de Bruyn (2005) to be the FWHM of the central peak in the RMTF divided by twice the signal to noise ratio of the peak. In this case, having a deconvolved spectrum will increase the signal-to-noise ratio and reduce the error in the $\phi_{\rm peak}$ RM value. As the produced $\phi_{\rm peak}$ map only includes points whose signal to noise radio exceeds 5σ the maximum error in the $\phi_{\rm peak}$ is given by $\Delta\phi_{\rm peak} = \frac{\rm FWHM_{RMTF}}{2\sigma} = \frac{44\,{\rm rad\,m^{-2}}}{10} = 4.4\,{\rm rad\,m^{-2}}$. This is the estimated maximum error for all peak Faraday depth values given in Figure 5.19.

The map of $\phi_{\rm peak}$ of $F(\phi)$ in Figure 5.6 gives values and RM structures very similar to those produced in the χ versus λ^2 fitting procedure made using the 2–4 GHz data only, with the 'ridge' in the southern lobe preserved. However, the map made using the RM synthesis has an inherently lower resolution, as the resolution of these images is limited to the resolution of the lowest frequency close to 1 GHz.

Plots of the spectra of $F(\phi)$ for various regions in Figure 5.6 are plotted in Figure 5.7, the spectra show that the RM structure in most regions is dominated by a single Faraday-thin component, however the deconvolution reveals some possible structure near this single component. Given the limited

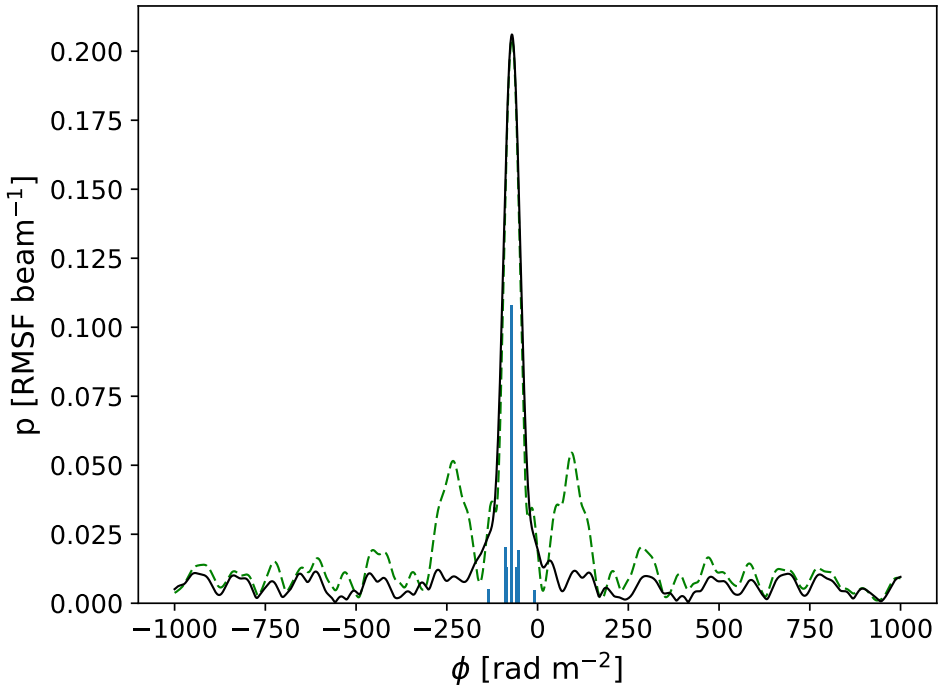

Figure 5.5: $F(\phi)$ for a high polarized intensity region in the Southern lobe, the dirty rotation measure synthesis spectrum is plotted in dashed green, the deconvolved clean spectrum is plotted in black with the clean components plotted as vertical blue bars.

resolution in $F(\phi)$, with a fitted Gaussian of FWHM 44 rad m^{-2}, which is close to the maximum theoretical resolution of 42 rad m^{-2}, the extended structure in ϕ is hard to verify. This is a situation where QU model fitting can help give a more detailed view of the polarization data.

5.2.2.2 *QU* model fitting

Model fitting of individual regions in the source can be advantageous, as it may reveal more subtle effects in the Faraday depth, such as multiple unresolved polarized components or extended structure in the RM, which may not be well resolved given the maximum resolution of the rotation measure synthesis. The best quality fit can infer the existence of structure, while also retrieving valuable measures of the overall depolarization by external screens, whose existence is implied by the presence of hydrogen external to the lobe. Strong depolarization could be evidence of mixing between the gas-shell and the radio jet as the synchrotron emitting plasma mixing with the Faraday rotating medium would cause much stronger internal depolarization.

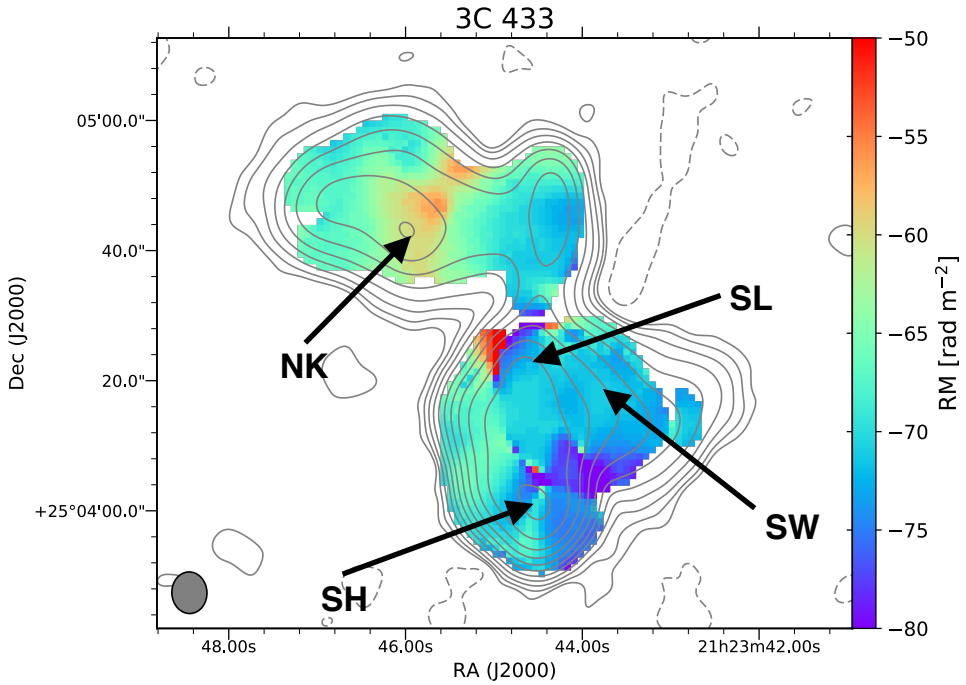

Figure 5.6: Rotation measure map featuring the $\phi_{\rm peak}$ RM value from the calculated $F(\phi)$ for each cell in the map using a frequency range of 1–4 GHz. Plotted are RM values for which the total polarized flux exceeds 5σ. The contours overlaid are for the L band data using a multi-frequency synthesis method centred on 1.4875 GHz and a tapered resolution of 6.4×5.4" at angle of 2.7 degrees ,the same as the $\phi_{\rm peak}$ map. Levels start at 1.25 mJy/beam and increase in factors of 2 with a negative contour at -1.25 mJy/beam

Figure 5.9 shows a model fit to a region around the Southern hotspot, which is labelled 'SH' in Figure 5.6. The plotted fractional polarization shows a "bow shape" with the fractional polarization decreasing towards both long and short λ^2. This is a clear indicator that more than a simple single RM component with some external depolarization is present, as was the case for the lobes of Coma A in Chapter 4. Both internal and external depolarization models were tested, but the model that best described the data with the least number of variables was a model with two polarized components and a common external depolarizing screen. The parameters of these components are laid out in Table 5.2. When the screen depolarization term is independently calculated for each component, the RM and χ_0 values for each component are quite similar to the case with a common depolarization term for each component; only the p_0 values differ by a few percent. This two component model fit for a common Faraday screen is given in Figure 5.9. As the plots for the model with individual depolarization terms for each component and those for a model with a common depolarization term are indistinguishable by eye, given that

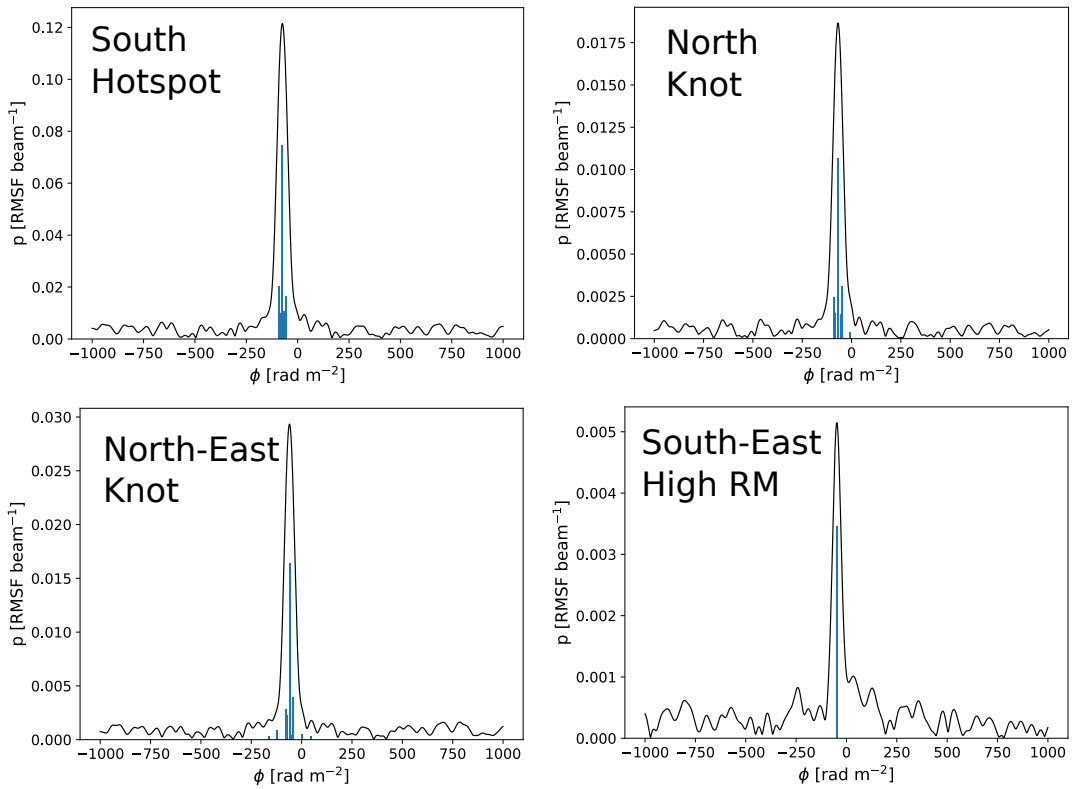

Figure 5.7: Plots of the RMCLEANed Faraday spectra for various regions in 3C 433, the location of clean components with intensities given as blue vertical lines . **Top left:** The distribution of Faraday depth along the line of sight for the Southern Hotspot which peaks at $-74 \pm 1\,\mathrm{rad\,m^{-2}}$. **Top right:** Polarized flux versus Faraday depth for the Northern knot peaking at $-72 \pm 2\,\mathrm{rad\,m^{-2}}$. **Bottom Left:** Similar plot as previous, but for the higher intensity knot feature in the North-Eastern extension with $\phi_{\mathrm{peak}} = -60 \pm 2\,\mathrm{rad\,m^{-2}}$. **Bottom Right:** The Faraday spectrum for the high RM region in the upper left section of the Southern lobe with $\phi_{\mathrm{peak}} = -48 \pm 3\,\mathrm{rad\,m^{-2}}$.

the fitting parameters from Table 5.2 are very similar only the plot for the model with a common depolarization term is shown.

From a physical standpoint this model makes sense, given our previous knowledge of 3C 433. Looking at the hotspot in the high resolution 8.4 GHz polarization maps in Black et al. (1992) and reproduced in Figure 5.8, two individual features can be made out in the Southern hotspot region, labelled S4 and S5 in Figure 5.8. Given the inferred presence of a considerable amount of neutral gas (Morganti et al. 2003) and diffuse X-ray emission, probably from excited gas (Miller & Brandt 2009) surrounding the Southern lobe, it is safe to assume a screen depolarization term will be affecting all the

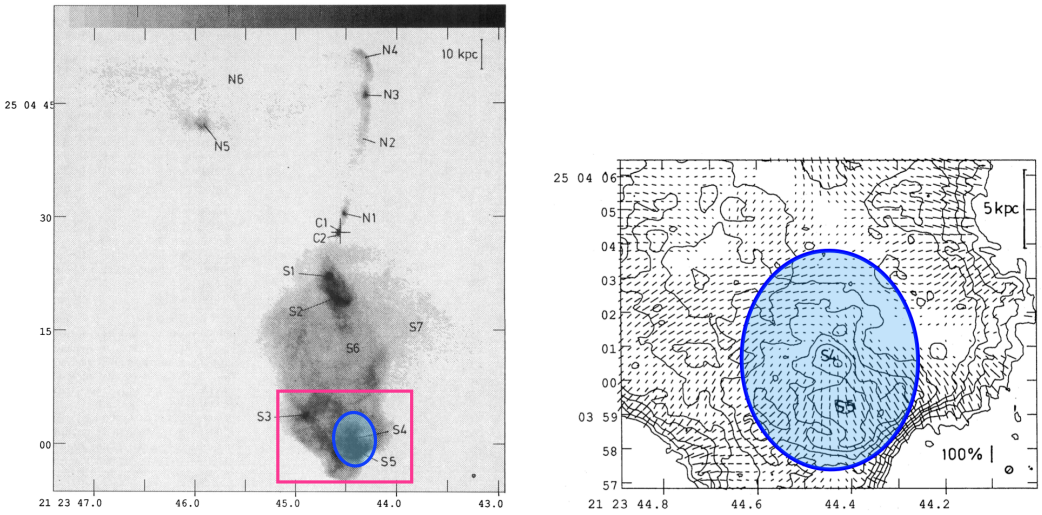

Figure 5.8: Maps of 3C 433 taken from Black et al. (1992) **Left panel:** A greyscale 0.25" high resolution map of 3C 433 with features labelled. The red box indicates the frame of the right panel, the blue ellipse is the beamsize of the wideband polarization data used in this study. **Right Panel:** The Southern lobe and hotspot of 3C 433 featuring the Stokes I contours and polarization vectors at 8.4 GHz which is taken from Black et al. (1992), note the locations of the 'S4' and 'S5' components. the contour levels stated in Black et al. (1992) are (-3, 3, 6, 10, 15, 20, 30, 40, 50, 60, 80, 100)$\times 15\,\mu$Jy beam^{-1}. The blue ellipse is the convolving beam and resolution of the wide-band polarimetric data, showing how these features would be unresolved at the lower resolution.

Table 5.2: Table outlining the *QU* fitting parameters for a 2 component fit with common Burn depolarization term to the 3C 433 Southern hotspot region and for 2 component fit with individual depolarization terms.

Model type	Comp no.	p_0 %	χ_0 °	RM rad m^{-2}	$\sigma_{\rm RM}$ rad m^{-2}
2 RM components, Common $\sigma_{\rm RM}$	1	8.8 ± 0.2	39 ± 1	-79.4±0.3	5.5±0.2
	2	6.2 ± 0.3	-5 ± 1	-70.4±0.4	5.5±0.2
2 RM components, Individual $\sigma_{\rm RM}$	1	10.9 ± 0.3	45 ± 1	-78.1±0.2	6.2±0.1
	2	8.7 ± 0.3	-11 ± 1	-72.5±0.2	6.4±0.2

polarization measurements and fits in any region in the Southern lobe.

The polarization angles are also quite consistent with the plotted angles in Figure 5.8 when comparing with the model for a common depolarization term. Looking at the upper S4 component with the polarization vectors aligned roughly vertically, this most likely corresponds to the second component with $\chi_{02} = -5°$, while the S5 component with angles almost perpendicular to the edge of the lobe corresponds to the component with $\chi_{01} = 39°$. However since the images are uncorrected for Faraday rotation, the angles may differ by a

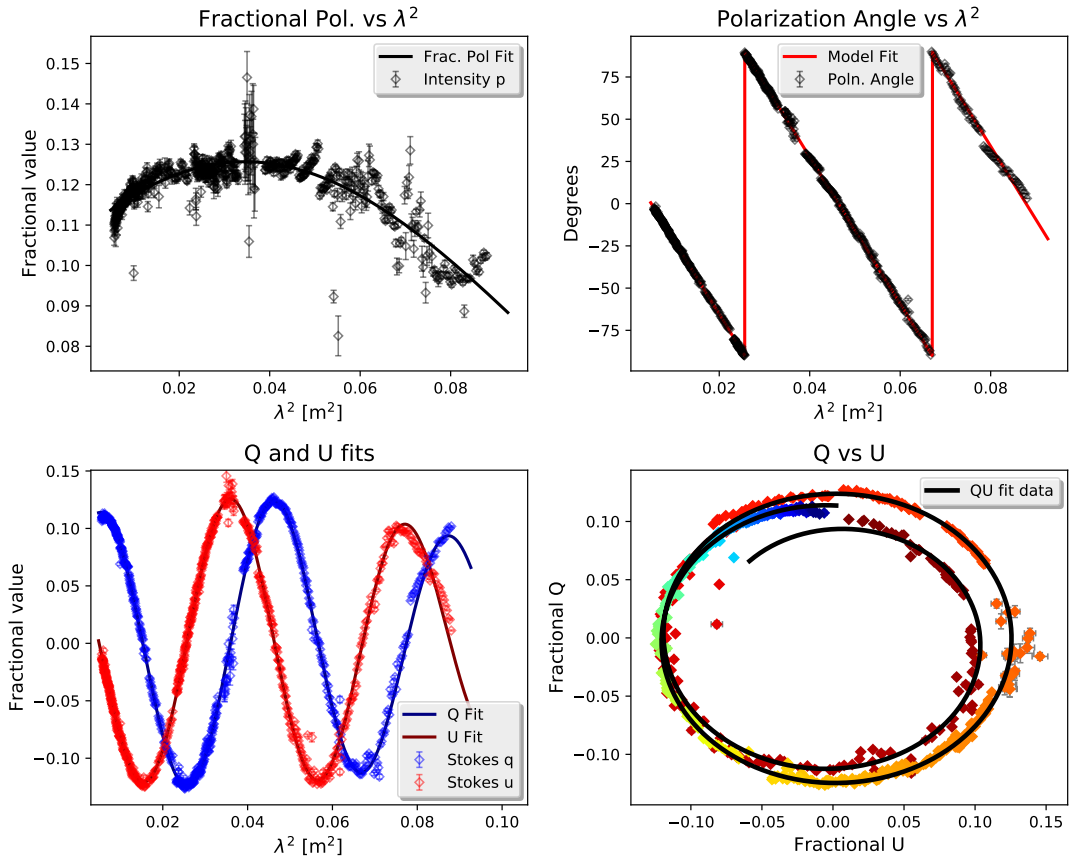

Figure 5.9: Summary of model fit for the Southern hotspot of 3C 433 for a model with 2 RM components with a common depolarization term.**Top Left:** Plot of the fractional polarization versus the wavelength squared with the calculated fractional polarization for the model fit overlaid as a solid black line. **Bottom Left:** Plots of the observed fractional Stokes Q (blue) and Stokes U (red) against wavelength squared with the calculated model fits overlaid. **Top Right:** Plot of the measured polarization angles against wavelength squared in black with the calculated model fit overlaid in red. **Bottom Right:** Plot of the fractional Stokes Q versus U with fit overlaid, the color of the points from red to blue indicates the observed frequency from 1–4 GHz

few degrees. Having access to previously published images of the source structure at high resolutions in the literature provides an interesting proof-of-concept for the *QU* fitting, as it can distinguish unresolved features spectrally. Unfortunately, the fractional polarization and rotation measures of the individual knots in the high resolution data are not given, however the overall rotation measures of the hotspot region agree with those from the map in Figure 5.2. The fractional polarizations at 1.2" and 4.9 GHz in van Breugel et al. (1983) show a very high ($\geq 40\%$) fractional polarization just to the right

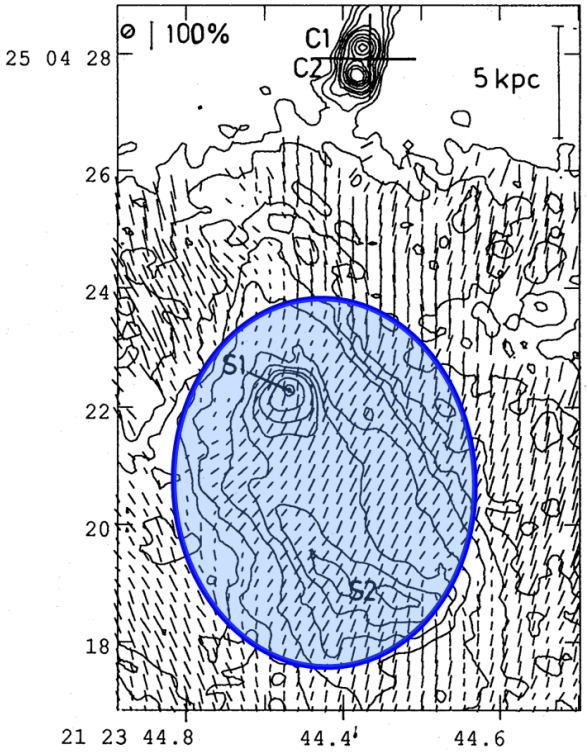

Figure 5.10: Stokes I contours and polarization vectors at 8.4 GHz from Figure 21 in Black et al. (1992) with the convolving beam for the 1–4 GHz model fit data overlaid showing how the individual component here may become unresolved.

of the hot spot, which can be seen in the map at 3 GHz in Figure 5.18, with lower $\sim 10\%$ values associated with the regions where the S4 and S5 components are located, indicating that the models fits are most likely probing these regions.

The depolarization is not as extreme as anticipated with $\sigma_{\mathrm{RM}} = 5.5\,\mathrm{rad\,m^{-2}}$ and there is no strong evidence for an internal depolarization process which means that the Southern hotspot is not mixing as strongly as anticipated with the external gas and may be merely pushing it away and causing some of the jet to deflect to the West as the jet moves through the shell. This contrasts with the results for Coma A, where strong depolarization is noted where the jet interacts with the ionised Hα shell. However there the jet has decelerated significantly after a collision and subsequent jet deflection with a gas cloud, and a slower jet may be more likely to mix into the medium rather than force it out of the way.

Looking at the upstream region of the Southern lobe with high intensity (labelled 'SL' in Figure 5.6), the polarization spectra show some significant

depolarization from, $\approx 25\%$ at 4 GHz to $\approx 13\%$ at 1 GHz at the 6.4×5.4" resolution used for all the images, with the spectrum plotted in Figure 5.11. The structure of the depolarization however does not fit well for a simple single RM component with screen depolarization. The unusual kink in the fractional polarization spectrum makes the appearance differ from the exponential decay expected for a single component, indicating that more likely a more complex structure is obscured within the observing beam, which is not unexpected given the knotty structure of this region shown at higher frequencies and resolutions.

At the resolution probed, this region is best fit by a 2 component RM model, however a more complex model cannot be ruled out. The images in Black et al. (1992), reproduced in Figure 5.10, do show two overall peaks in the Stokes I map at 8.4 GHz, named S1 and S2, making a two component fit a logical option. Again as with the Southern hotspot fits, both independent screen depolarization terms and a common one were fitted, as well as internal depolarization regimes for completeness. The best fit was one for a common depolarization term with the first term having $p_{01} = 0.112 \pm 0.001$, $\chi_{01} = 38.6 \pm 0.004°$, $\mathrm{RM}_1 = -55.17 \pm 0.01\,\mathrm{rad\,m^{-2}}$, and the second term having $p_{02} = 0.312 \pm 0.001$, $\chi_{02} = 157.9 \pm 0.004°$, $\mathrm{RM}_2 = -66.83 \pm 0.01\,\mathrm{rad\,m^{-2}}$, both with a common depolarizing screen term of $\sigma_{\mathrm{RM}} = 7.0 \pm 0.01\,\mathrm{rad\,m^{-2}}$. This is plotted in Figure 5.11. The fitted RM values are rather high for this region, and do not appear in the rotation measure maps of Figure 5.2 and 5.6, however little is known of the possible RM structure on smaller scales. The high fitted fractional polarization of 31.2% agrees with the high expected values from previous observations (van Breugel et al. 1983) of that region which predict even higher fractional polarizations of almost 40%, which are not recorded in the low resolution data, although they can be made out in the fractional polarization map at 3 GHz with a better resolution of just under 3". Comparing with the angles in Figure 5.10, the polarization angles do not appear to match up well: only S2 shows angles similar to the fitted $\chi_{02} = 157.9°$ with the S1 component not having consistent angles. One caveat may be that the individual features may have become slightly extended in the 1–4 GHz beam, or the scales probed at 1–4 GHz may include much more large scale lobe emission that may be invisible to the 8.4 GHz data and may be introduced into the fits, confusing the results.

The wing of diffuse emission to the right of the Southern lobe is also of interest, as it featured high polarization in the previously published higher

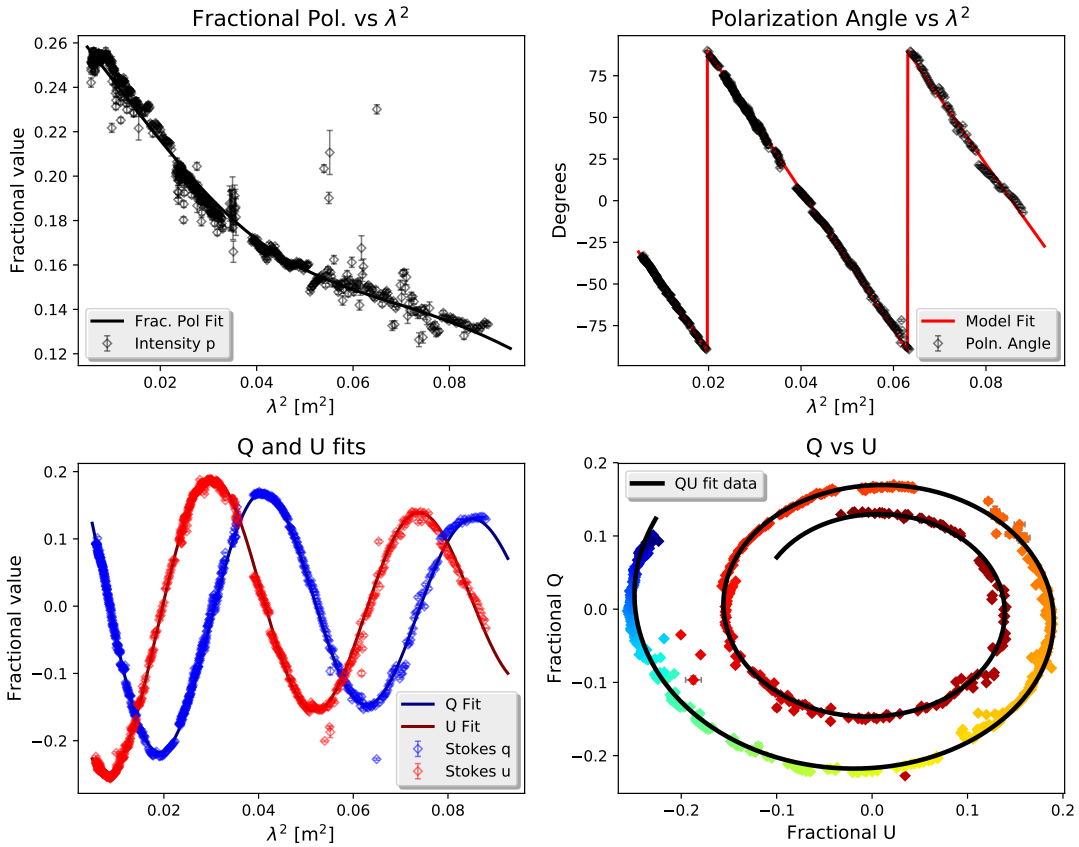

Figure 5.11: Summary of model fit for the upper region in the Southern lobe of 3C 433 for a model with 2 RM components with a common depolarization term. The plot layout in each panel is identical to that of Figure 5.9.

resolution maps at 1.48, 4.5 and 8.3 GHz (van Breugel et al. 1983, Black et al. 1992). This region is fit very well with just a single polarized component, with some external depolarization. The fitted parameters are $p_0 = 0.464 \pm 0.001$, $\chi_0 = 142.9 \pm 0.1°$, $\mathrm{RM} = -72.23 \pm 0.02\,\mathrm{rad\,m^{-2}}$, $\sigma_{\mathrm{RM}} = 4.66 \pm 0.02\,\mathrm{rad\,m^{-2}}$ and the fit to the data is plotted in Figure 5.12, for the region labelled 'SW' in Figure 5.6.

Similarly, the wing to the left of the Northern jet also shows a more single component dominated structure. Looking at the 'knot' or high intensity feature in this wing, labelled 'NK' in Figure 5.6, a single component fit describes the data best with $p_0 = 0.187 \pm 0.001$, $\chi_0 = 138.9 \pm 0.1°$, $\mathrm{RM} = -62.08 \pm 0.03\,\mathrm{rad\,m^{-2}}$, $\sigma_{\mathrm{RM}} = 4.08 \pm 0.04\,\mathrm{rad\,m^{-2}}$. A plot of the fit is given in Figure 5.13. In the higher resolution maps, it can be seen that the knot region is dominated by a single feature in Stokes I (see labelled feature N5 in Figure 5.8) making a single RM with a depolarization term the most

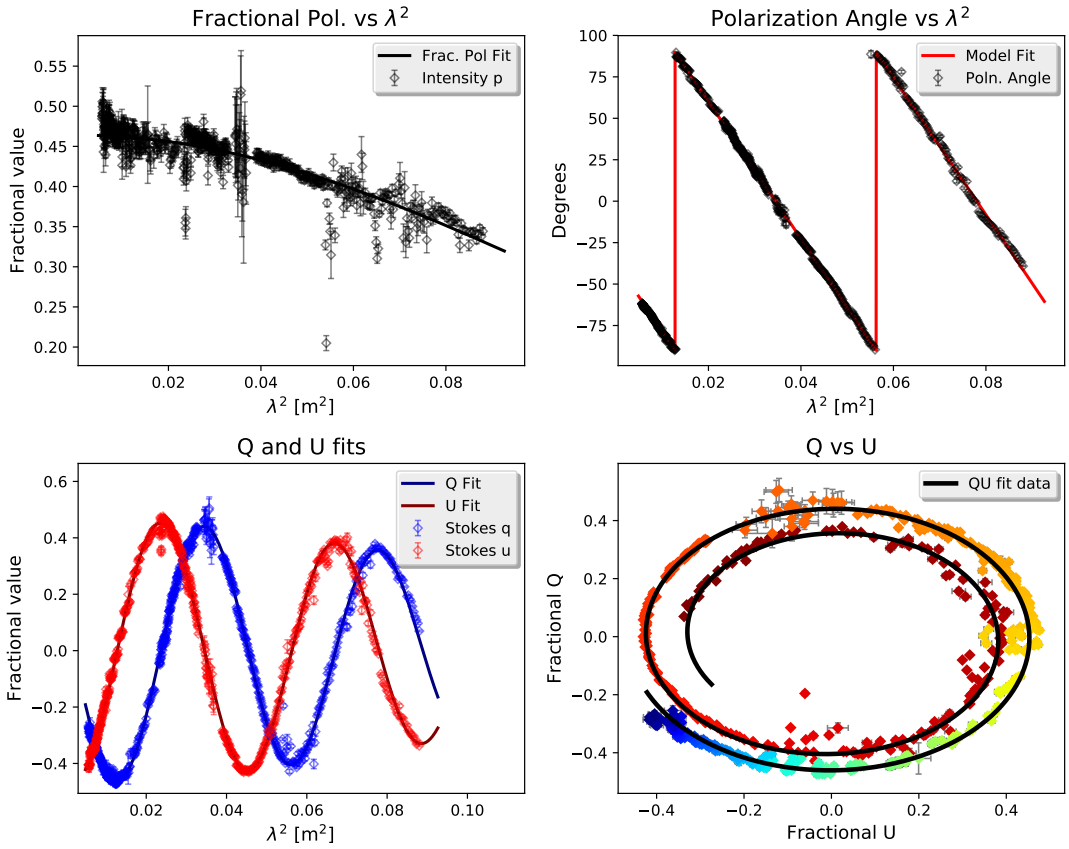

Figure 5.12: Summary of model fit for a region with high fractional polarization in the Eastern wing of the Southern lobe of 3C 433 for a model with 1RM component with a depolarization term. The plot layout for each panel is the same as that for Figure 5.9.

plausible option for the observed polarized spectrum from 1–4 GHz. It must be noted, however, that the values for this region in the fractional polarization spectrum are rather noisy, making a fit with more components and terms speculative, with a risk of over-interpreting what may just be noise or residual calibration error in the data, a further reason why a single component fit is a good conservative estimate. The RM is slightly less negative in this region in general, as can be seen in Figure 5.6, where the values rise to around -55 to -60 rad m^{-2}, compared to the values of ~ -70 rad m^{-2} which are common throughout the rest of the Northern and Southern lobes.

As was noted above, the Hα and HI observations originally intended to be included in this project are not yet calibrated and available for analysis. The new HI observations were designed to have a lower resolution than the observations of Morganti et al. (2003) allowing us to probe the large scale HI

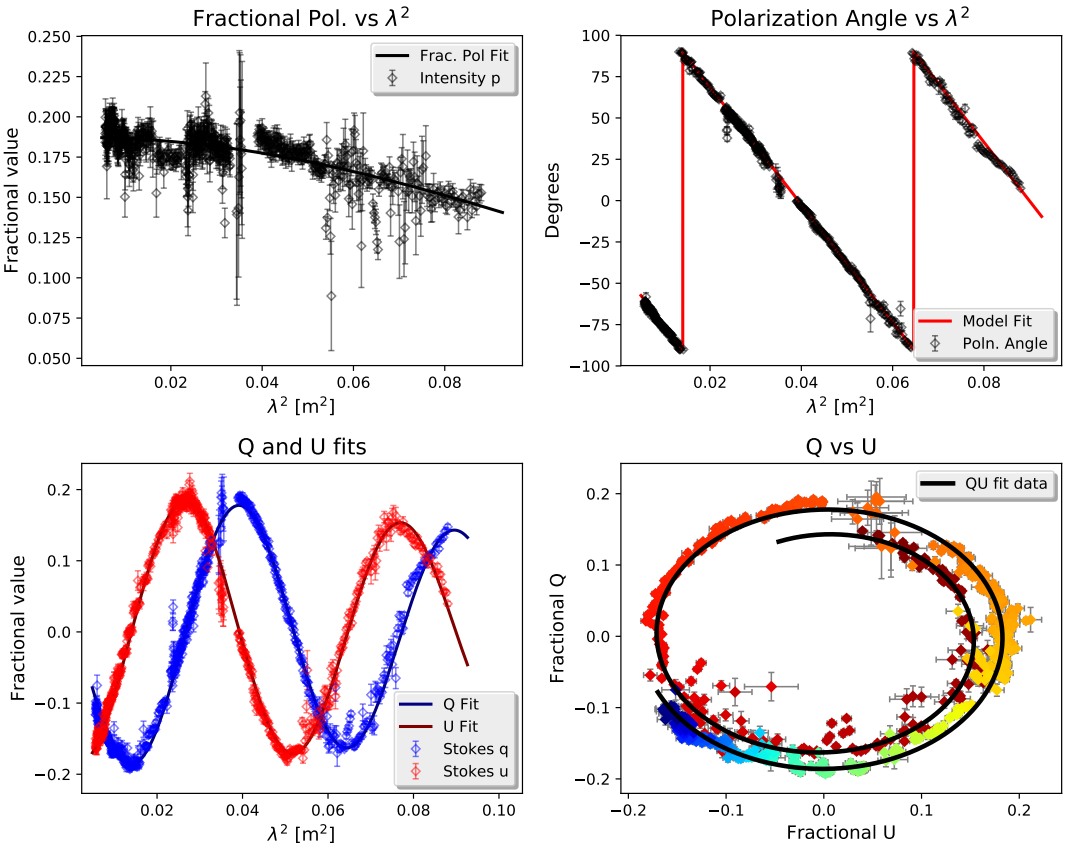

Figure 5.13: Summary of model fit for the knot in the North-Eastern wing of emission in 3C 433 for a model with 1RM component with a depolarization term. The plot layout for each panel is the same as that for Figure 5.9.

environment, if it is present. The Hα emission (if it was detected), could be utilised to estimate the electron density in the depolarizing screen of neutral and ionised gas, and, using the σ_{RM} and RM values, to directly calculate the magnetic field strengths in the ionised region surrounding the lobes, as was done successfully with Coma A. However a brief review can be done of existing data for other wavelengths. A map of the Hα structure of 3C 433 is published in Baum et al. (1988), where no large scale optical emission line flux is visible; only a dominant nuclear feature and an elongation to the North-West and South-East is visible from the host galaxy which the authors describe as being offset to the radio jet by $\sim 35°$. However considering the age of the data, more recent observations with modern optical telescopes could be more sensitive to further extended emission.

5.3 3C 382

This is a twin lobed radio galaxy at redshift $z = 0.05787$ (Eracleous & Halpern 2004), which corresponds to a projected distance of approx 1.13 kpc/". With a total angular size of this source of ~ 175" from hotspot to hotspot, this corresponds to a projected size of at least 200 kpc. An initial analysis and detailed maps of radio intensity are presented in Strom et al. (1978) at 1.4 and 4.8 GHz, Leahy & Perley (1991) at 1.4 GHz and Black et al. (1992) at 8.4 GHz, with polarization vectors overlaid.

Here, new wideband observations made with the VLA in the L (1–2 GHz) and S (2–4 GHz) bands are presented. Using these wide bands it is possible to create a Stokes I image with a very high dynamic range and accompanying spectral index map. This was done for both the 1–2 GHz data and the 2–4 GHz data for which images are presented in Figures 5.14 and 5.15 showing the small scale structure in and inner jet in the former, and the large scale lobes and diffuse emission in the latter.

The narrow jet can be made out in the Northern lobe, and the jet can also be seen close to the core on the Northern side, indicating that this jet is facing more towards the observer and is Doppler boosted, appearing brighter. A distinct knot can also be made out in the Northern lobe, where the narrow jet appears to be making a deflection of roughly 20° to the South of its original direction. In the S band spectral index map (Figure 5.14), the inner jet and its knots can be made out from their slightly flatter spectra, compared to the surrounding lobe medium. This is less visible in the 1–2 GHz map in Figure 5.15 where, most likely due to the lower resolution, the observing beam is incorporating some lobe flux making the spectrum appear steeper. The Northern lobe shows an unusual "S" shape, with an arch of higher intensity flux and higher fractional polarization tracing a path from the hotspot to the knot in the Northern lobe along the Southern edge of the lobe. A further faint arch of emission tracing the Northern edge of the lobe from the knot can also be made out. This high fractional polarization and the detailed polarization structure can be seen in the maps published in Strom et al. (1978), Leahy & Perley (1991) and Black et al. (1992) , as well as here, in Figure 5.18. The compact feature seen to the North-West of the Northern lobe is a background source, and is not associated with the radio emission from 3C 382 (NED cross ID SSTSL2 J183502.13+324221.9 in IR, unknown redshift and most likely a

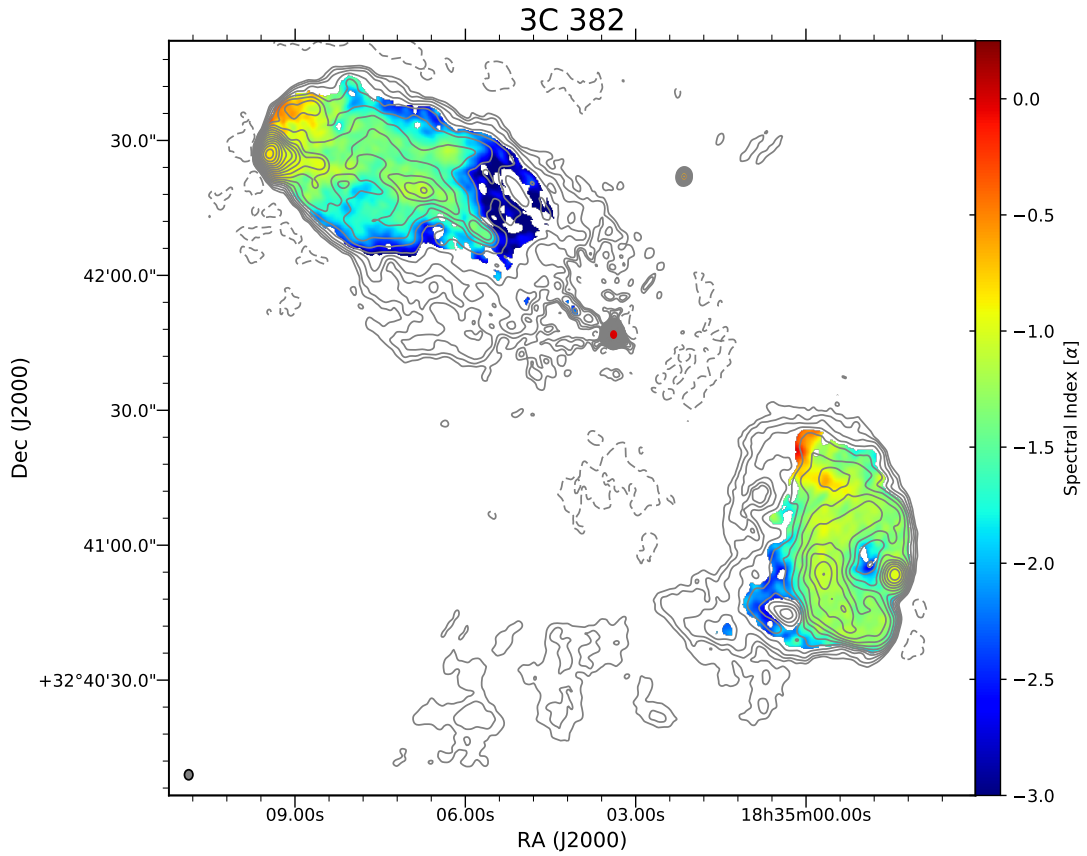

Figure 5.14: Map of 3C 382 at 3 GHz made using a multi-term multi-frequency synthesis imaging method for the 2–4 GHz, S band data. The spectral index is given in the colour scale with the Stokes I contours at 3 GHz overlaid, the levels start at 0.25 mJy beam^{-1} and increase in factors of $\sqrt{2}$ up to a maximum level of 128 mJy beam^{-1}, a negative dashed contour at -0.25 mJy beam^{-1}. The convolving beam is 2.24×1.88" with a beam position angle of 8.9°.

distant AGN due to high radio emission with spectral index, $\alpha \simeq -0.3$). VLBI monitoring of 3C 382 by the MOJAVE programme shows that within the unresolved VLA core, a jet structure towards the North-East can be seen, with the jet following the same direction as on the large scales; in the most recent image, shown here in Figure 5.16, the counter jet can also be made out.

3C 382 has been named a member of the cluster UGCl 447 (also known as ZwCl 1831.2+3154) by Zwicky et al. (1963) and was associated with that group again in Strom et al. (1978). However no exact red shift is known for this group, while it is known for 3C 382. In an optical analysis by Roche & Eales (2000), they suggest a barred spiral galaxy which lies just to the South of the Northern hotspot, approximately 85" at position angle of 67° (NED cross ID 2MASX J18350968+3242162), is interacting with the 3C 382 host, and

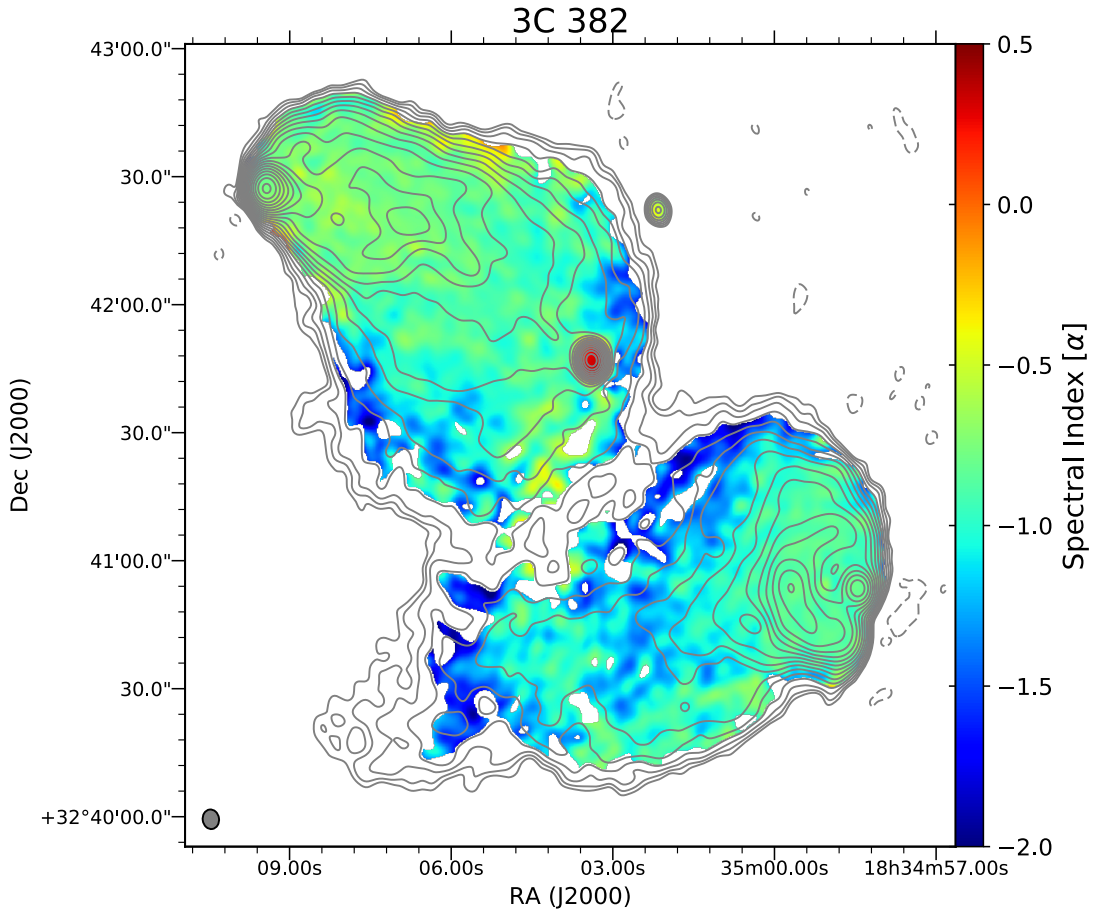

Figure 5.15: Map of 3C 382 at 1.5 GHz made using a multi-term multi-frequency synthesis imageing method for the 1–2 GHz, S band data. The spectral index is given in the colour scale with the Stokes I contours at 1.5 GHz overlaid, the levels start at 0.5 mJy beam^{-1} and increase in factors of $\sqrt{2}$ up to a maximum level of 256 mJy beam^{-1}, a negative dashed contour at -0.5 mJy beam^{-1}. The convolving beam is 4.61×3.83" with a beam position angle of -1.1°.

mention a trail of optical emission connecting the two galaxies. However, this connection is not visible in the images reproduced in that publication. Roche & Eales (2000) also mention that this galaxy may be the cause of the deflection in the jet, somehow attributing the location of the barred spiral with the deflecting knot however this spiral galaxy is actually located close to the Northern hotspot. While a connection and interaction between these two galaxies would be an interesting explanation for the 3C 382 radio structure, the evidence is only speculative.

In the Southern lobe, no narrow jet can be made out, however a prominent hotspot indicates the terminating point of the jet. Black et al. (1992) point out

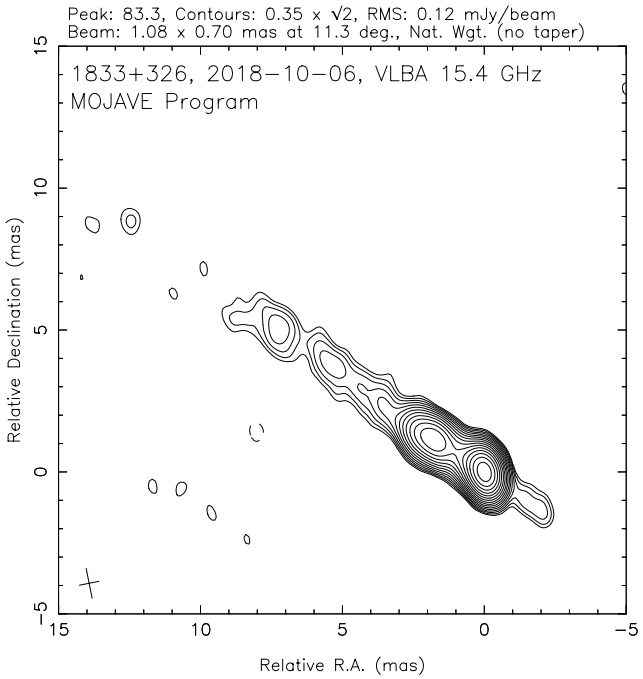

Figure 5.16: Parsec scale Stokes I contour map of 3C 382 at 15 GHz publicly available from the MOJAVE program (Lister et al. 2018).

a region of low polarization which bends towards the hotspot at the Northern end of the Southern lobe, which may be an indicator of an obscured jet. An unusual arc of more intense radio emission and high linear polarization, reminiscent of the arc in the Northern lobe, can be seen around the hotspot feature, however the orientation does not seem to hug the lobe along the jet direction. It is tempting to associate these rings in both lobes with precession of the radio jets, possibly due to interaction with the aforementioned neighbouring spiral galaxy, however there is no concrete evidence to support this.

There is also more diffuse radio emission associated with the Southern lobe, trailing off to the East from the Southern lobe, which is more prominent at lower frequencies and has a steeper spectral index indicating that this is older diffuse emission from the radio lobe.

3C 382 is also a known X-ray emitter, whose strong nuclear X-ray emission has been monitored using multiple instruments such as XMM-Newton and NuSTAR by Ursini et al. (2018), who interestingly compare the X-ray emission to that of a radio quiet Seyfert galaxy, hinting at a common emission mechanism.

5.3.1 Observations and data reduction

The observations of 3C 382 in the 1–2 and 2–4 GHz bands were observed in VLA B configuration on the 20th and 17th of September 2017, respectively. 3C 286 served as the primary flux density calibrator, bandpass and polarization angle calibrator. The phase calibrator was the unresolved source J1753+2848 (B2 1751+28) which was observed with a sufficient parallactic angle coverage to allow this source to serve as the polarization leakage calibrator. As with 3C 433, 3C 382 was calibrated using standard routines in CASA, with RFI identified and flagged using the automated routines *tfcrop* and *rflag*, as well as some manual flagging.

The calibrated data were then subjected to three iterations of phase self–calibration and one iteration of amplitude and phase self–calibration. The self calibration was done across the whole band using a multi-term multi-frequency synthesis technique (Rau & Cornwell 2011) with `nterms=3`, which produced a continuous model of source structure across the spectrum with a high dynamic range and good resolution, as well as good sampling of the large scale structure. The resulting high dynamic range Stokes I images with accompanying spectral index maps are shown in Figures 5.15 and 5.14. For the S-band 2–4 GHz data it must be noted that the uv coverage used undersamples the shorter baselines significantly, as can be seen by the lack of large scale emission seen in Figure 5.14, which is present in Figure 5.15. This means care must be taken when interpreting results of the QU model fitting and RM synthesis, especially for regions which show more extended emission. Measurements closer to 4 GHz particularly may not be correctly sampling the polarized flux, as large scale polarized (or depolarized) emission may not be incorporated into the data.

To calculate and present the rotation measures at the best resolution available, the higher resolution 2–4 GHz data were imaged in Stokes I, Q and U in 16 separate 128 MHz bins, averaging over each spectral window. The visibility data were tapered in the imaging process and the final images smoothed to have the same convolving beam of 3.5×3" with a zero degree position angle. The final RM map was produced with blanking applied such that polarization angles with errors greater than 3° were omitted from fits, any subsequently calculated RM values with errors from the fitting greater than 5 rad m^{-2} were omitted from the final map. The final map is shown in Figure 5.17 with intensity contours for 3 GHz at matched resolution overlaid. The fractional

polarization map at 3 GHz was made using the de-biased linear polarization intensity, so the blanking factor used for the fractional polarization was the Stokes I, in an effort to highlight any depolarized regions in the jet-lobe structures.

To analyse the data along the whole 1–4 GHz spectral range using RM synthesis and *QU* model fitting, the data were imaged in Stokes I, Q and U in discreet bins of 4 MHz for the 1–2 GHz data and 8 MHz for the 2–4 GHz data, ensuring the λ^2 space was well sampled, and that the images all had a sufficient dynamic range. The data were cleaned using a Clark CLEAN and the visibility data were weighted and tapered, and the images smoothed to ensure all images shared the same resolution and a convolving beam of 7.1×5.8", with a beam position angle at 7.4°.

5.3.2 Rotation measure Mapping

The higher resolution RM map is given in Figure 5.17, with the intrinsic polarization angle and 3 GHz fractional polarization map given in Figure 5.18. Overall, the rotation measure is patchy, with higher rotation measures calculated for the receding jet and lobe structures.

As with 3C 433, this RM mapping process was used to calculate the intrinsic polarization angle χ_0, plotted in Figure 5.18. This map agrees quite well with the polarization angle distribution at 8.4 GHz in Black et al. (1992) indicating the reliability of the calculated rotation measures. The intrinsic polarization angle is perpendicular to the edges of the lobes, as can be seen at the Southern side of the Northern lobe and around the Western end and around the ring feature in the Southern lobe. Inside the Southern lobe, the polarization angle is aligned with the direction from the core to the Southern hotspot, where the radio jet would most likely be found.

A de-biased fractional polarization map at 3 GHz is also given in Figure 5.18. This highlights the detailed polarization structure of the jet. The polarization map was made by de-biasing the polarized intensity map using standard methods in CASA (Leahy & Fernini 1989); The fractional polarization is plotted for all areas with Stokes I flux above 2 mJy beam^{-1}. Comparing this with the χ_0 map, the vectors are aligned perpendicular to the jet at the edges of the lobes, where there is a high $> 30\%$ polarization, meaning the associated magnetic field follows the edges of the lobes. Black et al. (1992) proposed that

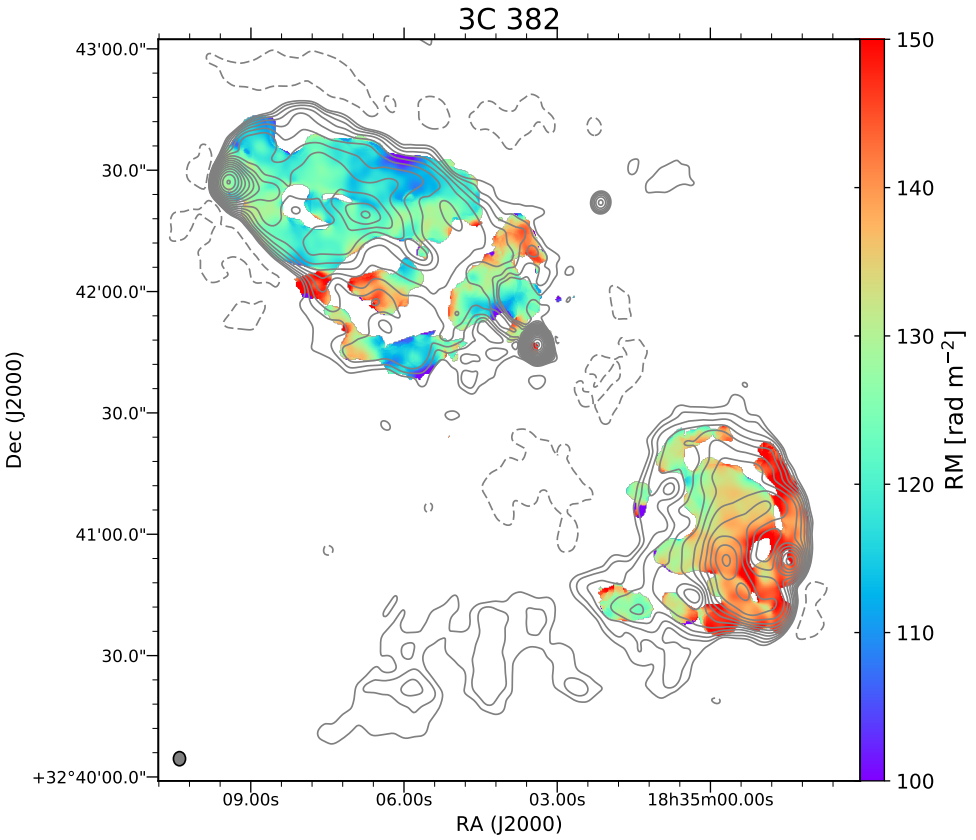

Figure 5.17: RM map of 3C 382 made using data from 16 frequencies from 2–4 GHz (S band), the rotation measure is given in the colour scale with intensity contours overlaid, which are for 3 GHz and created using the multi-term multi-frequency synthesis imaging technique. The levels start at 0.5 mJy beam^{-1} and increase in factors of $\sqrt{2}$ with a maximum level of 256 mJy beam^{-1}, a dashed negative contour at -0.5 mJy beam^{-1} is given also. The common convolving beam for all the images is 3×3.5" at $0°$.

the region of low fractional polarization tracing a curved path through the Southern lobe towards the hotspot is the outline of the obscured radio jet within the lobe. The change in direction and curl of this possible jet towards the hotspot is interesting, as the direction into which the "jet" is bent coincides with the trailing diffuse emission from the lobe out towards the South-East, possible evidence of some intergalactic or intracluster weather or wind impacting the source.

The rotation measure synthesis was again performed using the *pyrmsynth* PYTHON routine, with an RMCLEAN also performed to reduce the sidelobes resulting from convolution of the Faraday depth spectrum $F(\phi)$ with the RMTF. The resulting map of the peak RM value $\phi_{\rm peak}$ is presented in Figure 5.19. The FWHM of the RMTF corresponds to the maximum theoretical

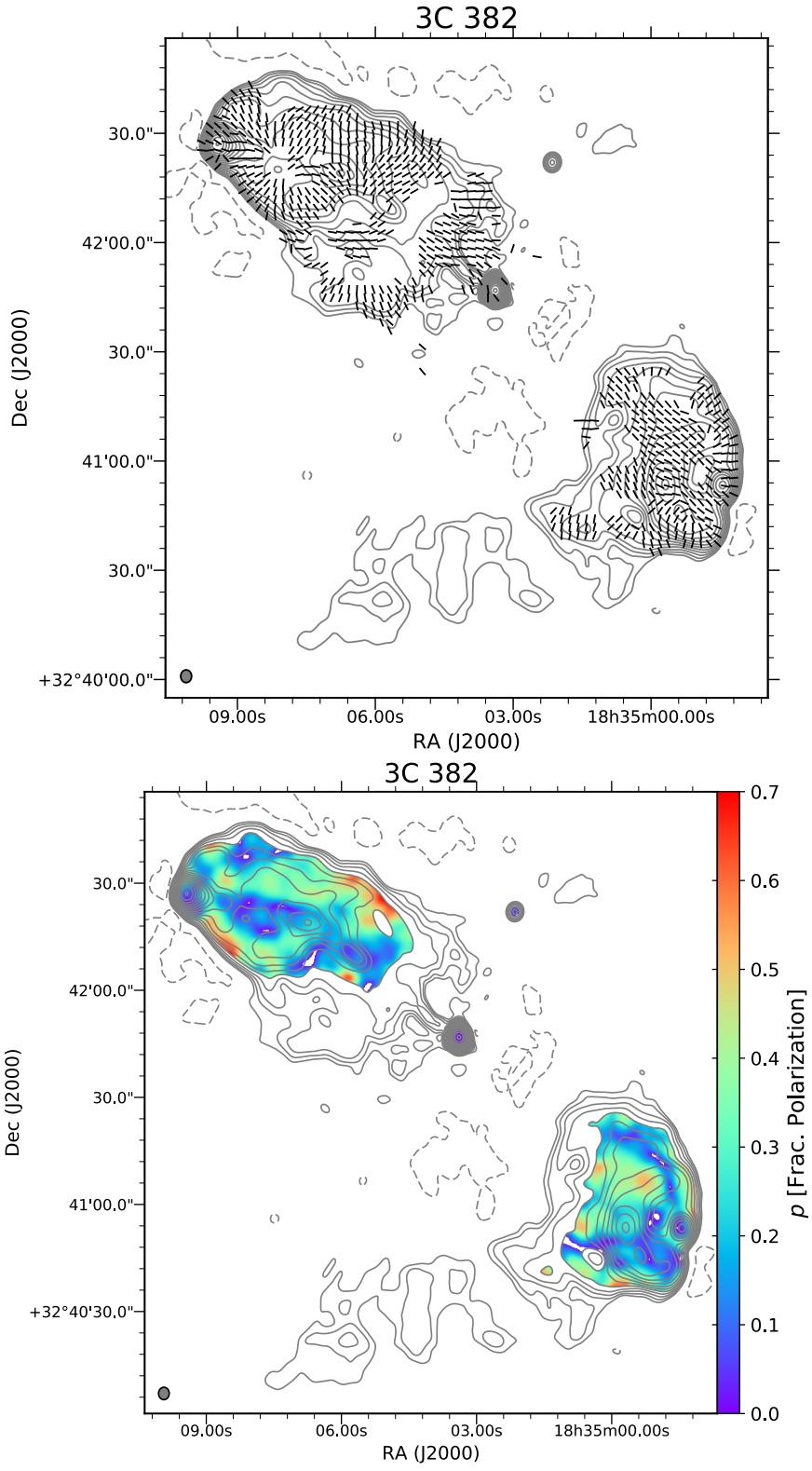

Figure 5.18: **Top:** Map of the intrinsic polarization angle χ_0 plotted as vectors, as this map was made in parallel to the RM map the resolution is identical at 3.5×3" at 0°, the contours and their levels are identical to those in Figure 5.17. **Bottom:** De-biased fractional polarization map for 3C 382 at 3 GHz, fractional polarization is plotted for all areas where Stokes I is > 2 mJy beam^{-1}, the Stokes I contours are identical to the top panel.

resolution of 42 rad m^{-2}. The $\phi_{\rm peak}$ map was made using peaks with $\geq 3\sigma$ signal to noise ratio meaning the maximum errors in the values in Figure 5.19 are $\frac{42}{2\times3} \approx 7$ rad m^{-2}. The $F(\phi)$ functions for some regions are presented in Figure 5.20, showing how within the limits of the resolution in ϕ, the Faraday depth is dominated by single components in ϕ.

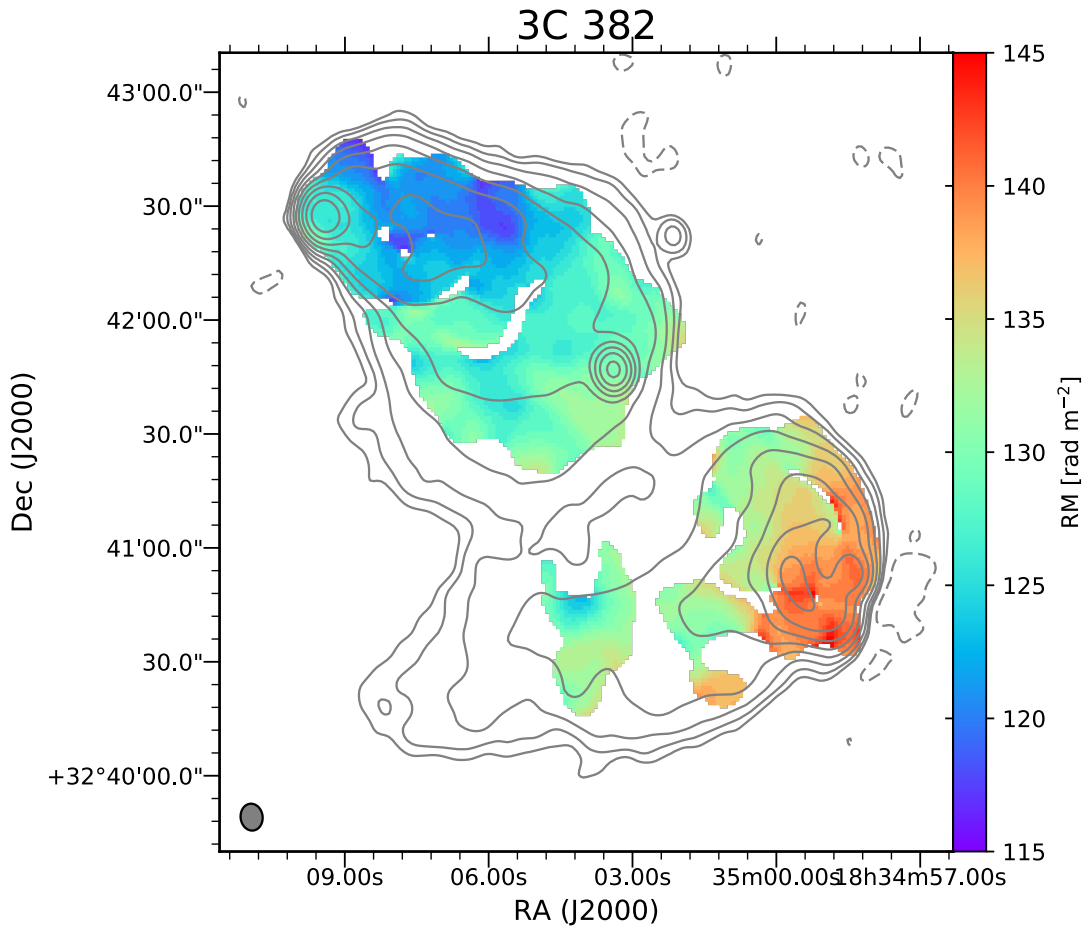

Figure 5.19: Map of the $\phi_{\rm peak}$ RM value for the lobes of 3C 382 made using data from 1–4 GHz using a channel width of 4 MHz from 1–2 GHz and 8 MHz from 2–4 GHz. The Stokes I contours shown were made using a map made using a multi frequency synthesis technique in the 1–2 GHz range with a uv taper to ensure a common resolution to the RM map. The levels start at 0.75 mJy beam^{-1} and increase in factors of 2, with the highest contour at 192 mJy beam^{-1}. The common convolving beam for all the images is 7.1×5.8", with a beam position angle at 7.4°

Looking at the map of $\phi_{\rm peak}$ the RM shows some structure over the entire jet, with RM values agreeing with the higher resolution map in Figure 5.17. There is a gradient in the rotation measure from one end of the jet to the other, which now appears smoother, due to the lower resolution and the larger scales

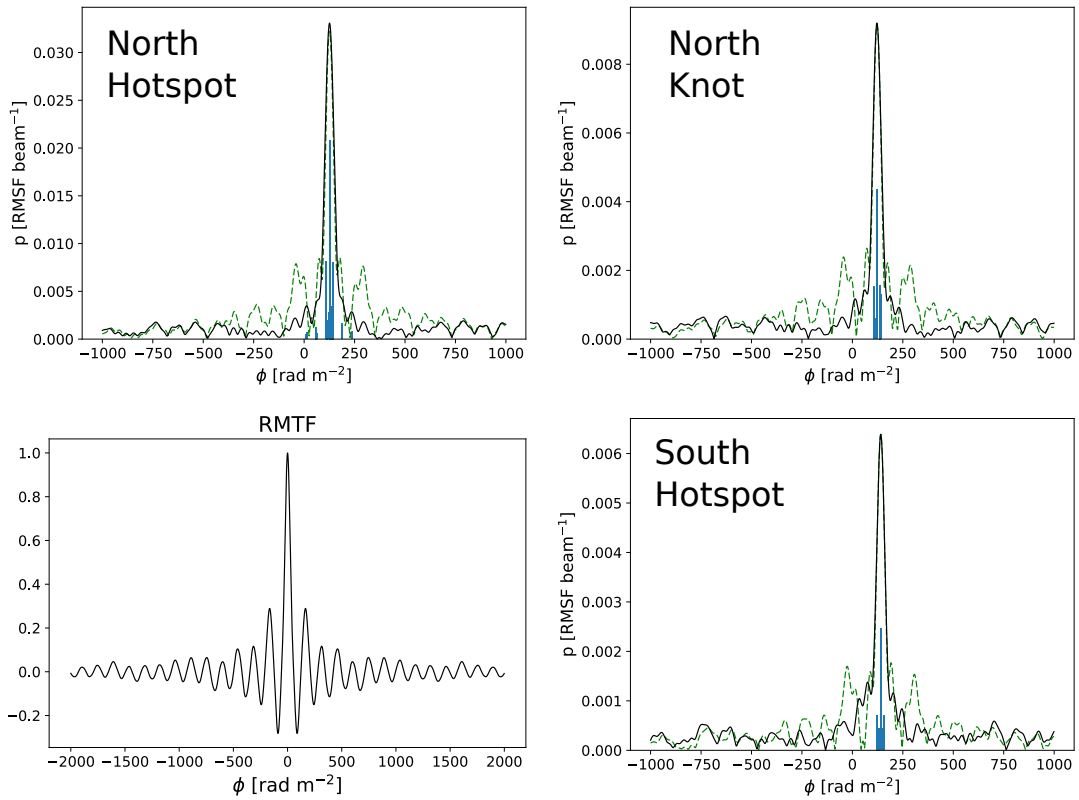

Figure 5.20: A selection of plots of the Faraday spectra of 3C 382 from the RM synthesis. The green dashed lines correspond to the dirty spectra, the solid black line corresponds to the cleaned spectrum and the blue bars represents the clean components.**Top Left:** $F(\phi)$ for the Northern hotspot in 3C 382, the $\phi_{\rm peak} = 126 \pm 1\,{\rm rad\,m^{-2}}$.**Top Right:** The $F(\phi)$ for the knot in the Northern lobe where the jet changes direction with $\phi_{\rm peak} = 122 \pm 2\,{\rm rad\,m^{-2}}$. **Bottom Left:** The RMTF calculated and used in the synthesis process. **Bottom Right:** The $F(\phi)$ for the Southern hotspot with a calculated $\phi_{\rm peak} = 141 \pm 3\,{\rm rad\,m^{-2}}$.

sampled by the 1–2 GHz data. Overall, the magnitude of the RM changes from 120 to 140 rad m^{-2} from the Eastern to the Western hotspot. This may be related to the fact that the Eastern jet is approaching and the Western jet is receding, and therefore there is more foreground intergalactic medium that could be supplying the magneto-ionic material amplifying the rotation measure.

5.3.3 *QU* Model fitting

To investigate the spectral behaviour of the polarization, it is an interesting to use *QU* model fitting for various regions along the jet structure, to analyse

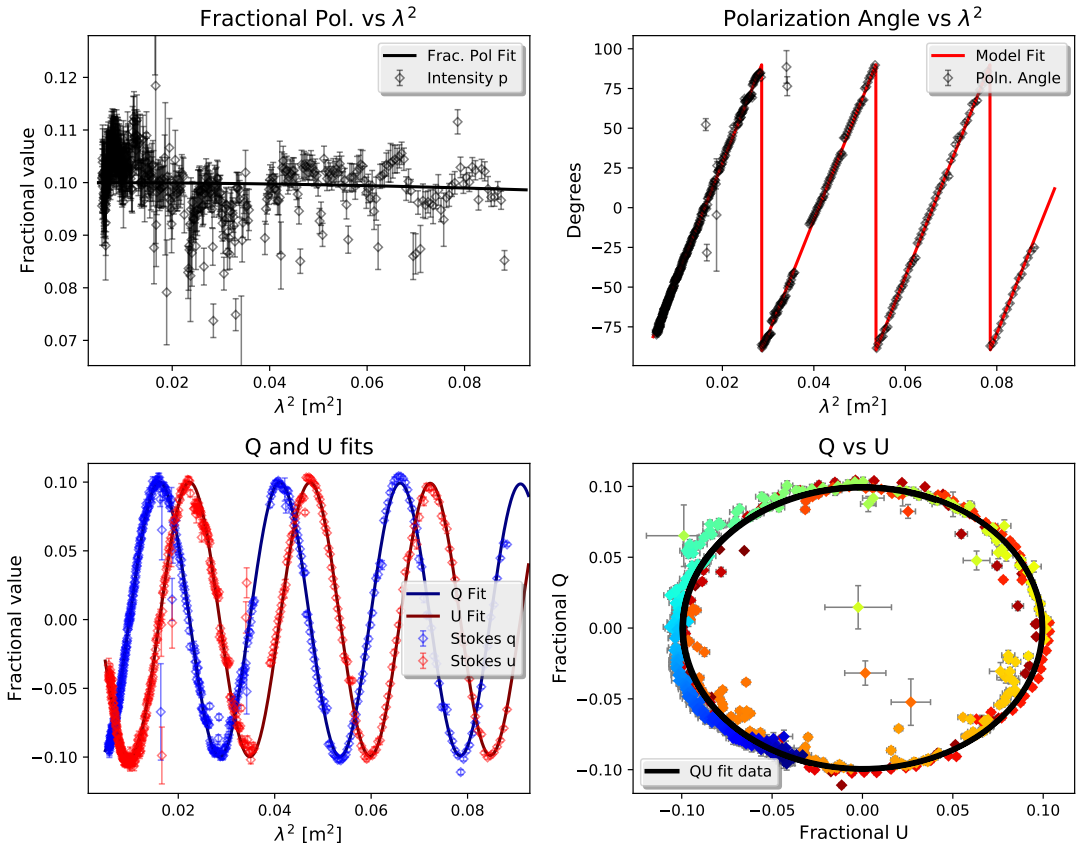

Figure 5.21: Summary of model fit for the knot in the Northern hotspot of 3C 382 for a model with 1RM component with a depolarization term. The plot layout for each panel is the same as that for Figure 5.9.

whether multiple unresolved components or extended structure in Faraday depth, that could be identified with internal Faraday dispersion in the spectra can be detected. The Stokes I, Q and U images made for the RM synthesis were used for this analysis also.

Fitting for the Northern hotspot shows that this region exhibits very low depolarization, and fits for a single RM component with a depolarizing screen work quite well, as can be seen in Figure 5.21. The fractional polarization spectrum shows little variation apart from some minor fluctuations which are most likely instrumental effects from imperfect calibration and not due to a physical effect in the source. The fitted parameters are: $p_0 = 0.1 \pm 0.0002$, $\mathrm{RM} = 125.9 \pm 0.03\,\mathrm{rad\,m^{-2}}$, $\chi_0 = 63.7 \pm 0.07°$, $\sigma_{\mathrm{RM}} = 0.9 \pm 0.2\,\mathrm{rad\,m^{-2}}$. The RM value is in good agreement with the result from the RM synthesis.

The core also shows an interesting spectrum with reverse depolarization. The fractional polarization at 1 GHz is approximately 2.5% and decreases towards

zero at 4 GHz. This is a strong indicator that a more complex structure in polarization is present within the unresolved core. This complex structure could be multiple polarized components interacting with each other, or an internal Faraday dispersion process or ordered magnetic field causing an unresolved gradient of the RM values, both of which result in reverse depolarization. The best fit model to the data has 2 polarized components with individual depolarization terms. It is difficult to ascribe this affect to an RM gradient, as the full pattern of a sinc function cannot be made out clearly, with an increase towards zero wavelength in the fractional polarization, as in Figure 2.9. The best fit parameters to the data are $p_{01} = 0.023 \pm 0.002$, $\chi_{01} = 174 \pm 2°$, $\mathrm{RM}_1 = 136.5 \pm 0.3\,\mathrm{rad\,m^{-2}}$, $\sigma_{\mathrm{RM1}} = 0.8 \pm 0.9\,\mathrm{rad\,m^{-2}}$ for the first component, and $p_{02} = 0.022 \pm 0.002$, $\chi_{02} = 83 \pm 2°$, $\mathrm{RM}_1 2 = 125.3 \pm 0.8\,\mathrm{rad\,m^{-2}}$, $\sigma_{\mathrm{RM2}} = 9.6 \pm 0.9\,\mathrm{rad\,m^{-2}}$ for the second component. Looking at the fit to the core in Figure 5.22, there are some appreciable small scale fluctuations in the data however these need not be over-interpreted at such low fractional polarizations, where noise across the band can be expected, as was the case in Coma A, most likely due to an imperfect D-term calibration. Care must be taken with over interpreting the data at higher frequencies as some large scale polarized flux may be absent from the data given the lack of short baselines in the 2–4 GHz data. The model fit results are difficult to reconcile with observations at high frequencies and resolutions with the VLA, as the figures in Black et al. (1992) show no resolved structure or polarization in the core. While multiple knots and features are visible in the VLBI images of 3C 382 at 15 GHz (Figure 5.16) the source shows little to no polarization here, with an upper limit of 0.6% polarization quoted for this epoch in the MOJAVE database[3] (Lister et al. 2018).

The Southern hotspot shows slightly more complex structure, with the expected higher depolarization. The high frequency end, toward 4 GHz, shows some fluctuation, which was not as prevalent in the spectrum for the Northern hotspot. However this may be due to an instrumental effect, or due to missing large scale flux from the lack of short baselines at the higher frequencies, and should not be over-interpreted in the fitting . A single component fit does give a good fit of the longer wavelength data with $p_0 = 0.08 \pm 0.0005$, $\mathrm{RM} = 140.2 \pm 0.1\,\mathrm{rad\,m^{-2}}$, $\chi_0 = 61.8 \pm 0.3°$, $\sigma_{\mathrm{RM}} = 3.4 \pm 0.2\,\mathrm{rad\,m^{-2}}$, plotted in Figure 5.23. The p_0 value calculated here lies in the range calculated for the 6 cm WSRT observation of Strom et al. (1978), who calculated the fractional

[3] http://www.physics.purdue.edu/astro/MOJAVE/allsources.html

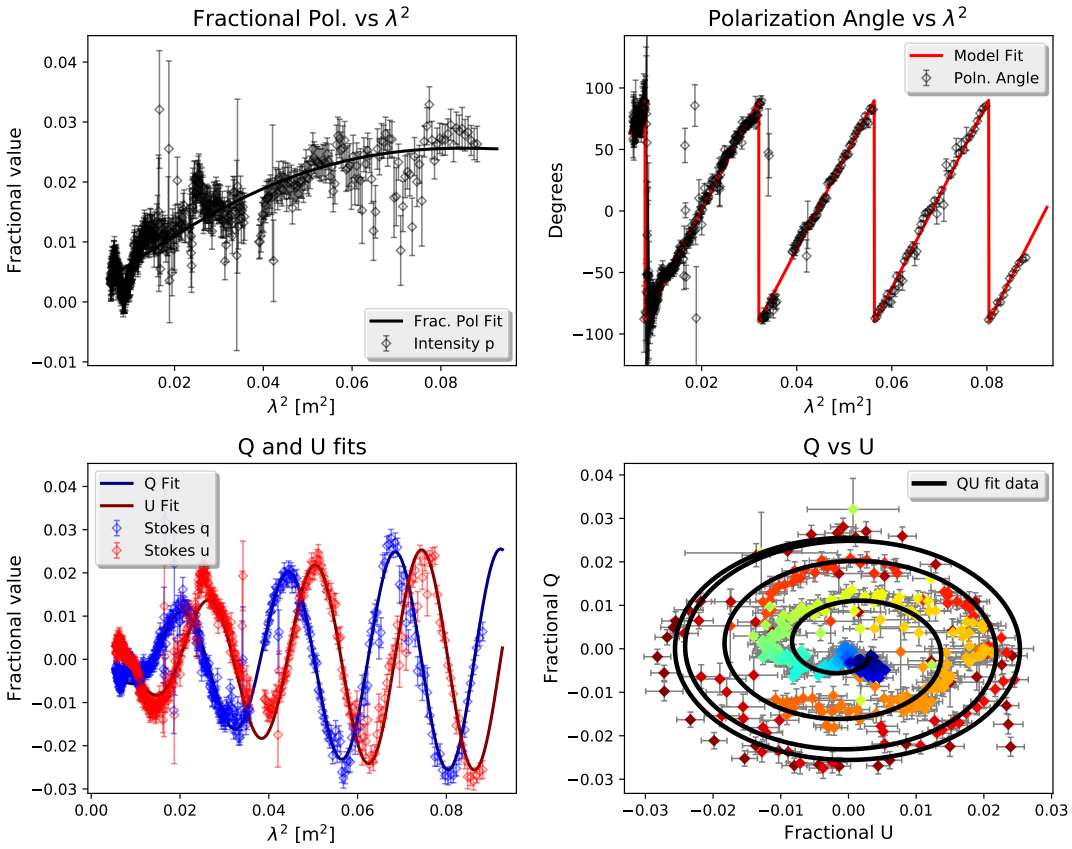

Figure 5.22: Summary of model fit for the core of 3C 382 for a model with 2 RM components with independent depolarization terms. The plot layout for each panel is the same as that for Figure 5.9.

polarization in the region of the hotspot to be $\simeq 10\%$.

The single component nature of the polarization model with an external Faraday screen fits the data well and the observed gradient in the RM from one hotspot to the other suggests this RM is very likely due to the surrounding inter galactic medium. Both the magnitude of the RM and the depolarizing term σ_{RM} are higher in the Southern hotspot with $\mathrm{RM} \simeq 140$ and $\sigma_{\mathrm{RM}} = 3.4\,\mathrm{rad\,m^{-2}}$, which is associated with the counter-jet facing away from the observer, so that more Faraday rotating medium and depolarizing Faraday screen material are present in the foreground of this structure. If the unusual bump at higher frequencies of $\simeq 1.5\%$ in the Southern hotspot is due to a real effect, then more intense depolarization is inferred, making $\sigma_{\mathrm{RM}} = 3.4\,\mathrm{rad\,m^{-2}}$ a good lower limit. This makes the lobes of 3C 382 a clear example of the Laing-Garrington effect. (Garrington et al. 1988, Laing 1988).

It is also noteworthy that according to the coordinates and values of the

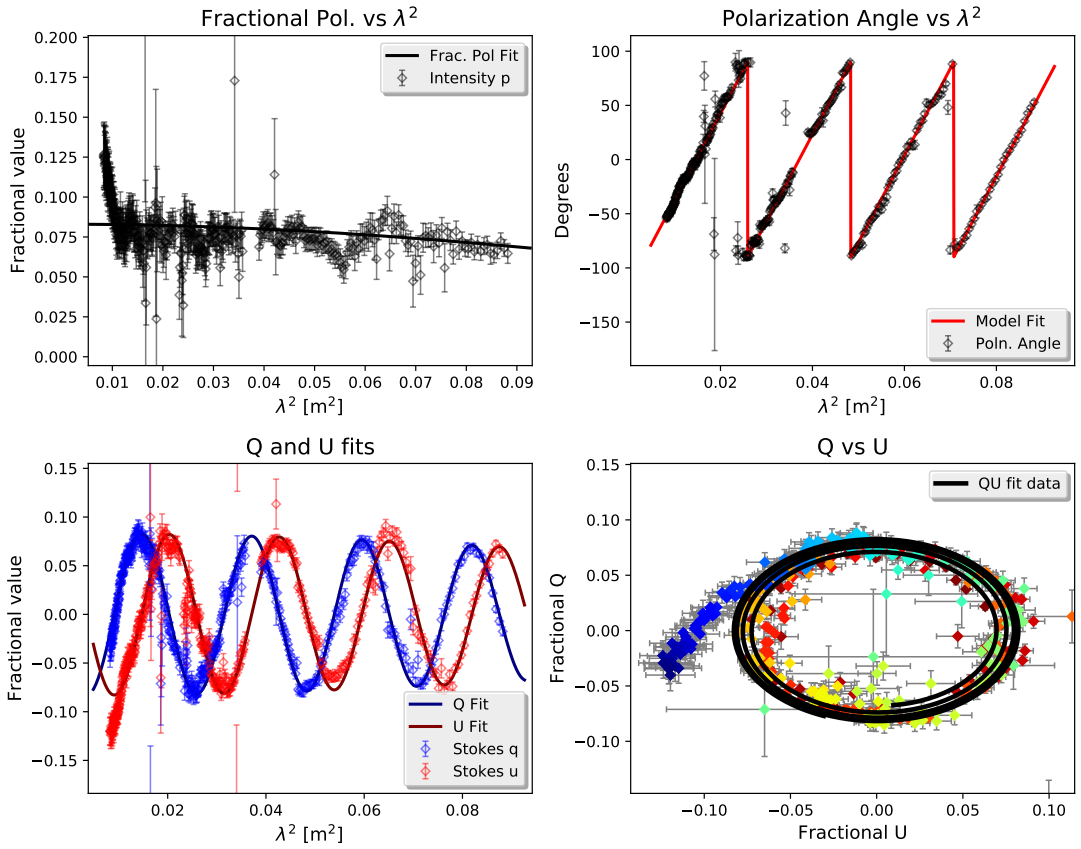

Figure 5.23: Summary of model fit for the Southern hotspot of 3C 382 for a model with 1RM component with a depolarization term. The plot layout for each panel is the same as that for Figure 5.9.

integrated rotation measures from Taylor et al. (2009), the individual lobes are ascribed separate integrated rotation measures of $109 \pm 9\,\mathrm{rad\,m^{-2}}$ and $122.8 \pm 6\,\mathrm{rad\,m^{-2}}$ for the Northern and Southern lobes respectively. This difference in RM could be due to a Galactic foreground effect, and a sudden change in the Galactic foreground magnetic field could be occurring. However, from investigating the rotation measure map and seeing that this gradient lies exactly along the jet axis, the gradient is more likely due to asymmetry in the projection of the lobes. A common Galactic or IGM associated Faraday depth of $\sim 100\,\mathrm{rad\,m^{-2}}$ is likely present, as the RM of the Northern lobe should be lower and closer to zero, since it has the least amount of Faraday rotating material in front of it local to the source. The lower Galactic latitude of 17.44° for 3C 382 suggests more Galactic material in the foreground is likely causing this contributed $\sim 100\,\mathrm{rad\,m^{-2}}$ of integrated RM.

This considerable change in RM is indicative of some kind of group

environment around the source effecting the rotation measure, which is likely given rise to the trailing diffuse emission to the South-East. No such trail of emission can be seen in the North, however the Northern lobe does appear more elongated to the South-East in the 1–2 GHz image, with a steep spectral index in Figure 5.15. Recall though, that the deflection of the Northern jet to the East will cause any tailing emission to appear less pronounced, which may be at work here also. This may be due to some intra-cluster or intergalactic effect, or to the purported interaction with the spiral galaxy to the North-East (Roche & Eales 2000), or simply due to the possible motion of 3C 382 to the North-West. However, due to the increase in the magnitude of RM across the source, the first two options are more likely.

The inclination of this jet to the observer is likely considerable, as the AGN is classified as a broad line radio galaxy (BLRG), indicating a close viewing angle to the host AGN allowing for the broad emission lines to be observed, and the jet is observable on VLBI scales (see Figure 5.16). The deflection of the jet in the North however, confuses this somewhat, making an exact inclination estimate difficult from the RM data alone.

As was the case for 3C 433, deep Hα and HI observations taken as part of this project are not yet calibrated and available for analysis. Looking at the literature, there is little evidence for large scale ionised emission. The X-ray image data published previously for this source do not indicate any large scale diffuse emission. Hodges-Kluck et al. (2010) note that no diffuse emission was detected in CHANDRA data, only a strong nuclear component. A small amount of diffuse emission is detected about of 20–30" around the core in Gliozzi et al. (2007) which was presumed to be thermal blackbody or bremsstrahlung. This may suggest some population of material around the galaxy; however this was not detected at the distances from the core where the lobes are found. This hints at a fairly rarified environment surrounding 3C 382, however some IGM is likely to exist local to the source, given the asymmetry in the RM distribution across the lobes.

5.4 Summary

Presented here is an analysis of the polarization structure of 3C 433 and 3C 382, previously unknown and unpublished high resolution rotation

measure and intrinsic polarization angle maps in the 2–4 GHz range, and an in depth Faraday depth analysis using rotation measure synthesis at 1–4 GHz, creating the first known kpc scale RM maps for these sources to date. Depolarization model fits were obtained for unresolved and extended features in order to probe and understand the structure in detail.

3C 433 shows relatively low depolarization across the 1–4 GHz bands, which is surprising considering the known HI and X-ray environments published previously. This indicates that little mixing or violent interaction is occurring on the scales probed in this study, however the low polarization troughs seen at higher frequencies and resolutions may be evidence of some interaction with the group atmosphere, which may be causing the contorted X or Z shape of the radio jets and lobes.

3C 382 also shows relatively low depolarization, however this source is a prime example of the Laing-Garrington effect, with the receding jet showing more depolarization and an amplified RM, indicating the presence of some group atmosphere, however rarified it may be. The RM asymmetry shows a gradient in the RM from end to end, from 120 – 140 rad m^{-2}. Polarization model fits show that the hotspot has a relatively simple structure with a single RM component dominating, while the core has a more complex structure with 2 components; however this cannot be confirmed with known VLBI or high resolution VLA observations.

The B–configuration S-band observations of these objects show the potential power of the VLA sky survey (VLASS), which aims to map the Northern sky using 2–4 GHz observations in the same VLA B configuration. The S–band polarization data displayed here show the possibilities of the data products from this survey.

Chapter 6

Conclusions

This thesis has dealt in depth with the magnetic fields in AGN jets on kiloparsec scales, using a variety of approaches:

1. A search for statistically significant transverse RM gradients across AGN jets on kiloparsec scales, taken to be an indicator of toroidal magnetic-field component, has been carried out as part of this thesis. This has led to the detection of 8 statistically significant transverse RM gradients on kiloparsec scales. The effects of the "cosmic battery", a process in the accretion disk of a black hole that has been supposed to provide the source helical magnetic field needed to launch and collimate astrophysical jets on parsec scales have been investigated. This model makes the very specific prediction that the toroidal magnetic field on parsec and kiloparsec scales should be associated with inward and outward currents, respectively.

2. Another feature of these jets is the interaction between large scale AGN jets and their surrounding media and how this affects the observed polarization and rotation measure. This has been studied using polarization and RM mapping, rotation measure synthesis, QU fitting and a joint analysis with optical data. This analysis has helped provide evidence for the possible origins of the the wide variety of jet morphologies observed in three sources in detail, and enabled estimation of the magnetic field in the vicinity of Coma A.

6.1 Magnetic fields in AGN jets on large scales: The Cosmic Battery

It is believed that a helical magnetic field should be produced at the jet base by the combination of rotation and outflow, but it was initially thought impossible to detect kiloparsec–scale toroidal fields because the RM distribution would be dominated by a turbulent component. For this reason, searches for transverse RM gradients indicating the presence of a toroidal magnetic field component initially focused on parsec scales observable with VLBI, and about 50 AGN jets with transverse RM gradients have been detected to date (Gabuzda, Nagle & Roche 2018). The results presented in this thesis show that the toroidal field component of the initially helical magnetic field can persist on to the larger kiloparsec scales. The cosmic battery (Contopoulos et al. 2009) is a method by which the seed field that ultimately produces these helical fields can be generated by currents in the accretion disk. The model predicts that helical fields with associated inward electrical currents should dominate on small scales observable with VLBI, which has been the focus of intense study and now has been proven to be the case (Gabuzda, Nagle & Roche 2018).The model also predicts that toroidal fields with associated outward electrical currents are should dominate on kiloparsec scales, but this possibility was virtually unstudied until the work carried out in this thesis. A large scale study considered together with results for the small and intermediate scales probed with VLBI helps paint a whole picture of the system of electrical currents and fields in the jets of AGN.

In this thesis 9 objects were studied in total, and of these 6 featured strong evidence for the existence of toroidal magnetic fields in their jet structure. This was done through an in-depth study of the Faraday rotation measure and in particular transverse gradients in the rotation measure that were statistically significant. In two cases the, the transverse RM gradients were detected across both jets, bringing the total number of cases detected to 8. The direction of these gradients plays a very important role also, of the 8 significant results 6 showed gradients that indicated a toroidal magnetic field component with an associated outward electrical current in the jet, as is predicted for the system of magnetic fields associated with the cosmic battery. The sources NGC 6251, 3C 465, Coma A, A2142a, 5C 4.114 all show evidence of large scale toroidal fields in their jets. NGC 6251 shows a highly significant gradient which

changes sign across the jet when an integrated RM value has been subtracted, highly indicative of a toroidal field. 3C 465 shows significant RM gradients in a large portion of its Eastern jet with significant gradients spanning swathes of the jet ,10's of arcseconds in length. Coma A shows an impressive RM gradient that can be seen in high resolution archival data as well as in more recent wideband VLA observations, albeit at a lower resolution. A2142a and 5C 4.114 were found to have significant transverse gradients in their jets with the latter featuring significant gradients in both of its kiloparsec scale jets. Only IC 4296 shows toroidal fields with associated inward current. It is interesting that this object has a known dense atmosphere surrounding it, observed in the X-ray, which may be affecting the observed magnetic field structure.

The remaining sources 3C 303, 5C 4.152 and 3C 219 showed some tentative evidence of transverse RM gradients however these gradients proved not to be significant and/or monotonic enough to be trustworthy. 3C 303 features a gradient in one knot in the jet that had been reported previously, albeit without a robust statistical analysis of the errors in the RM and with an RM map made with data for only 2 frequencies. When the original data were calibrated again and a third frequency at a similar resolution was added, the transverse RM gradient was visible by eye, but had a maximum significance of only 1.5σ, too low to be considered a true physical gradient and more likely a spurious detection. 5C 4.152 shows evidence of gradients in both of its jets, however the significance of the transverse RM gradients is too low ($1.5–1.7\sigma$ at most) due to a combination of high noise in the data, observation over a relatively short span of wavelengths, and the possibility that this is simply a spurious result. 3C 219 has a gradient across a small portion of its Southern lobe that is quite significant however the RM values are substantially not monotonic within allowed tolerances and the gradient features in only a very small portion of the jet.

Taken on their own these results would be only suggestive concerning a predominance of outward jet currents on kiloparsec scales. However, when added to the data initially compiled by Christodoulou et al. (2016) for transverse RM gradients on scales greater than 10–20 parsec, they provide a convincing demonstration that the dominant currents are outward on kiloparsec scales with the probability of the presence for outward currents being spurious being only 0.3%.

Future work in this field is especially interesting in the Square Kilometre Array

(SKA) era given the development of new arrays in the southern hemisphere such as MeerKAT and ASKAP, as well as SKA itself. These telescopes will make detailed, high dynamic range maps at the centimetre wavelengths probed by the VLA. Surveys could also play an important role; the upcoming VLA sky survey (VLASS) aims to map the entire Northern sky using the S-band 2–4 GHz range and produce maps of the polarized emission and Faraday rotation of the bright individual sources with arcsecond scale resolution. This allows for the identification of many more rotation measure gradients, perhaps even utilising machine learning to do so. Similar surveys of the Southern sky creates even more opportunity for detection of evidence for helical magnetic fields in jets and the possibility that these jets form characteristic global patterns. The main aim of this would be to considerably increase the sample size of objects featuring evidence for toroidal/ helical magnetic fields in their jets and if the preference for outward electrical currents in the jets remains.

6.2 The interplay between external gas and the lobes of the radio galaxy Coma A

A comprehensive broadband radio polarization and Faraday rotation study of the nearby radio galaxy Coma A was presented in this thesis. Broadband VLA observations in the 1–2 GHz and 2–4 GHz ranges were analysed using RM synthesis and QU-model fitting. Large variations in the observed degree of polarization were observed over the radio galaxy, which is indicative of Faraday depolarization. Large variations in the RM were also observed across the Southern lobe, indicating a substantial change in the morphology of the jet and lobe. In conjunction with this, higher resolution archival observations at 4.9 and 15 GHz were also analysed, along with deep H α observations showing strong spatial correlation with the depolarized regions and the H α emission.

An external Faraday depolarizing screen inferred in this analysis is consistent with the broadband polarization data across most of the radio lobes. Due to the clear anti-correlation between the polarized emission and H α, this external Faraday screen is identified as the ionised gas seen in H α arcs and filaments surrounding the radio lobes. The H α emission is most likely caused by shock-ionisation of a gas disk (seen in neutral hydrogen) by the expanding radio lobes.

The H α image in combination with the Faraday rotation and depolarization results was used to estimate the magnetic field strength in this ionised gas surrounding the lobe. Magnetic field strengths of $< 1\,\mu$G were derived in the H α gas across most of the radio lobes, consistent with expectations for the magnetisation of gas in the local intergalactic medium. However, one particular H α filament that cuts across the southern lobe is clearly associated with a strong depolarization 'trough', this can be associated with internal Faraday depolarization, where the radio plasma mixes with the ionised Hα gas. One caveat is the volume filing factor of the ionised gas which is difficult to directly calculate and can only be either estimated from literature or calculated when pressure equilibrium with the radio lobe is assumed, which was done for the strongly depolarizing southern filament. Using this method a lower limit of $0.075\,\mu$G is calculated with a possible upper limit being of the order of the radio lobe field strength. This is one of the clearest direct observational examples of internal Faraday depolarization in the lobe of a radio galaxy. This adds to the complex ways that radio jets and lobes can interact with their environment, providing another means of "feedback" on local gas, which can both inhibit further star formation activity and substantially modify the evolution of radio galaxies.

6.3 Rotation measure analysis of 3C 433 and 3C 382 using wideband observations

In light of the successful study of the radio galaxy Coma A, further study into two further AGN was carried out. Wideband VLA observations of 3C 433 and 3C 382 were taken in the L and S bands from 1–4 GHz and a similar analysis was performed. Detailed maps of the rotation measure were not previously published for these sources. Using the wideband capabilities of the VLA, new methods for investigating the polarized emission from these jets could be used, such as rotation measure synthesis and QU model fitting. The former yield accurate rotation measure values along with information about how extended the unresolved flux was in Faraday depth and whether unresolved structures could be made out using the Faraday spectra. The latter allowed for an even more detailed view of unresolved structures, allowing for identification of possible multiple polarized components and internal or external Faraday dispersion.

3C 433 is an example of an 'X' or 'Z' shaped radio galaxy and is a hybrid morphology radio source (HYMORS) with antisymmetric wings of radio emission from each of its jets. The Southern jet is much brighter and typical of an FR II with a hotspot and lobe, however a contorted jet structure within the lobe has been proposed. The Northern jet is much fainter and more like an FR I, however the jet does terminate in a dim hotspot. The polarization structure of 3C 433 showed that most of the extended structure was dominated by single component, Faraday thin emission with surprisingly low depolarization, especially at the Southern hotspot where X-ray emission and HI had been detected previously. The model fits for the hotspot reveal a two component polarization structure with a common depolarization screen; the individual components can be made out in older archival observations published previously, and the common depolarization screen term may be due to a gas shell proposed to be surrounding the source (Gopal-Krishna et al. 2012). This large scale shell of gas is theorized to have been emitted after merger activity in the 3C 433 host, with the radio jets moving though it and the rotating shell causing the observed antisymmetric wings. Indeed this was also proposed earlier, as the unusual appearance of the Southern jet has been ascribed to it corkscrewing into a dense IGM (van Breugel et al. 1983).

The radio galaxy 3C 382 has a typical FR II structure with two large lobes and hotspots. The inner jet can be seen within the Northern lobe, with a visible knot where the jet deflects by $\sim 20^{\circ}$. The jet terminates at a bright hotspot. The polarization structure of the Northern lobe is quite detailed, with arcs of highly polarized ($> 30\%$ at 20cm) emission hugging the Southern edge of the lobe, and with the inferred intrinsic magnetic field hugging the lobe also. The Southern lobe features a hotspot and arc of high intensity emission forming a ring with the hotspot, which also has a high fractional polarization. There is a trail of diffuse emission out to the South-East, however this is not mirrored as much in the Northern lobe. Some elongation of the lobe to the left can be seen in the 20 cm images, however not as extreme as in the Southern lobe. As this is the lobe associated with the counter-jet, no narrow jet can be made out, however an arc of low fraction polarization is traced through the northern end of this lobe to the hotspot, which might indicate the presence of an obscured jet as suggested by Black et al. (1992).

Rotation measure maps were produced by traditional χ versus λ^2 fitting and rotation measure synthesis to investigate the detailed Faraday structure. The map of the peak rotation measure $\phi_{\rm peak}$ from the RM-synthesis showed a

gradient along the jet from one hotspot to the other, with the magnitude of the RM increasing toward the end of the counter jet. This is most likely a feature of the Laing-Garrington effect, where the larger volume of magneto-ionic material along the line of sight to the counter jet amplifies the rotation measure considerably by $\sim 25\,\mathrm{rad\,m^{-2}}$ from end to end. QU model fits of both the hotspots showed a single component with the Northern hotspot having a depolarization of almost zero, while the Southern hotspot featured a depolarization term of $\sigma_{\mathrm{RM}} = 3.2\,\mathrm{rad\,m^{-2}}$. A group environment of some kind probably exists here, but has yet to be observed at other wavelengths.

The analysis of the 2–4 GHz S–band observations in the VLA B configuration of these objects shows the potential of the VLA Sky Survey (VLASS), which will map the Northern sky using 2–4 GHz observations in the VLA B configuration.

Further work in the area of the interactions between radio lobes and their external media, as was done with Coma A, 3C 433 and 3C 382, could include more extensive deep X-ray images, as well as continuing the ongoing work on the H α images of the latter two sources. Another possibility is to investigate the neutral hydrogen in the form of H I. The new eROSITA X-ray telescope will provide information on large scale low resolution environments in galaxy clusters and AGN environments, while deep CHANDRA observations can offer information on the high resolution X-ray features seen in AGN jet cores and knots. The consideration of spectral line and high energy emission information is highly useful in investigating the environments around AGN.

A further new frontier in radio astronomical imaging of AGN is in the low frequency regime observed using LOFAR from 10–230 MHz. These low-frequency observations can reveal diffuse steep spectrum emission from jets, including polarization information (O'Sullivan et al. 2018). Long baseline interferometry with LOFAR is also possible, with arcsecond and even subarcsecond resolution images of AGN jets (Harris et al. 2019) achievable with the international LOFAR telescope, allowing for the first time comparable resolutions of high frequency VLA and low frequency LOFAR observations.

References

Algaba, J. C., Asada, K. & Nakamura, M. (2013), A Rotation Measure Gradient on the M87 VLA Jet, *in* 'The Innermost Regions of Relativistic Jets and Their Magnetic Fields, Granada, Spain, Edited by José L. Gómez', Vol. 61 of *European Physical Journal Web of Conferences*, p. 07003.

Anderson, C. S., Gaensler, B. M., Heald, G. H., O'Sullivan, S. P., Kaczmarek, J. F. & Feain, I. J. (2018), 'Broadband radio polarimetry of Fornax A, I: Depolarized patches generated by advected thermal material from NGC 1316', *The Astrophysical Journal* **855:41**(1), 27.

Anderson, C. S., O'Sullivan, S. P., Heald, G. H., Hodgson, T., Pasetto, A. & Gaensler, B. M. (2019), 'Blazar jet evolution revealed by multi-epoch broad-band radio polarimetry', *Monthly Notices of the Royal Astronomical Society* **485**(3), 3600–3622.

Antonucci, R. (1993), 'Unified models for active galactic nuclei and quasars.', *Annual Review of Astronomy and Astrophysics* **31**, 473–521.

Asada, K., Inoue, M., Uchida, Y., Kameno, S., Fujisawa, K., Iguchi, S. & Mutoh, M. (2002), 'A Helical Magnetic Field in the Jet of 3C 273', *Publications of the Astronomical Society of Japan* **54**, L39–L43.

Athreya, R. M., Kapahi, V. K., McCarthy, P. J. & van Breugel, W. (1998), 'Large rotation measures in radio galaxies at Z > 2', *Astronomy & Astrophysics* **329**, 809–820.

Barlow, R. (1993), *Statistics: A Guide to the Use of Statistical Methods in the Physical Sciences*, Manchester Physics Series, Wiley.

Baum, S. A., Heckman, T. M., Bridle, A., van Breugel, W. J. M. & Miley, G. K. (1988), 'Extended optical-line-emitting gas in radio galaxies - Broad-band optical, narrow-band optical, and radio imaging of a representative sample', *The Astrophysical Journal Supplement Series* **68**, 643.

Beck, R. & Krause, M. (2005), 'Revised equipartition and minimum energy formula for magnetic field strength estimates from radio synchrotron observations', *Astronomische Nachrichten* **326**(6), 414–427.

Beckmann, V. & Shrader, C. R. (2012), *Active galactic nuclei*, Wiley-VCH, Weinheim, Germany.

Bell, M. R. & Enßlin, T. A. (2012), 'Faraday synthesis. The synergy of aperture and rotation measure synthesis', *Astronomy & Astrophysics* **540**, A80.

Benbow, W. & VERITAS Collaboration (2012), Highlights of the VERITAS blazar program, *in* F. A. Aharonian, W. Hofmann & F. M. Rieger, eds, 'American Institute of Physics Conference Series', Vol. 1505 of *American Institute of Physics Conference Series*, pp. 482–485.

Black, A. R. S., Baum, S. A., Leahy, J. P., Perley, R. A., Riley, J. M. & Scheuer, P. A. G. (1992), 'A study of FRII radio galaxies with $z < 0.15$ – I. High-resolution maps of eight sources at 3.6 cm', *Monthly Notices of the Royal Astronomy Society* **256**(2), 186–208.

Blandford, R. D. & Payne, D. G. (1982), 'Hydromagnetic flows from accretion discs and the production of radio jets', *Monthly Notices of the Royal Astronomy Society* **199**(4), 883–903.

Blandford, R. D. & Rees, M. J. (1978), Some comments on radiation mechanisms in Lacertids., *in* A. M. Wolfe, ed., 'BL Lac Objects', pp. 328–341.

Blandford, R. D. & Znajek, R. L. (1977), 'Electromagnetic extraction of energy from Kerr black holes', *Monthly Notices of the Royal Astronomical Society* **179**(3), 433–456.

Blandford, R., Meier, D. & Readhead, A. (2019), 'Relativistic Jets from Active Galactic Nuclei', *Annual Reviews of Astronomy and Astrophysics* **57**, 467–509.

Bonafede, A., Feretti, L., Murgia, M., Govoni, F., Giovannini, G., Dallacasa, D., Dolag, K. & Taylor, G. B. (2010), 'The Coma cluster magnetic field from Faraday rotation measures', *Astronomy & Astrophysics* **513**, A30.

Böttcher, M., Harris, D. E. D. & Krawczynski, H. (2012), *Relativistic jets from active galactic nuclei*, Wiley-VCH, Weinheim, Germany.

Brentjens, M. A. & de Bruyn, a. G. (2005), 'Faraday rotation measure synthesis', *Astronomy & Astrophysics* **441**(3), 1217–1228.

Bridle, A. H., Fomalont, E. B., Palimaka, J. J. & Willis, A. G. (1981), 'VLA observation of radio/optical knots in 3C 277.3 = Coma A', *The Astrophysical Journal* **248**, 499.

Broderick, A. E. & McKinney, J. C. (2010), 'Parsec-scale Faraday Rotation Measures from General Relativistic Magnetohydrodynamic Simulations of Active Galactic Nucleus Jets', *The Astrophysical Journal* **725**(1), 750–773.

Burn, B. J. (1966), 'On the Depolarization of Discrete Radio Sources by Faraday Dispersion', *Monthly Notices of the Royal Astronomy Society* **133**(1), 67–83.

Cantó, J., Curiel, S. & Martínez-Gómez, E. (2009), 'A simple algorithm for optimization and model fitting: AGA (asexual genetic algorithm)', *Astronomy & Astrophysics* **501**(3), 1259–1268.

Cantwell, T. (2018), Low frequency radio observations of galaxy clusters and groups, PhD thesis, University of Manchester.

Capetti, A., Celotti, A., Chiaberge, M., de Ruiter, H. R., Fanti, R., Morganti, R. & Parma, P. (2002), 'The HST survey of the B2 sample of radio-galaxies: Optical nuclei and the FR I/BL Lac unified scheme', *Astronomy & Astrophysics* **383**(1), 104–111.

Chatterjee, K., Liska, M., Tchekhovskoy, A. & Markoff, S. B. (2019), 'Accelerating AGN jets to parsec scales using general relativistic MHD simulations', *Monthly Notices of the Royal Astronomical Society* **19**(May), 1–19.

Cheung, C. C., Harris, D. E. & Stawarz, Ł. (2007), 'Superluminal Radio Features in the M87 Jet and the Site of Flaring TeV Gamma-Ray Emission', *The Astrophysical Journal Letters* **663**(2), L65–L68.

Chiaberge, M., Capetti, A. & Celotti, A. (1999), 'The HST view of FR I radio galaxies: evidence for non-thermal nuclear sources', *Astronomy & Astrophysics* **349**, 77–87.

Christodoulou, D. M., Gabuzda, D. C., Knuettel, S., Contopoulos, I., Kazanas, D. & Coughlan, C. P. (2016), 'Dominance of outflowing electric currents on decaparsec to kiloparsec scales in extragalactic jets', *Astronomy & Astrophysics* **591**, A61.

Clark, B. G. (1980), 'An efficient implementation of the algorithm 'CLEAN", *Astronomy & Astrophysics* **89**(3), 377.

Clarke, D. A., Bridle, A. H., Burns, J. O., Perley, R. A. & Norman, M. L. (1992), 'Origin of the structures and polarization in the classical double 3C 219', *The Astrophysical Journal* **385**, 173.

Contopoulos, I., Christodoulou, D. M., Kazanas, D. & Gabuzda, D. C. (2009), 'the Invariant Twist of Magnetic Fields in the Relativistic Jets of Active Galactic Nuclei', *The Astrophysical Journal* **702**(2), L148–L152.

Contopoulos, I. & Kazanas, D. (1998), 'A Cosmic Battery', *The Astrophysical Journal* **508**(2), 859–863.

Contopoulos, I., Nathanail, A., Sądowski, A., Kazanas, D. & Narayan, R. (2018), 'Numerical simulations of the Cosmic Battery in accretion flows around astrophysical black holes', *Monthly Notices of the Royal Astronomy Society* **473**(1), 721–727.

Conway, R. G. & Kronberg, P. P. (1969), 'Interferometric measurement of polarization distribution in radio sources', *Monthly Notices of the Royal Astronomy Society* **142**(1), 11.

Cornwell, T. J. (2008), 'Multiscale CLEAN Deconvolution of Radio Synthesis Images', *IEEE Journal of Selected Topics in Signal Processing* **2**(5), 793–801.

Coughlan, C. P. (2014), The Development of New Methods for High Resolution Radio Astronomy Imaging, PhD thesis, University College Cork.

Croke, S. M., O'Sullivan, S. P. & Gabuzda, D. C. (2010), 'The parsec-scale distributions of intensity, linear polarization and Faraday rotation in the core and jet of Mrk501 at 8.4-1.6 GHz', *Monthly Notices of the Royal Astronomy Society* **402**(1), 259–270.

Curtis, H. (1918), 'Descriptions of 762 Nebulae and Clusters Photographed with the Crossley Reflector', *Publications of Lick Observatory* **13**, 9–42.

de Gasperin, F. (2017), 'Multifrequency study of a new hybrid morphology radio source', *Monthly Notices of the Royal Astronomy Society* **467**(2), 2234–2240.

De Young, D. S. (1993), 'On the Relation between Fanaroff-Riley Types I and II Radio Galaxies', *The Astrophysical Journal Letters* **405**, L13.

Dursi, L. J. & Pfrommer, C. (2008), 'Draping of Cluster Magnetic Fields over Bullets and Bubbles—Morphology and Dynamic Effects', *The Astrophysical Journal* **677**, 993–1018.

Eilek, J. A., Burns, J. O., Odea, C. P. & Owen, F. N. (1984), 'What bends 3c 465?', *The Astrophysical Journal* **278**, 37.

Eilek, J. A. & Owen, F. N. (2002), 'Magnetic Fields in Cluster Cores: Faraday Rotation in A400 and A2634', *The Astrophysical Journal* **567**(1), 202–220.

Eracleous, M. & Halpern, J. P. (2004), 'Accurate Redshifts and Classifications for 110 Radio-Loud Active Galactic Nuclei', *The Astrophysical Journal Supplement Series* **150**(1), 181–186.

Evans, D. A., Hardcastle, M. J., Croston, J. H., Worrall, D. M. & Birkinshaw, M. (2005), 'Chandra and XMM-Newton observations of NGC 6251', *Monthly Notices of the Royal Astronomy Society* **359**(1), 363–382.

Event Horizon Telescope Collaboration (2019), 'First M87 Event Horizon Telescope Results. I. The Shadow of the Supermassive Black Hole', *The Astrophysical Journal Supplement Letters* **875**(1), L1.

Fabian, A. C. (2012), 'Observational Evidence of AGN Feedback', *Annual Review of Astronomy and Astrophysics* **50**, 455–89.

Fanaroff, B. L. & Riley, J. M. (1974), 'The Morphology of Extragalactic Radio Sources of High and Low Luminosity', *Monthly Notices of the Royal Astronomy Society* **167**(1), 31P–36P.

Gabuzda, D. (2008), Radiation Processes in the Universe: Synchrotron Radiation and Propagation Effects, *in* '2nd MCCT-SKADS Training School. Radio Astronomy: Fundamentals and the New Instruments', p. 9.

Gabuzda, D. C., Cantwell, T. M. & Cawthorne, T. V. (2014), 'Magnetic field structure of the extended 3C 380 jet', *Monthly Notices of the Royal Astronomy Society* **438**(1), L1–L5.

Gabuzda, D. C., Knuettel, S. & Bonafede, A. (2015), 'Evidence for a Toroidal Magnetic-Field Component in 5C4.114 on Kiloparsec Scales', *Astronomy & Astrophysics* **583**, A96.

Gabuzda, D. C., Knuettel, S. & Reardon, B. (2015), 'Transverse Faraday-Rotation Gradients Across the Jets of 15 Active Galactic Nuclei', *Monthly Notices of the Royal Astronomical Society* **450**(3), 2441–2450.

Gabuzda, D. C., Knuettel, S., Richardson, F., Kyprianou, J. & Spillane, M. (2018), First results of 1.4–5.0 ghz vlba observations of the mojave–ii agns, *in* 'Proceedings of the 14th European VLBI Network Symposium & Users Meeting. 8-11 October 2018', Vol. 344.

Gabuzda, D. C., Nagle, M. & Roche, N. (2018), 'The jets of AGN as giant coaxial cables', *Astronomy & Astrophysics* **612**(A67), A67.

Gabuzda, D. C., Reichstein, A. R. & O'Neill, E. L. (2014), 'Are spine-sheath polarization structures in the jets of active galactic nuclei associated with helical magnetic fields?', *Monthly Notices of the Royal Astronomy Society* **444**(1), 172–184.

Gabuzda, D. C., Roche, N., Kirwan, A., Knuettel, S., Nagle, M. & Houston, C. (2017), 'Parsec Scale Faraday-Rotation Structure Across the Jets of 9 Active Galactic Nuclei', *Monthly Notices of the Royal Astronomy Society* **472**(2), 1792–1801.

Gaensler, B. M. (2005), 'The Magnetic Field of the Large Magellanic Cloud Revealed Through Faraday Rotation', *Science* **307**(5715), 1610–1612.

Gan, Z., Li, H., Li, S. & Yuan, F. (2017), 'Three-dimensional Magnetohydrodynamical Simulations of the Morphology of Head–Tail Radio Galaxies Based on the Magnetic Tower Jet Model', *The Astrophysical Journal* **839**(1), 14.

Garrington, S. T., Leahy, J. P., Conway, R. G. & Laingt, R. A. (1988), 'A systematic asymmetry in the polarization properties of double radio sources with one jet', *Nature* **331**(6152), 147–149.

Gawronski, M. P., Marecki, A., Kunert-Bajraszewska, M. & Kus, A. J. (2006), 'Hybrid morphology radio sources from the FIRST survey', *Astronomy & Astrophysics* **447**, 63–70.

Ghez, A. M., Salim, S., Weinberg, N. N., Lu, J. R., Do, T., Dunn, J. K., Matthews, K., Morris, M. R., Yelda, S., Becklin, E. E., Kremenek, T., Milosavljevic, M. & Naiman, J. (2008), 'Measuring Distance and Properties of the Milky Way's Central Supermassive Black Hole with Stellar Orbits', *The Astrophysical Journal* **689**(2), 1044–1062.

Ghisellini, G. & Celotti, A. (2001), 'The dividing line between FR I and FR II radio-galaxies', *Astronomy & Astrophysics* **379**, L1–L4.

Ghisellini, G., Righi, C., Costamante, L. & Tavecchio, F. (2017), 'The Fermi blazar sequence', *Monthly Notices of the Royal Astronomy Society* **469**(1), 255–266.

Gliozzi, M., Sambruna, R. M., Eracleous, M. & Yaqoob, T. (2007), 'The Nature of a Broad-Line Radio Galaxy: Simultaneous RXTE and Chandra HETG Observations of 3C 382', *The Astrophysical Journal* **664**(1), 88–100.

Globus, N. & Levinson, A. (2016), 'The collimation of magnetic jets by disc winds', *Monthly Notices of the Royal Astronomy Society* **461**(3), 2605–2615.

Gómez, J. L., Lobanov, A. P., Bruni, G., Kovalev, Y. Y., Marscher, A. P., Jorstad, S. G., Mizuno, Y., Bach, U., Sokolovsky, K. V., Anderson, J. M., Galindo, P., Kardashev, N. S. & Lisakov, M. M. (2016), 'Probing the innermost regions of agn jets and their magnetic fields with radioastron. i. imaging bl lacertae at 21 microarcsecond resolution', *The Astrophysical Journal* **817**(2), 96.

Gopal-Krishna, Biermann, P. L., Gergely, L. Á. & Wiita, P. J. (2012), 'On the origin of X-shaped radio galaxies', *Research in Astronomy and Astrophysics* **12**(2), 127–146.

Gopal-Krishna & Wiita, P. J. (2000*a*), 'Extragalactic radio sources with hybrid morphology: implications for the Fanaroff-Riley dichotomy', *Astronomy & Astrophysics* **363**, 507–516.

Gopal-Krishna & Wiita, P. J. (2000*b*), 'Superdisks in Radio Galaxies', *The Astrophysical Journal* **529**, 189–200.

Govoni, F., Dolag, K., Murgia, M., Feretti, L., Schindler, S., Giovannini, G., Boschin, W., Vacca, V. & Bonafede, A. (2010), 'Rotation measures of radio sources in hot galaxy clusters', *Astronomy & Astrophysics* **522**(8), 105.

Grossová, R., Werner, N., Rajpurohit, K., Mernier, F., Lakhchaura, K., Gabányi, K., Canning, R. E. A., Nulsen, P., Massaro, F., Sun, M., Connor, T., King, A., Allen, S. W., Frisbie, R. L. S., Donahue, M. & Fabian, A. C. (2019), 'Powerful AGN jets and unbalanced cooling in the hot atmosphere of IC 4296', *Mpnthly Notices of the Royal Astronomy Society* **488**(2), 1917–1925.

Guidetti, D., Laing, R. A., Bridle, A. H., Parma, P. & Gregorini, L. (2011), 'Ordered magnetic fields around radio galaxies: Evidence for interaction with the environment', *Monthly Notices of the Royal Astronomy Society* **413**(4), 2525–2544.

Guidetti, D., Laing, R. A., Murgia, M., Govoni, F., Gregorini, L. & Parma, P. (2010), 'Astrophysics Structure of the magnetoionic medium around the Fanaroff-Riley Class I radio galaxy 3C 449', *Astronomy & Astrophysics* **514**, 50.

Hardcastle, M. J., Evans, D. A. & Croston, J. H. (2007), 'Hot and cold gas accretion and feedback in radio-loud active galaxies', *Monthly Notices of the Royal Astronomy Societey* **376**(4), 1849–1856.

Harris, D. E., Moldón, J., Oonk, J. R. R., Massaro, F., Paggi, A., Deller, A., Godfrey, L., Morganti, R. & Jorstad, S. G. (2019), 'LOFAR Observations of 4C+19.44: On the Discovery of Low-frequency Spectral Curvature in Relativistic Jet Knots', *The Astrophysical Journal* **873**(1), 21.

Heald, G., Braun, R. & Edmonds, R. (2009), 'The Westerbork SINGS survey', *Astronomy & Astrophysics* **503**(2), 409–435.

Heckman, T. & Best, P. (2014), 'The Co-Evolution of Galaxies and Supermassive Black Holes: Insights from Surveys of the Contemporary Universe', *Annual Review of Astronomy and Astrophysics* **52**, 589–660.

Heckman, T. M. (1980), 'An optical and radio survey of the nuclei of bright galaxies. Activity in normal galactic nuclei.', *Astronomy & Astrophysicss* **500**, 187–199.

Hernán-Caballero, A., Spoon, H. W. W., Lebouteiller, V., Rupke, D. S. N. & Barry, D. P. (2016), 'The infrared database of extragalactic observables from Spitzer – I. The redshift catalogue', *Monthly Notices of the Royal Astronomical Society* **455**(2), 1796–1806.

Hewett, P. C. & Wild, V. (2010), 'Improved redshifts for SDSS quasar spectra', *Monthly Notices of the Royal Astronomy Society* **405**(4), 2302–2316.

Hewitt, A. & Burbidge, G. (1991), 'An Optical Catalog of Extragalactic Emission-Line Objects Similar to Quasi-stellar Objects', *The Astrophysical Journal Supplement Series* **75**, 297.

Hodges-Kluck, E. J., Reynolds, C. S., Cheung, C. C. & Miller, M. C. (2010), 'The Chandra View of Nearby X-Shaped Radio Galaxies', *The Astrophysical Journal* **710**(2), 1205–1227.

Högbom, J. A. (1974), 'Aperture Synthesis with a Non-Regular Distribution of Interferometer Baselines', *Astronomy & Astrophysics Supplement* **15**, 417.

Hovatta, T., Lister, M. L., Aller, M. F., Aller, H. D., Homan, D. C., Kovalev, Y. Y., Pushkarev, A. B. & Savolainen, T. (2012), 'MOJAVE: Monitoring of jets in active galactic nuclei with VLBA experiments. VIII. Faraday rotation in parsec-scale AGN jets', *The Astronomical Journal* **144**(4), 105.

Jorstad, S. & Marscher, A. (2016), 'The VLBA-BU-BLAZAR Multi-Wavelength Monitoring Program', *Galaxies* **4**, 47.

Kellermann, K. I., Sramek, R., Schmidt, M., Shaffer, D. B. & Green, R. (1989), 'VLA Observations of Objects in the Palomar Bright Quasar Survey', *The Astronomical Journal* **98**, 1195.

Khachikian, E. Y. & Weedman, D. W. (1974), 'An atlas of Seyfert galaxies.', *The Astrophysical Journal* **192**, 581–589.

Killeen, N. E. B., Bicknell, G. V. & Ekers, R. D. (1986), 'The radio galaxy IC 4296 (PKS 1333 - 33). I - Multifrequency Very Large Array observations', *The Astrophysical Journal* **302**, 306.

Kim, J. Y., Krichbaum, T. P., Lu, R. S., Ros, E., Bach, U., Bremer, M., de Vicente, P., Lindqvist, M. & Zensus, J. A. (2018), 'The limb-brightened jet of M87 down to the 7 Schwarzschild radii scale', *Astronomy & Astrophysics* **616**, A188.

Knuettel, S. & Gabuzda, D. (2019), Toroidal magnetic fields and associated currents in agn jets on kiloparsec scales, *in* 'Proceedings of the 14th European VLBI Network Symposium & Users Meeting. 8-11 October 2018', Vol. 344.

Knuettel, S., Gabuzda, D. & O'Sullivan, S. (2017), 'Evidence for Toroidal B-Field Components in AGN Jets on Kiloparsec Scales', *Galaxies* **5**, 61.

Knuettel, S., O'Sullivan, S. P., Curiel, S. & Emonts, B. H. C. (2019), 'The magnetic field strength of the Faraday screen surrounding the radio galaxy Coma A', *Monthly Notices of the Royal Astronomy Societey* **482**(4), 4606–4616.

Kronberg, P. P., Lovelace, R. V. E., Lapenta, G. & Colgate, S. A. (2011), 'Measurement of the electric current in a kpc-scale jet', *The Astrophysical Journal Letters* **741**(1), L15.

Laing, R. A. (1981), 'Magnetic fields in extragalactic radio sources.', *The Astrophysical Journal* **248**, 87–104.

Laing, R. A. (1988), 'The sidedness of jets and depolarization in powerful extragalactic radio sources', *Nature* **331**, 149–151.

Laing, R. A., Bridle, A. H., Parma, P. & Murgia, M. (2008), 'Structures of the magnetoionic media around the Fanaroff-Riley Class I radio galaxies 3C 31 and Hydra A', *Monthly Notices of the Royal Astronomy Society* **391**, 521–549.

Leahy, J. P. & Perley, R. A. (1991), 'VLA images of 23 extragalactic radio sources', *The Astronomical Journal* **102**(2), 537–561.

Leahy, P. & Fernini, I. (1989), VLA Scientific Memorandum No. 161 Correction Schemes for Polarized Intensity, Technical report, National Radio Astronomy Observatory.

Levinson, A. & Globus, N. (2017), 'Reconfinement of highly magnetized jets: implications for HST-1 in M87', *Monthly Notices of the Royal Astronomy Society* **465**(2), 1608–1612.

Lister, M., Aller, M., Aller, H., Hodge, M., Homan, D., Kovalev, Y., Pushkarev, A. & Savolainen, T. (2018), 'MOJAVE. XV. VLBA 15 GHz Total intensity and polarization maps of 437 parsec-scale AGN jets from 1996 to 2017', *The Astrophysical Journal Supplement Series* **234**(1), 12.

Lovelace, R. V. E. (1976), 'Dynamo model of double radio sources', *Nature* **262**(5570), 649–652.

Lynden-Bell, D. (1969), 'Galactic Nuclei as Collapsed Old Quasars', *Nature* **223**(5207), 690–694.

Mack, K.-H., Kerp, J. & Klein, U. (1997), 'The X-ray jet and halo of NGC 6251', *Astonomy & Astrophysics* **324**, 870–876.

Mahmud, M., Coughlan, C. P., Murphy, E., Gabuzda, D. C. & Hallahan, D. R. (2013), 'Connecting magnetic towers with Faraday rotation gradients in active galactic nuclei jets', *Monthly Notices of the Royal Astronomy Society* **431**(1), 695–709.

Mao, S. A., Carilli, C., Gaensler, B. M., Wucknitz, O., Keeton, C., Basu, A., Beck, R., Kronberg, P. P. & Zweibel, E. (2017), 'Detection of microgauss coherent magnetic fields in a galaxy five billion years ago', *Nature Astronomy* **1**(9), 621–626.

Mao, S. A., Gaensler, B. M., Stanimirović, S., Haverkorn, M., McClure-Griffiths, N. M., Staveley-Smith, L. & Dickey, J. M. (2008), 'A Radio and Optical

Polarization Study of the Magnetic Field in the Small Magellanic Cloud', *The Astrophysical Journal* **688**(2), 1029–1049.

Marscher, A. P., Jorstad, S. G., D'Arcangelo, F. D., Smith, P. S., Williams, G. G., Larionov, V. M., Oh, H., Olmstead, A. R., Aller, M. F., Aller, H. D., McHardy, I. M., Lähteenmäki, A., Tornikoski, M., Valtaoja, E., Hagen-Thorn, V. A., Kopatskaya, E. N., Gear, W. K., Tosti, G., Kurtanidze, O., Nikolashvili, M., Sigua, L., Miller, H. R. & Ryle, W. T. (2008), 'The inner jet of an active galactic nucleus as revealed by a radio-to-γ-ray outburst', *Nature* **452**(7190), 966–969.

McClure-Griffiths, N. M., Madsen, G. J., Gaensler, B. M., McConnell, D. & Schnitzeler, D. H. F. M. (2010), 'Measurement of a magnetic field in a leading arm high-velocity cloud ', *The Astrophysical Journal* **725**(1), 275–281.

McKinney, J. C. (2006), 'General relativistic magnetohydrodynamic simulations of the jet formation and large-scale propagation from black hole accretion systems', *Monthly Notices of the Royal Astronomy Society* **368**(4), 1561–1582.

McKinney, J. C. & Blandford, R. D. (2009), 'Stability of relativistic jets from rotating, accreting black holes via fully three-dimensional magnetohydrodynamic simulations', *Monthly Notices of the Royal Astronomical Society: Letters* **394**(1), L126–L130.

Merloni, A. & Heinz, S. (2008), 'A synthesis model for AGN evolution: supermassive black holes growth and feedback modes', *Monthly Notices of the Royal Astronomy Society* **388**(3), 1011–1030.

Miller, B. P. & Brandt, W. N. (2009), 'Chandra observations of the hybrid morphology radio sources 3C 433 and 4C 65.15: FR IIs with asymmetric environments', *Astrophysical Journal* **695**(1), 755–764.

Mirabel, I. (1989), 'Atomic hydrogen in the powerful radio-infrared galaxies 4C 12.50 and 3C 433', *The Astrophysical Journal Letters* **340**, L13–L16.

Morganti, R., Oosterloo, T. A., Tinti, S., Tadhunter, C. N., Wills, K. A. & van Moorsel, G. (2002), 'Large-scale gas disk around the radio galaxy Coma A', *Astronomy & Astrophysics* **387**(3), 830–837.

Morganti, R., Oosterloo, T., Tadhunter, C. & Emonts, B. (2003), 'Large-scale H

I structures and the origin of radio galaxies', *New Astronomy Reviews* **47**(4-5), 273–277.

Motter, J. C. & Gabuzda, D. C. (2017), '18–22 cm VLBA Faraday rotation studies of six AGN jets', *Monthly Notices of the Royal Astromomy Society* **467**(3), 2648–2663.

Nakamura, M., Asada, K., Hada, K., Pu, H.-Y., Noble, S., Tseng, C., Toma, K., Kino, M., Nagai, H., Takahashi, K., Algaba, J.-C., Orienti, M., Akiyama, K., Doi, A., Giovannini, G., Giroletti, M., Honma, M., Koyama, S., Lico, R., Niinuma, K. & Tazaki, F. (2018), 'Parabolic Jets from the Spinning Black Hole in M87', *The Astrophysical Journal* **868**(2), 146.

Osterbrock, D. E., Koski, A. T. & Phillips, M. M. (1975), 'Broad Balmer Emission Lines in Radio Galaxies', *The Astrophysical Journal Letters* **197**, L41.

Osterbrock, D. E. & Pogge, R. W. (1985), 'The spectra of narrow-line Seyfert 1 galaxies.', *The Astrophysical Journal* **297**, 166–176.

O'Sullivan, S. P., Brown, S., Robishaw, T., Schnitzeler, D. H. F. M., Mcclure-Griffiths, N. M., Feain, I. J., Taylor, A. R., Gaensler, B. M., Landecker, T. L., Harvey-Smith, L. & Carretti, E. (2012), 'Complex Faraday depth structure of active galactic nuclei as revealed by broad-band radio polarimetry', *Monthly Notices of the Royal Astronomical Society* **421**(4), 3300–3315.

O'Sullivan, S. P., Brüggen, M., Van Eck, C. L., Hardcastle, M. J., Haverkorn, M., Shimwell, T. W., Tasse, C., Vacca, V., Horellou, C. & Heald, G. (2018), 'Untangling cosmic magnetic fields: Faraday tomography at metrewavelengths with LOFAR', *Galaxies* **6**(4).

O'Sullivan, S. P., Feain, I. J., McClure-Griffiths, N. M., Ekers, R. D., Carretti, E., Robishaw, T., Mao, S. A., Gaensler, B. M., Bland-Hawthorn, J. & Stawarz (2013), 'Thermal plasma in the giant lobes of the radio galaxy Centaurus A', *The Astrophysical Journal* **764**(2), 162.

Owen, F. N. & Rudnick, L. (1976), 'Radio sources with wide-angle tails in Abell clusters of galaxies.', *The Astrophysical Journal Letters* **205**, L1–L4.

Pearson, T. J., Unwin, S. C., Cohen, M. H., Linfield, R. P., Readhead, A. C. S., Seielstad, G. A., Simon, R. S. & Walker, R. C. (1981), 'Superluminal expansion of quasar 3C273', *Nature* **290**(5805), 365–368.

Perley, R. A., Bridle, A. H. & Willis, A. G. (1984), 'High-resolution VLA observations of the radio jet in NGC 6251', *The Astrophysical Journal Supplement Series* **54**, 291.

Perley, R. A. & Butler, B. J. (2017), 'An Accurate Flux Density Scale from 50 MHz to 50 GHz', *The Astrophysical Journal Supplement Series* **230**(1), 7.

Perley, R. & Sault, B. (2014), EVLA Memo 178 Stability of EVLA Polarizers at L, S, C, and X Bands, Technical report, National Radio Astronomy Observatory.

Planck Collaboration (2016), '*Planck* 2015 results', *Astronomy & Astrophysics* **594**, A11.

Rau, U. & Cornwell, T. J. (2011), 'A multi-scale multi-frequency deconvolution algorithm for synthesis imaging in radio interferometry', *Astronomy & Astrophysics* **532**, A71.

Roche, N. & Eales, S. A. (2000), 'Optical/ultraviolet morphology and alignment of low-redshift radio galaxies', *Monthly Notices of the Royal Astronomy Society* **317**(1), 120–140.

Rowan-Robinson, M. (1977), 'On the unity of activity in galaxies.', *The Astrophysical Journal* **213**, 635–647.

Rybicki, G. B. & Lightman, A. P. (1979), *Radiative processes in astrophysics*, Wiley, New York.

Salpeter, E. E. (1964), 'Accretion of Interstellar Matter by Massive Objects.', *The Astrophysical Journal* **140**, 796.

Sbarrato, T., Ghisellini, G., Maraschi, L. & Colpi, M. (2012), 'The relation between broad lines and γ-ray luminosities in fermi blazars', *Monthly Notices of the Royal Astronomy Society* **421**(2), 1764–1778.

Schure, K. M., Bell, A. R., O'C Drury, L. & Bykov, A. M. (2012), 'Diffusive Shock Acceleration and Magnetic Field Amplification', *Space Science Reviews* **173**, 491–519.

Simard-Normandin, M., Kronberg, P. P. & Button, S. (1981), 'The Faraday rotation measures of extragalactic radio sources', *The Astrophysical Journal Supplement Series* **45**, 97.

Smith, R. J., Lucey, J. R., Hudson, M. J., Schlegel, D. J. & Davies, R. L. (2000), 'Streaming motions of galaxy clusters within 12000kms^{-1} - I. New

spectroscopic data', *Monthly Notices of the Royal Astronomy Society* **313**(3), 469–490.

Sokoloff, D. D., Bykov, A. A., Shukurov, A., Berkhuijsen, E. M., Beck, R. & Poezd, A. D. (1998), 'Depolarization and Faraday effects in galaxies', *Monthly Notices of the Royal Astronomy Society* **299**(1), 189–206.

Solorzano-Inarrea, C. & Tadhunter, C. N. (2003), 'INTEGRAL spectroscopy of three powerful radio galaxies: Jet-cloud interactions seen in 3-D', *Monthly Notices of the Royal Astronomy Society* **340**(3), 705–721.

Stawarz, Tanaka, Y. T., Madejski, G., O'Sullivan, S. P., Cheung, C. C., Feain, I. J., Fukazawa, Y., Gandhi, P., Hardcastle, M. J., Kataoka, J., Ostrowski, M., Reville, B., Siemiginowska, A., Simionescu, A., Takahashi, T., Takei, Y., Takeuchi, Y. & Werner, N. (2013), 'Giant lobes of Centaurus a radio galaxy observed with the Suzaku x-ray satellite', *The Astrophysical Journal* **766**(1), 48.

Strom, R. G., Willis, A. G. & Wilson, A. S. (1978), 'Two-frequency high resolution observations of 3C 382 and 3C 386.', *Astronomy & Astrophysics* **68**, 367–379.

Struble, M. F. & Rood, H. J. (1999), 'A Compilation of Redshifts and Velocity Dispersions for ACO Clusters', *The Astrophysical Journal Supplement Series* **125**(1), 35–71.

Tadhunter, C. N., Villar-Martin, M., Morganti, R., Bland-Hawthorn, J. & Axon, D. (2000), 'The large-scale distribution of warm ionized gas around nearby radio galaxies with jet-cloud interactions', *Monthly Notices of the Royal Astronomy Society* **314**(4), 849–857.

Taylor, A. R., Stil, J. M. & Sunstrum, C. (2009), 'A Rotation Measure Image of the Sky', *The Astrophysical Journal* **702**(2), 1230–1236.

Tchekhovskoy, A. & Bromberg, O. (2016), 'Three-dimensional relativistic MHD simulations of active galactic nuclei jets: Magnetic kink instability and Fanaroff-Riley dichotomy', *Monthly Notices of the Royal Astronomy Society* **461**(1), L46–L50.

Thompson, A. R. (1999), Fundamentals of Radio Interferometry, *in* G. B. Taylor, C. L. Carilli & R. A. Perley, eds, 'Synthesis Imaging in Radio Astronomy II', Vol. 180 of *Astronomical Society of the Pacific Conference Series*, p. 11.

Thompson, A. R., Moran, J. M. & Swenson, G. W. (2017), *Interferometry and Synthesis in Radio Astronomy*, Astronomy and Astrophysics Library, 3 edn, Springer International Publishing, Cham, Switzerland.

Tilak, A., O'Dea, C. P., Tadhunter, C., Wills, K., Morganti, R., Baum, S. A., Koekemoer, A. M. & Dallacasa, D. (2005), 'Resolving the shocks in radio galaxy nebulae:hubble space telescopeand radio imaging of 3c 171, 3c 277.3, and PKS 2250-41', *The Astronomical Journal* **130**(6), 2513–2521.

Urry, C. M. & Padovani, P. (1995), 'Unified Schemes for Radio-Loud Active Galactic Nuclei', *Publications of the Astronomical Society of the Pacific* **107**, 803.

Ursini, F., Petrucci, P. O., Matt, G., Bianchi, S., Cappi, M., Dadina, M., Grandi, P., Torresi, E., Ballantyne, D. R., De Marco, B., De Rosa, A., Giroletti, M., Malzac, J., Marinucci, A., Middei, R., Ponti, G. & Tortosa, A. (2018), 'Radio/X-ray monitoring of the broad-line radio galaxy 3C 382. High-energy view with XMM-Newton and NuSTAR', *Monthly Notices of the Royal Astronomy Society* **478**(2), 2663–2675.

van Breugel, W., Balick, B., Heckman, T., Miley, G. & Helfand, D. (1983), 'The peculiar radio galaxy 3C 433', *The Astrophysical Journal* **88**(1), 40–54.

van Breugel, W., Heckman, T. & Miley, G. (1984), 'Optical line emission associated with the radio galaxy 4C 26.42 in the cluster of galaxies Abell 1795', *The Astrophysical Journal* **276**, 79.

van Breugel, W., Miley, G., Heckman, T., Butcher, H. & Bridle, A. (1985), 'Optical emission-line gas associated with the radio source 3C 277.3', *The Astrophysical Journal* **290**, 496.

Walker, R. C., Hardee, P. E., Davies, F. B., Ly, C. & Junor, W. (2018), 'The Structure and Dynamics of the Subparsec Jet in M87 Based on 50 VLBA Observations over 17 Years at 43 GHz', *The Astrophysical Journal* **855**(2), 128.

Wegner, G., Bernardi, M., Willmer, C. N. A., da Costa, L. N., Alonso, M. V., Pellegrini, P. S., Maia, M. A. G., Chaves, O. L. & Rité, C. (2003), 'Redshift-Distance Survey of Early-Type Galaxies: Spectroscopic Data', *The Astronomical Journal* **126**(5), 2268–2280.

Wegner, G., Colless, M., Saglia, R. P., McMahan, R. K., Davies, R. L., Burstein, D. & Baggley, G. (1999), 'The peculiar motions of early-type galaxies in two

distant regions - II. The spectroscopic data', *Monthly Notices of the Royal Astronomy Socitey* **305**(2), 259–296.

Wills, K. A., Tadhunter, C. N., Robinson, T. G. & Morganti, R. (2002), 'The ultraviolet excess in nearby powerful radio galaxies: evidence for a young stellar component', *Monthly Notices of the Royal Astronomy Society* **333**(1), 211–221.

Worrall, D. M., Birkinshaw, M. & Young, A. J. (2016), 'X-rays associated with the jet–cloud-interacting radio galaxy 3C 277.3 (Coma A): implications for energy deposition', *Monthly Notices of the Royal Astronomy Society* **458**(1), 174–183.

Wright, E. L. (2006), 'A Cosmology Calculator for the World Wide Web', *Publications of the Astronomical Society of the Pacific* **118**, 1711–1715.

Zwicky, F., Herzog, E. & Wild, P. (1963), *Catalogue of galaxies and of clusters of galaxies, Vol. 2*, Pasadena: California Institute of Technology (CIT).